SP-31

# SPECIAL PUBLICATION OF NATIONAL AEROSPACE LABORATORY

## SP-31

Government-Industry Specific Joint Research on
## The Advanced Aircraft Component Technologies

**Final Report**

May 1996

National Aerospace Laboratory
Mitsubishi Heavy Industries, Ltd
Kawasaki Heavy Industries, Ltd
Fuji Heavy Industries, Ltd

Government-Industry Specific Joint Research on

# The Advanced Aircraft Component Technologies

Final Report

May 1996

National Aerospace Laboratory
Mitsubishi Heavy Industries, Ltd
Kawasaki Heavy Industries, Ltd
Fuji Heavy Industries, Ltd

# PREFACE

The Science and Technology Agency (STA) of the Japanese Government set up a framework in 1986 to promote research collaboration between the national research institutes under its supervision and the domestic industries in order to encourage the industrial sector to avail themselves of the potential and the resources possessed by the national research institutes. The framework, tentatively translated here as the 'Government-Industry Joint Research Programs on Specific Topics', has since been instrumental in accelerating the technology transfer from the governmental research level to the industrial activities. The research works reported in the present volume were carried out within this framework for the period of 1992 to 1994.

For years, the National Aerospace Laboratory (NAL) had been engaged in the research of high speed aircraft technologies ranging from supersonic transports to space planes, mainly in the fields of propulsion and structure, including materials. Most of this research had been of a preliminary and in-house nature. As the subsonic aircraft technologies maturing, the research incentive within NAL was shifting toward the higher speed regimes, and the need was felt of deliberately strengthening the research efforts in this direction. Meanwhile, the Society of the Japanese Aerospace Companies (SJAC) set forth in 1989 under the auspice of the Ministry of International Trade and Industry a systematic feasibility study of developing a second generation supersonic civil transport and provided the member companies the incentives for the endeavor to establish the technological readiness for the prospective project launch . The member companies had to begin the research at a very basic level since they had had scarce experience in supersonic aircraft technologies. It was a matter of course for both NAL and the industry to join forces by utilizing the frame work provided by STA.

In the initial proposal of joint research, made by NAL to the industry, only issues in the fields of structure and materials were listed as research themes. The industry countered the proposal by adding issues in the field of aerodynamics, which was then agreed upon by NAL. With the former disciplines, NAL and the industry had been engaged in in-house research and hence in some aspects were able to work on state-of-the-art themes. In the latter discipline, however, both NAL and the industry had had no substantial back ground to start with, and thus had to begin almost from scratch. Altogether seven themes were addressed in this joint research, two in aerodynamics, four in structural dynamics, and one in material properties. The level reached after the 3-year endeavor may differ from theme to theme, and the achievements are to be judged not by the level we are at now but by the advancement we have made so far. What is common to all the themes addressed is that the research is in fact halfway to the goal with much room for further development. It is hoped that the closure of this joint research be transformed into the beginning of another research endeavor.

<div align="right">

**Masao EBIHARA**
NAL Representative to the Joint Research

</div>

# CONTENTS

1

# OIL FLOW VISUALIZATION ON VEHICLE MODELS IN SUPERSONIC FLOWS

Junich NODA, Atsushi TATE, Hideo SEKINE,
Mitsunori WATANABE, Takashi YOSHINAGA
Aerodynamics Division
National Aerospace Laboratory
Chofu-City, Tokyo, Japan

Nobuyuki TSUBOI, Masaru KODAMA, Takeshi KAEDA,
Keiji SATO, Hideki NOMOTO
Mitsubishi Heavy Industry Co., Ltd
Nagoya, Japan

## SUMMARY

Flow visualization on the surface of an advanced aircraft or a supersonic transport and other vehicle models has been carried out using the supersonic wind tunnel of the National Aerospace Laboratory with the test section of 1 m × 1 m. In the present flow visualization study, (1) the application methods of a mixture of oil and pigment such as an oil dots method and an oil film method, (2) the effect of the property of oil on streak lines using silicone oil and paraffin oil (liquid paraffin), (3) a print method to obtain panoramic view on a circular cylinder, and (4) a liquid crystal method have been examined. Oil film method is found to be advantageous than oil dots method in supersonic flow. Paraffin oil draws streaks, while silicone oil draw no streaks. Liquid crystal did not visualize the necklace vortices in front of the engine nacelles.

## I. INTRODUCTORY REMARKS

### I-1. Flow Visualization Methods in Supersonic Flow

To find the features of the surface oil flow visualization on a vehicle model installed in the NAL 1 m × 1 m supersonic wind tunnel, we have tested several materials and methods.

(1) An oil dots method and an oil film method using machine oil and Titanium dioxide ($TiO_2$) as pigment (1992) were tested.

(2) The visualization of surface streak lines, separation lines and reattachment lines using two kinds of oils: silicone oil with a typical low surface tension coefficient and paraffin oil with a large tension coefficient, with carbon black as pigment (1993).

(3) A print method was developed to take the flow pattern of oil on a sheet of soft paper (1993).

(4) The possibility of visualizing the necklace vortices produced on the wing surface in front of the engine nacelles was examined by a liquid crystal method (1994).

### I-2. The Features of Each Method

#### ( 1 ) Oil Dots Method [1]

A mixture of high viscous oil and pigment is used. The oil mixture is dotted with a brush by hand or with a special tool to supply a constant amount as a dot. Flow direction is easily defined. If dots are of the same size we can qualitatively infer whether or not the shear stress is great by the length of traces. The defect of this method is that it takes time to plot dots for preparation.

## ( 2 )  Oil Film Method

A mixture of high viscosity oil and pigment is applied by patting the model surface with a sponge so that the thickness becomes fairly constant. The direction of the surface flow is visible but the magnitude of the shear stress is roughly estimated only through the thickness of the remaining mixture after the blow down. Depending on the kind of oil streaks appear.

## ( 3 )  Print Method

We have developed a print method to press the oil flow pattern of a circular cylinder on a piece of paper so that it visualizes the panoramic surface flow pattern of a 360 deg roll angle. We also applied the method to visualize the internal surface flow of a channel such as a intake model of a supersonic transport engine, where we cannot take photographs of the flow pattern on the side wall as a projection without distortion.

## ( 4 )  Liquid Crystal Method [2],[3],[4]

We have tested a liquid crystal to define the separation line of the necklace vortices in front of the engine nacelles utilizing the recovery temperature drop. The liquid crystal reflects lights of particular wave lengths depending on the temperature of it

In the following section we show the results of experiments conducted for each year.

### 1-3. Wind Tunnel and Models

The flow visualization was conducted on the surface of a supersonic transport model (0.7315 m) and other supersonic vehicle models and on the wind tunnel wall using the NAL 1 m×1 m supersonic wind tunnel. The Mach number range of this wind tunnel is from 1.4 to 4.0. The Reynolds number ranges from 2 to $5 \times 10^7$ per 1 meter. Dynamic pressure varies between 65 and 155kPa. The duration of the flow reaches a maximum of 40 s.

## II. OIL DOTS METHOD AND OIL FILM METHOD (1992)

### II-1 . Introduction

The surface flow of a model is often visualizing by an oil dots method[1] or an oil film method. In the oil dots method the surface of a model is dotted with a mixture of oil and pigment using a small brush or a special tool to push out the same amount of oil per dot. After the blow down of the wind tunnel, each oil dot draws a trace of some distance downstream by the skin friction of the surface flow from the upstream region. The length of a trace roughly corresponds to the magnitude of the shear stress. The direction of the trace shows the direction of the shear stress at that point. Because the friction in a hypersonic wind tunnel is smaller than in a conventional blow-down supersonic wind tunnel, the overlapping of the traces in a hypersonic wind tunnel test is more easily controlled than in the supersonic wind tunnel test by selecting the viscosity of oil. The oil dots method is, therefore, often used in hypersonic flow to visualize blunted models such as a Gemini type reentry vehicle.

The purpose of the present experiment is to compare both methods on a supersonic transport model in a supersonic flow using the same mixture of machine oil and titanium dioxide ($TiO_2$). The flow visualization is intended to find out; 1) how the separation occurs at the end of the wings, how the shock boundary layer interference occurs between the engine and the wings, and how the separation of the vortices along the streak affect the flow on the wings. Another purpose is to observe 2) how the artificial roughness produce the flow downstream.

### II-2. Application of Oil Mixtures

We applied dots of a mixture of machine oil and the powder of $TiO_2$ (white) using a tool to supply a constant volume dot (AD7000Z controller, made by

Iwashita Eng. Co.) to the upper left side of the supersonic transport model ( horizontal main wing and vertical and horizontal tail wings ) . On the other hand, we coated the right side of the supersonic transport model with the oil mixture by tapping the surface with a sponge. We prepared the model to test the oil film method and the oil dots method at the same time as shown in Fig. 1. After exposing the model at an angle of attack of $a$ =8.7 deg to the flow of $M_{\infty}$=2.03, we took a photograph of oil flow patterns on the model. Fig. 2. shows the oil flow on the main wings, and Fig.3 shows the oil flow pattern on the vertical tail plane.

## II-3. Results of Experiment
### ( 1 )  Comparison of the Two Methods

Because of the large shear stress acting on the surface of the wing the oil mixture of the dots drew long traces, which overlapped each other. As a result, the distance of a trace becomes vague and only the direction of the oil flow is found. This pattern helps roughly overview the whole flow pattern on the wing. On the other hand, the oil film method shows details of the flow direction, which are clearer than the one by the dots method. To avoid damage by a large load on the model and on the sting at the start of blows, the supersonic wind tunnel is usually started holding the angle of attack at $a$ =0 deg. After the supersonic flow is established, the angle of attack of the model is varied to the test angle $a = a_0$ deg. Thus, in the oil dots method the traces draw some distance during the time at $a$ =0 deg. The traces begin to draw different directions at $a = a_0$. As the results traces blur or overlap on the former traces during the test time at $a = a_0$ deg. This overlap of traces sometimes confuses the judgement of the flow direction when we use an oil mixture with low viscosity. The blur of the trace by the dots method in Fig.2 and Fig.3 is caused by this difference of flowing directions of traces at $a$ =0 deg and at $a = a_0$. On the other hand in the oil film method usually the former pattern at $a$ =0 deg is wiped away when the test time at $a = a_0$ deg is greater than the build-up time of the flow at $a$ =0 deg. In Fig.2 both methods show separation lines and reattachment line of vortices produced by the streaks upstream, and the vortices originated at the junctions of streaks and the main wings.

### ( 2 )  Artificial Roughness along the Leading Edges

To promote the transition of the boundary layer on the model surface small disks of 2 mm diameter are attached in line along the leading edges of the wings as shown in Figs. 2 and 3 and near the nose of the fuselage. About 10 to 20 times the diameter of the disk downstream from the disks, the oil flow draws similar streaks. The streaks, then, changes to blur, where the transition to turbulent boundary layer seems to occur. This transition is clearly identified by the oil film method. From the present experiments, the oil film method draws better flow patterns of transition than by the dots method.

## II-4. Supplementary Experiments

In Fig. 3 oil streaks starting from the upstream region of the roughness disks never make contact with the disks. After making detours around the disks the streaks draw downstream. To examine the detour of streaks around a disk we conducted a supplementary experiment utilizing the boundary layer on the wall of the supersonic wind tunnel 1 m downstream of the test section. Although the boundary layer with a thickness of about 80 mm is turbulent, there is a laminar subboundary layer close to the wall. The 14 disks of 10 mm diameter and 1 mm thickness are attached to the wall in line at intervals of 20 mm, as shown in Figs. 4 and 5. Four disks are overlapped on the two figures. To obtain flow pattern around the disks we applied a mixture of paraffin and $TiO_2$ with a couple of drops of oleic acid as belts 30 mm in width on the upstream region and downstream region parallel to the disks. The test was conducted at Mach number

3.0.

Fig. 4 shows that the streaks of the mixture in front of the disks always detour them making necklace vortices. This is the same as what we observed on the edges of the wings. The fine streaks appear downstream at a point 25 times of the diameter of disk.

Fig. 5 shows that turbulent wedges exist just behind the disks, where the oil mixture is wiped away about 4 times diameter downstream by large shear stress. A white region follows the wiped region, where fine lines suddenly mixed with each other. As the oil mixture flows further downstream steaks begin to appear again. This is the feature of paraffin when it is used for oil flow visualization. This pattern is similar to what we have observed around and behind the 2 mm diameter disks as roughness on the supersonic transport model. When we used silicone oil instead of paraffin these fine long trace does not appear as, will be shown next.

## II-5. Conclusions

( 1 ) An oil film method is advantageous than an oil dots method in supersonic flow to make a surface flow visible..

( 2 ) Paraffin oil tends to make streaks on surface flow, while silicone oil does not.

## III. TRACES OF SILICONE AND PARAFFIN OILS (1993)

### III-1 . Introduction

In studying the oil flow visualization of a supersonic transport model in 1992 we found that an oil film method is superior to an oil dots methods in the supersonic flow regime. In 1993 we have studied surface flow patterns of several vehicle models using the oil film method. This study include models of the Orbital Reentry Experiment vehicle (OREX) and circular cylinders at high angles of attack where a side force acts. For circular cylinders we developed a printing method which demonstrated panoramic views of the flow pattern around the cylinders.

### III-2 . Experimental Methods

Because the one shot view of a photograph is limited to a certain area of a 3-dimensional model, the photographs of oil flow patterns of circular cylinder models at high angles of attack do not show the whole flow pattern on the models at one time. To observe the oil flow pattern as a panoramic one, we tried printing the pattern on a piece of paper by wrapping the cylinder with it.

### III-3 . Results of Experiment

( 1 ) Skin Friction Traces on the Wall

It is well known that the surface tension coefficient of oil affect the oil flow pattern in flow visualization. By a print method, we examined the effect of the surface tension coefficients of oils on the oil flow traces. Two kinds of oils, silicone (500cs) and paraffin oils, were tested, because the surface tension coefficient of silicone oil is smaller than that of paraffin oil. We mixed each oil with carbon black powder. We applied thin coats of each oil mixture to the wind tunnel wall by tapping it with a sponge brush, then we exposed the wall to a flow of Mach 2.0 for 20s. We print these patterns on two sheets of soft paper by pressing them on the wall. The paper is the type generally used to cover sliding doors, being the goods on the market. Fig. 6(a) is a pattern made by a mixture of silicone oil and carbon black, which shows the flow pattern made only behind the disks attached for roughness. On the other hand, Fig. 6(b) is a pattern made by a mixture of paraffin and carbon black with the same disks upstream, showing fine streaks indicating the surface flow direction. Comparing these figures, it can be seen that to visualize the flow

direction on a model paraffin oil works better than silicon oil. The property of paraffin oil to draw streaks, however, acts to destroy a bubble or separation line, as shown next.

## (2) Visualization on a Reentry Capsule Model

Oil flow visualization on the surface of a model of the Orbital Reentry Experiment vehicle (OREX) is conducted using silicone and paraffin oils at Mach number $M_\infty = 3.0$.[5] The contour of the OREX model is composed of a spherical nose section of 50 mm radius and a following conical flare of 113.3 mm diameter with an apex half angle of 50 deg. The first derivatives of the two curved surfaces at the joint line are the same; however, the second derivatives are different. If we assume that there is no friction, the velocity is accelerated downstream on a spherical nose, while the velocity on a cone surface with constant half apex angle is constant. Thus, some irregular flow field will occur at the junction line of the two shapes.

Fig. 7(a) shows a photograph of oil flow visualization made by a mixture of silicone oil and titanium dioxide $(TiO_2)$. There are no visible streaks; however, at the joint line the oil mixture stopped once, forming a thick circle. The thickness suddenly becomes thin toward the downstream region. It seems that the laminar boundary layer separated once at the joint line. The real cause of the ring is not known yet.

Fig. 7(b) shows the oil flow visualization of the same model using a mixture of paraffin oil and titanium dioxide $(TiO_2)$, where the streaks or skin friction lines appear clearly. The oil mixture once deposits near the joint line as a ring; however, the streaks pass the ring downstream. In this case the streaks have the effect of letting the oil mixture break through the ring and flow downstream. A clear difference is observed between the two oil mixtures.

## (3) Visualization of Separated Flow on Circular Cylinders [6]

Fig. 8(a) is a schlieren photograph of a circular cylinder at an angle of attack of $a = 25$ deg in a free stream Mach number $M_\infty = 2.02$ ($Re_\infty = 1.26 \times 10^7$ based on the length). In spite of the axisymmetric shape of the model side force acts due to the asymmetric separation of vortices behind the cylinder. Fig. 8(b) shows the separation lines and reattachment lines of vortices visualized by a mixture of paraffin oil and $TiO_2$, where the large shear stress regions are visualized. This photograph is not enough to tell how the side flow behaves.

To obtain the whole flow pattern around the cylinder surface we employed a printing method. After we exposed the cylinder coated to an oil mixture in the supersonic flow for a certain time at a constant $a$, we stopped the flow without changing the angle of attack $a$ of the model. We gently wrapped the cylinder with a sheet of soft paper, pattern was printed on the paper as a panoramic view for a roll angle of $0 < \phi < 360$ deg.

Fig. 9(a) shows a printed skin friction flow pattern using a mixture of silicone oil and carbon black on a circular cylinder 400 mm in length and 54 mm in diameter. The experiment was carried out at $a = 15$ deg, for $M_\infty = 1.77$ with the Reynolds number $1.12 \times 10^7$ based on the cylinder length. Because we visualized the cylinder using silicone oil, only the separation lines are observed. The angle of attack of $a = 15$ deg is not so large as to produce an asymmetric separation, thus, the flow pattern is symmetric with respect to the meridian line of 180 deg, showing that the side force is not acting.

Fig. 9(b) shows the separation lines of the same cylinder model at an angle of attack of 25 deg for $M_\infty = 1.77$ with the Reynolds number $1.06 \times 10^7$. The secondary separation line on the left side shifts to the meridian line of 180 deg, thus the side force is acting under this flow condition.

Fig. 10(a) shows a printed flow pattern on an ellipsoidally blunted cylinder visualized with the mixture of paraffin oil and carbon black at $a = 27$ deg for $M_\infty = 1.5$. The blunted nose diameter ratio of the cylinder is a/b=1/6, where a is the diameter of the ellipsoidal nose shape in the axial direction and b is the

diameter in the radial direction. Detailed streaks of the skin friction line are observed. Since the flow pattern is symmetric, this figure means that side force is not acting.

Fig. 10(b) shows a printed flow pattern on the same ellipsoidally blunted cylinder at $a$ = 28 deg for Mach number $M_\infty$=1.61. The flow pattern is similar to Fig. 9(b), showing the asymmetric separation of the secondary separation line on the left side of the cylinder. This suggests that side force is acting.

### III-4. Conclusions

An oil film method was tested using paraffin oil and silicone oil for the surface flow visualization of models in supersonic flows.

(1) Paraffin oil tends to make streaks on the models, making the surface flow direction clear. Silicone oil does not draw streaks.

(2) A print method visualizes the panoramic view of separation lines and reattachment lines on the surface of a cylindrical body.

## IV. Surface Flow Visualization with Liquid Crystal (1994)

### IV-1. Introduction

Surface flow visualization with a mixture of oil and pigment is a conventional and simple method to demonstrate the flow pattern on a model. The method requires coating with the mixture at each time the wind tunnel is blown. To save time and work for the preparation we tried using tested liquid crystals to visualize the flow pattern on a vehicle model. As a coating, liquid crystal is enclosed in microcapsules surrounded by Arabian gum and gelatin. The liquid crystal changes the wave length of reflecting light at particular temperatures. Before we apply a coat of the liquid crystal to the surface of a model we apply a black coating to the model to prevent the reflection of light which reaches the model surface through the liquid crystal coat. By observing the time-dependent variation of the color on the model surface, we can define the local variation of the temperature on the model. This method has demonstrated the measurement of the heating rate on a vehicle model in a hypersonic wind tunnel. The recovery factor and the recovery temperature on a model depend on whether the flow is laminar or turbulent. Utilizing this difference, some researchers have shown that liquid crystal is useful in visualizing turbulent wedges, separation lines and transition lines on the surface of a wing model in the transonic region by selecting suitable phase change temperatures of liquid crystals[2, 3, 4].

In the present experiment, we have conducted tests to determine out whether liquid crystal is useful in visualizing the flow pattern on a total supersonic transport model. This is based on the fact that the adiabatic recovery temperature on the model surface is lower than the stagnation temperature of the air stored in the tank and the recovery temperature on the wall is different, depending on whether the flow is laminar or turbulent and on the local heat transfer rate. The necklace vortices produced on the main wings in front of the engines are the focus of our test.

### IV-2. Model and Liquid Crystal

We have utilized the lower side of a supersonic transport model to visualize temperature variations with liquid crystal. Since this model is fabricated to measure the aerodynamic forces by six-force balance, a number of small disks 2 mm in diameter are attached in line as roughness on the leading edges of wings and on the nose section of the fuselage to simulate the turbulent boundary layer in the real flight of a transport. We applied a black coating (SSM-8, made by Nippon Capsule Products) to the model to prevent reflection of light on the model metal surface. After the black coating was completely dry we applied a coating of the liquid crystal (RM-02, made by the same company). The color

change temperatures are -1.2, 0.1, 1.0, 2.3 and 3.1 deg C, for which different colors correspond. These specimens are shown later. In Fig. 12 the coated transport model is shown. We recorded the color change of the transport model in wind tunnel tests with on an 8 mm video camera. Later we printed out the typical frames of the color change with a video printer.

## IV-3 .Results and Discussions

We carried out the experiment three times at the angle of $\alpha = 0°$.

| Test run # | $Re_\infty$ | $T_0(°C)$ | $M_\infty$ | $Ta(° C)$ | L. crystal# |
|---|---|---|---|---|---|
| 16182 | $2.151 \times 10^7$ | 17.5 | 2.02 | 14.2 | RM02 |
| 16183 | $2.124 \times 10^7$ | 17.3 | 2.02 | 14.2 | RM02 |
| 16184 | $2.117 \times 10^7$ | 17.3 | 2.01 | 14.3 | RM02+RM810 |

Reference length is the total model length, $\ell = 0.7315$ m.

Figs. 13(a), (b), (c), (d), (e), (f) and (g) show the color change of the model during the wind tunnel test at Run #16183. Against our expectation the color change at the wings caused by the necklace vortices under the interaction of the boundary layer and the shock wave around the engine nacelles were not clearly demonstrated.

Fig. 13(b) shows the photograph at 5 s after the start of the blow. Judging from the color the temperature begins to drop at the leading edge of the main wings and at the edges of the engine nacelle. In Fig. 13(c) at 10 s the temperatures of the leading edge of strakes and the whole main wings begin to drop. In Fig. 13(d) at 15s the temperature begins to drop on the whole strake and the fuselage. As shown in Fig. 13(e) at 20 s and Fig. 13(f) at 23 s the fuselage temperatures finally begin to decrease. For reference Fig. 13(g) 20 s later from the end of the blow is shown. Because of the adiabatic expansion of the surrounding air the temperature of the model suddenly begins to drop. Thus the model suddenly changes color to that of a lower temperature. The correspondence of the color and the temperature is shown on the side of Fig. 13(g).

In these Figures, the interaction regions between the boundary layer and the shock wave due to the existence of the nacelles of the engines were not observed by color change. It seems that a difference of temperature large enough to change the color of the liquid crystal did not occur because the roughness is attached to the edge of the transport model to change the surface flow turbulent. We infer the reasons as follows:

The adiabatic recovery temperature $T_{aw}$ is determined by a recovery factor r.

$$T_{aw} = T_\infty \{1 + r(\gamma - 1) \; M_\infty^2/2\} \qquad (1)$$

At a stagnation point r=1.0, thus $T_{aw}=T_0$. Generally, r< 1.0, so that,

$$T_0 = T_\infty \{1 + (\gamma - 1) \; M_\infty^2/2\}$$
$$\geq T_\infty \{1 + r(\gamma - 1) \; M_\infty^2/2\} = T_{aw} \qquad (2)$$

Take Pr as the Prandtl number with the value Pr=0.72. For a laminar boundary layer, the recovery factor of a surface parallel to the free stream is $r=Pr^{0.5}$, yielding r=0.849, while for a turbulent boundary layer, the recovery factor is $r=Pr^{0.33}$, yielding r=0.896. In either case, the surface recovery temperature $T_{aw}$ becomes lower than the stagnation temperature $T_0$ so that the surface temperature begins to fall after the wind tunnel blows. If a laminar boundary layer turns to a turbulent boundary layer on a surface across a certain border line upstream the engine nacelles the recovery factor r changes from 0.849 to 0.896. Consequently, the adiabatic recovery wall temperature $T_{aw}$ in the turbulent region is higher than in the laminar region. The heating rate, however, becomes greater in the turbulent region than in the laminar region. Thus the surface

temperature in the turbulent region must have decreased faster than the laminar region across the border. A clear color difference must exist across the border if the dissipation of heat is small. In the present experiment, however, the boundary layer was artificially changed to turbulent by the roughness at the edge of the model and that the model was made of metal with a large heat conductivity. Consequently, a temperature difference caused by the change from the laminar boundary layer to the turbulent boundary layer does not exist so that the necklace vortices in front of the engine nacelle were not captured by the present liquid crystal method.

### IV-4.Conclusions

The liquid crystal method of observing the temperature difference was not useful in detecting the location of the necklace vortices in front of the engine nacelles on a transport model where the boundary layer is artificially changed to turbulent.

## V. CONCLUDING REMARKS

Surface flow visualization of supersonic vehicles was conducted using silicone oil, paraffin oil and powders of titanium dioxide and carbon black. The visualization experiments concludes that:

( 1 ) An oil film method is advantageous than an oil dots method in supersonic flow to make a surface flow visible.

( 2 ) Paraffin oil tends to make streaks on surface flow, while silicone oil does not.

( 3 ) A print method visualizes the panoramic view of separation lines, reattachment lines, and streaks of skin friction lines on the surface of a cylindrical body.

( 4 ) The liquid crystal method of observing the temperature difference was not useful in detecting the location of the necklace vortices in front of the engine nacelles on a transport model where the boundary layer is artificially changed to turbulent.

REFERENCES

( 1 ) Y. Yamamoto, M. Watanabe, S. Nomura, T. Koyama, K. Hozumi, A. Yoshizawa, T. Ito, and H. Takatuka; Oil Flow Patterns on a Series of Capsule-Type Reentry Vehicles at Hypersonic Speeds, NAL TM-557, Nov. 1986.

( 2 ) N. Sudani,M. Sato, H. Kanda, and K. Matsuno; Flow Visualization Studies on Side wall Effects in Two-Dimensional Transonic Airfoil Testing; AIAA Paper 93-0090, January 1993.

( 3 ) M. Noguchi, Y. Ishida, N. Sudani, M. Sato, and H. Kanda; Measurement of the Boundary Layer Transition Point over a 2-D LFC Airfoil in Transonic Flow Using Liquid Crystals, NAL TM-679, March 1995.

( 4 ) T. Asanuma; Handbook for Flow Visualization ( New ed.) Asakurashoten 1992.

( 5 ) J. Noda, A. Tate, H. Sekine, M. Watanabe and T. Yoshinaga; Oil Flow Visualization on Bodies in Supersonic Flows, 26th Fluid Dynamics Conference (Japan), Oct., 1994.

( 6 ) A. Tate, M. Watanabe, J. Noda, H. Sekine and T. Yoshinaga; Side Force Acting on Blunted Circular Cylinder Bodies at High Angles of Attack in Supersonic Flow, NAL TR-1255, Dec. 1994.
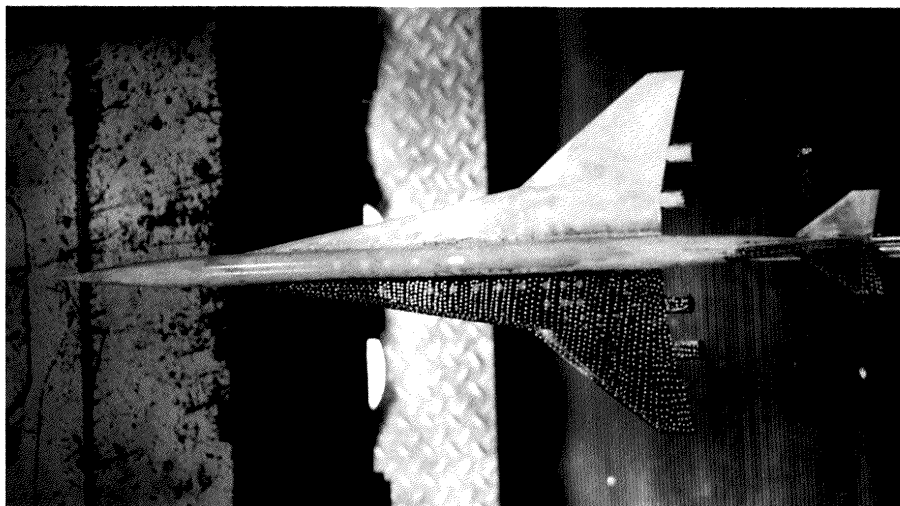
Fig.1 Preparation for surface flow visualization by an oil dots method (left) and an oil film method (right).
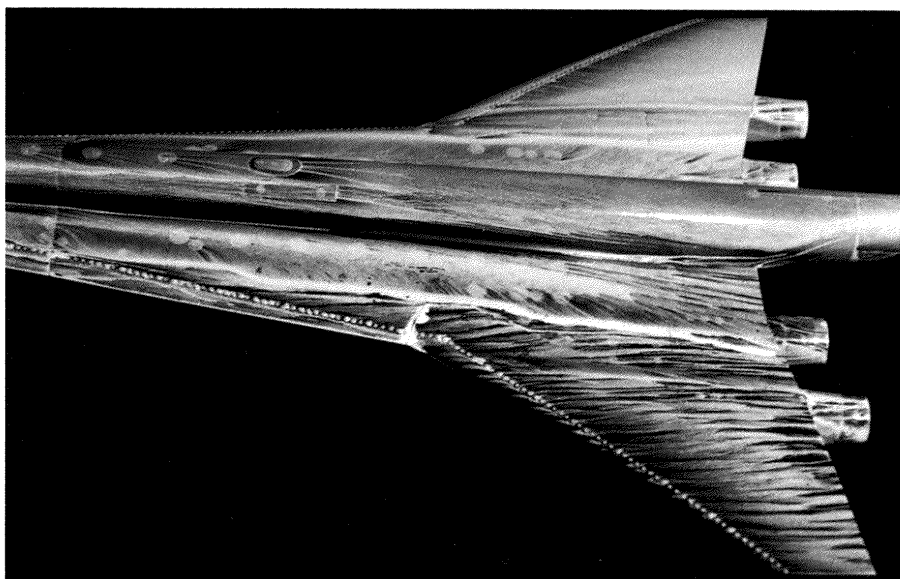


Fig.2 Oil flow visualization near the main wings.
Vortex separation lines, reattachment line on fuselage and transition after artificial roughness are visible.
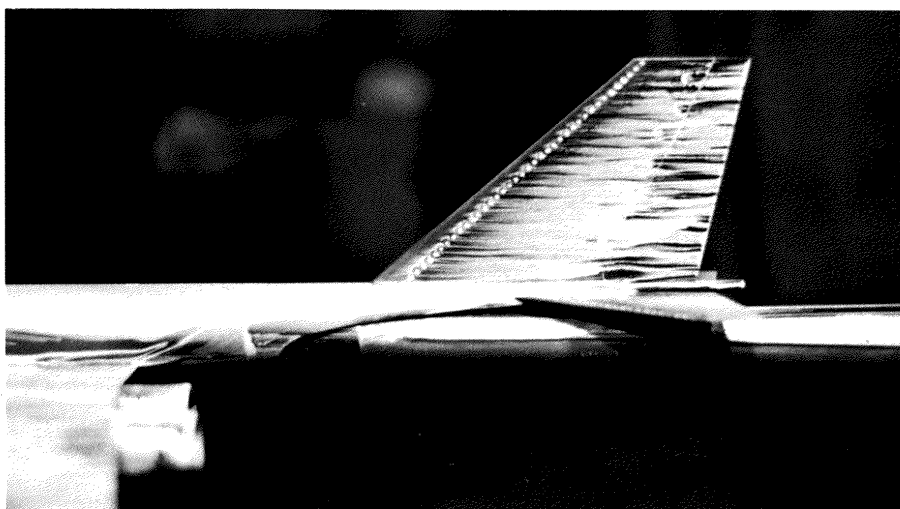


Fig.3 Flow Visualization near the vertical tail plane.
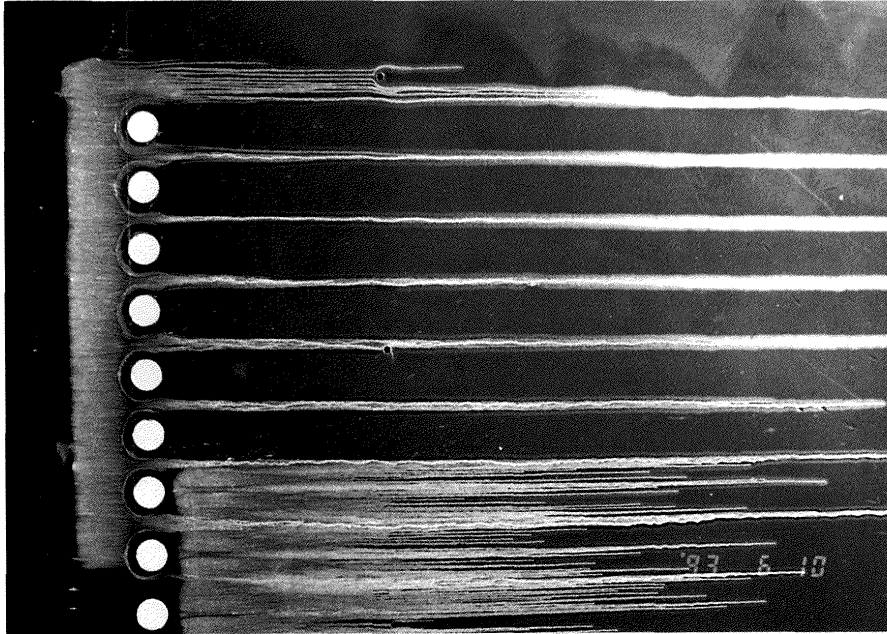Note the flow around the artificial roughness.

Fig.4 Simulation of roughness disks on the transport model using the wall of the supersonic wind tunnel (1m × 1m). Disks 10mm $\phi$ with 1mm thickness are attached at 20mm intervals. The mixture of paraffin oil and $TiO_2$ is applied in front of the disks.
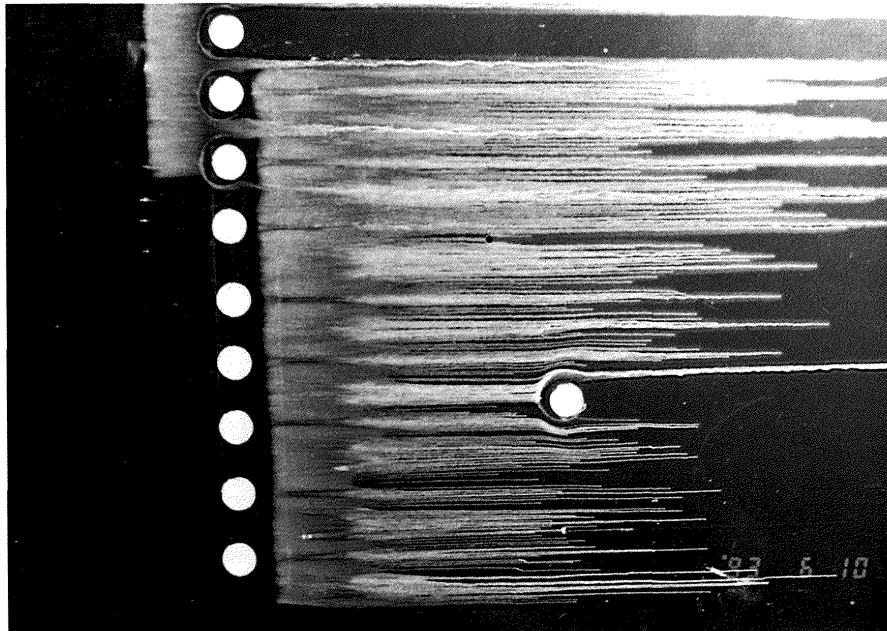


Fig.5 Simulation of roughness disks on the wall of the supersonic wind tunnel. Disks 10mm $\phi$ with 1mm thickness are attached at 20mm intervals. A mixture of paraffin oil and $TiO_2$ is applied behind the disks. Turbulent wedges appear after the disks wiping oil downstream.

Fig.6(a) Surface flow downstream of disks by a mixture of silicone oil and carbon black is printed on a sheet of soft paper. Streak is invisible. $M_\infty = 2.0$



Fig.6(b) Surface flow downstream of disks by a mixture of paraffin oil and carbon black is printed on a sheet of soft paper. Streaks are observed. $M_\infty = 2.0$
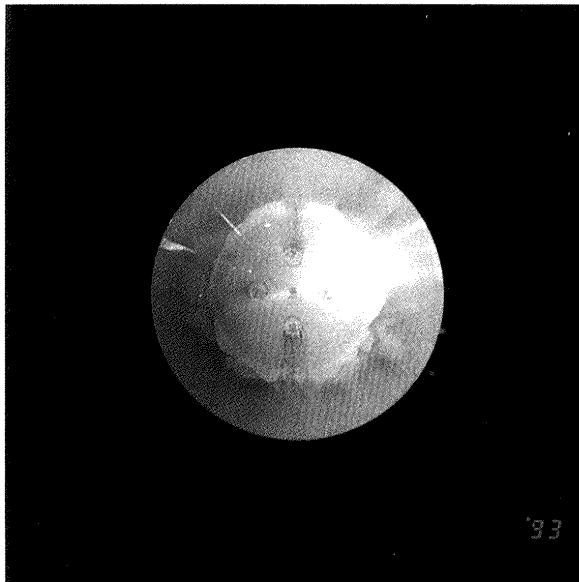


Fig.7(a) Surface oil flow on a Orbital Reentry Experiment vehicle (OREX) model using a mixture of silicone oil and $TiO_2$. A ring is observed at the junction line of curvatures.
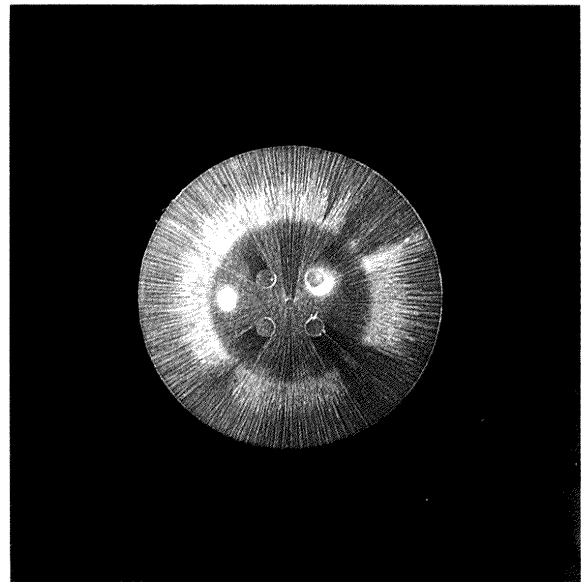


Fig.7(b) Surface oil flow on a Orbital Reentry Experiment vehicle (OREX) model using a mixture of paraffin oil and $TiO_2$. A ring is observed at the junction line of curvatures. Streaks wash the deposited mixture downstream.
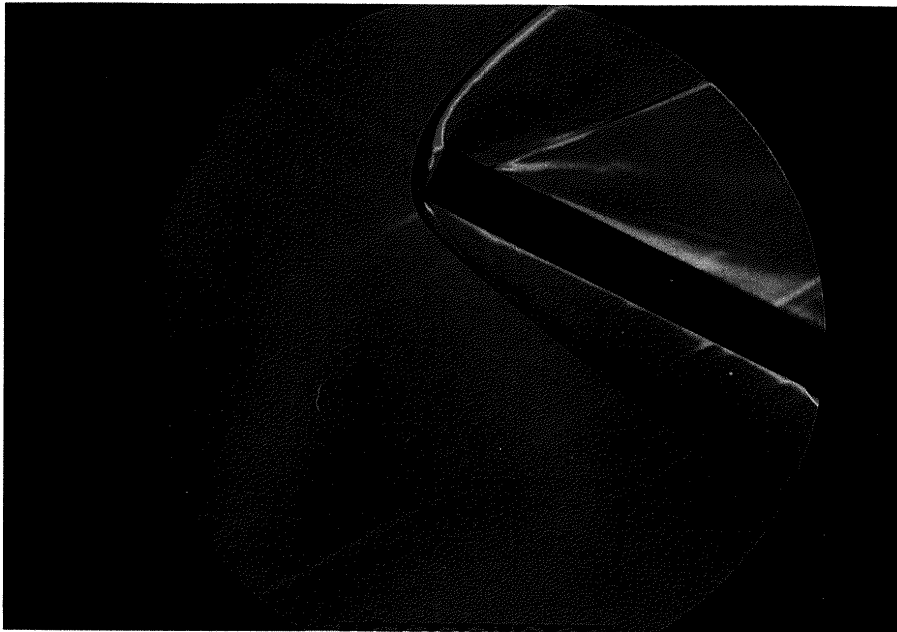
Fig.8(a)  Schlieren  photograph  of  a  cylinder  at  $\alpha = 25$  deg  for $M_\infty = 2.02$  $(Re_\infty = 1.26 \times 10^7)$.  Side  force  is  acting.
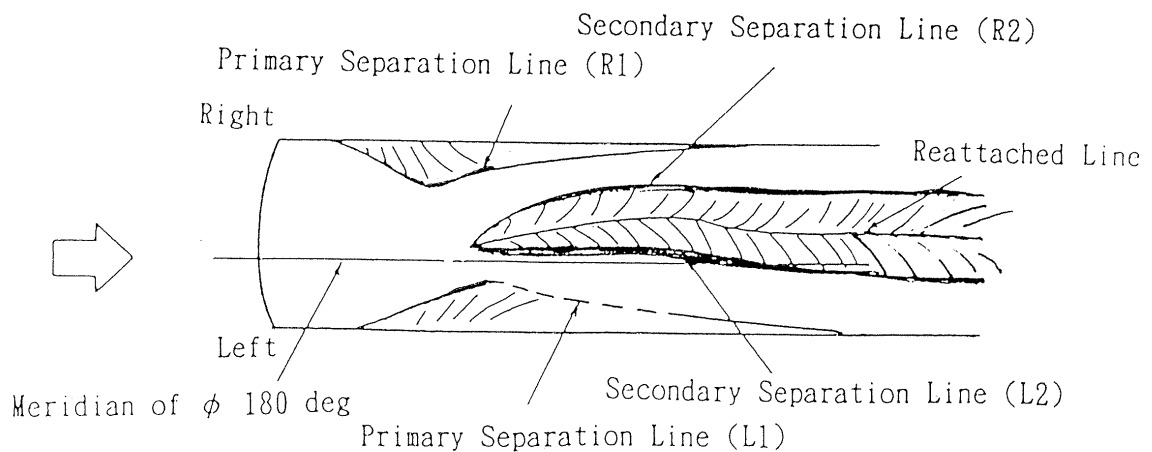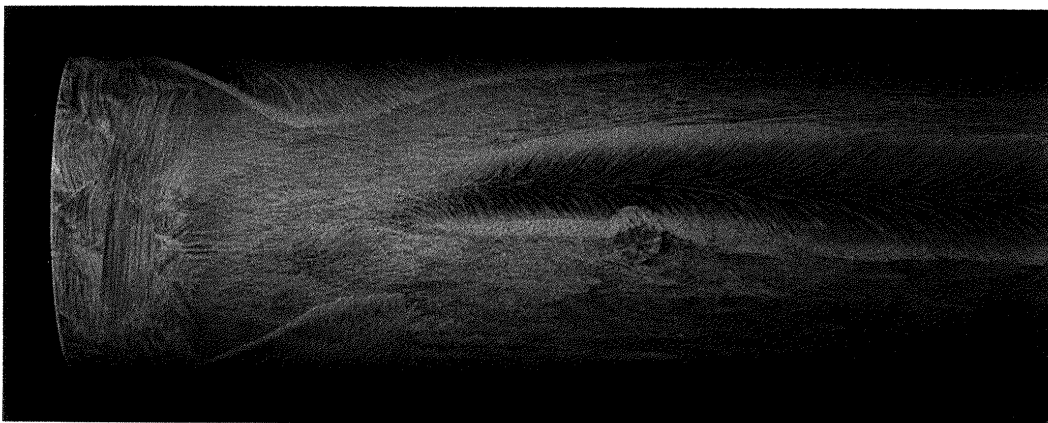


Fig.8(b)  Oil  flow  pattern  on  the  lee  side  of  the  cylinder  of Fig.8(a)  with  a  mixture  of  paraffin  oil  and  $TiO_2$.  The separation  lines  on  the  sides  and  the  reattachment  region with  large  shear  stress  on  the  lee  side  are  observed.
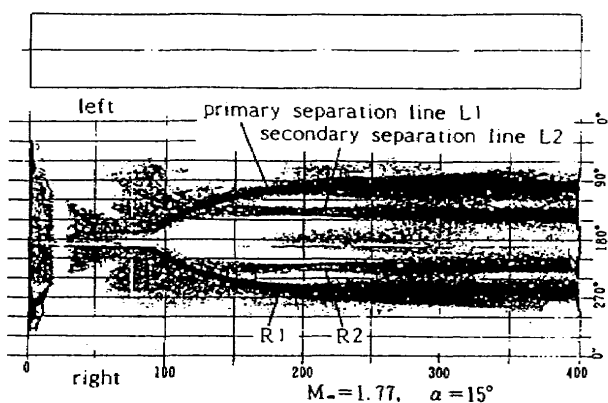
Fig.9(a) Printed figure of surface oil flow of a flat faced cylinder for roll angle $0 \leq \phi \leq 360$. Mixture of silicone oil and carbon black is used. Separation lines are visible, however, streak is invisible. $\alpha = 15$ deg, $M_\infty = 1.77$, $Re_\infty = 1.12 \times 10^7$. No side force acts.
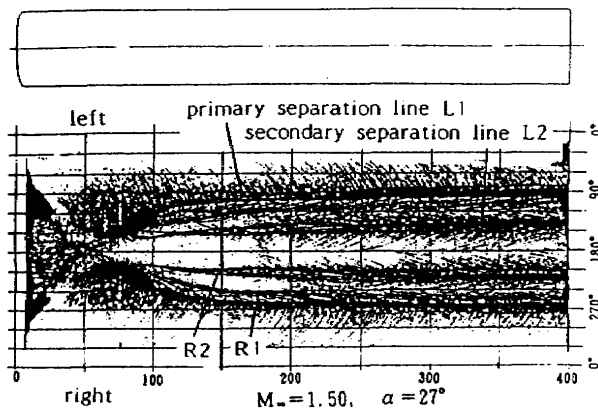


Fig.10(a) Printed figure of surface oil flow of an ellipsoidally blunted cylinder ($b/a = 1/6$) for roll angle $0 \leq \phi \leq 360$. Mixture of paraffin oil and carbon black is used. Separation lines, reattachment lines and streaks are visible. $\alpha = 27$ deg, $M_\infty = 1.50$, $Re_\infty = 1.06 \times 10^7$.
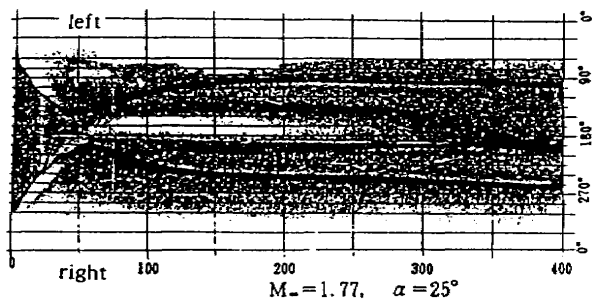


Fig.9(b) Printed figure of surface oil flow of a flat faced cylinder. Mixture of silicone oil and carbon black is used. Secondary separation lines are asymmetric, thus, side force is acting. $\alpha = 25$ deg, $M_\infty = 1.77$, $Re_\infty = 1.12 \times 10^7$.
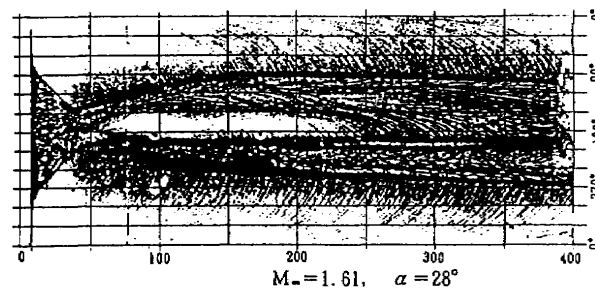


Fig.10(b) Printed figure of surface oil flow of an ellipsoidally blunted cylinder ($b/a = 1/6$). Mixture of paraffin oil and carbon black is used. Separation lines, reattachment lines and streaks are visible. $\alpha = 28$ deg, $M_\infty = 1.61$, $Re_\infty = 1.06 \times 10^7$.
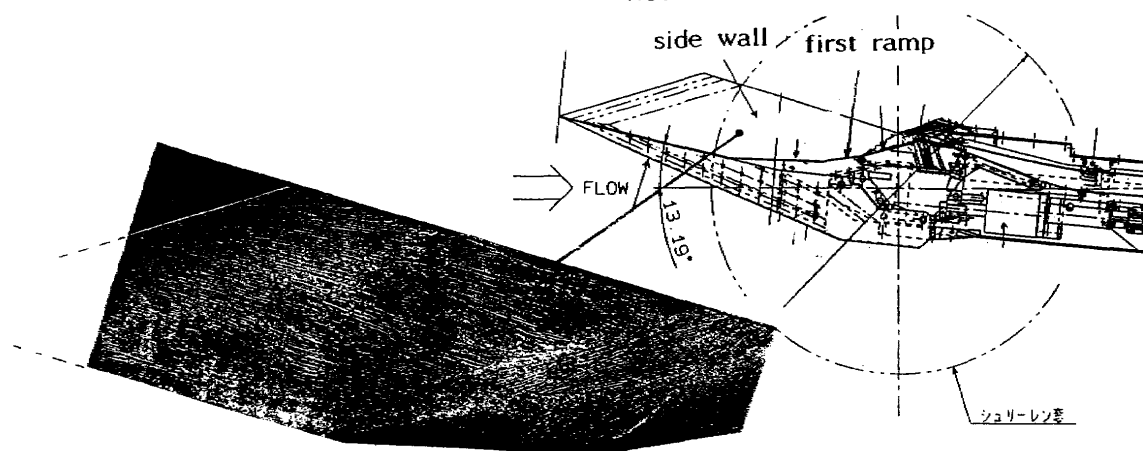


Fig.11 Visualization of side wall flow of supersonic engine intake model by print method at $M_\infty = 3.5$. Mixture of paraffin and $TiO_2$ is used. Shock wave boundary layer interaction from the first ramp corner is observed.
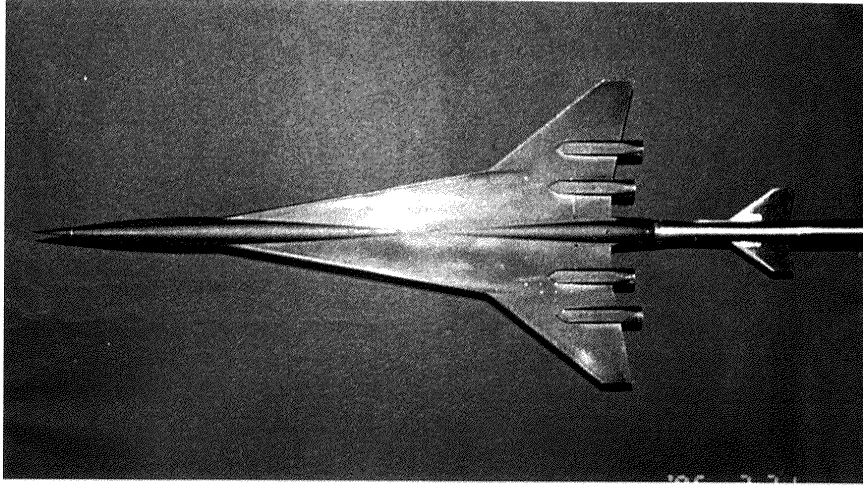
Fig.12 Lower side of supersonic transport model is coated with liquid crystal paint. Four engine nacelles are attached.
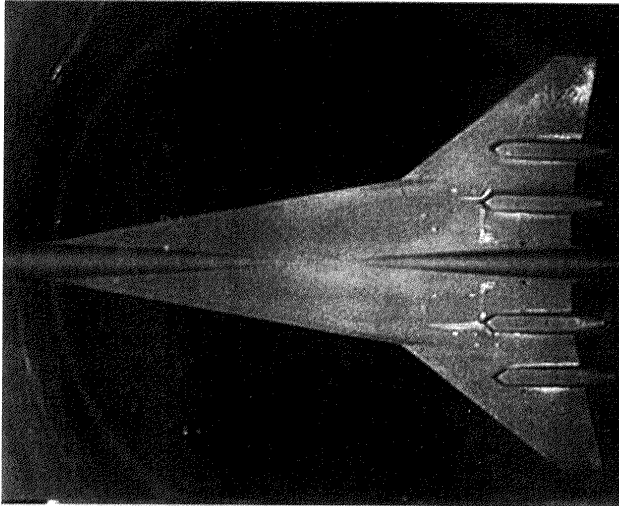


Fig.13(a) Transport model just before the blow at $\alpha$ =0 deg for $M_\infty$=2.0, t=0s.
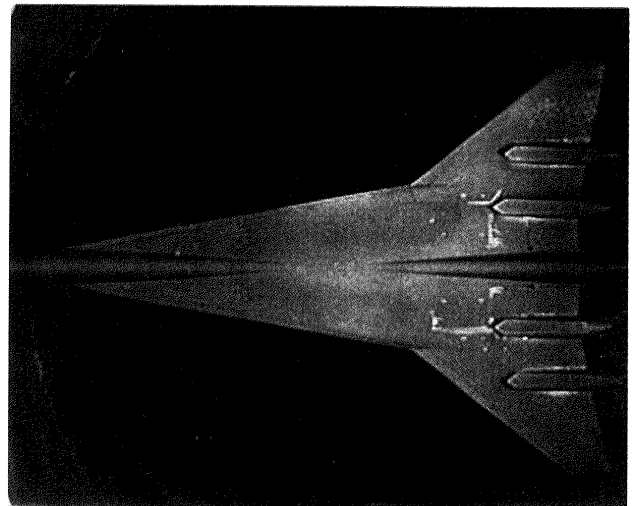


Fig.13(b) Transport model after the blow. t=5s.
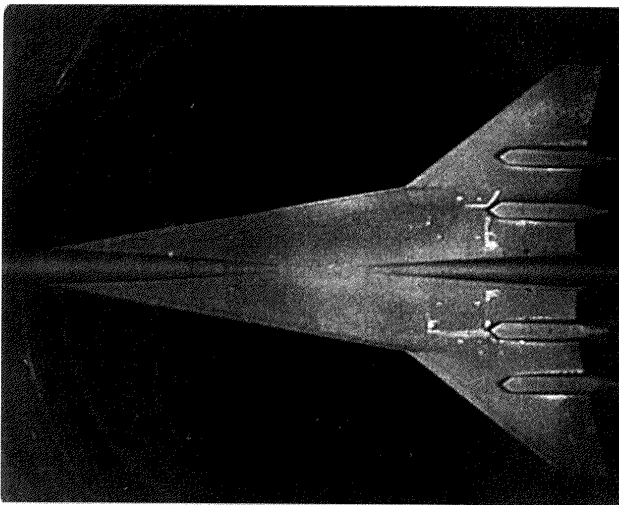


Fig.13(c) Transport model after the blow. t=10s.
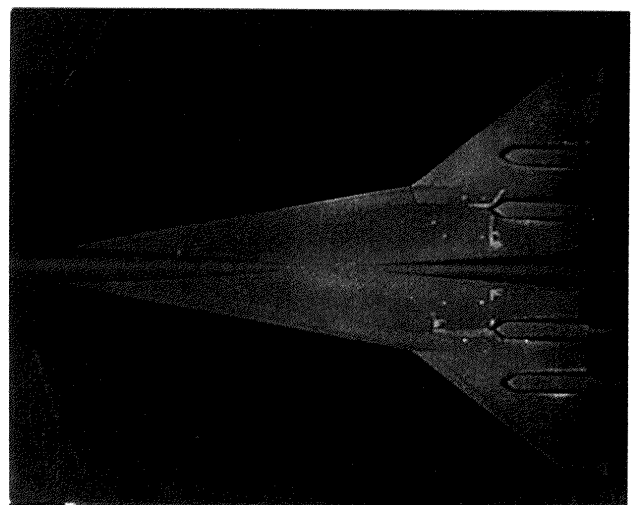


Fig.13(d) Transport model after the blow. t=15s.

Fig.13(e) Transport model after the blow. t=20s.



Fig.13(f) Transport model after the blow. t=23s.



Fig.13(g) Transport model after the stop of the blow. t=20s.

**2**

# Drag Measurement of a Complete Aircraft Model in Wind Tunnel Testing

Nobuyuki TSUBOI, Takeshi KAIDEN, Hideki NOMOTO, Masaru KODAMA and Keiji SATO

*Mitsubishi Heavy Industries, Ltd. , Nagoya, Japan*

and

Takashi YOSHINAGA, Junichi NODA, Hideo SEKINE, Atsushi TATE and Mitsunori WATANABE

*National Aerospace Laboratory, Tokyo, Japan*

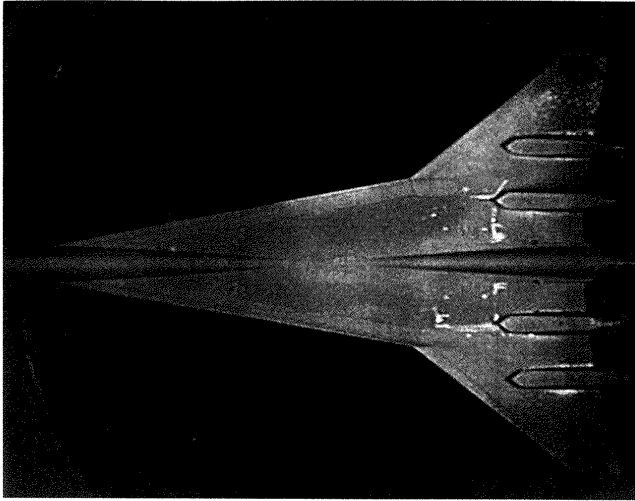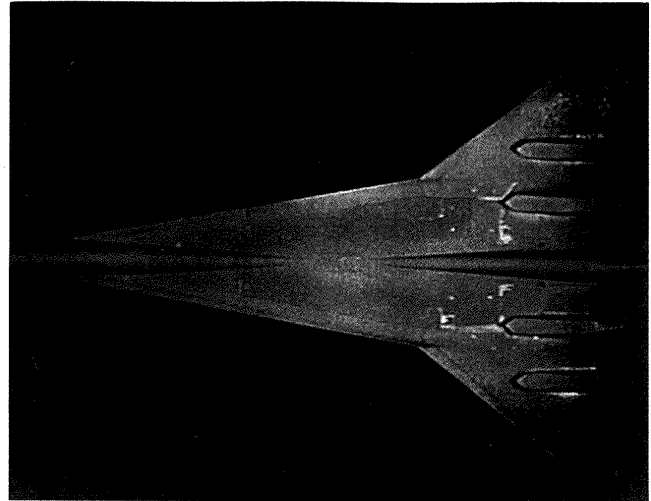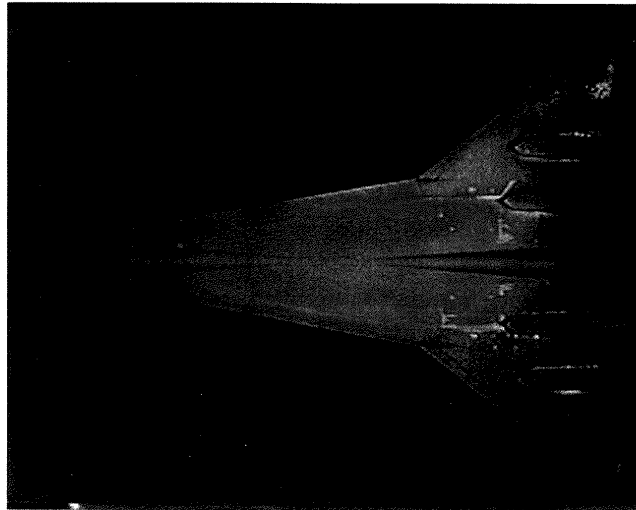## 1  Introduction

National Aerospace Laboratory and Mitsubishi Heavy Industries executed a series of research on high speed wind tunnel testing of a scale model of a supersonic transport aircraft from 1992 to 1994. The research history for those three years is shown in Figure 1. In 1992, wind tunnel testing of a complete aircraft was conducted to obtain basic aerodynamic characteristics at supersonic speeds. As a result, it was found that the neutral point moved backward approximately 6 % at $M = 2.0$ when no trim was taken. In 1993, based on the above result, wind tunnel testing for stabilizer control effectiveness was conducted to schedule the center of gravity in order to eliminate any drag increment due to trim. However, the maximum lift to drag ratio(at $M = 2.0$, with trim, corrected to actual size) obtained in 1992 and 1993 was 7.2, which is not higher than that of the Concorde. One of the causes was thought to be a spillage forward of the nacelles as a result of oil flow testing in 1992. Hence, in 1994, wind tunnel testing was conducted to investigate the cause of the spillage. The purpose of this paper is to report the results, by year, of the research conducted from 1992 to 1994.

## 2  Wind Tunnel Testing in 1992

### 2.1  Purpose of the Wind Tunnel Testing

- Evaluation of Basic Aerodynamic Characteristics at Supersonic Speed

### 2.2  Test Conditions

(1) Wind Tunnel
  - Supersonic Wind Tunnel of National Aerospace Laboratory

(2) Flow Conditions
  - $M = 1.4, 1.7, 2.0$
  - $\alpha = -2° \sim 12°$
  - $\beta = 0°, 5°$
  - $Re = 6.3 \sim 7.3 \times 10^6$ (Based on M.A.C.)

(3) Measurement
  - Six-Component Forces of a Complete Aircraft Configuration
  - Oil Flow on Upper and Lower Surface of Main Wing
  - Static and Total Pressure at Nacelle Nozzle Exit
  - Schlieren Photograph around a Complete Aircraft

(4) Wind Tunnel Test Model

The wind tunnel test model is based on the supersonic transport configuration[1] with a horizontal tail as a result of the study in 1991 conducted by Mitsubishi Heavy Industries. The model outline drawing is shown in Figure 2 and the model installation concept in the wind tunnel is shown in Figure 3.

## 2.3   Results and Discussions

(1) Results of Six-Component Forces

The lift to drag ratio $(L/D) \sim CL$ curve at $M = 2.0$ is shown in Figure 4. It is understood that the maximum lift to drag ratio ( with no trim, corrected to actual size ) at cruise Mach number ( 2.0 ) is 7.3 at $CL = 0.125$. Since the maximum lift to drag ratio of the Concorde is 7.3 $(M = 2.05)$[2] , the lift to drag ratio of the proposed configuration is equal to that of the Concorde. The neutral point calculated from the results of the wind tunnel testing is shown in Figure 5. It is 61.4 % M.A.C. at $M = 0.6$ but it moves backward approximately 6 % at supersonic speeds. Since some trim drag increment and some maximum lift to drag ratio reduction are included by the neutral point moving backward, the center of gravity position should be scheduled to prevent the trim drag increment.

(2) Results of Flow Visualization

A Schlieren photograph at $M = 2.0$ is shown in Figure 6. In this photograph, it can be seen that a shock wave propagates from the nacelle on the under surface of the model to the rear of the model. It is considered that the shock wave is generated at the external compression type air intake.

(3) Results of Oil Flow

Oil flow testing results at $M = 2.0$ is shown in Figure 7. It is considered that the oil flow pattern in front of the nacelle is due to spillage, which results in reduction of the lift to drag ratio.

## 2.4   Summary

Results of wind tunnel testing in 1992 are summarized as follows:

(1) The basic aerodynamic characteristics of a complete aircraft at supersonic speed was obtained and the maximum lift to drag ratio of 7.3 ( with no trim, corrected to actual size ) at $M = 2.0$ was acquired.

(2) The neutral point at supersonic speed moves backward approximately 6 % in comparison with that at subsonic speed.

(3) Oil Flow testing around the nacelle at supersonic cruise speed shows that spillage occurs at the air intake.

Therefore, it was determined that in order to prevent any trim drag increment, wind tunnel testing acquire data on the stabilizer control effectiveness for the optimum center of gravity position should be conducted in 1993.

# 3 Wind Tunnel Testing in 1993

## 3.1 Purpose of the Wind Tunnel Testing

- Acquisition of the Stabilizer Control Effectiveness

## 3.2 Test Conditions

### (1) Wind Tunnel

- Supersonic Wind Tunnel of National Aerospace Laboratory

### (2) Flow Conditions

- $M = 1.4, 1.7, 2.0$
- $\alpha = -2° \sim 12°$
- $\beta = 0°$
- $Re = 6.3 \sim 7.3 \times 10^6$ (Based on M.A.C.)

### (3) Measurement

- Six-Component Forces of a Complete Aircraft Configuration
- Schlieren Photograph around a Complete Aircraft

### (4) Wind Tunnel Test Model

The strut sting shown in Figure 8 was fabricated in order to deflect the stabilizer at both positive and negative angles.

## 3.3 Results and Discussions

### (1) Results of Six-Component Forces

Pitching moment coefficient versus stabilizer deflection angle is shown in Figure 9. From the fact that the difference $\Delta Cm$ at negative deflection angles from $Cm$ with $\delta h = 0°$ is higher than that at positive deflection angles, it is understood that the control effectiveness at a negative deflection angle is higher than that at a positive one. For the above reason, it is considered that since the fairing is provided on the fuselage aft under surface, the flow from the aircraft under surface to the upper surface is included and thus control effectiveness at positive deflection angles is reduced.

### (2) Results of Calculation of Optimum Center of Gravity

Figure 10 shows the relation between drag coefficient at 1G trim and center of gravity at various Mach numbers. Maximum lift to drag ratio on the trim flight at $M = 2.0$ is 7.2. Optimum centers of gravity that minimize the trim drag are nearly 66 % at any Mach number. As a result of the arithmetic averaging of the optimum centers of gravity at $M = 1.7$ and 2.0, those at speeds of $M = 1.5 \sim 2.0$ are determined to be 66.5 % (Figure 11).

Figure 12 shows lift to drag ratio with and without a longitudinal stability compensation control. Without longitudinal stability compensation control, the longitudinal stability is negative with the center of gravity of 66.5 %. Hence, in order to provide positive longitudinal stability without compensation control, the center of gravity should be 20.1 % forward from the position where the trim drag is minimum, and thus the lift to drag ratio should be decreased to 5.4. On the other hand, with compensation control, the center of gravity can be located at the optimum position and thus the lift to drag ratio can be improve by 1.8 over than without such control. Hence, it can be said that the use of longitudinal stability compensation control is an effective means to improve lift to drag ratio.

## 3.4   Summary

Results of wind tunnel testing in 1993 are summarized as follows:

(1) The stabilizer control effectiveness was acquired and the optimum center of gravity was obtained.

(2) The maximum lift to drag ratio of 7.2 at $M = 2.0$ (with trim, corrected to actual size) was obtained.

(3) It could be confirmed that the longitudinal stability compensation control was effective for improvement of lift to drag ratio.

As a result of the 1993 tests, the lift to drag with trim could be acquired by stabilizer control effectiveness at supersonic cruise speed. Hence, it was determined that the spillage phenomenon in front of the nacelle ( refer to the oil flow testing results in 1992 ) that was considered to be a cause of drag increment, should be investigated in 1994 in order to improve lift to drag ratio.

# 4   Wind Tunnel Testing in 1994

## 4.1   Purpose of the Wind Tunnel Testing

- Investigation of the Spillage in front of the Nacelle
- Evaluation of the Effect of Azimuthal Angle of Nacelle

## 4.2   Background of Wind Tunnel Testing

As a result of oil flow tests in 1992, spillage was observed in front of the nacelle on the wing under surface. The cause has been thought to be that the boundary layer flows into the nacelle inside, the flow is choked in the nacelle and the spillage consequently occurs since the diverter height is less than the boundary layer thickness $\delta$ on the wing surface ( estimated using the Van-Driest method ) at the wind tunnel testing Reynolds number. Therefore, the cause of the spillage in front of the nacelle should be investigated by using various diverter heights taller than the boundary layer thickness.

On the other hand, changing the azimuthal angle of the nacelle can be considered as one method to reduce drag of complete aircraft due to the wing/nacelle interaction[3]. The nacelles in this configuration were attached to the wing in parallel to the body axis. But as a result of wind tunnel testing in 1992, the flow around the nacelles on the wing under surface had some azimuthal angles in the spanwise direction and their angles were approximately 1.8° for the inboard nacelle and 3.0° for the outboard nacelle. Since those are considered to be the cause of drag increment, the possibility of reducing the drag of the complete aircraft should be investigated by changing the axis of the nacelle so that they are parallel to the out flow on the wing under surface.

Based on the above background, the wind tunnel testing was conducted.

## 4.3   Test Conditions

(1) Wind Tunnel
  - Supersonic Wind Tunnel of National Aerospace Laboratory

(2) Flow Conditions
  - $M = 2.0$
  - $\alpha = -2° \sim 12°$
  - $\beta = 0°$
  - $Re = 7.3 \times 10^6$ (Based on M.A.C.)

(3) Measurement
- Six-Component Forces of a Complete Aircraft Configuration
- Oil Flow on Lower Surface of Main Wing
- Static and Total Pressure at Nacelle Nozzle Exit
- Schlieren Photograph around Complete Aircraft

(4) Wind Tunnel Test Model

In order to conduct (i) the change of diverter height and (ii) the change of azimuthal angle of nacelle based on the model used in 1992 and 1993, some spacers of the same plane figure as the diverter were fabricated to change the height and the azimuthal angel by being inserted between the diverter and the wing(Figure 13).

## 4.4 Results and Discussions

(1) Effect of Diverter Height

(a) Oil Flow Results

(i) Oil Flow on the Wing under Surface

Figure 14 shows results of oil flow around the nacelles on the wing under surface with various diverter heights. As the case of the original diverter height ( Figure 14(a)) and the case of the diverter height equal to $\delta$ (boundary layer thickness on wing at air intake)(Figure 14(b)) are compared with each other, the oil flow patterns between the inboard and outboard nacelle are different from each other. It is considered that the compression waves generated by the interaction between the nacelle and the boundary layer affect the flow on the wing under surface. When a diverter height of $\delta$ (Figure 14(b)) a diverter height of 5 $\delta$ (Figure 14 (c)) are compared with each other, it can be seen that the separation line between the left and right inboard nacelles for the latter is wider than that for the former. But it is considered that the oil flow patterns around the nacelles are not affected so much even though the diverter height is changed.

Next, testing with closed nacelle exits was conducted to investigate whether the choking existed in the nacelle internal flow. The separation line with closed nacelle exits (Figure 14(d) left) is moved farther upstream than with opened nacelle exits (Figure 14(d) right), and also the flow patterns between the inboard and outboard nacelles are much different. From the above fact, it is thought that the nacelle internal flow is not choked even at the original diverter height.

(ii) Oil Flow on the Side of Nacelle

Figure 15 shows the results of oil flow on the side of the nacelle in case of various diverter heights. With the original diverter height (Figure 15(a)), the shock wave reflection traces are seen on the side of the inboard nacelle and those traces are also seen both when the diverter height is equal to $\delta$ (Figure 15(b)) and when it is equal to $5\delta$ (Figure 15(c)). Hence, it can be said that diverter height variation has no influence on the oil flow pattern on the side of the nacelle.

(b) Mass Flow Ratio of Nacelle Internal Flow

Mass flow ratio of nacelle internal flow is calculated from the total pressure in the nacelle using Rayleigh's formula for pitot tubes. As a result, with the original diverter height for which it was considered that the nacelle internal flow might be choked due to the wing surface boundary layer flowing into the nacelle, the mass flow ratio of nacelle internal flow at $\alpha = 0°$ was 92 % (obtained in 1992). But even when the diverter height was $5\delta$ (this obviously was assuming that the wing surface boundary layer did not go into the nacelle

and thus the nacelle internal flow was not choked ), the mass flow ratio of nacelle internal flow at $\alpha = 0°$ was 94 %. Therefore, it is considered that the nacelle internal flow is not choked and flows sufficiently.

As a result of the wind tunnel testing with various diverter heights, it is found that flow goes sufficiently in the nacelle with the original diverter height. So, it can be concluded that the oil flow pattern on the wing under surface is not affected by spillage generated due to choking in the nacelle.

(2) Effect of Change of Nacelle Azimuthal Angle

Figure 16 shows $\Delta C_{D0}$ with various nacelle azimuthal angles. When the nacelle azimuthal angle was changed, with diverter heights of $2\delta$ and $5\delta$ , the variation of drag coefficient is a few counts and no significant effect of nacelle azimuthal angle was observed. It is considered that since base drag generated at the aft end of the diverter was large, the effect of change of nacelle azimuthal angle could not be captured.

(3) Study of the Flowfield Structure near the Nacelle

According to the results in paragraph (1), it is found that the oil flow pattern observed with the original diverter height is not separated shock wave caused by choking in the nacelle. Hence, the flowfield structure near the nacelle is studied in detail since the oil flow pattern is considered to be caused by physical phenomenon which is the interaction between the shock wave and the boundary layer.

(a) Flowfield with the Interaction between Shock Wave and Boundary Layer

When a wedge on a flat plate is placed in a supersonic flow (Figure 17), it is well known that a significant physical phenomenon can be observed[3,4]. That is, the shock wave near the flat plate bifurcates into a separation shock wave and a rear shock wave due to the interaction with the boundary layer on the flat plate, and consequently forms a $\lambda$ shaped shock wave. The boundary layer separates from the flat plate at S1 due to the interaction with the separation shock wave. The separated shock flow is accelerated by expansion waves ( which are generated due to the rear shock wave interacting with the separated boundary layer ) between contact discontinuity and the separated boundary layer passing through the rear shock wave. The accelerated flow impinges upon the flat plate at A1 but some flow is directed back upstream. This reserve flow then encounters secondary separation at S2. Hence, separation lines of S1 and S2, and the attachment line A1 should be seen in oil flow testing.

(b) Flowfield near the Nacelle

Figure 18 shows results of oil flow on the wing under surface with the diverter height of $\delta$. Primary separation line S1 and secondary separation line S2 similar to those in Figure 17 which, it is supposed, occur due to the interaction between the shock wave generated at air intake and the boundary layer, can be seen on the wing under surface. But the attachment line can not clearly be seen in Figure 18. The separation line S3, which are made by combining S1 and S2, can be seen between the inboard and outboard nacelles. In Figure 18, shock wave traces D can be seen on the lower surfaces of the inboard and outboard nacelles. Similar traces can be seen on the side of the nacelle (Figure 19 (a)). These traces are considered to be made by the shock wave from the air intake (Figure 19(b)).

By the above results, it is found that the oil flow pattern on the wing under surface is due to the complicated interaction between the shock waves from the nacelles and the boundary layer.

## 4.5 Summary

Results of wind tunnel testing in 1994 are summarized as follows:

(1) It is considered that the oil flow pattern in front of the nacelle is not caused by the spillage but rather by the complicated interaction between the shock waves from the nacelle and the boundary layer on the wing under surface.

    (a) No essential change of oil flow pattern can be seen with various diverter heights and it can be concluded that the spillage is a small amount even with the original diverter height judging from the mass flow ratio of the nacelle internal flow.

    (b) As the oil flow results in the wind tunnel testing are compared with the structure of the flowfield for a wedge mounted on a flat plate at supersonic speed, it can be concluded that the oil flow pattern in front of the nacelle is due to the interaction between the shock waves from the nacelle and the flat plate boundary layer.

(2) Little effect on the drag of the complete aircraft with various azimuthal angles of nacelle is obtained in this wind tunnel testing.

## 5 Conclusions

High speed wind tunnel testing using a full configuration scale model of a supersonic transport and the evaluation of its aerodynamic characteristics were conducted from 1992 to 1994. As a result, it is concluded that even a small scale model investigation of aerodynamic characteristics can be performed. It is considered that more wind tunnel testing needs to be conducted using lager models to realize improvement of the aerodynamic characteristics of the supersonic transport.

## References

[1] Takami, H. and Kawashima, E., "Aerodynamic Characteristics of a Next Generation High-Speed Civil Transport," AIAA Paper 92-4229, 1992.

[2] Collard, D., "Concorde Airframe Design and Development," SAE912162.

[3] Landum, E. J., "Effect of Nacelle Orientation on the Aerodynamic Characteristics of an Arrow Wing-Body Configuration at Mach Number 2.03,' NASA TN D-3284, 1966.

[4] Knight, D. D. and Horstman, C. C., "Structure of Supersonic Turbulent Flow Past a Shape Fin," AIAA J Vol.25, No.10, p.1331-1337, 1987.

[5] Schmisseur, J. D. and Dolling, D. S., "Actual Wall Pressure near Separation in Highly Swept Turbulent Interactions," AIAA J. Vol.32, No.6, p.1151-1157, 1994.

| Item | Year | 1992 | 1993 | 1994 |
|---|---|---|---|---|
| Estimation of Basic Aerodynamic Characteristics | | ←——→ | | |
| Aquisition of Stabilizer Control Effectiveness | | | ←——→ | |
| Estimation of Wing/Nacelle Interaction | | | | ←——→ |

Estimation of Stabilizer
Control Effectiveness

Aquisition of Wing/Nacelle
Interaction
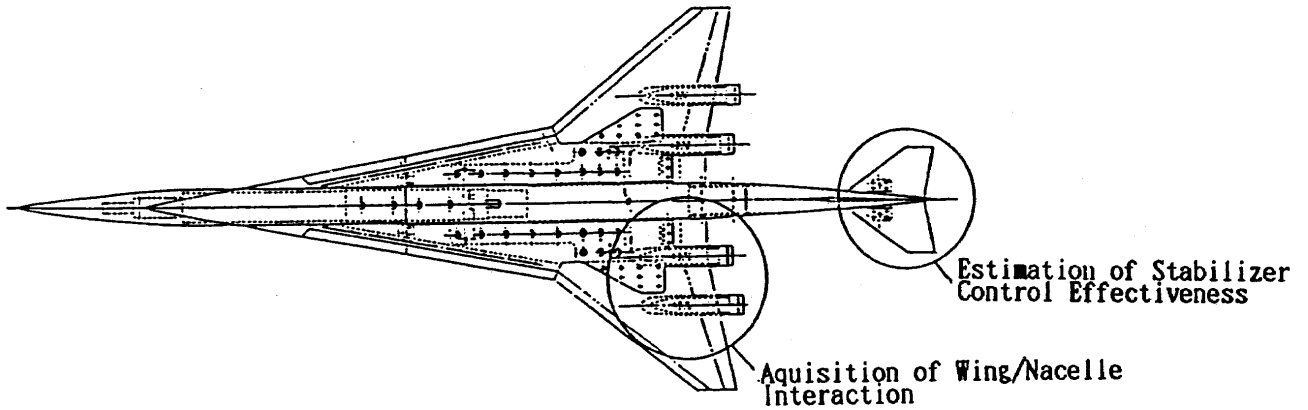
Figure 1　Research History for 3 Years

0.7315 m

0.2891 m
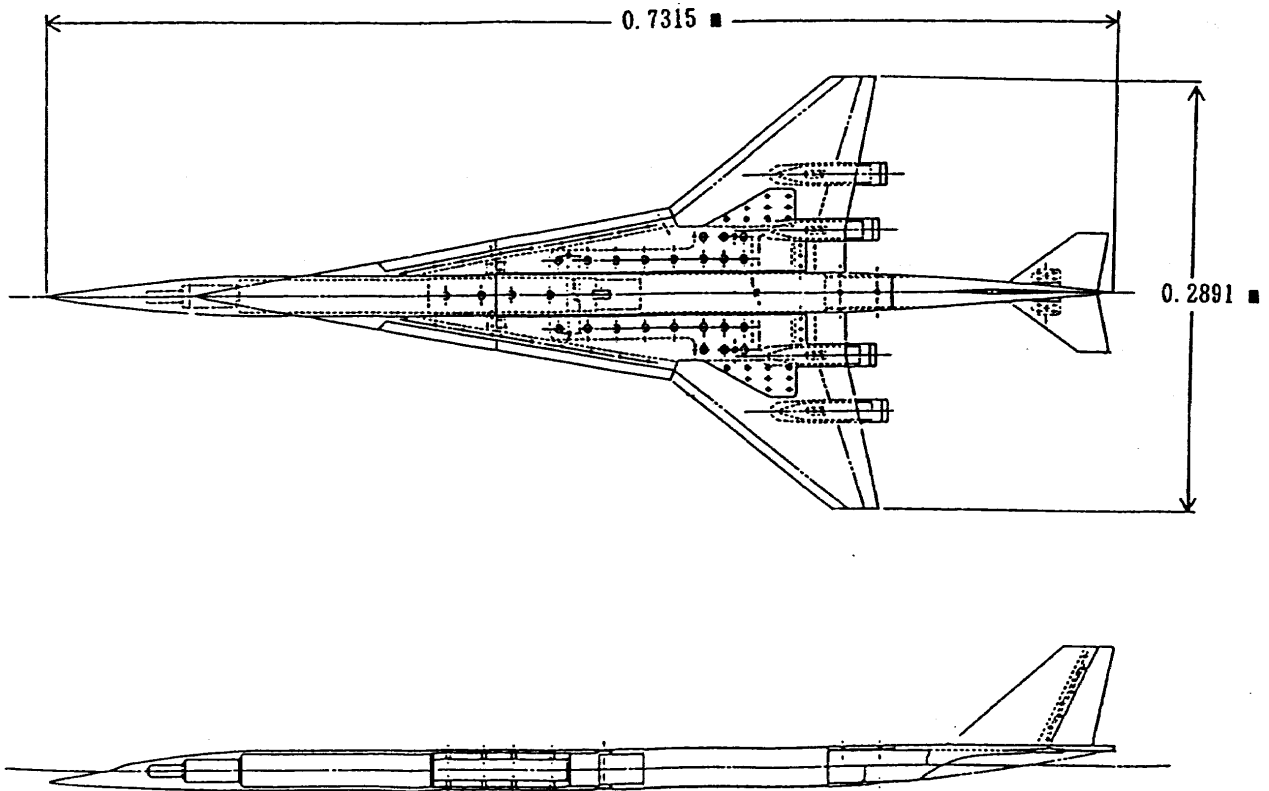
Figure 2　Model Outline Drawing
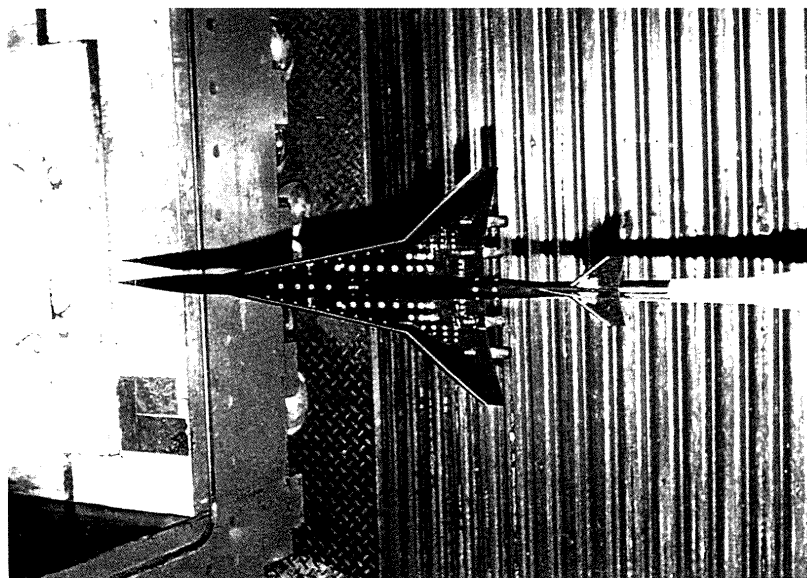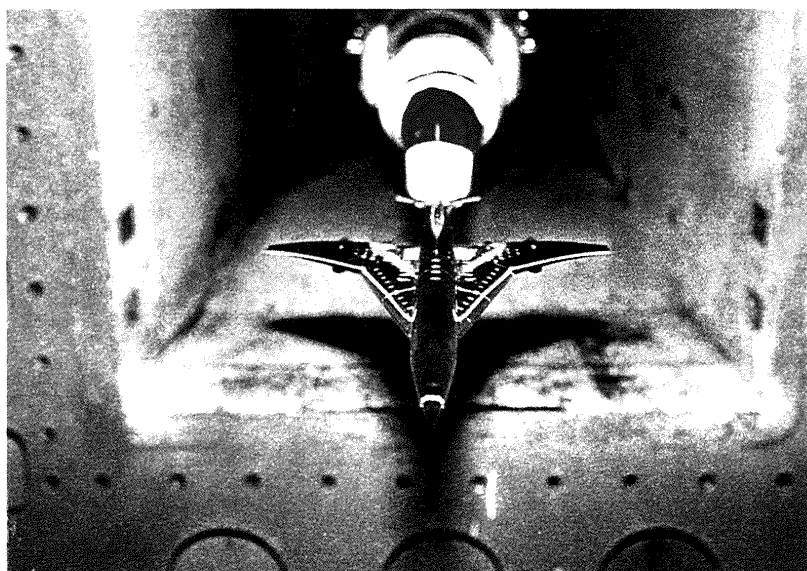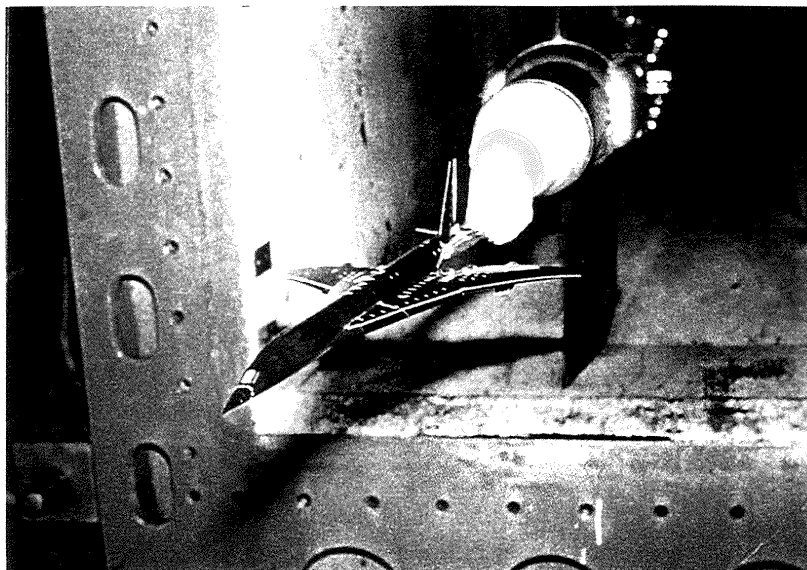
Figure 3　Model Installation Concept in Wind Tunnel

L/D
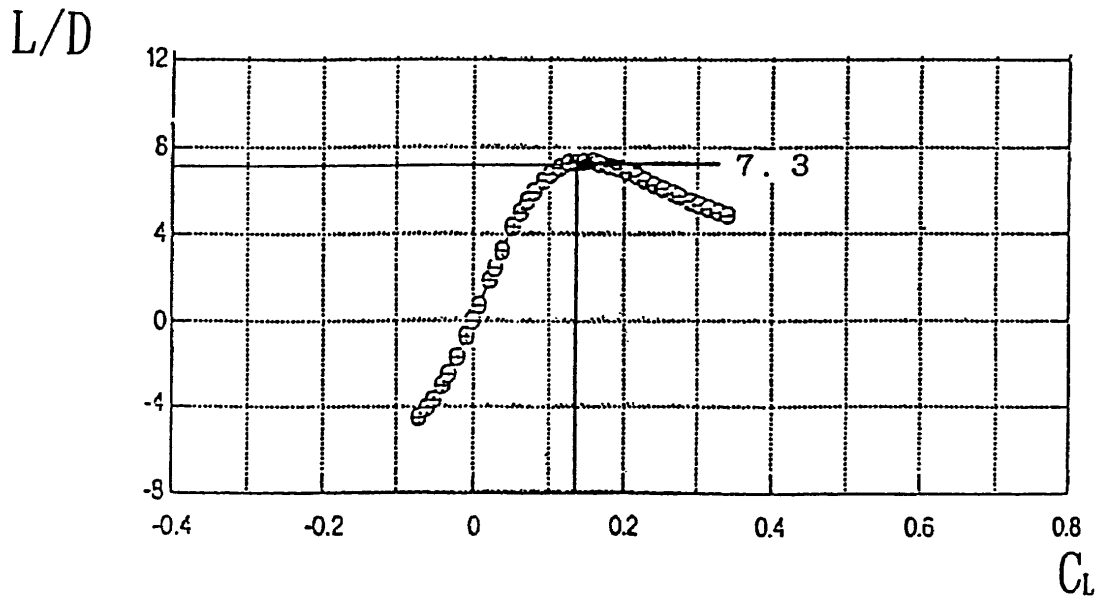


Figure 4  Lift to Drag Ratio($L/D$) $\sim CL$ at $M = 2.0$
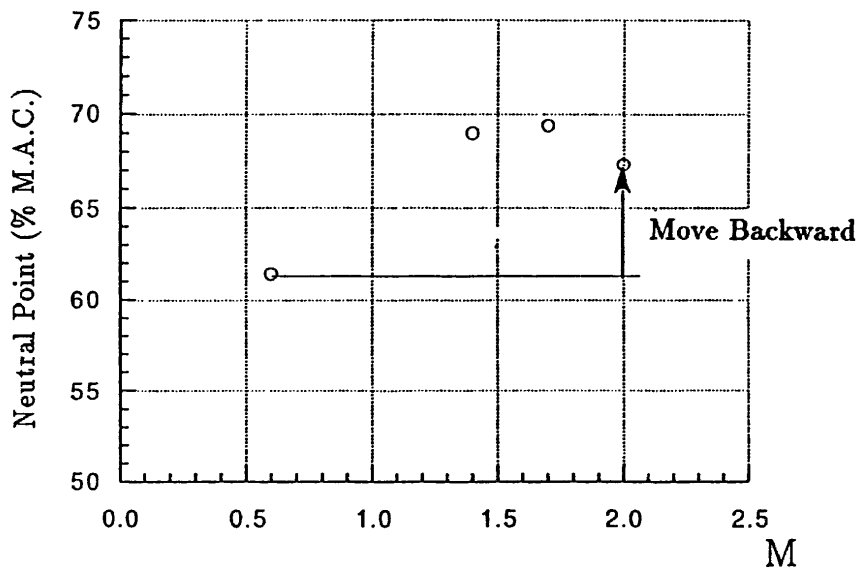


Figure 5  Neutral Point Variation at Various Mach Number
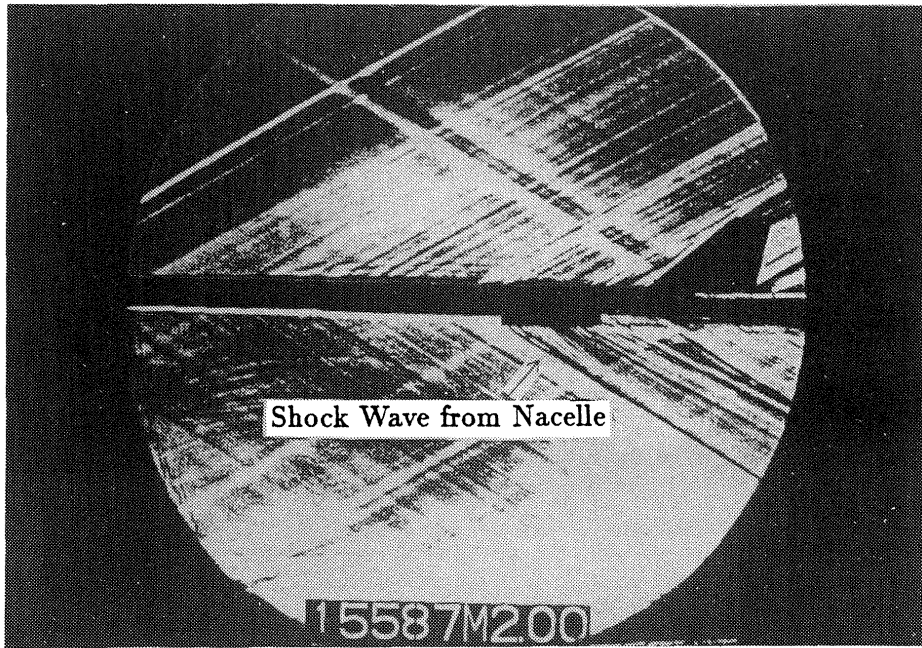
Figure 6 Schlieren Photograph at $M = 2.0$ and $\alpha \simeq 0°$
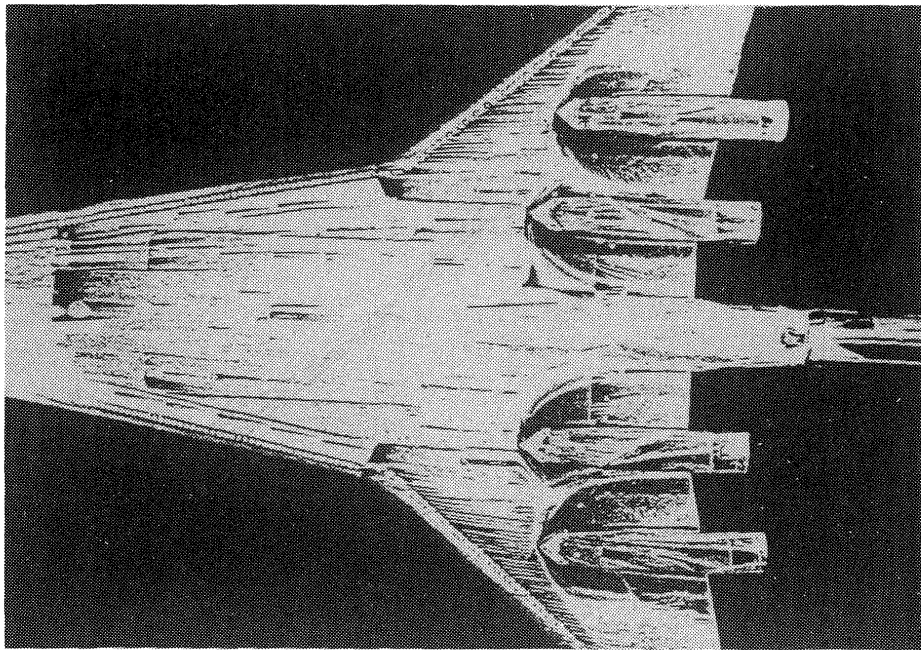


Figure 7 Oil Flow at M=2.0 and $\alpha = 0.8°$

Strut Sting

Dummy Sting (Aft Sting)
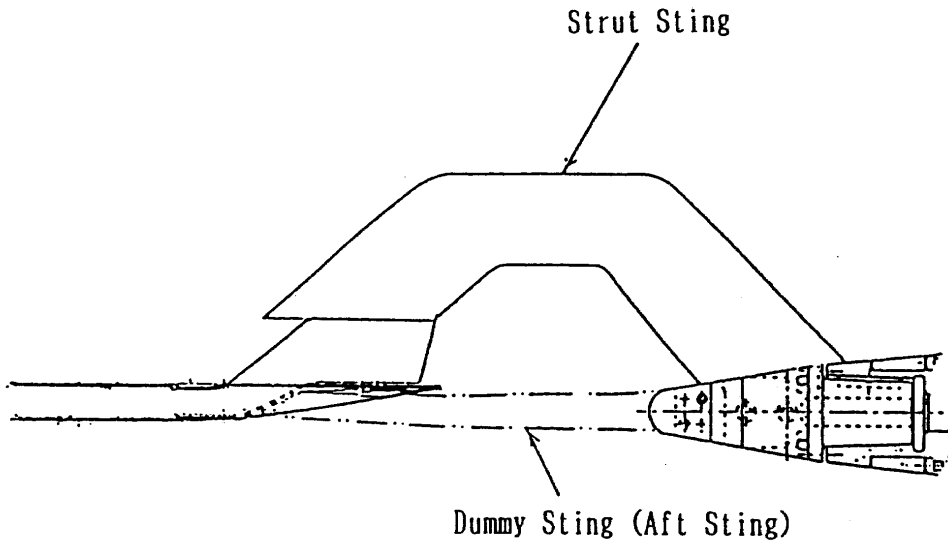
Figure 8   Model Supporting System
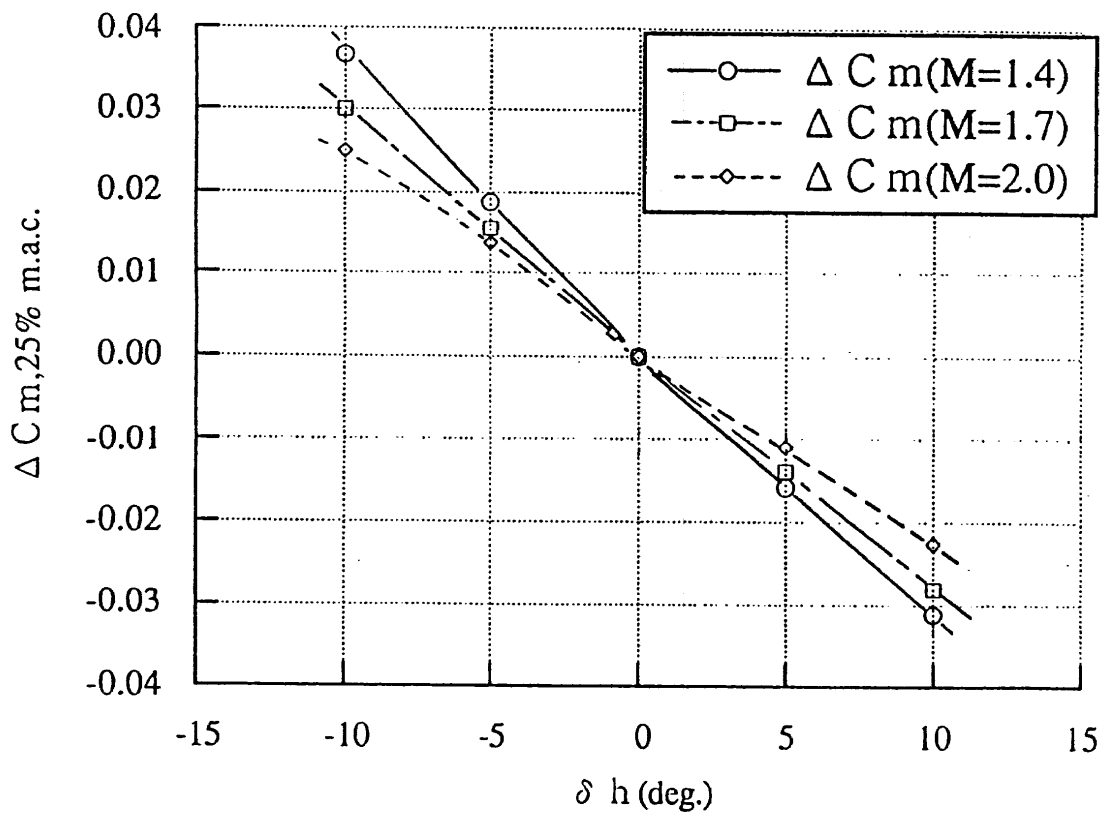
Figure 9   Effect of Stabilizer Deflection
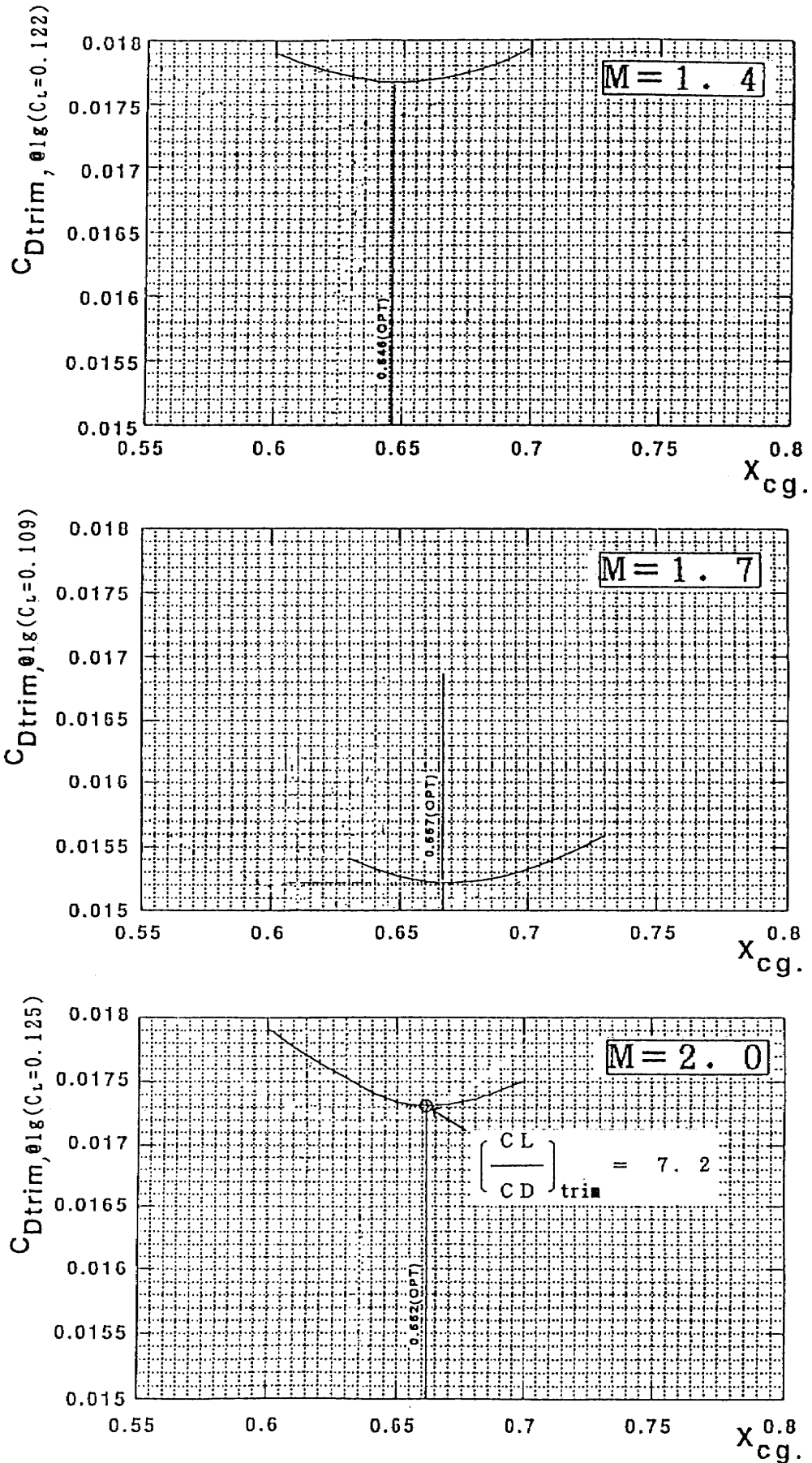
Figure 10　CD trim ～ Optimum Center of Gravity
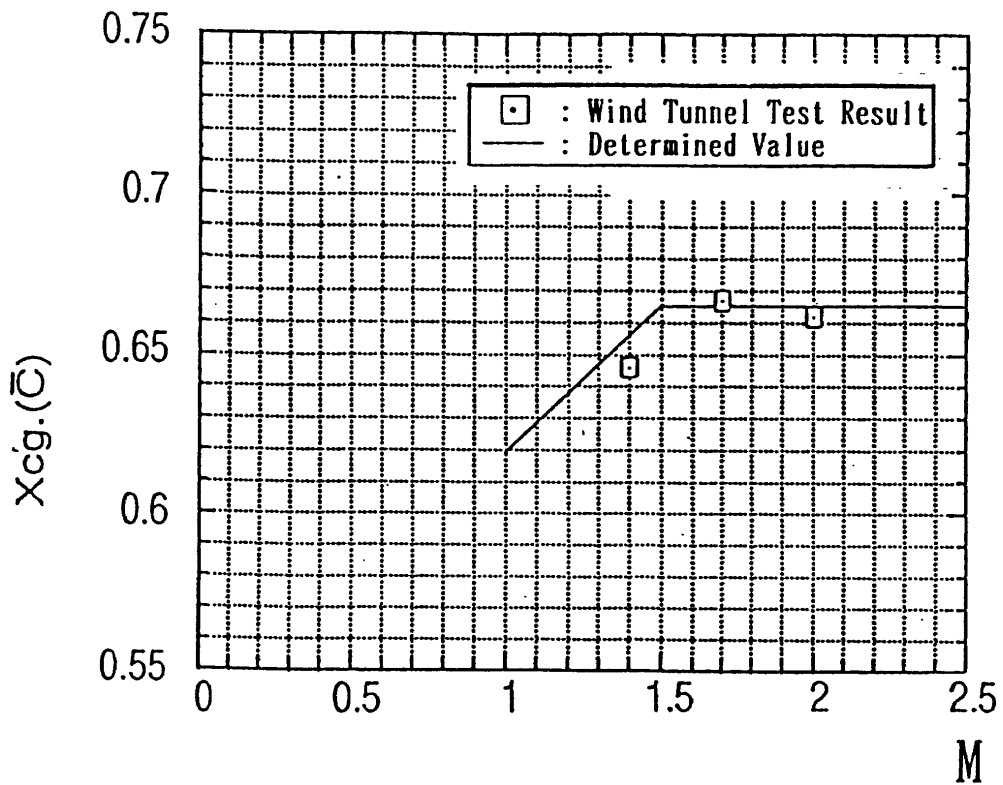
Figure 11   Determination of Optimum Center of Gravity
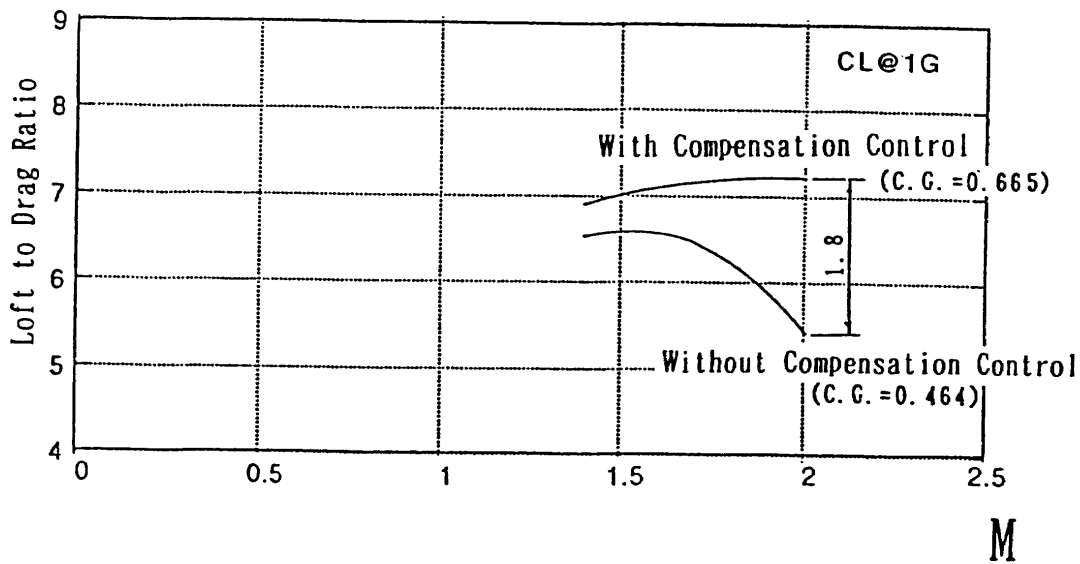


Figure 12   Effect of Longitudinal Stability Compensation Control for Lift to Drag

SST Complete Aircraft Model

Upper View

Nacelle

Side View

▨ : Spacer (Fabricated)

▧ : Diverter

(a) Spacer Position

50% Point in Nacelle Length

Outboard

1. 5°
(0. 9°)

3. 0°
(1. 8°)
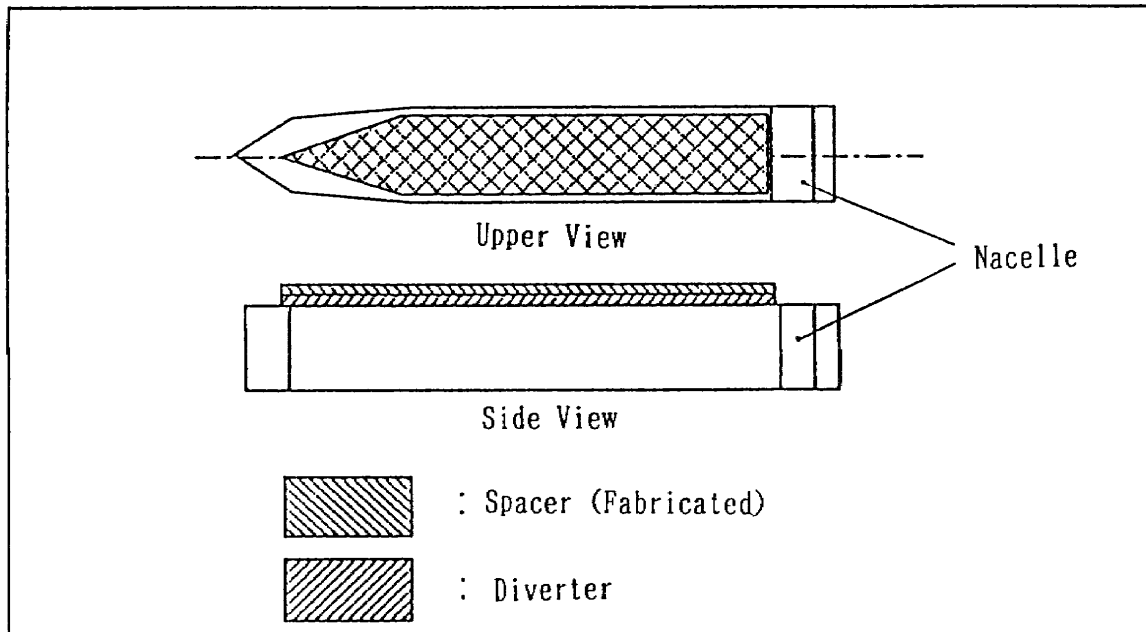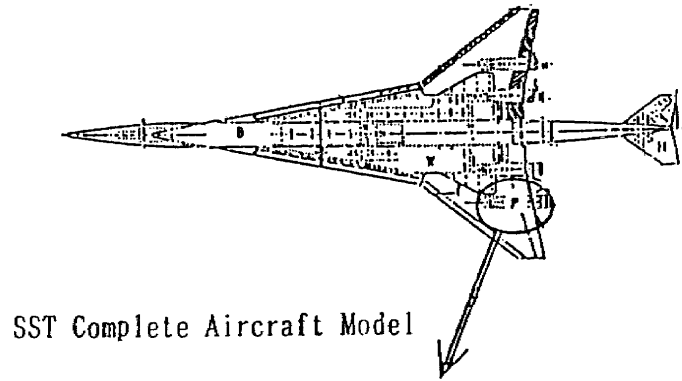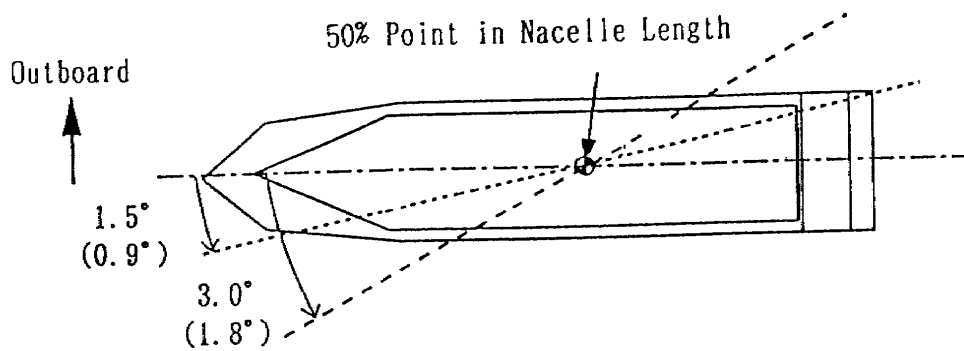
(b) Nacelle Azimuthal Angle (For Outboard Nacelle)
(Angles for the inboard nacelle are shown in parentheses.)

Figure 13   Fabricated Spacer

(a) Original Diverter Height
(Less than Boundary Layer Thickness δ)



(b) Diverter Height of δ
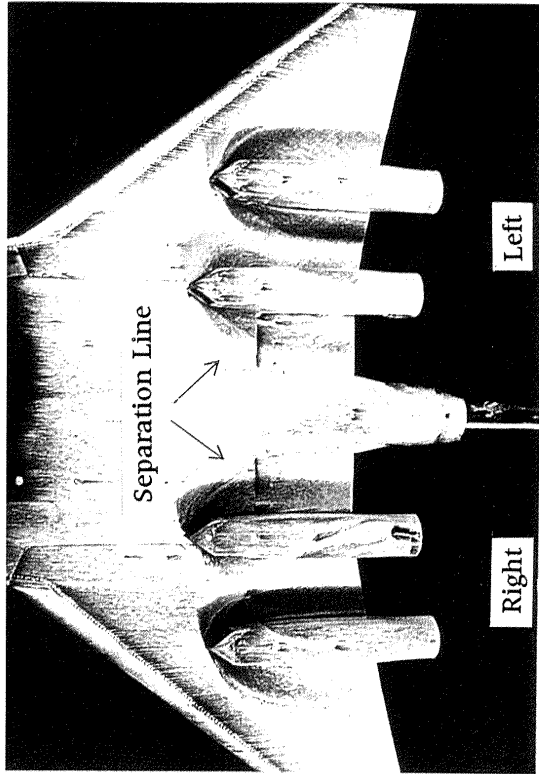


(c) Diverter Height of 5δ
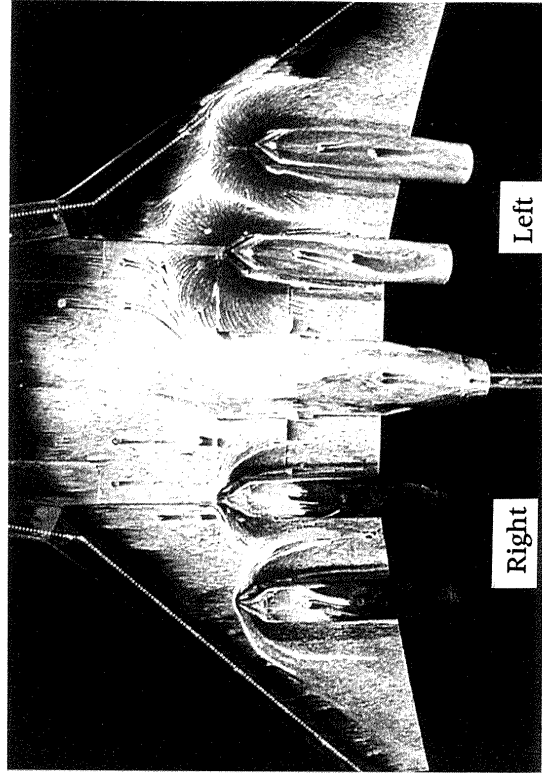


(d) Original Diverter Height (Left Nacelle Outlet is closed.)
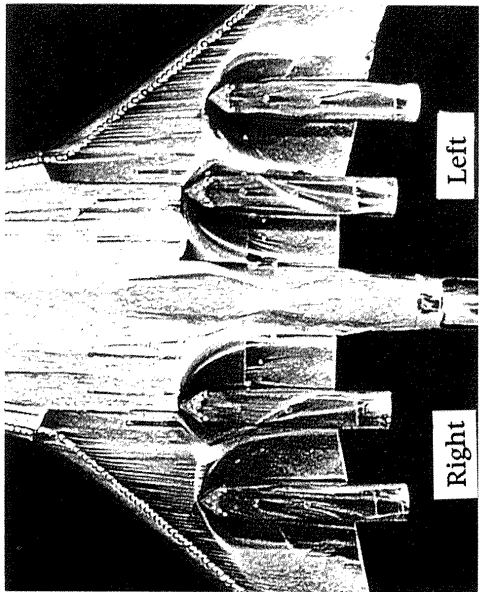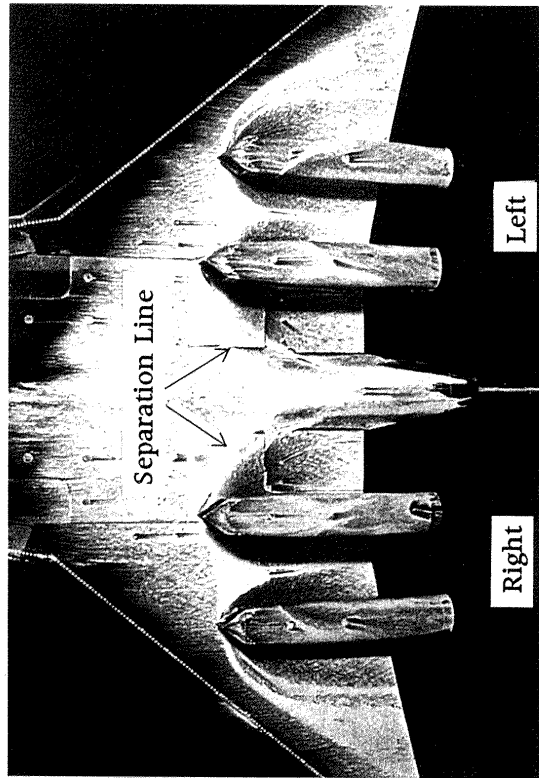
Figure 14   Effect of Diverter Height on the Wing Surface in Oil Flow Photograph (Wing Under Surface)
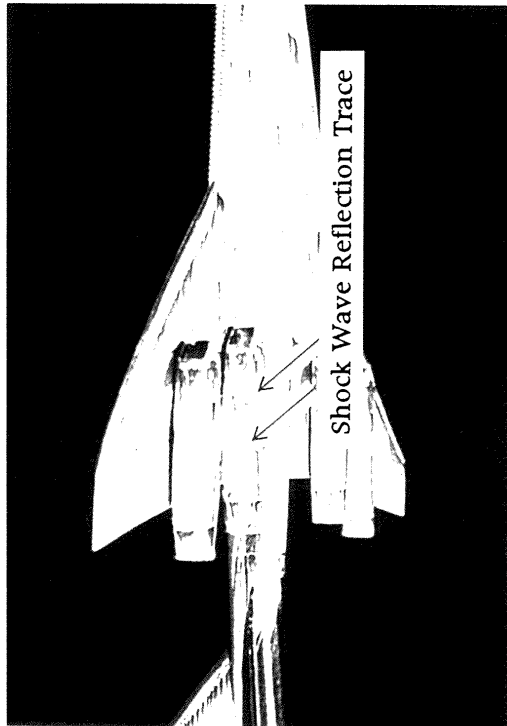
(b) Diverter Height of δ



(a) Original Diverter Height
(Less than Boundary Layer Thickness δ)
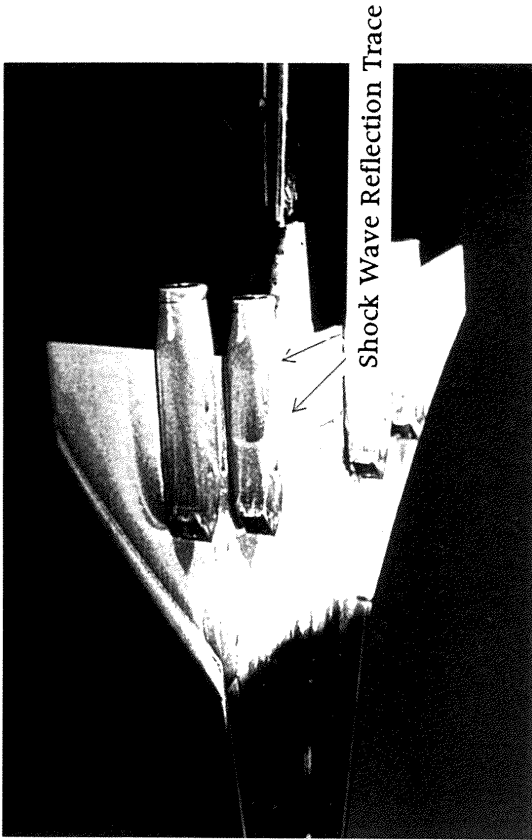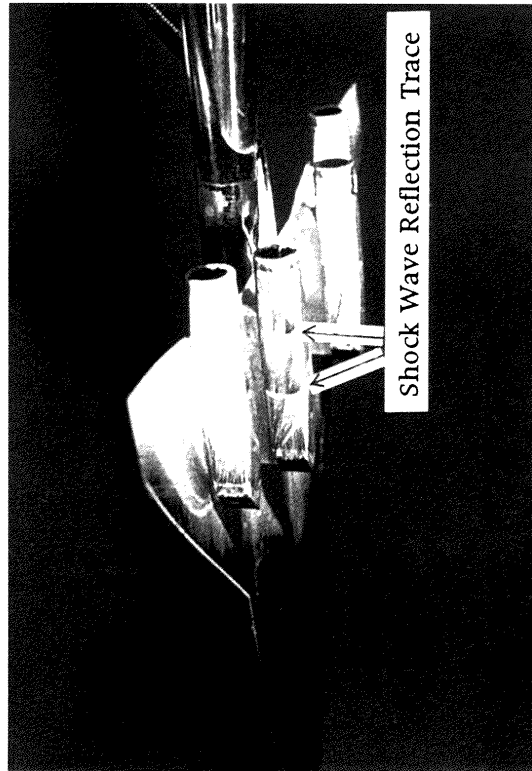


(c) Diverter Height of 5δ

Figure 15   Effect of Diverter Height on the Wing Surface in Oil Flow Photograph (Side of Nacelle)
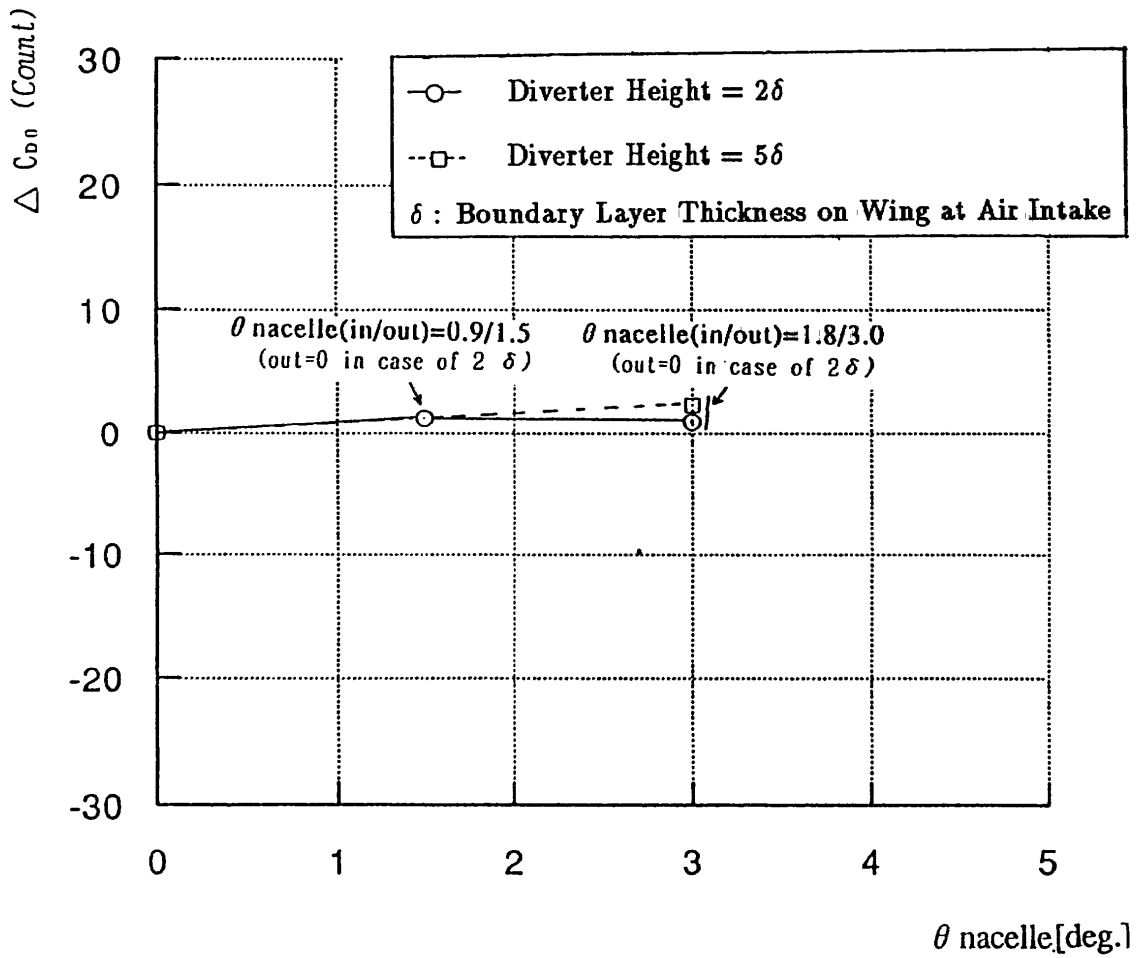
Figure 16    Effect of Change of Nacelle Azimuthal angle

Shock Wave generated at the Wedge

Uniform Flow V

Separation Shock Wave

Rear Shock Wave

Boundary Layer
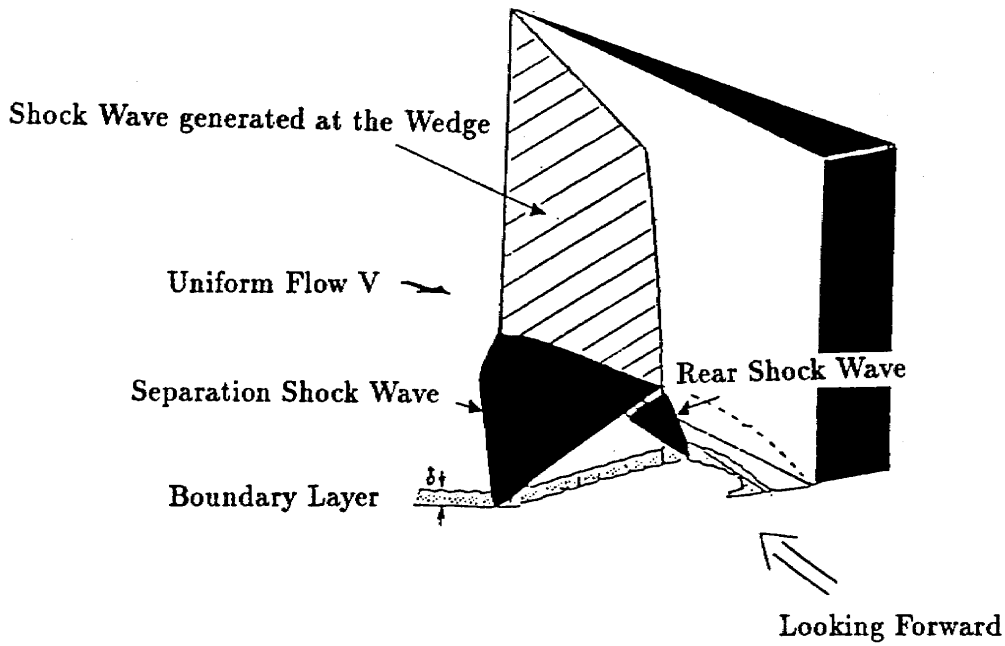
Looking Forward

(a) Flow Field around a Wedge on a Flat Plate in Supersonic Speed Flow

Cross Flow to V

Shock Wave generated
at Wedge

Expansion Wave

Contact Discontinuity

Separation Shock Wave

Rear Shock
Wave

Boundary Layer

Vortex

Wedge

S1

S2

A1

Primary Separation Line    Secondary Separation Line    Attachment Line
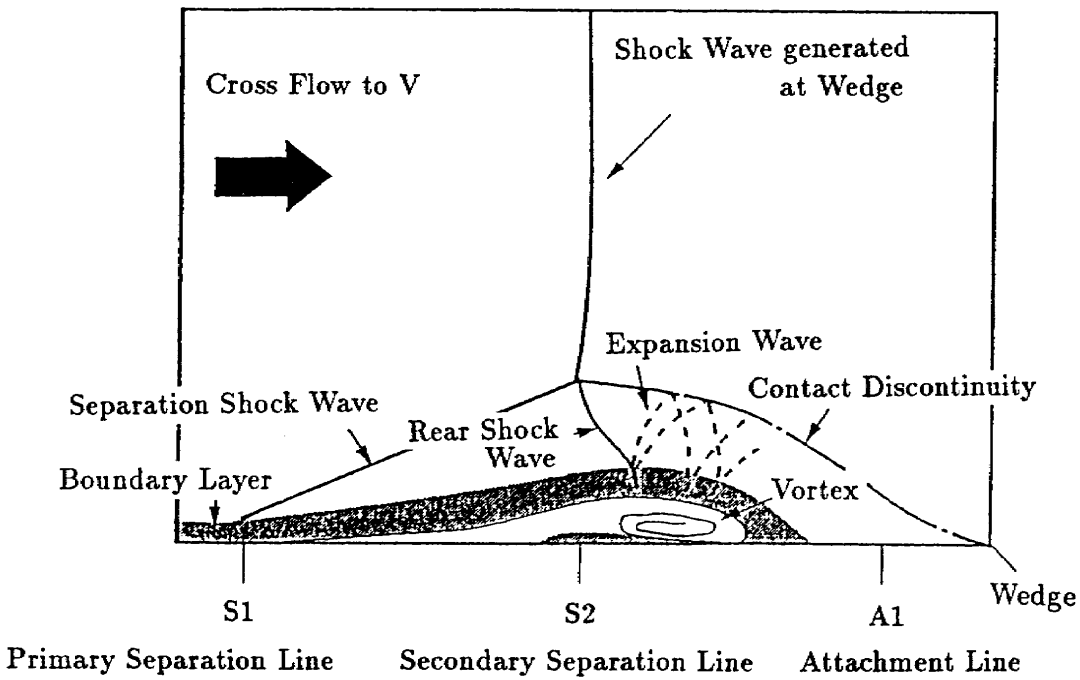
(b) Flow Field of Interaction between Shock Wave and Boundary Layer
(Looking Forward of (a))

Figure 17    Conceptual Figure of Flow Field of Interaction
between Shock Wave and Boundary Layer
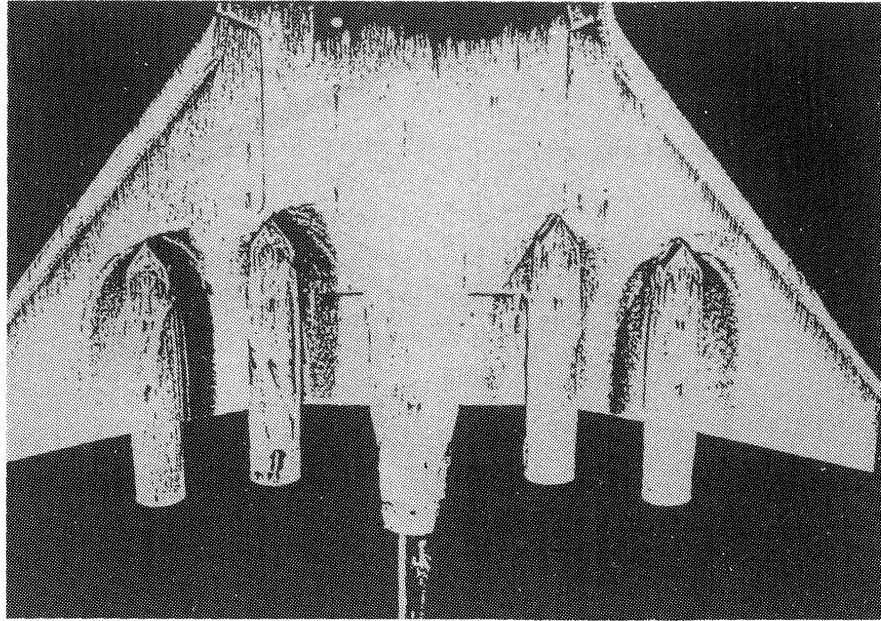
(a) Oil Flow Photograph
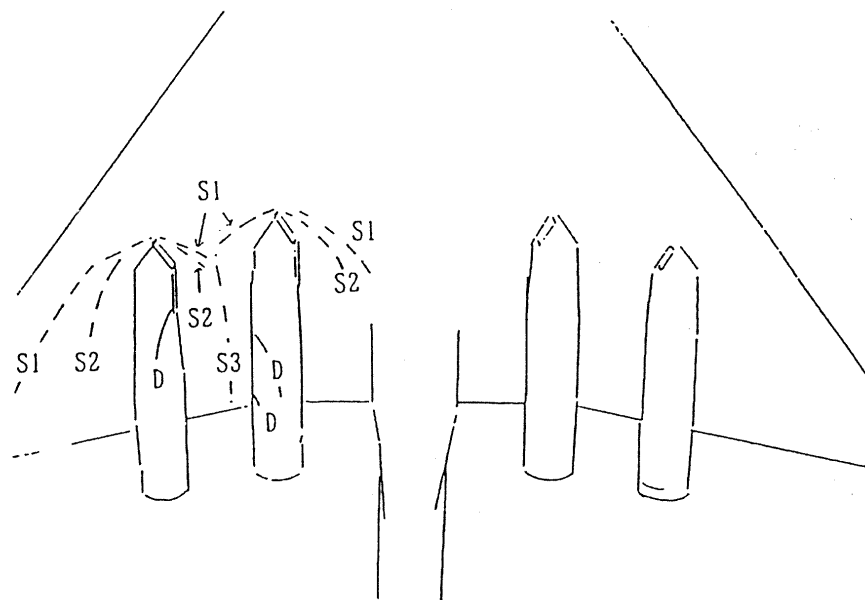
S1 : Primary Separation Line
S2 : Secondary Separation Line
S3 : Combined Separation Line of Primary and Secondary Separation Line
D  : Shock Wave Trace

(b) Schematic of Oil Flow

Figure 18   Outline of Wing under Surface Flow Field
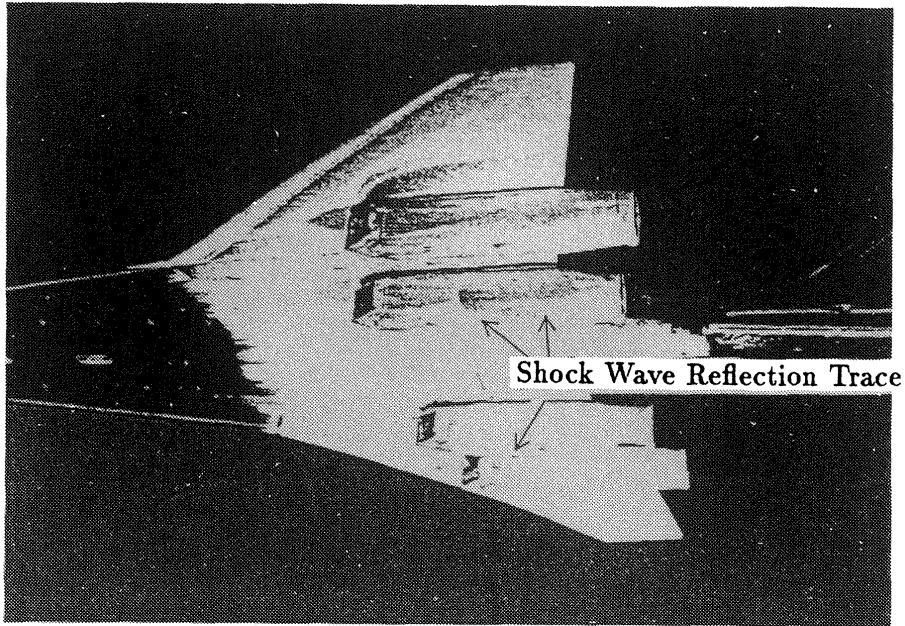
(a) Shock Wave Reflection Trace on Side of Nacelle



$\overline{\overline{\phantom{===}}}$ : Shock Wave

D : Shock Wave Reflection Trace
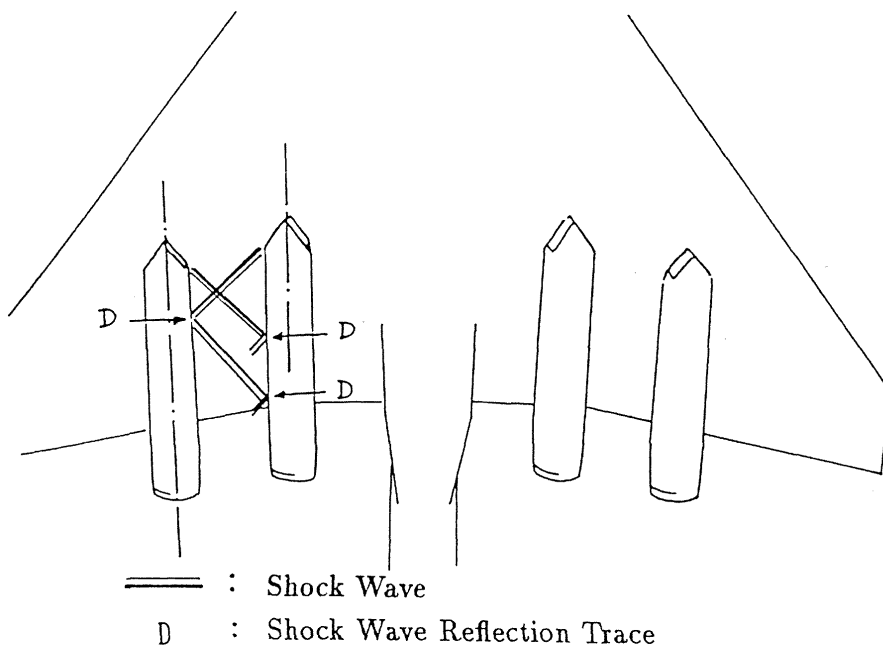
(b) Interaction of Shock Waves between Inboard and Outboard Nacelles

Figure 19   Outline of Flowfield on Side of Nacelle

**3**

# Prediction method of boundary layer transition in 3-D compressible flow

Yoji Ishida

National Aerospace Laboratory

Aircraft Aerodynamics Division

## 1. Introduction

The requirement for a highly accurate method of predicting the 3-D compressible boundary layer transition location over a wing and body of a real aircraft is now increasing in relation to the worldwide trend of developing a so called "next generation" high speed civil transport (HSCT) or space plane with a large drag reduction.

Accurate prediction of transition location is crucial to the successful design of drag reduction techniques such as laminar-flow-control(LFC) and natural laminar flow(NLF). Direct numerical simulation of the transition process with the Navier-Stokes equation , the most rigorous treatment, is however still far beyond the capability of current computers, and is not practicable in the design phase. We must therefore rely on some approximate methods. The $e^N$ method ,for example, is one of these and is a semi-empirical method in the sense that the factor N for the transition is determined only empirically about 9. But its less empiricism than other methods stimulates us to apply it to the three-dimensional boundary layer, although it is not so straightforward.

The numerical system for predicting the transition location of the boundary layers over supersonic wings described in this report consists of the calculations of the three-dimensional boundary layer , its linear stability characteristics and N factor. Each of the three calculations requires a lot of computing time and a rather complex interference procedure (interpolation or extrapolation of the data) between each calculation. Therefore to save computing time and make the resultant numerical system as simple as possible an efficient algorithm must be adopted:  we have used the same computing algorithm for both the boundary layer and the linear stability calculation. The outline of the system will be described in this report.

## 2.   $e^N$ method

## 2.1   Governing equation

We examine if small disturbances $(u, v, w, p, T, \rho)$ superimposed to 3-D compressible laminar boundary layer — the basic flow — would spatially grow or decay. The fundamental assumption in the analysis is that the basic flow is parallel, i.e. a function of only the y ordinate and the resultant governing equation for the disturbances derived from both the Navier-Stokes equation and the energy equation can be linearized because of the small disturbance assumption. The disturbances are written as

$$(u, v, w) = \left[\tilde{u}(y), \tilde{v}(y), \tilde{w}(y)\right]\exp\left[i(\alpha x + \beta z - \omega t)\right]$$

$$p = \tilde{p}(y)\exp\left[i(\alpha x + \beta z - \omega t)\right]$$

$$T = \tilde{T}(y)\exp\left[i(\alpha x + \beta z - \omega t)\right] \tag{1}$$

$$\rho = \tilde{\rho}(y)\exp\left[i(\alpha x + \beta z - \omega t)\right]$$

in which all variables are non-dimensionalized by some reference velocity and length. Then the disturbance equations are described in term of $(\tilde{u}, \tilde{v}, \tilde{w}, \tilde{p}, \tilde{T}, \tilde{\rho})$ , their y derivatives , wave numbers $\alpha$ and $\beta$ , frequency $\omega$ and basic flow velocities $U(y), W(y)$. The boundary condition is

$$\tilde{u} = \tilde{v} = \tilde{w} = \tilde{T} = 0, \quad \text{at } y = 0$$

$$\tilde{u}, \tilde{v}, \tilde{w}, \tilde{T} \to 0 \quad \text{as } y \to \infty \tag{2}$$

Following Mack[2], the disturbance equations are transformed into a system of first order ordinary differential equations

$$\frac{d\phi_i}{dy} = \sum_{j=1}^{8} a_{ij}\phi_j \qquad (i = 1, 2, \cdots 8) \tag{3}$$

where

$$\phi_1 = \alpha\tilde{u} + \beta\tilde{w}, \quad \phi_2 = d\phi_1/dy, \quad \phi_3 = \tilde{v}, \quad \phi_4 = \tilde{p},$$

$$\phi_5 = \tilde{T}, \quad \phi_6 = d\phi_5/dy, \quad \phi_7 = \alpha\tilde{w} - \beta\tilde{u}, \quad \phi_8 = d\phi_7/dy, \tag{4}$$

and then the boundary condition equation (2) becomes

$$\phi_1 = \phi_3 = \phi_5 = \phi_7 = 0 \quad \text{at } y = 0$$

$$\phi_1, \phi_3, \phi_5, \phi_7 \to 0 \quad \text{as } y \to \infty. \tag{5}$$

We solve equation (3), following Malik[1], by the Euler-Maclaurin finite difference scheme:

$$\Psi^k - \Psi^{k-1} = \Delta_1\left(\frac{d\Psi^k}{dy} + \frac{d\Psi^{k-1}}{dy}\right) - \Delta_2\left(\frac{d^2\Psi^k}{dy^2} + \frac{d^2\Psi^{k-1}}{dy^2}\right) + o(h_k^5) , \tag{6}$$

where $\Delta_1 = h_k/2, \quad \Delta_2 = h_k^2/12$. To apply equation (6) to equation (3), we put

$$\Psi = \{\phi_i\} , \quad d\Psi/dy = \{\sum_{j=1}^{8} a_{ij}\phi_j\} , \quad d^2\Psi/dy^2 = \{\sum_{j=1}^{8} b_{ij}\phi_j\} \tag{7}$$

where

$$b_{ij} = da_{ij}/dy + \sum_{l=1}^{8} a_{il}a_{lj} .$$

Substitution of equation (7) into equation (6) yields

$$\phi_j^k - \Delta_1 \sum_{j=1}^{8} a_{ij}^k \phi_j^k + \Delta_2 \sum_{j=1}^{8} b_{ij}^k \phi_j^k$$

$$- \{ \phi_j^{k-1} - \Delta_1 \sum_{j=1}^{8} a_{ij}^{k-1} \phi_j^{k-1} + \Delta_2 \sum_{j=1}^{8} b_{ij}^{k-1} \phi_j^{k-1} \} = 0,$$

which is rewritten as

$$\sum_{j=1}^{8} P_{ij}^k \phi_j^k + \sum_{j=1}^{8} Q_{ij}^k \phi_j^{k-1} = 0 \quad , \tag{8}$$

where

$$P_{ij}^k = \begin{cases} -\Delta_1 a_{ij}^k + \Delta_2 b_{ij}^k & (i \neq j) \\ \\ 1 - \Delta_1 a_{ij}^k + \Delta_2 b_{ij}^k & (i=j) \end{cases}$$

$$Q_{ij}^k = \begin{cases} -\Delta_1 a_{ij}^{k-1} + \Delta_2 b_{ij}^{k-1} & (i \neq j) \\ \\ 1 - \Delta_1 a_{ij}^{k-1} + \Delta_2 b_{ij}^{k-1} & (i=j). \end{cases}$$

## 2.2 Solution of eigenvalue problem and calculation of the N factor

As is well known , equation (8) and boundary condition (5) constitute an eigenvalue problem. To get its non-trivial solution we first drop the boundary condition $\phi_1 = 0$ and instead impose $\phi_4 = 1$ (this means that p is normalized);

$$\phi_3 = \phi_5 = \phi_7 = 0, \phi_4 = 1 \qquad \text{at } y=0 , \tag{9a}$$

$$\phi_1, \phi_3, \phi_5, \phi_7 \rightarrow 0, \qquad \text{as } y \rightarrow \infty, \tag{9b}$$

and then determine the eigenvalues to satisfy the dropped condition.

Numerical treatment of the boundary condition, equation (9b), is not easy in this form and so, following Mack[2] ,we replaced the condition by analytic solution of equation (3) which can be obtained by using the fact that as at y $\rightarrow \infty$ the characteristics of the basic flow are constant and y derivatives of flow variables are zero, $a_{ij}$ in the right hand side of equation (3) becomes constant $\bar{a}_{ij}$.

Now equations (8), with boundary condition (9), are expressed in matrix-vector form

$$\Pi \delta = r \tag{10}$$

where   $\Pi, \delta$ and  $r$  are

$$
\Pi = \begin{bmatrix} A_0 & C_0 & & & \\ B_1 & A_1 & C_1 & & \\ & & \cdots & & \\ & & B_i & A_i & C_i \\ & & & \cdots & \\ & & & B_{j-1} & A_{j-1} & C_{j-1} \end{bmatrix} \quad \delta = \begin{bmatrix} \delta_0 \\ \delta_1 \\ \delta_i \\ \delta_{j-1} \\ \delta_j \end{bmatrix} \quad r = \begin{bmatrix} r_0 \\ r_1 \\ r_i \\ r_{j-1} \\ r_j \end{bmatrix} \tag{11}
$$

where

$$
\delta_j = \begin{bmatrix} (\phi_1)_j \\ (\phi_2)_j \\ \\ (\phi_8)_j \end{bmatrix} \qquad r_j = \begin{bmatrix} (r_1)_j \\ (r_2)_j \\ \\ (r_8)_j \end{bmatrix}
$$

and  $A_j, B_j, C_j$ are the $8 \times 8$ matrix (details are omitted here).

The solution of equation (10) which can be obtained   by the block-elimination method depends on  $\alpha, \beta, \omega, R$  i.e.

$$
\delta = \delta(\alpha, \beta, \omega, R) \tag{12}
$$

which in the spatial amplification theory (i.e. $\omega$ =real) means that  $\delta$  depends on six scalar quantities $(\alpha_r, \alpha_i, \beta_r, \beta_i, \omega, R)$. The dropped boundary condition

$$
\phi_1(\alpha, \beta, \omega, R) = 0 \qquad \text{at y=0} \tag{13}
$$

can determine only two eigenvalues. In the spatial amplification theory $\omega$ and R are given and thus a relationship between two wave numbers  $\alpha$  and $\beta$  is required. The relationship can be computed by making use of concepts based on group velocity using the saddle-point method (Gaster[3], Cebeci-Stewartson[4]).

According to this method, let us consider an oscillatory disturbance with period $2\pi/\omega$ generated at the origin so that the disturbance at large finite values of x,z may be assumed to be of the form

$$
\widetilde{Q}(x, y, z, t) = e^{-i\omega t} \int_c Q(\alpha, \beta, \omega) e^{i(\alpha x + \beta z)} \, d\beta \tag{14}
$$

where c is a contour in the complex plane of $\beta$ extending to $\infty$ in either direction.  $Q$ is a determinate function whose properties are such that the integral converges.  $\alpha$  in equation (14) is a function of $\beta$  and $\omega$ found by solving equation (10). Now for any ray in the (x,z) plane and passing through

the origin, we can write

$$z = x \tan \gamma \tag{15}$$

with $\gamma$ denoting a constant, and look for the dominant contribution to $Q$ along this ray as $x \to \infty$. This comes from the saddle point $\beta^*$ of $\alpha x + \beta z$, regarded as a function of $\beta$, which occurs when

$$\left( \frac{\partial \alpha}{\partial \beta} \right)_{\omega R} x + z = 0 \quad . \tag{16}$$

Since x and z are real, the imaginary part of $\partial \alpha / \partial \beta$ must be zero to satisfy eqation (16). Combining equations (15) and (16) we can write the relation

$$\left( \frac{\partial \alpha}{\partial \beta} \right)_{\omega, R} = -\frac{z}{x} = -\tan \gamma \tag{17}$$

which gives another relationship between $\alpha$ and $\beta$ and the wave orientaion and growth direction of the disturbance. Now we can solve equation (10) with equations (13) and (17). Before describing details of the solution procedure, we describe how to use the solution in the $e^N$ method.

### 2.2.1 Neutral stability curve — Zarf [4)-8)]

The growth rate of spatially developing disturbance $\Gamma$ is given from equation (17) as

$$\Gamma = \alpha_i - \beta_i \tan \gamma = \alpha_i - \beta_i \left( \partial \alpha / \partial \beta \right)_i \tag{18}$$

where $\Gamma < 0$ means amplified, $\Gamma > 0$ damped and $\Gamma = 0$ neutral. In order that $\Gamma = 0$ for any $\gamma$, the conditions

$$\alpha_i = \beta_i = 0 \quad \text{and} \quad \partial \alpha / \partial \beta = real \tag{19}$$

must be satisfied. The neutral stability curve on which the condition is satisfied is refered to as Zarf by Cebeci. In the $e^N$ method the integration of the growth rate starts from the neutral point, so we must first determine the Zarf.

First fix the starting point of calculation (x,z) near the leading edge. The velocity and temperature distributions of the basic flow and Reynolds number are now given. Then equation (13) is written as

$$\phi_i(\alpha, \beta, \omega) = 0. \tag{20}$$

$\alpha_i, \beta_i$ being zero from equation (19), the relation contains three unknowns $(\alpha_r, \beta_r, \omega)$. The second equation in equation (19) and equation (20) can now determine $\alpha_r$, $\beta_r$ and $\omega$ as follows. When $\omega$ is constant in equation (20), it gives

$$d\phi_1 = \left(\frac{\partial\phi_1}{\partial a}\right)_\beta da + \left(\frac{\partial\phi_1}{\partial\beta}\right)_\alpha d\beta = 0 \tag{21}$$

Therefore $\partial\alpha/\partial\beta l$ in equation (19) is given by

$$\frac{\partial\alpha}{\partial\beta} = -\frac{\left(\partial\phi_1/\partial\beta\right)_\alpha}{\left(\partial\phi_1/\partial\alpha\right)_\beta} = e \quad . \tag{22}$$

As we use an iteration method to get the solutions of $\alpha,\beta,\omega$, it is necessary to calculate the corrections $(\delta\alpha,\delta\beta,\delta\omega)$ to initial guesses of $(\alpha^v,\beta^v,\omega^v)$. If we expand equation (20) about $(\alpha^v,\beta^v,\omega^v)$ and neglect higher order terms, we get

$$\phi_{1r} + \frac{\partial\phi_{1r}}{\partial\alpha}\delta\alpha + \frac{\partial\phi_{1r}}{\partial\beta}\delta\beta + \frac{\partial\phi_{1r}}{\partial\omega}\delta\omega = 0 \tag{23a}$$

$$\phi_{1i} + \frac{\partial\phi_{1i}}{\partial\alpha}\delta\alpha + \frac{\partial\phi_{1i}}{\partial\beta}\delta\beta + \frac{\partial\phi_{1i}}{\partial\omega}\delta\omega = 0 \quad . \tag{23b}$$

Similarly if we expand equation (22), we get

$$e + \frac{\partial e}{\partial\alpha}\delta\alpha + \frac{\partial e}{\partial\beta}\delta\beta + \frac{\partial e}{\partial\omega}\delta\omega = 0 \tag{24}$$

The imaginary part of $\alpha,\beta$ are zero and so is that of $d\alpha/d\beta$ or $e$. Therefore we must seek the values of $\alpha,\beta,\omega$ which makes the imaginary part of equation (26) zero, i.e.

$$e_i + \frac{\partial e_i}{\partial\alpha}\delta\alpha + \frac{\partial e_i}{\partial\beta}\delta\beta + \frac{\partial e_i}{\partial\omega}\delta\omega = 0 \tag{25}$$

If we solve equation (23) and (25) for $\delta\alpha,\delta\beta,\delta\omega$, we get

$$\delta\alpha = \left[\phi_{1r}\left(\phi_{1i\omega}e_{i\beta} - \phi_{1i\beta}e_{i\omega}\right) + \phi_{1i}\left(\phi_{1r\beta}e_{i\omega} - e_{i\beta}\phi_{1r\omega}\right) - e_i\left(\phi_{1r\omega}\phi_{1i\omega} - \phi_{1r\omega}\phi_{1i\beta}\right)\right]/\Delta \tag{26a}$$

$$\delta\beta = \left[\phi_{1r}\left(\phi_{1i\omega}e_i - \phi_{1i}e_{i\omega}\right) - \phi_{1i\alpha}\left(\phi_{1r\omega}e_i - e_i\phi_{1r\omega}\right) + e_{i\alpha}\left(\phi_{1r\omega}\phi_i - \phi_{1r}\phi_{1i\omega}\right)\right]/\Delta \tag{26b}$$

$$\delta\omega = \left[\phi_{1r\alpha}\left(\phi_{1i}e_{i\beta} - \phi_{1i\beta}e_i\right) - \phi_{1i\alpha}\left(\phi_{1r}e_{i\beta} - e_i\phi_{1r\beta}\right) + e_{i\alpha}\left(\phi_{1r}\phi_{1i\beta} - \phi_{1r\beta}\phi_{1i}\right)\right]/\Delta \tag{26c}$$

where

$$\Delta = e_{i\alpha}\left(\phi_{1r\beta}\phi_{1i\omega} - \phi_{1i\beta}\phi_{1r\omega}\right) - e_{i\beta}\left(\phi_{1r\alpha}\phi_{1i\omega} - \phi_{1i\alpha}\phi_{1r\omega}\right) - e_{i\omega}\left(\phi_{1r\alpha}\phi_{1i\beta} - \phi_{1i\alpha}\phi_{1r\beta}\right) \tag{27}$$

and suffix $i$ and $r$ means imaginary and real part, respectively and suffix $\alpha,\beta$ and $\omega$ means partial derivatives for each variable. The iteration will be continued until these correction terms $\delta\alpha,\delta\beta,\delta\omega$ becomes less than $\varepsilon$, a specified small quantity. When $\delta\alpha = \delta\beta = \delta\omega = 0$, equation (25) certainly gives $e_i = 0$.

The derivatives $\phi_{1\alpha},\phi_{1\beta}$ and $e_\alpha,e_\beta$ in equations (22),(23) and (24) are obtained as follows. From equation (22)

$$e = -\frac{\phi_{1\beta}}{\phi_{1\alpha}}$$

we can get the partial derivatives of $e$ as follows:

$$e_\alpha = -\frac{\phi_{1\beta\alpha}}{\phi_{1\alpha}} + \frac{\phi_{1\beta}}{\phi_{1\alpha}^2}\phi_{1\alpha\alpha} \tag{28a}$$

$$e_\beta = -\frac{\phi_{1\beta\beta}}{\phi_{1\alpha}} + \frac{\phi_{1\beta}}{\phi_{1\alpha}^2}\phi_{1\alpha\beta} \tag{28b}$$

$$e_\omega = -\frac{\phi_{1\beta\omega}}{\phi_{1\alpha}} + \frac{\phi_{1\beta}}{\phi_{1\alpha}^2}\phi_{1\alpha\omega} \tag{28c}$$

The $\alpha, \beta$ and $\omega$ derivatives of $\phi_1$ in equation (28) are calculated as follows: for example in the case of $\phi_{1\alpha\beta}$, if we first differentiate equation (10) with $\alpha$ and then with $\beta$, we get

$$\Pi\frac{\partial^2\delta}{\partial\alpha\partial\beta} = -\frac{\partial\Pi}{\partial\beta}\frac{\partial\delta}{\partial\alpha} - \frac{\partial\Pi}{\partial\alpha}\frac{\partial\delta}{\partial\beta} - \frac{\partial^2\Pi}{\partial\alpha\partial\beta}\delta \tag{29}$$

As the coefficient matrix $\Pi$ of this equation is the same as that of equation (10), we can use the solution algorithm of equation (10) when the right hand side of equation (29) is known. The derivatives of $\Pi$ can immediately be obtained from equation (11) and $\partial\delta/\partial\alpha, \partial\delta/\partial\beta$ can be obtained by solving the following equations

$$\Pi\frac{\partial\delta}{\partial\alpha} = -\frac{\partial\Pi}{\partial\alpha}\delta, \quad\text{and}\quad \Pi\frac{\partial\delta}{\partial\beta} = -\frac{\partial\Pi}{\partial\beta}\delta \tag{30}$$

In the same way the $\alpha\alpha, \beta\beta, \alpha\omega, \beta\omega$ derivatives can be obtained.

We now summarize the first step of eigenvalue calculation on Zarf :

( I ) solve equation (10) for some initial guess of $\alpha, \beta, \omega$ .

( II ) if the value of $\phi_1$ at y=0 does not satisfy equation (20), the correction terms $\delta\alpha, \delta\beta, \delta\omega$ are calculated from equation (26).

( III ) if $\delta\alpha, \delta\beta, \delta\omega < \varepsilon$ the iteration is stopped, and if not, return to step ( I ) and repeat the same procedure. When the iteration finishes, $e$ is the real value which gives the direction of wave propagation.

(IV) repeat the calculation of the eigenvalues for various (x,z) positions.

In practical calculation some care is required because, although in this method a good initial guess for the eigenvalues is required to give a converged value, it is rather difficult to give such a value. Thus we start the calculation from the basic flow whose eigenvalue is already known, for example the flat plate flow, and then vary the flow gradually to the target flow with gradual change of eigenvalues.

## 2.2.2 computation of eigenvalues for general point

For the basic flow at a general point on a supersonic wing surface $\alpha_r, \alpha_i, \beta_r$ and $\beta_i$ in equation (13) and (17) are solved for a given frequency $\omega$ and Reynolds number R by Newton's method. The solution procedure is almost the same as that for Zarf except that the corrections are obtained in the following manner. First expanding equation (13) about some initial guess of $\alpha_r, \alpha_i, \beta_r, \beta_i$ we get

$$\phi_{1r} + \frac{\partial \phi_{1r}}{\partial \alpha_r} \delta\alpha_r + \frac{\partial \phi_{1r}}{\partial \alpha_i} \delta\alpha_i + \frac{\partial \phi_{1r}}{\partial \beta_r} \delta\beta_r + \frac{\partial \phi_{1r}}{\partial \beta_i} \delta\beta_i = 0$$

$$\phi_{1i} + \frac{\partial \phi_{1i}}{\partial \alpha_r} \delta\alpha_r + \frac{\partial \phi_{1i}}{\partial \alpha_i} \delta\alpha_i + \frac{\partial \phi_{1i}}{\partial \beta_r} \delta\beta_r + \frac{\partial \phi_{1i}}{\partial \beta_i} \delta\beta_i = 0$$

and then from equation (17) and (24),

$$e_r + \frac{\partial e_r}{\partial \alpha_r} \delta\alpha_r + \frac{\partial e_r}{\partial \alpha_i} \delta\alpha_i + \frac{\partial e_r}{\partial \beta_r} \delta\beta_r + \frac{\partial e_r}{\partial \beta_i} \delta\beta_i = -z / x = \gamma$$

$$e_i + \frac{\partial e_i}{\partial \alpha_r} \delta\alpha_r + \frac{\partial e_i}{\partial \alpha_i} \delta\alpha_i + \frac{\partial e_i}{\partial \beta_r} \delta\beta_r + \frac{\partial e_i}{\partial \beta_i} \delta\beta_i = 0$$

We can now solve these four equations for the corrections $\delta\alpha_r, \delta\alpha_i, \delta\beta_r, \delta\beta_i$ to the initial guess values.

At any downstream position x the initial guess may be given by the values of the previous calculation step $x - \Delta x$.

## 2.2.3 Prediction of the transition point

In three-dimensional flow, the N factor is calculated from

$$N = -\int_{x_o}^{x} \Gamma \, dx \tag{31}$$

where

$$\Gamma = \alpha_i - \beta_i \tau . \tag{32}$$
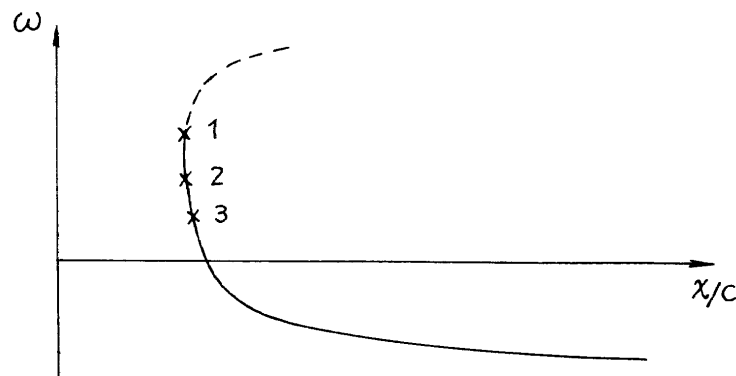


Fig.1    Schematic curve of zarf

The detailed procedure of the transition point is as follows:

① First calculate the neutral stability curve (zarf) for some x positions (figure 1)

② Start the calculation from, for example, position 1 in figure 1, $x_1/c$. At the next x/c step solve the eigenvalue problem with the frequency $\omega = \omega_1$ at $x_1/c$ and the relation

$$\partial\alpha/\partial\beta = \left(\partial\alpha/\partial\beta\right)_{x=x_1} = -\tau^{(1)}$$

to get $\alpha$ and $\beta$ which give $\Gamma$ from equation (32). Repeat the eigenvalue problem for various $\tau^{(1)}$ and find $\tau = \tau_{min}$ for which $\Gamma = \Gamma_{min}$. Then proceed to the next x/c step.

③ The values of $\Gamma = \Gamma_{min}$ which corresponds to $\tau = \tau_{min}$ at each x/c step give the N factor for the frequency $\omega_1$ from equation (31).

④ Repeat steps ② and ③ for other frequencies $\omega_2, \omega_3, \cdots$. (we do not consider a negative $\omega$ because its growth rate is smaller than that of a positive $\omega$.)

⑤ Finally we can obtain a family of N factor curves as is shown in figure 2. If we choose nine as the value of N as a criterion of the transition, the transition point is given by $(x/c)_{tr}$ in the figure.
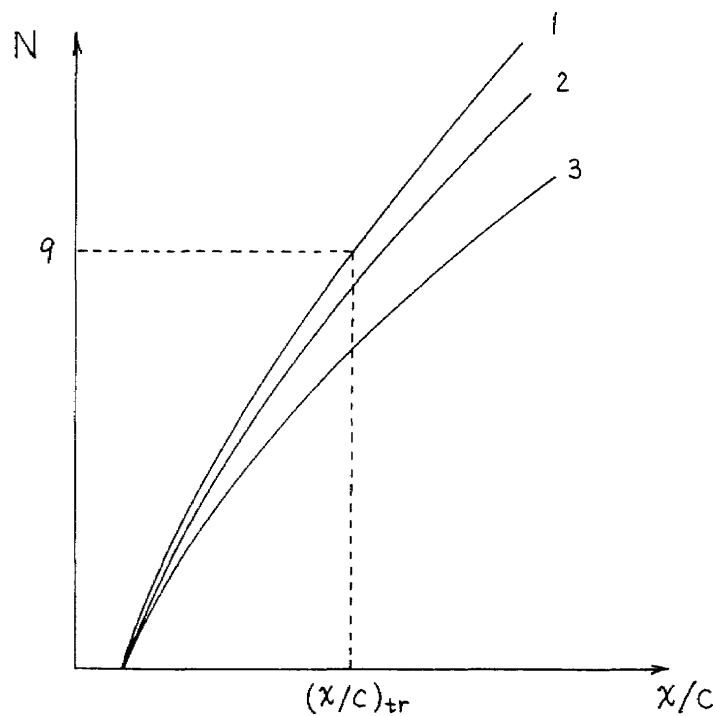


Fig.2 prediction of transition point by $e^N$ method

NACA0012 ($\alpha = 0°$ , Rc=7×10⁶) with suction ($v_w = v_{w0}$)

—— Euler-Maclaurin scheme

－－－ Itoh scheme

$\omega^* =$

25000 ($Hz$)

35000

55000
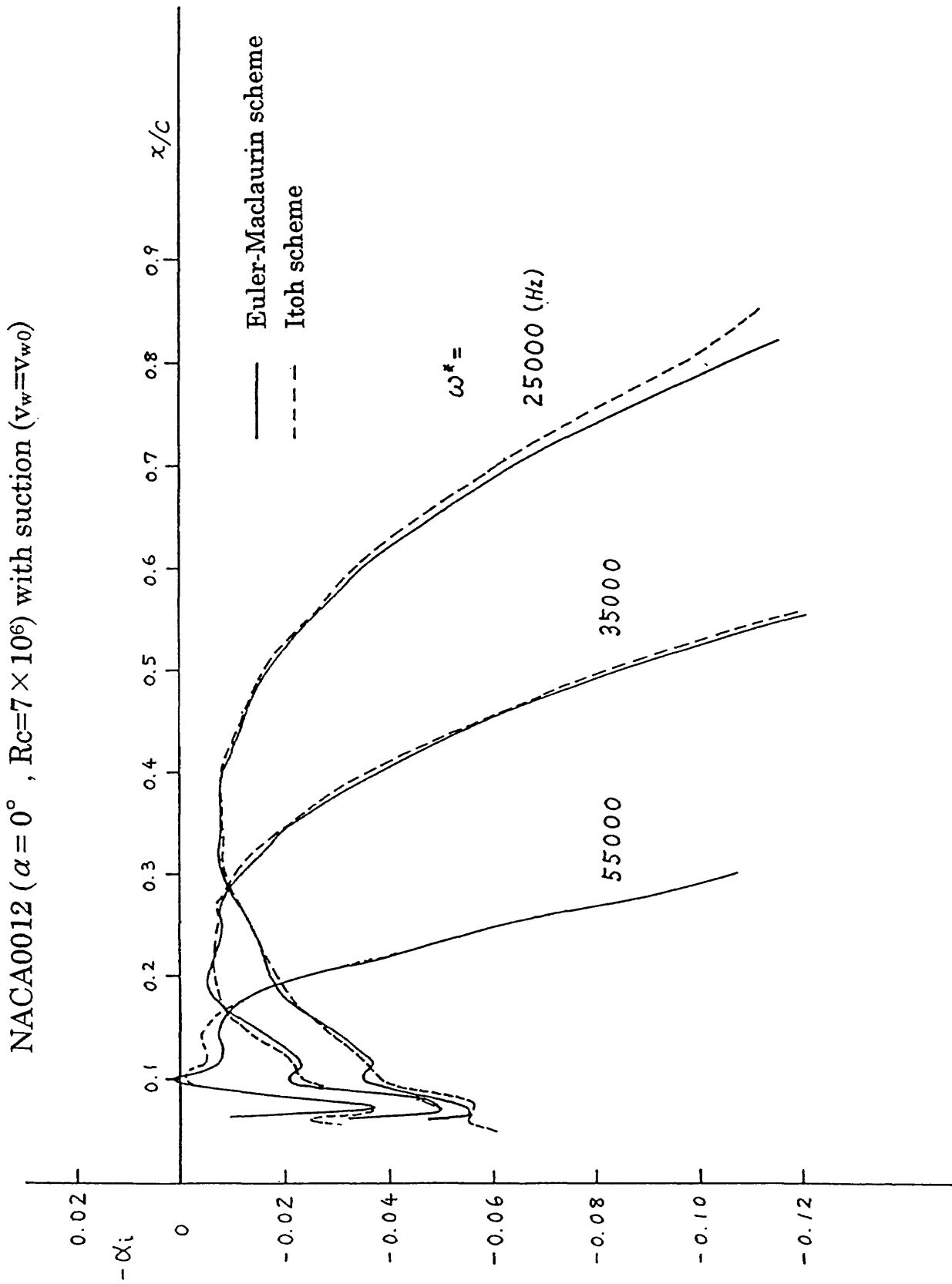
Fig.3　Accuracy of the Euler-Maclaurin scheme

## 2.3 Result

We have already finished the mathematical formulation of the linear stability calculation and now are developing a program code. Final results will be published in the near future. However as an incompressible version of the method is now available, we have executed a spatial linear stability calculation for the incompressible laminar boundary layer on the NACA0012 airfoil with suction ($\alpha = 0°$, $R=7 \times 10^6$) to check the accuracy of the Euler-Maclaurin scheme. The result in figure 3 shows a comparison of amplification rate $-\alpha_i$ between the Itoh (ref.9) and E-M schemes. The agreement is good and the E-M scheme has a good degree of accuracy.

## 3. Boundary layer calculation

As was stated in the introduction, we have used the same algorithm as that of the linear stability theory stated in §2 for the solution of the boundary layer equation. Thus only the outline of the solution procedure will be described. Following Iyer[10] the 3-D compressible boundary layer equation written in the body-fitted non-orthogonal curvilinear coordinate system is transformed into a system of partially differential equation:

continuity equation;

$$W_\varsigma = A_1 F_\xi + A_2 F + A_3 G_\eta + A_4 G \tag{33}$$

$\xi$ - momentum equation;

$$(IL - WF)_\varsigma = B_1 (F^2)_\xi + B_2 (FG)_\eta + B_3 F^2 + B_4 FG + B_5 G^2 + B_6 \theta \tag{34}$$

$\eta$ - momentum equation;

$$(IM - WG)_\varsigma = C_1 (FG)_\xi + C_2 (G^2)_\eta + C_3 F^2 + C_4 FG + C_5 G^2 + C_6 \theta \tag{35}$$

energy equation;

$$(I/P_r - WH)_\varsigma = D_1 (FH)_\xi + D_2 (GH)_\eta + D_3 FH + D_4 GH + D_5 \tag{36}$$

where $F = u/u_e, G = v/v_r$ and

$$F_\varsigma = L \tag{37}$$

$$G_\varsigma = M \tag{38}$$

$$H_\varsigma = I \tag{39}$$

(for the nomenclature see original paper). Equations (33)~(39) can be written in the vector form as

$$Q_\varsigma = R \tag{40}$$

where

$$Q = (Q_i) = (W, lL - WF, lM - WG, l_p l - WH, F, G, H) \tag{41}$$

Equation (40) has the identical form as equation (10) and thus the same solution algorithm can be used. In real calculation, equation (40) is further transformed into the equation of the solution vector $S$,

$$S_\varsigma = R^* \tag{42}$$

where

$$S = (S_i) = (W, F, G, H, L, M, T) \tag{43}$$

and then is solved for $S_i$. Of course there are some different points between the system of equation (10) and of equation (40) or (42). The first difference is that the latter is a nonlinear system. The second is that the right hand side of equations (33)~(36) i.e. (42) contain $\xi$ and $\eta$ derivatives and thus the former term is approximated by a finite difference scheme with second order accuracy and the latter by a second order or zigzag scheme respectively, depending on the sign of the cross flow velocity component. The third is that the boundary condition is different, it is homogeneous and non-homogeneous in the stability and boundary layer calculations respectively. However it is only an apparent difference, because the stability calculation also uses a non-homogeneous boundary condition as a technique for getting a nontrivial solution. In this way the system of equation (42) can now be solved with the same algorithm as equation (10) except that as the former is nonlinear about the solution vector it must be solved iteratively by using Newton's method, the calculation in each iteration being, of course, the same.

## 4. Conclusion

In this report we propose an efficient numerical calculation method of the transition location of the boundary layer over a supersonic wing which consists of the boundary layer, its linear stability and N factor calculations. We have used the same solution algorithm for both boundary layer and linear stability calculations to save computing time and make the calculation system as simple as possible.

# REFERENCES

1. M.R. Malik: Numerical Methods for Hypersonic Boundary Layer Stability. *J. Compt. Phys.* vol.86, pp.376-413 (1990).

2. L.M. Mack: Computation of the Stability of the Laminar Compressible Boundary Layer. *Methods of Computational Physics* (ed. B.A.Alder, S.Ferncach, M.Rotenberg), vol.4 (1965), pp.247-299, Academic Press, NY.

3. M.Gaster: A Theoretical Model of a Wave Packet in the Boundary Layer on a Flat Plate. *Proc. Roy. Soc. London, Series a.347,* 1975, pp.271-289.

4. T. Cebeci and K. Stewartson: On Stability and Transition in Three-dimensional Flows. *AIAA Jour.,* vol.18, No.4, April 1980, pp.398-405.

5. T. Cebeci and K. Stewartson: Asymptotic Properties of the Zarf. *AIAA Jour.,* vol.19, no.6, June 1981, pp.806-807.

6. T.Cebeci, H.H.Chen, D.Arnal and T.T.Huang: Three-Dimensional Linear Stability Approach to Transition on Wings and Bodies of Revolution at Incidence. *AIAA Jour.,* vol.29, no.12, Dec.1991, pp.2077-2085.

7. T.Cebeci and H.H.Chen: Numerical Method for Predicting Transition in Three-Dimensional Flows by Spatial Amplification Theory. *AIAA Jour.* vol.30, no.8, Aug. 1992, pp.1072-1979.

8. T.Cebeci, A.A.Khattab,H.H.Chen and L.T.Chen: An Approach to the Design of Wings: The Role of Mathematics, Physics and Economics. AIAA-92-0286. Jan.1992.

9. Yoji Ishida and Nobutake Itoh: Application of the eN method to Calculations of Laminar Flow Control. *Proceedings of the Third NAL symposium on Aircraft Computational Aerodynamics,* NAL SP-5, 1985, pp.131-138

10. V.Iyer: Three-Dimensional Boundary-Layer Program (BL3D) for Swept Subsonic or Supersonic Wings With Application to Laminar Flow Control. *NASA Contractor Report 4531,* August 1993.

# 4

# LINEAR STABILITY ANALYSIS OF A COMPRESSIBLE BOUNDARY LAYER COMPUTED BY NAVIER-STOKES CODE

**Toshiyuki NOMURA**
Aircraft Aerodynamics Division
National Aerospace Laboratory
Tokyo, Japan

## 1. Introduction

Development of high-accuracy schemes and improvement of computers in the aspects of both operational speed and memory have enabled Navier-Stokes code to compute boundary layers for stability analysis instead of a boundary-layer code. It is therefore important to verify how accurate the boundary layers computed by Navier-Stokes code are.

For numerical simulation of the supersonic flow around an infinite swept cylinder, the number of cells needed in order to eliminate the dependence of the boundary-layer flow on the computational grid is investigated. In comparison between the boundary-layer flow converged by the diagonalized ADI scheme and that converged by the LU-SGS scheme, the way the two kinds of time-marching methods affect the flow is also investigated. And furthermore, the linear stability analysis of the boundary layer at the attachment line is performed.

## 2. Navier-Stokes Code

The governing equations are the conservation form of the thin-layer Navier-Stokes equations, which are numerically solved by the finite-volume scheme.

$$\frac{\partial \hat{Q}}{\partial t} + \frac{\partial \hat{E}}{\partial \xi} + \frac{\partial \hat{F}}{\partial \eta} + \frac{\partial \hat{G}}{\partial \zeta} = \frac{1}{Re}\frac{\partial \hat{F}_v}{\partial \eta}$$

### 2.1 Numerical Fluxes

The inviscid fluxes $\hat{E}$, $\hat{F}$ and $\hat{G}$ are computed by the Chakravarthy-Osher TVD scheme[1]. The first-order accurate flux at the cell interface is given by

$$\hat{E}_{j+1/2} = \frac{1}{2}(\hat{E}_j + \hat{E}_{j+1}) - \frac{1}{2} T_{\xi,j+1/2}(\hat{A}^+_{\xi,j+1/2} - \hat{A}^-_{\xi,j+1/2}) T^{-1}_{\xi,j+1/2}(Q_{j+1} - Q_j),$$

$$\hat{A} = \frac{\partial \hat{E}}{\partial Q} = T_\xi \hat{A}_\xi T_\xi^{-1}, \quad \lambda^\pm_\xi = \frac{1}{2}(\lambda_\xi \pm |\lambda_\xi|).$$

$\hat{A}_\xi$ is the diagonal matrix that consists of the eigenvalues $\lambda_\xi$ of the Jacobian matrix $\hat{A}$, and $T_\xi$ is the similarity-transformation matrix that consists of the right eigenvectors of $\hat{A}$. $\hat{A}^+_\xi$ is the matrix where $\lambda_\xi$ in $\hat{A}_\xi$ are replaced by $\lambda^+_\xi$, and $\hat{A}^-_\xi$ is the matrix where $\lambda_\xi$ in $\hat{A}_\xi$ are replaced by $\lambda^-_\xi$. Density, velocities and enthalpy at the cell interface are computed using Roe's special averaging procedure. The accuracy of the above flux can be raised to the third order by adding the correction terms with the minmod limiter.

The viscous flux $\hat{F}_v$ is computed on the basis of Gauss's theorem.

### 2.2 Diagonalized ADI Scheme

The diagonalized ADI scheme by Pulliam and Chaussee[2] can be written as

$$T_\xi(I + \frac{\Delta t}{V}D_\xi \hat{A}_\xi)T_\xi^{-1} T_\eta(I + \frac{\Delta t}{V}D_\eta \hat{A}_\eta)T_\eta^{-1} T_\zeta(I + \frac{\Delta t}{V}D_\zeta \hat{A}_\zeta)T_\zeta^{-1} \Delta Q = -\frac{\Delta t}{V}\hat{R},$$

$$\hat{A} = \frac{\partial \hat{E}}{\partial Q} = T_\xi \hat{A}_\xi T_\xi^{-1}, \quad \hat{B} = \frac{\partial \hat{F}}{\partial Q} = T_\eta \hat{A}_\eta T_\eta^{-1}, \quad \hat{C} = \frac{\partial \hat{G}}{\partial Q} = T_\zeta \hat{A}_\zeta T_\zeta^{-1},$$

$$\hat{R} = D_\xi \hat{E} + D_\eta \hat{F} + D_\zeta \hat{G} - \frac{1}{Re}D_\eta \hat{F}_v.$$

$D$ is a difference operator. The left hand of the ADI scheme is a block-tridiagonal system, and meanwhile the left hand of the diagonalized ADI scheme is a scalar-tridiagonal one. That makes the fast inversion of the left hand possible.

## 2.3 LU-SGS Scheme

The LU-SGS scheme by Yoon and Jameson[3] can be written as

$$L D^{-1} U \Delta Q = -\frac{\Delta t}{V} \hat{R},$$

$$L = I + \frac{\Delta t}{V} (D_\xi^- \hat{A}^+ + D_\eta^- \hat{B}^+ + D_\zeta^- \hat{C}^+ - \hat{A}^- - \hat{B}^- - \hat{C}^-),$$

$$D = I + \frac{\Delta t}{V} (\hat{A}^+ - \hat{A}^- + \hat{B}^+ - \hat{B}^- + \hat{C}^+ - \hat{C}^-),$$

$$U = I + \frac{\Delta t}{V} (D_\xi^+ \hat{A}^- + D_\eta^+ \hat{B}^- + D_\zeta^+ \hat{C}^- + \hat{A}^+ + \hat{B}^+ + \hat{C}^+),$$

$$\hat{A}^\pm = \frac{1}{2} [\hat{A} \pm \rho_\xi I], \hat{B}^\pm = \frac{1}{2} [\hat{B} \pm \rho_\eta I], \hat{C}^\pm = \frac{1}{2} [\hat{C} \pm \rho_\zeta I],$$

$$\rho_\xi = \kappa max\{ |\lambda_\xi| \}, \rho_\eta = \kappa max\{ |\lambda_\eta| \}, \rho_\zeta = \kappa max\{ |\lambda_\zeta| \}.$$

$\kappa$ is a constant that is greater than or equal to 1. $D^-$ is a backward-difference operator, and $D^+$ is a forward-difference operator. The approximation of the Jacobian matrices not only improves the stability of the scheme but substantially removes the inversion of the left hand.

## 2.4 Computational Grid

Three kinds of C-type grids, which differ in density, are generated for the infinite cylinder with a swept angle of $60°$ shown in Fig. 1. Grid B of medium density is shown in Fig. 2. The grid generator is based on Takanashi's method[4]. The number of grid points, the minimum spacing in the attachment-line boundary layer, the Courant number and the time steps for convergence are tabulated in Table 1 for each grid. The time-marching method used is the diagonalized ADI scheme.

The Mach number of the free stream is 3.5, and the Reynolds number based on the diameter of the cylinder is $1.05 \times 10^6$.

## 3. Linear Stability-Analysis Code

The nonconservation form of the Navier-Stokes equations in Cartesian coordinates is linearized by substituting fluctuation quantities into it, and then the parallel-flow approximation is made. Assuming the fluctuation quantities normal-mode, stability equations are obtained that can be written as

$$[ \tilde{u}(y), \tilde{v}(y), \tilde{w}(y), \tilde{p}(y), \tilde{\tau}(y) ] e^{i(\alpha x + \beta z - \omega t)},$$

$$(AD^2 + BD + C) \tilde{\phi} = 0, \tilde{\phi} = (\alpha \tilde{u} + \beta \tilde{w}, \tilde{v}, \tilde{p}, \tilde{\tau}, \alpha \tilde{w} - \beta \tilde{u})^T, D \equiv d/dy.$$

$\tau$ is temperature. $A, B$ and $C$ are 5×5 matrices computed on the basis of the velocity profiles and temperature one in the boundary layer. Here the temporal stability is dealt with. $\alpha$ and $\beta$ are the real wavenumbers specified, and $\omega$ is the complex frequency unknown. The Malik-Orszag global method[5] is applied to the stability equations, and then $\omega$ is obtained.

## 4. Results

The dependence of the boundary-layer flow on the computational grid is investigated, and the effect of the time-marching method on the flow is also investigated. And furthermore, the linear stability analysis of the boundary layer at the attachment line is performed.

### 4.1 Dependence of the Boundary-Layer Flow on the Grid

The boundary-layer flows computed with each grid are compared. The time-marching method used is the diagonalized ADI scheme that includes the local time step with the constant Courant number shown in Table 1.

The velocity and temperature profiles at the position of $\theta = 0°$ are shown in Fig. 3. Grid A has 8 cells between the wall and the boundary-layer edge, Grid B 14 cells, and Grid C 28 cells. Though Grid A appears coarse, the physical quantities at the cell centers coincide with those obtained with the other grids except near the wall. There is no

difference between the profiles of Grid B and Grid C.

The velocity and temperature profiles at the position of θ = 90° are shown in Fig. 4. Grid A has 9 cells between the wall and the boundary-layer edge, Grid B 17 cells, and Grid C 32 cells. The velocity profiles of Grid A slightly deviate from the others. The temperature profile of Grid A is a little higher near the wall than the others. There is no difference between the profiles of Grid B and Grid C.

In consequence, Grid B appears to have enough density to eliminate the dependence of the boundary-layer flow on the grid.

### 4.2 Effect of the Time-Marching Method on the Boundary-Layer Flow

A comparison is made between the boundary-layer flow converged by the diagonalized ADI scheme and that converged by the LU-SGS scheme. The LU-SGS scheme includes the local time step with the Courant number of 1, and the time is marched by 4000 steps. Grid B is employed in both cases.

The velocity and temperature profiles at the position of θ = 0° are shown in Fig. 5. There is no difference between the two velocity profiles, and meanwhile the temperature profile converged by the LU-SGS scheme is a little higher near the wall than that converged by the diagonalized ADI scheme.

The velocity and temperature profiles at the position of θ = 90° are shown in Fig. 6. The two velocity profiles coincide with each other precisely, and the same can be said of the temperature profiles.

In consequence, the usage of the two different time-marching methods yields very little difference between the converged flows.

### 4.3 Linear Stability Analysis of the Boundary Layer at the Attachment Line

The temporal stability is investigated for the laminar boundary layer at the attachment line. The boundary layer is computed using Grid B and the diagonalized ADI scheme. The wavenumber vector of the disturbances is inclined at 60° from Z coordinate. The obtained ranges, where the disturbances grow, are shown in Fig. 7 with the neutral-stability curves by Malik[6]. Both are in good agreement, which shows that the boundary layer is accurate enough to perform the stability analysis. $F$, $\bar{R}$ and $\zeta$ in Fig. 7 are defined as

$$F = \frac{2 \pi V_e}{W_e^2} f, \bar{R} = \frac{W_e \zeta}{V_e}, \zeta = \left[ \frac{V_e}{dU_e/dX} \right]_{X=0}^{1/2},$$

where $e$ refers to the conditions at the boundary-layer edge.

## 5. Conclusions

The compressible boundary-layer flow on an infinite swept cylinder is computed by Navier-Stokes code with the grid density changed or with the time-marching method replaced. The dependence of the boundary-layer flow on the grid appears to be eliminated by employing a grid as dense as Grid B. There is very little difference between the boundary-layer flow converged by the diagonalized ADI scheme and that converged by the LU-SGS scheme. And furthermore, the results of the stability analysis of the boundary layer at the attachment line agree fairly well with those obtained by Malik.

### References

[1] Chakravarthy, S. R., "Development of Upwind Schemes for the Euler Equations," NASA CR 4043, 1987.

[2] Pulliam, T. H. and Chaussee, D. S., "A Diagonal Form of an Implicit Approximate-Factorization Algorithm," J. Comp. Phys., Vol. 39, pp. 347-363, 1981.

[3] Yoon, S. and Kwak, D., "An Implicit Three-Dimensional Navier-Stokes Solver for Compressible Flow," AIAA Paper 91-1555-CP, June 1991.

[4] Takanashi, S. and Takemoto, M., "A Method of Generating Structured-Grids for Complex Geometries and Its Application to the Navier-Stokes Simulation," CFD J., Vol. 2, No. 2, pp. 209-218, 1993.

[5] Malik, M. R., " Finite-Difference Solution of the Compressible Stability Eigenvalue Problem," NASA CR 3584, 1982.

[6] Malik, M. R. and Beckwith, I. E., " Stability of a Supersonic Boundary Layer along a Swept Leading Edge," AGARD CP 438, pp. 3-1 to 3-9, 1988.

|  | Points($\xi \times \eta$) | Min. spacing($y^+$) | Courant no. | Time steps |
|---|---|---|---|---|
| Grid A | 112× 46 | 1.658471 | 1 | 4000 |
| Grid B | 224× 91 | 0.4233750 | 2 | 4000 |
| Grid C | 448×181 | 0.1064922 | 8 | 6000 |

Table 1: Computational grids
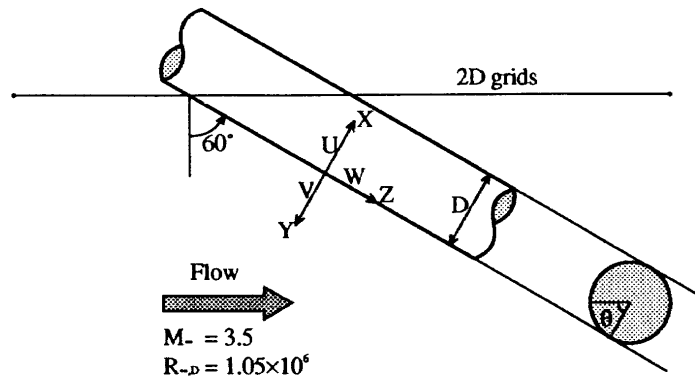
Fig. 1: Infinite swept cylinder

Fig. 2: Grid B ( 224 × 91 )

Fig. 3: Velocity and temperature profiles ( θ = 0° )

·······: Grid A, ─·─·─: Grid B, ───────: Grid C



Fig. 4: Velocity and temperature profiles ( θ = 90° )
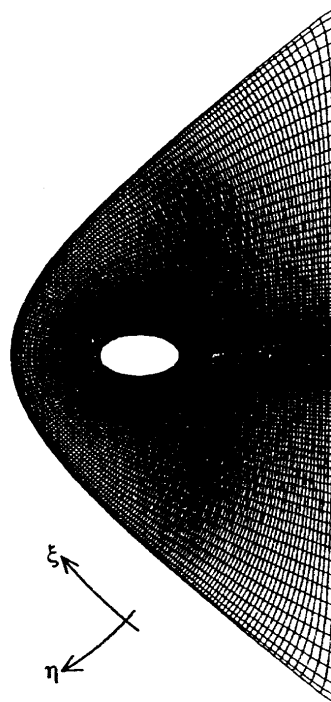
·······: Grid A, ─·─·─: Grid B, ───────: Grid C



Fig. 5: Velocity and temperature profiles ( θ = 0° )
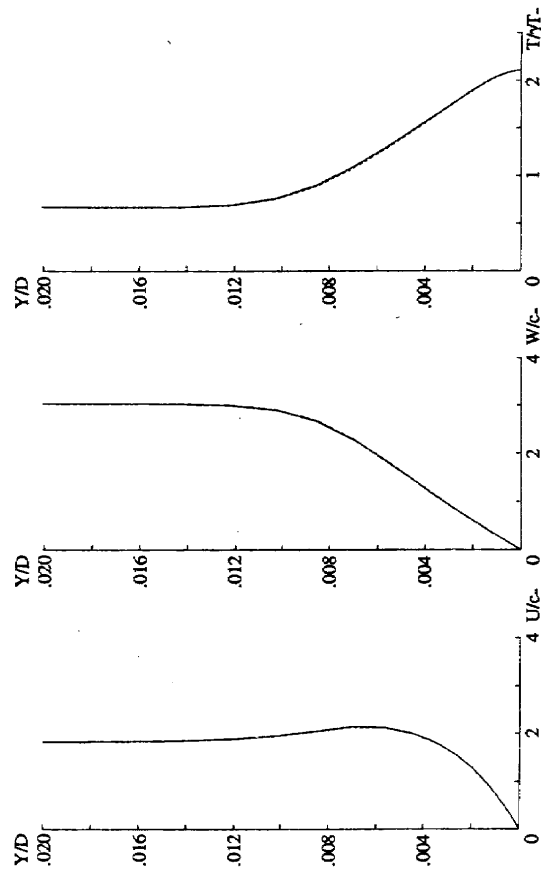
------: ADI, ───────: LU-SGS



Fig. 6: Velocity and temperature profiles ( θ = 90° )

------: ADI, ───────: LU-SGS

F×10⁴

1.2

R₋ᴅ×10⁻⁶
1.05

0.8

0.4

0        1000        2000  R̄

Frequency – Reynolds number

Cr

0.7

R₋ᴅ×10⁻⁶
1.05

0.5

0.3

0        1000        2000  R̄

Phase speed – Reynolds number
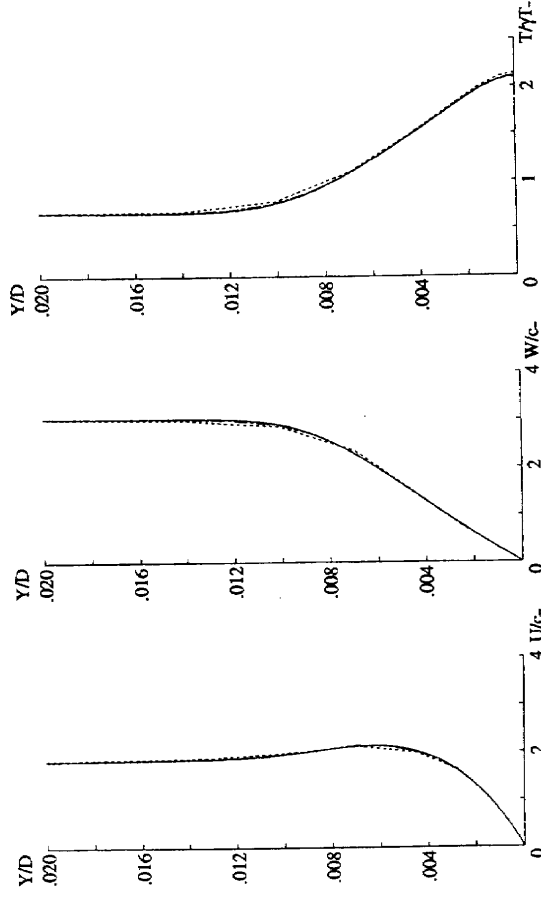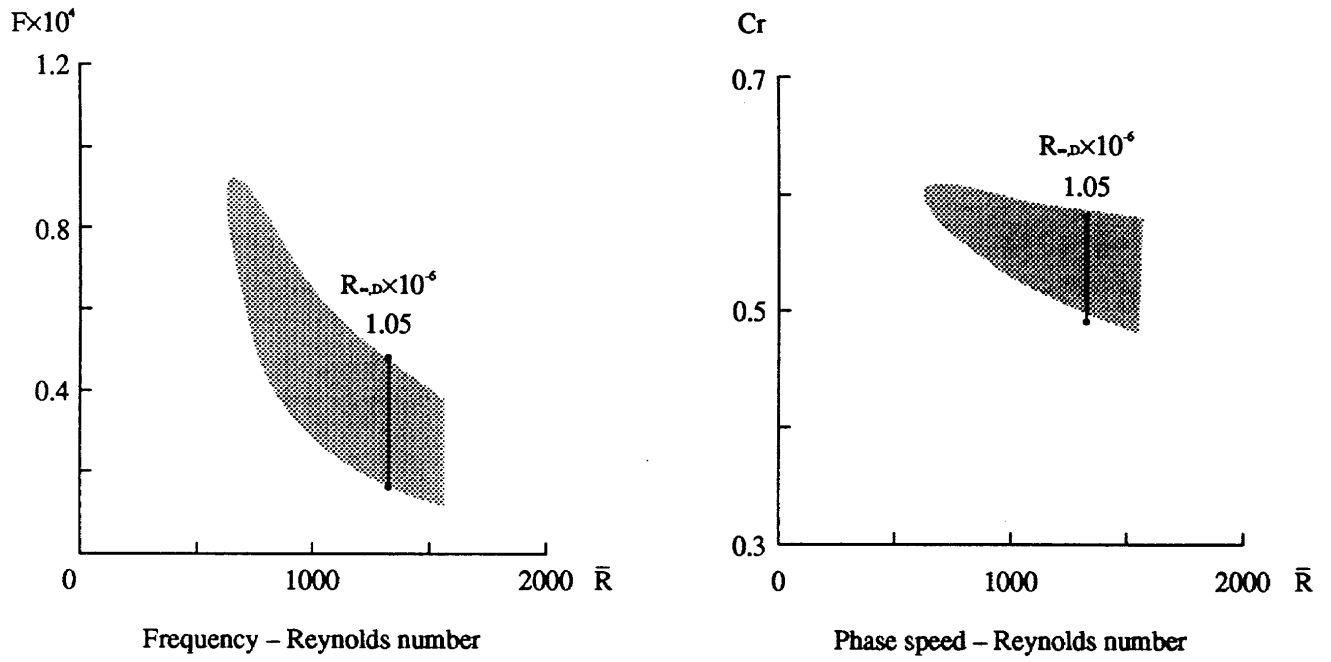
Fig. 7: Unstable ranges

# 5

## NUMERICAL STUDY ON TRANSITION PREDICTION METHOD AND EXPERIMENTAL STUDY ON EFFECT OF SUPERSONIC LAMINAR FLOW CONTROL

Kenji YOSHIDA and Hirokage OGOSHI

Gifu Technical Institute

Kawasaki heavy Industries , Ltd.

Kakamigahara , Gifu , Japan

Youji ISHIDA and Masayosi NOGUCHI

Aircraft Aerodynamics Division

National Aerospace Laboratory

Tokyo , Japan

## ABSTRACT

To develop an aerodynamic design system applying supersonic laminar flow control (SLFC) , numerical study on a transition prediction method and experimental study on the effect of SLFC were performed . In the first phase of our study , we developed an analysis system of linear stability and then obtained good validation for the estimated amplification rate in several typical cases . In the second phase , we developed a transition prediction system by applying an empirical $e^N$ method and then obtained good validation for the estimated N-factor in two typical cases . In the third phase , we carried out wind tunnel tests using an originally designed warped delta wing model , to obtain some data of transition and the effect of SLFC under supersonic flow condition . And finally we tried to analyze the transition characteristics of our model and obtained the useful result of $N \doteqdot 7$ at transition at Mach 1.4 .

## 1. INTRODUCTION

It is well known that laminar flow control (LFC) is one of the most effective technologies for improving aerodynamic characteristics of a transport aircraft , for example , a next generation SST . To develop the aerodynamic design system with supersonic laminar flow control (SLFC) , it is , first of all , necessary to understand transition phenomenon in a 3-dimensional compressible boundary layer . But such phenomenon is more difficult than that in a low speed boundary layer . The reason is based on the complexity due to the compressibility , 3-dimensionality , and nonlinearity . Even now there is little useful experimental data and information on SLFC , because of such difficulties .

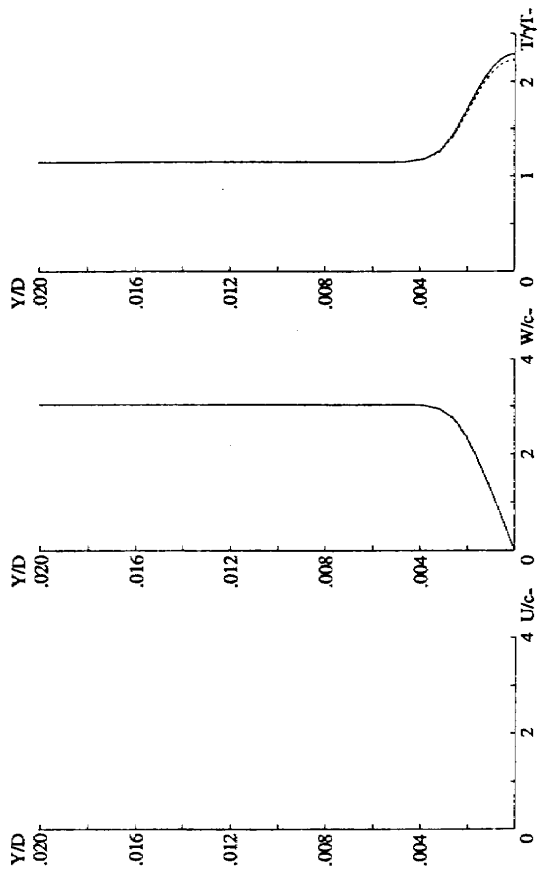As a first step , therefore , we started to investigate such transition phenomenon of a 3-dimensional compressible boundary layer numerically and experimentally . In the numerical approach , to understand the physical mechanism of the transition phenomenon , we analyzed linear stability characteristics and estimated transition position by using the empirical $e^N$ method . On the other hand , in the experimental approach , to obtain some c data in developing the design

system with SLFC , we carried out wind tunnel tests on SLFC in cooperation with NAL , using a model with a suction system .

Our study consists of 3 phases . In the first phase , we derived the formulation on linear stability of a 3-dimensional compressible boundary layer c to the spatial theory[1,2] , and developed a system for calculating the eigenvalue and amplification rate of small disturbances . Then we validated it in several typical cases by comparing our estimated amplification rates with those by other workers . In the second phase , we investigated the spatial growth of amplification rate and developed a transition prediction method based on the empirical $e^N$ method . This method consists of calculating the "N-factor" through the integration of several amplification rates and comparing it with the empirically obtained N-value which corresponds to the transition of the boundary layer . In the third phase , we carried out wind tunnel tests using an originally designed warped delta wing model and obtained some useful data for the transition and the effect of SLFC . Then we tried to analyze the transition characteristics of our test model using the present prediction method .

The purpose of this paper is to summarize the principal results of our study . The results of the first , second and third phase are described in section 2 , 3 and 4 respectively .

## 2. STUDY ON LINEAR STABILITY OF 3-DIMENSIONAL COMPRESSIBLE BOUNDARY LAYER

### 2.1 Formulation

### 1) Basic equation

Present formulation is based on the following assumptions .

① simple plane wave disturbances

$$\{u',v',w',p',T',\rho',\mu'\} \equiv q'(x,y,z,t) = \tilde{q}(y)\,e^{i(\alpha x+\beta z-\omega t)}$$

Here $(x,y,z)$ are the coordinates of streamwise direction , thickness direction of boundary layer and spanwise direction , $(u,v,w)$ the $(x,y,z)$ components of velocity , $(p,T,\rho,\mu)$ a pressure , temperature , density and viscosity respectively . And $\omega$ is a circular frequency (real) and $\alpha,\beta$ the components of wave number vector (complex) .

② parallel mean flow

$$\{U,V,W,P,T,\rho,\mu\} = \{U(y),0,W(y),1,T(y),\rho(y),\mu(y)\}$$

Then the basic equation generally can be summarized in the following form [1,2] .

$$\frac{d\varphi_i}{dy} = \sum_{j=1}^{8} a_{ij}\,\varphi_j \quad , \quad i = 1,8 \tag{1}$$

where $\varphi_1 = \alpha\,\tilde{u} + \beta\,\tilde{w}$ , $\varphi_2 = \dfrac{d\varphi_1}{dy}$ , $\varphi_3 = \tilde{v}$ , $\varphi_4 = \tilde{p}$ ,

$\varphi_5 = \tilde{T}$ , $\varphi_6 = \dfrac{d\varphi_5}{dy}$ , $\varphi_7 = \alpha\,\tilde{w} - \beta\,\tilde{u}$ , $\varphi_8 = \dfrac{d\varphi_7}{dy}$

Here these quantities are non-dimensionalized with boundary layer thickness and reference quantities at the edge of boundary layer . And the matrix $a_{ij}$ is related to the boundary layer

profiles of velocity , temperature , etc. . Those details are described in Appendix I .

## 2) Boundary condition

Generally the boundary condition in linear stability analysis is that all disturbances vanish at the wall and the edge of the boundary layer as follows :

$$\varphi_1 = \varphi_3 = \varphi_5 = \varphi_7 = 0 \quad , \quad at \; y = 0$$

$$\varphi_1 \, , \, \varphi_3 \, , \, \varphi_5 \, , \, \varphi_7 \to 0 \quad , \quad as \; y \to \infty \tag{2}$$

Here the combination of the above homogeneous basic equation and such boundary condition leads to trivial solutions , except for only one case where each parameter of the matrix is equal to the eigenvalue respectively . Therefore we must solve the so-called eigenvalue problem .

## 2.2 Method of Solution

To solve this eigenvalue problem , we adapted the method described in ref. 2 . The details are summarized in Appendix III and the main features are as follows :

① Integration from edge to wall by the 4th order Runge-Kutta-Gill method

② Application of analytical solution on the initial values at the edge (see Appendix II)

③ Use of the orthonormalization technique by Gram-Schmidt[3] to remove the errors due to numerical integration (see Appendix IV)

④ Iteration by the Newton method with a "pseudo" boundary condition

## 2.3 Validation of Present Formulation

As a first step , we tried to validate present formulation in two typical cases .

## 1) 2-dimensional incompressible viscous flow

First of all , under the assumptions of 2-dimensionality and incompressibility , the following relations are obtained :

$$W = \frac{dW}{dy} = 0 \quad , \quad \tilde{w} = 0 \quad \Rightarrow \quad \varphi_1 = \alpha \tilde{u} \quad , \quad \varphi_7 = -\beta \tilde{u} \tag{3}$$

$$\beta = 0 \quad \Rightarrow \quad \varphi_7 = \varphi_8 = 0 \tag{4}$$

$$T \, , \, \frac{dT}{dy} \; : \text{unnecessary} \quad \Rightarrow \quad \varphi_5 = \varphi_6 \; : \text{unnecessary} \tag{5}$$

Then we can derive the governing equation for $\varphi_3 = \tilde{v}$ from eq. (1) as follows :

$$\left\{ \frac{1}{R} \left( \frac{d^2}{dy^2} - \alpha^2 \right)^2 - i(\alpha U - \omega) \left( \frac{d^2}{dy^2} - \alpha^2 \right) + i\alpha \frac{d^2 U}{dy^2} \right\} \varphi_3 = 0 \tag{6}$$

This is completely equal to the well-known Orr-Sommerfeld equation

## 2) 2-dimensional compressible inviscid flow

Next , under the assumptions of 2-dimensionality (3) and 3-dimensional disturbance ($\beta \neq 0$) , the following inviscid condition is added :

$$\mu = \frac{d\mu}{dy} = \frac{d\mu}{dT} = 0 \quad , \quad R \rightarrow \infty \tag{7}$$

Then we can derive the governing equation for $\varphi_4 = \tilde{p}$ from eq. (1) as follows :

$$\left\{ \frac{d^2}{dy^2} - \frac{d}{dy}(\ln \tilde{M}^2)\frac{d}{dy} - (\alpha^2 + \beta^2)(1 - \tilde{M}^2) \right\}\varphi_4 = 0 \quad , \quad \tilde{M} \equiv \frac{(\alpha U - \omega)M_e}{\sqrt{(\alpha^2 + \beta^2)T}} \tag{8}$$

This is completely equal to the equation derived by Lees & Lin [4] and Mack [5] .

## 2.4 Numerical Validation

As the next step , we numerically investigated eigenvalue characteristics in some typical cases .

### 1) 2-dimensional disturbance on flat plate boundary layer

First of all , we analyzed a case of incompressible flat plate , namely Blasius boundary layer , and obtained the result summarized in Fig.1 . This figure shows the comparison of a neutral curve between the present estimation and the famous solution by Tollmien-Schlichting . Here the abscissa indicates Reynolds number based on displacement thickness $\delta^*$ and the ordinate denotes the wave number of disturbance which is non-dimensionalized with $\delta^*$  As seen in this figure , we obtained  good agreement .

Next we analyzed some compressible cases and summarized the results in Fig.2 and 3 , comparing with the results by Arnal [6] . Fig.2 shows several eigenvalues corresponding to stable or unstable states of the boundary layer at Mach 2.2 in the plane of Reynolds number and wave number . And Fig.3 shows the neutral curve on the boundary layer at Mach 3.0 . As seen in these figures , we could mostly obtain good agreement .

### 2) 3-dimensional disturbance on flat plate boundary layer

As a typical case including 3-dimensionality , first of all , we investigated the maximum amplification rate of 3-dimensional disturbance on the 2-dimensional compressible flat plate boundary layer , and obtained the result shown in Fig.4 . Here the abscissa indicates the Mach number of the mean flow , and the ordinate denotes maximum amplification rate . And $\psi$ is the angle between the directions of mean flow and propagation of disturbance . As seen in this figure , we obtained good agreement with the result by Mack [5] .

### 3) 2-dimensional disturbance on Falkner-Skan-Cooke boundary layer

As the next case on 3-dimensionality , we investigated 2-dimensional disturbance on the boundary layer of simple 3-dimensional flow over an infinite swept wing with a wedge-shaped cross-section . Usually the characteristics of the boundary layer on this wing are predicted by the solution of the well-known Falkner-Skan-Cooke boundary layer equation [7] .

Fig.5 shows the relation between maximum amplification rate and sweep angle , compared with the result by Mack [1]. Here the abscissa indicates sweep angle and the ordinate denotes the maximum

amplification rate divided by the value for the Blasius boundary layer . As seen in this figure , we could not obtain good agreement quantitatively but found it qualitatively . Presently we are considering that the quantitative difference originated in a numerical error in the calculation of boundary layer profiles .

## 3. STUDY ON TRANSITION PREDICTION METHOD

Recently it is well known that the current $e^N$ method is widely used to predict the transition position . This method consists of the following two parts . The first part consists of estimating the amplification rates of several disturbances , and the other consists of comparing the integrated amplification rates called "N-factor" , with a specified value derived empirically according to a lot of experimental data on transition . In this study , we first investigated the formulation of the $e^N$ method and then validated it through typical numerical analysis .

### 3.1 Formulation of the $e^N$ Method
### 1) Definition of amplitude of disturbance

According to the assumption of small plane wave disturbance , the amplitude $A$ on 3-dimensional disturbance is defined as follows :

$$\ln\left(\frac{A}{A_0}\right) = \int_C \left(-\alpha_i dx_s - \beta_i dy_s\right) = \int_C d\sigma \tag{9}$$

where $A_0$ is the amplitude at the neutral point . Here in this formulation , for convenience we adapted the so-called streamline coordinate , which is different from that in previous stability formulations . That is, the direction of the streamline at the edge of the boundary layer is indicated by $x_s$, the direction of cross-flow $y_s$ .

### 2) Assumption for the amplification of disturbance

Unless the path for integration is specified , we can not calculate the above integration . Moreover some supplementary relations between wave number $(\alpha_r, \beta_r)$ and amplification rate $(\alpha_i, \beta_i)$ are necessary . Presently some models are suggested to solve this problem . Through detailed investigation of these models , we decided to adapt the following approach :

According to the assumption of specifying the amplification direction $(\theta)$ suggested by Mack , first of all , we can simplify the formulation as follows :

$$\frac{dy_s}{dx_s} = \tan\theta \quad , \quad \beta_i = \alpha_i \tan\overline{\psi} \quad \Rightarrow \quad d\sigma = -\alpha_i(1 + \tan\overline{\psi}\tan\theta)dx_s \tag{10}$$

Here $\overline{\psi}$ is treated as a parameter .

Then we assume $\theta = 0$ , because this assumption simplifies the present method and it is physically reasonable to consider that the most dominate direction is the streamline direction . And finally we obtain the following relation .

$$d\sigma = -\alpha_i dx_s = -\frac{\alpha_i}{\cos\phi_e}dx_c \tag{11}$$

where $x_c$ stands for the coordinate in the chordwise direction normal to the leading edge and $\phi_e$ the local sweep angle at the edge . On the other hand , $\overline{\psi}$ is not explicitly included in this expression , but the influence of $\overline{\psi}$ , namely $\beta_i$ is implicitly reflected by $\alpha_i(\psi,\overline{\psi},f,R(x_c))$ . Here $\psi \equiv \tan^{-1}\left(\frac{\beta_r}{\alpha_r}\right)$ , $f = \frac{\omega}{2\pi}$

## 3) Method to estimate N-factor

Presently it is known that there are several methods to estimate the N-factor based on the above definition of the amplitude of disturbance . Among them , we adapted the following Envelop Method[8] .

$$N = \underset{\psi}{Max}\ \underset{\overline{\psi}}{Max}\ \underset{f}{Max}\left[\ln\left(\frac{A}{A_0}\right)_{\psi,\overline{\psi},f}\right] \tag{12}$$

$$\ln\left(\frac{A}{A_0}\right)_{\psi,\overline{\psi},f} = \int_C d\sigma = \int_{x_{c0}}^{x_c}\frac{-\alpha_i(x_c;\psi,\overline{\psi},f)}{\cos\phi_e(x_c)}dx_c = \int_{\xi_{c0}}^{\xi_c}\frac{f(x_c;\psi,\overline{\psi},f)}{\cos\phi_e}d\xi \tag{13}$$

$$f(x_c;\psi,\overline{\psi},f) \equiv -\alpha_i(x_c;\psi,\overline{\psi},f)\cdot\delta(x_c) \quad , \quad \xi_c \equiv \frac{x_c}{\delta}$$

Here $\underset{\psi}{Max}, \underset{\overline{\psi}}{Max}, \underset{f}{Max}$ stand for choosing local maximum values for $\psi,\overline{\psi},f$ at each $x_c$ respectively . Therefore N corresponds to the envelop for every curve .

## 3.2 Validation of Present $e^N$ Method

To validate our $e^N$ method , we investigated transition characteristics in the following two cases .

## 1) 2-dimensional incompressible flat plate flow (Blasius flow)

First of all , we analyzed the relation between amplification rate $(-\alpha_i\delta)$ and frequency $(f)$ in the range of various Reynolds number based on boundary layer thickness (Rd) , using our linear stability formulation . One of those results is shown in Fig. 6 . Then using these relations , we summarized the estimated N-factor as shown in the lower part of Fig. 7 . Here the upper part of this figure shows the result by Arnal[8] . In a comparing them , we obtained good agreement . And since it is experimentally observed that the natural transition exists in the range indicated by the black arrow in Fig. 7 , we can estimate that the N-factor corresponding to the transition is about 8 to 10 .

## 2) 3-dimensional incompressible infinite swept flat plate flow

For another validation , we investigated the wind tunnel test on a swept flat plate carried out at DFVLR[9] . In the analysis of such a flow field , the so-called Falkner-Skan-Cooke boundary

layer approach is approximately effective . Therefore , using this approach , we estimated the N-factor and summarized the result in the lower part of Fig. 8 . Here the upper part shows the result estimated by DFVLR using temporal theory . As seen in this figure , we obtained good agreement except for lower frequencies .

Since in ref. 9 it is stated that transition was not observed in the test because of a weak adverse pressure gradient , we can estimate that the transition N-factor is more than 12 .

## 4. STUDY ON WIND TUNNEL TESTS FOR SUPERSONIC LAMINAR FLOW CONTROL

The main objective of our wind tunnel tests is to obtain some useful data for understanding transition phenomenon at supersonic speed and developing a transition prediction system including the effect of SLFC . Therefore we originally designed a wing model with the suction system for SLFC and carried out the tests at the 2m×2m transonic wind tunnel of the National Aerospace Laboratory (NAL) . Then we analyzed the transition characteristics using our prediction system and compared the estimated result with the test result .

### 4.1 Wind Tunnel Test

### 1) Outline of present wind tunnel tests

Our tunnel model is a half-mounted wing model , as shown in Fig. 9 , and it has a special upper surface with about 60,000 tiny holes ( 0.1 mm diameter ) for suction of air . Its planform is a simple one , namely delta shaped , but its surface is a little complicated , because the "warped surface" , which was designed originally for minimizing lift-dependent drag , is applied to this model .

We carried out wind tunnel test twice . As our attention is directed to supersonic speed , the test case at M=1.4 was emphasized . In those tests , we measured force and pressure on the surface and in the wake . Also we tried to obtain the transition characteristics by using two visualization techniques , that is , monitoring by an infrared camera and a liquid crystal .

Our wind tunnel tests consist of the following three parts . The first part is a "fundamental test" to obtain the fundamental characteristics of our model . The second part is a "suction test" to investigate the effect on the suction of the boundary layer . And the third part is a "visualization test" to understand the transition characteristics .

### 2) Summary of test results

In the fundamental test , since we obtained good agreement between the estimated and measured pressure distributions under design conditions , we validated our warped surface design method . However , the influence of the tunnel wall was made clear by the reduction of lift slope .

In the suction test , we couldn't find any significant effect in either the characteristics of total drag or the distribution of total pressure loss in the wake . And presently we are considering that the reason is based on (1) a stronger cross flow instability than we had

predicted and (2) the small suction surface . Therefore we need to improve our model to obtain useful data on SLFC .

In the visualization test , using the liquid crystal technique , we observed the natural transition in the condition of the existing accelerated region on the forward part of the lower surface . This condition was chosen to realize the delay of the natural transition . (Here the reason why we didn't give the upper surface a coat of liquid crystal is based on the existence of the suction surface . ) The natural transition characteristics obtained through the other pattern of liquid crystal is summarized in Fig. 10 . As seen in this figure , we found that the location of transition was about 6% local chord length at the condition of N=1.4 and $\alpha$=8°

On the other hand , in the test with an infrared camera , we couldn't clearly observe the natural transition . Presently we are considering that the reason is based on the influence of other sources , for example , lighting , porous wall , beams , etc.. Therefore at the next step , such surrounding should be improved as much as possible .

## 4.2 Study of Transition Characteristics Based on Test Results

As one validation of our transition prediction method , we investigated the transition characteristics of the present wind tunnel model . First of all , we analyzed the 3-dimensional compressible laminar boundary layer based on the measured pressure distribution , using the method described in ref. 10 . Then we solved the eigenvalue problem and estimated the N-factor .

The results are as follows .

## 1) Influence of $\overline{\psi}$

As there are some parameters such as $f$, $\psi$ and $\overline{\psi}$ in our method , the influence of these parameters on the amplification rate of disturbance should be investigated in detail . First of all , we investigated the influence of $\overline{\psi}$ .

Generally we have supposed that the transition phenomenon of our model is mainly dominated by cross flow instability , because of its highly swept leading edge . Therefore we paid attention to the case of $\psi \doteqdot 70 \sim 90°$ . Consequently we found that the amplification rate had the largest value at the condition of $\overline{\psi}=0°$ .

## 2) Influence of $\psi$

Next we investigated the influence of $\psi$ in the condition of $\overline{\psi}=0°$ . And we ascertained that the amplification rate at $\psi > 0°$ was larger than that at $\psi < 0°$ . This is easily understandable when considering the relation between the sweep angle and the direction of cross flow . Therefore the condition of $0° < \psi < 90°$ is enough for the present analysis .

## 3) Estimation of N-factor

Fig. 11 shows the estimated N-factor on the lower surface of our model at the condition of

M=1.4 , $\alpha$ =8° and 40% semi-span position . As seen in this figure , the disturbance with $f$ =60 kHz generates the largest N near the region of the leading edge , and the disturbance with $f$ =40 kHz does so at the rear part .

Generally , in the $e^N$ method , the location of transition is predicted by comparing the estimated N-factor with the empirical N value corresponding to the transition . For a 3-dimensional compressible boundary layer , however , the reasonable value of transition N-factor has not been estimated empirically yet . Therefore , in this stage , we can't completely predict the location of transition . It is very important to gather a lot of experimental data to estimate the reasonable N value . And from this standpoint , we tried to estimate the N value based on the present test result .

In our liquid crystal visualization test , it was observed that the transition was located at a position about 6% local chord rearward from the leading edge . Therefore we can estimate that the transition N value is nearly equal to 7 . This value is less than the N value of 8 to 10 usually used on 2-dimensional incompressible flat plate flows , as we mentioned above . Here we consider that this value is roughly valid , because of the fact that the transition Reynolds number on a compressible boundary layer is generally less than on an incompressible one .

But present estimation is not extremely precise because of the existence of some factors influencing transition , such as turbulence of the freestream , the number in the porous wall , the boundary layer on the tunnel wall , and so on . Therefore a lot of wind tunnel tests should be carried out using several models of which the transition position is well known .

## 5. CONCLUDING REMARKS

As a first step in developing a design system for supersonic laminar flow control (SLFC) , we first investigated the linear stability of the 3-dimensional compressible boundary layer and then developed a transition prediction system according to the current $e^N$ method . Next we carried out wind tunnel tests using the model designed originally for SLFC , to understand the effect of SLFC and to obtain useful data for it . Unfortunately , though the effect of SLFC wasn't made clear because of the large swept angle and small suction surface of our model , we could obtain information on the natural transition through the visualization test using a liquid crystal . Then comparing this test result with the analysis for the transition of our model by the present method , we ascertained that the transition N value was about 7 . To improve the precision of present estimation , however , it is necessary to continue further study in wind tunnel tests .

## REFERENCES

1) L.M. Mack : " Boundary-Layer Linear Stability Theory " , Special Course on
   Stability and Transition of Laminar Flow , AGARD Rep. No.709, 3-1~81, 1984

2) N. M. El-Hady : " Nonparallel Stability of Three-Dimensional Compressible Boundary Layers , Part I - Stability Analysis " , NASA CR-3245 , 1980

3) Tatsumi , Gotoh : "Stability Theory of Flow " , Sangyou Tosyo, 1976

4) L. Lees and C. C. Lin : " Investigation of The Stability of The Laminar Boundary Layer in A Compressible Fluid " , NACA TN-1115 , 1946

5) L. M. Mack : "Linear Stablilty Theory and the Problem of Supersonic Boundary-Layer Transition " , AIAA J. Vol.13 , No.3 , pp.278-289 , 1975

6) D. Arnal : " Stability and Transition of Two-Dimensional Laminar Boundary Layers in Compressible Flow over An Adiabatic Wall " , La  Recherche Aerospatiale No.1988-4

7) L. Rosenhead (Ed.) : " Laminar Boundary Layer " , Dover Publications Inc.,1961

8) D. ARNAL : " Boundary layer transition : prediction  based  on linear theory " , AGARD FDP/VKI Special Course on Progress in Transition Modelling , AGARD Report 793 , 1993

9) F. Meyer and L. Kleiser : "Numerical Investigation of Transition in 3D Boundary Layers , AGARD-CP-438 , 16-1 , 1989

10) T. Cebeci , K. Kaups and J. A. Ramsey : NASA CR-2777

## APPENDIX I . DETAIL EXPRESSION FOR THE MATRIX $\{a_{ij}\}$

In the following expression, $R$ denotes the Reynolds number based on velocity, density, viscosity at the edge of boundary layer respectively and boundary layer thickness, and $\gamma$, $\sigma$ and $M_e$ indicate the ratio of specific heat $(=1.4)$, Prandtl number and Mach number at the edge of boundary layer, respectively.

$$\{a_{ij}\} = \begin{pmatrix} 0 & 1 & 0 & 0 & 0 & 0 & 0 & 0 \\ a_{21} & a_{22} & a_{23} & a_{24} & a_{25} & a_{26} & 0 & 0 \\ -i & 0 & a_{33} & a_{34} & a_{35} & 0 & 0 & 0 \\ a_{41} & a_{42} & a_{43} & a_{44} & a_{45} & a_{46} & 0 & 0 \\ 0 & 0 & 0 & 0 & 0 & 1 & 0 & 0 \\ 0 & a_{62} & a_{63} & a_{64} & a_{65} & a_{66} & 0 & a_{68} \\ 0 & 0 & 0 & 0 & 0 & 0 & 0 & 1 \\ 0 & 0 & a_{83} & 0 & a_{85} & a_{86} & a_{87} & a_{88} \end{pmatrix} \tag{A1}$$

$$a_{21} = i\rho\frac{R}{\mu}(\alpha U + \beta W - \omega) + \alpha^2 + \beta^2$$

$$a_{22} = -\frac{1}{\mu}\frac{d\mu}{dy}$$

$$a_{23} = \frac{\rho R}{\mu}\left(\alpha\frac{dU}{dy} + \beta\frac{dW}{dy}\right) + (\alpha^2 + \beta^2)\left(-\frac{i}{3T}\frac{dT}{dy} - \frac{i}{\mu}\frac{d\mu}{dy}\right)$$

$$a_{24} = (\alpha^2 + \beta^2)\left\{\frac{iR}{\mu} - \frac{(\alpha U + \beta W - \omega)\gamma M_e^2}{3\rho T}\right\}$$

$$a_{25} = \frac{(\alpha U + \beta W - \omega)(\alpha^2 + \beta^2)}{3T} - \frac{1}{\mu}\frac{\partial}{\partial y}\left\{\frac{d\mu}{dT}\left(\alpha\frac{dU}{dy} + \beta\frac{dW}{dy}\right)\right\}$$

$$a_{26} = -\frac{1}{\mu}\frac{d\mu}{dT}\left(\alpha\frac{dU}{dy} + \beta\frac{dW}{dy}\right)$$

$$a_{33} = \frac{1}{T}\frac{dT}{dy}.$$

$$a_{34} = -\frac{i}{\rho}(\alpha U + \beta W - \omega)\frac{\gamma M_e^2}{T}$$

$$a_{35} = \frac{i}{T}(\alpha U + \beta W - \omega)$$

$$a_{41} = \frac{1}{1+c}\left\{-\frac{i}{R}\left(\frac{4\mu}{3T}+2\frac{d\mu}{dT}\right)\frac{dT}{dy}\right\} \quad , \quad c \equiv \frac{4}{3}\frac{i\gamma M_e^2\mu(aU+\beta W-\omega)}{\rho RT}$$

$$a_{42} = \frac{1}{1+c}\left(-\frac{i\mu}{R}\right)$$

$$a_{43} = \frac{1}{1+c}\left[\frac{4\mu}{3RT}\left\{\frac{d^2T}{dy^2}+\frac{1}{\mu}\frac{d\mu}{dT}\left(\frac{dT}{dy}\right)^2\right\}-i\rho(aU+\beta W-\omega)-\frac{\mu}{R}\left(\alpha^2+\beta^2\right)\right]$$

$$a_{44} = -\frac{1}{1+c}\frac{4}{3}\frac{i\gamma M_e^2\mu}{\rho RT}\left\{\left(\frac{1}{\mu}\frac{d\mu}{dT}+\frac{1}{T}\right)\frac{dT}{dy}(aU+\beta W-\omega)+\alpha\frac{dU}{dy}+\beta\frac{dW}{dy}\right\}$$

$$a_{45} = \frac{1}{1+c}\left\{\frac{4}{3}\frac{i(aU+\beta W-\omega)}{RT}\frac{d\mu}{dT}\frac{dT}{dy}+i\left(\frac{4\mu}{3RT}+\frac{1}{R}\frac{d\mu}{dT}\right)\left(\alpha\frac{dU}{dy}+\beta\frac{dW}{dy}\right)\right\}$$

$$a_{46} = \frac{1}{1+c}\frac{4}{3}\frac{i\mu(aU+\beta W-\omega)}{RT}$$

$$a_{62} = -2(\gamma-1)\sigma M_e^2\frac{1}{\alpha^2+\beta^2}\left(\alpha\frac{dU}{dy}+\beta\frac{dW}{dy}\right)$$

$$a_{63} = \frac{\sigma R\rho}{\mu}\frac{dT}{dy}-2i(\gamma-1)\sigma M_e^2\left(\alpha\frac{dU}{dy}+\beta\frac{dW}{dy}\right)$$

$$a_{64} = -i(\gamma-1)M_e^2\frac{\sigma R}{\mu}(\alpha U+\beta W-\omega)$$

$$a_{65} = i\frac{\sigma R\rho}{\mu}(\alpha U+\beta W-\omega)-\frac{(\gamma-1)\sigma M_e^2}{\mu}\frac{d\mu}{dT}\left\{\left(\frac{dU}{dy}\right)^2+\left(\frac{dW}{dy}\right)^2\right\}-(\alpha^2+\beta^2)-\frac{1}{\mu}\frac{d^2\mu}{dy^2}$$

$$a_{66} = -\frac{2}{\mu}\frac{d\mu}{dy}$$

$$a_{68} = -2(\gamma-1)\sigma M_e^2\frac{1}{\alpha^2+\beta^2}\left(\alpha\frac{dW}{dy}-\beta\frac{dU}{dy}\right)$$

$$a_{83} = \frac{\rho R}{\mu}\left(\alpha\frac{dW}{dy}-\beta\frac{dU}{dy}\right)$$

$$a_{85} = -\frac{1}{\mu}\frac{d}{dy}\left\{\frac{d\mu}{dT}\left(\alpha\frac{dW}{dy}-\beta\frac{dU}{dy}\right)\right\}$$

$$a_{86} = -\frac{1}{\mu}\frac{d\mu}{dT}\left(\alpha\frac{dW}{dy}-\beta\frac{dU}{dy}\right)$$

$$a_{87} = a_{21}$$

$$a_{88} = -\frac{1}{\mu}\frac{d\mu}{dy}$$

## APPENDIX II. ANALYTICAL SOLUTION AT THE EDGE OF BOUNDARY LAYER

At the edge of boundary layer , the following relation is generally specified .

$$\{U,W,T,\rho,\mu\} = \{\,1,W_1,1,1,1\,\}$$ (A2)

And all derivatives on $y$ are equal to 0 . Then all components of the matrix $\{a_{i,j}\}$ are constant and simplified as follows :

$$\{a_{i,j}(y \geq \delta)\} \equiv \{\bar{a}_{i,j}\} = \begin{pmatrix} 0 & 1 & 0 & 0 & 0 & 0 & 0 & 0 \\ \bar{a}_{21} & 0 & 0 & \bar{a}_{24} & \bar{a}_{25} & 0 & 0 & 0 \\ -i & 0 & 0 & \bar{a}_{34} & \bar{a}_{35} & 0 & 0 & 0 \\ 0 & \bar{a}_{42} & \bar{a}_{43} & 0 & 0 & \bar{a}_{46} & 0 & 0 \\ 0 & 0 & 0 & 0 & 0 & 1 & 0 & 0 \\ 0 & 0 & 0 & \bar{a}_{64} & \bar{a}_{65} & 0 & 0 & 0 \\ 0 & 0 & 0 & 0 & 0 & 0 & 0 & 1 \\ 0 & 0 & 0 & 0 & 0 & 0 & \bar{a}_{87} & 0 \end{pmatrix} = const.$$ (A3)

If we consider the basic equation above the edge , we can derive the next equation .

$$\frac{d\bar{\varphi}_i}{dy} = \sum_{j=1}^{8} \bar{a}_{i,j}\,\bar{\varphi}_j \quad , \quad i = 1 \sim 8$$ (A4)

where $\bar{\varphi}_i \equiv \varphi_i(y \geq \delta)$ .

Using the eigenvalues and eigenfunctions of the matrix $\{\bar{a}_{i,j}\}$ , we can obtain the solution $\bar{\varphi}_i$ of this equation analytically in accordance with the following procedure .

First of all , introducing Equation (A4) ,

$$\psi_1 = \bar{\varphi}_1 \quad , \quad \psi_2 = \bar{\varphi}_4 \quad , \quad \psi_3 = \bar{\varphi}_5 \quad and \quad \psi_4 = \bar{\varphi}_7 \quad \text{is rewritten as follows :}$$

$$\frac{d^2}{dy^2}\begin{pmatrix} \psi_1 \\ \psi_2 \\ \psi_3 \\ \psi_4 \end{pmatrix} = \begin{pmatrix} A_{11} & A_{12} & A_{13} & 0 \\ 0 & A_{22} & A_{23} & 0 \\ 0 & A_{32} & A_{33} & 0 \\ 0 & 0 & 0 & A_{44} \end{pmatrix}\begin{pmatrix} \psi_1 \\ \psi_2 \\ \psi_3 \\ \psi_4 \end{pmatrix}$$ (A5)

where

$$A_{11} = \bar{a}_{21} \quad , \quad A_{12} = \bar{a}_{24} \quad , \quad A_{13} = \bar{a}_{25}$$

$$A_{22} = \bar{a}_{42}\bar{a}_{24} + \bar{a}_{43}\bar{a}_{34} + \bar{a}_{46}\bar{a}_{64} \quad , \quad A_{23} = \bar{a}_{42}\bar{a}_{25} + \bar{a}_{43}\bar{a}_{35} + \bar{a}_{46}\bar{a}_{65}$$

$$A_{32} = \bar{a}_{64} \quad , \quad A_{33} = \bar{a}_{65}$$

$$A_{44} = A_{11}$$

Next if we assume a typical solution such as $\psi \propto e^{\lambda y}$ , we can analytically obtain the eigenvalues $\lambda_i$ of the matrix $\{A_{i,j}\}$ through the following eigenvalue equation .

$$\begin{vmatrix} A_{11} - \lambda^2 & A_{12} & A_{13} & 0 \\ 0 & A_{22} - \lambda^2 & A_{23} & 0 \\ 0 & A_{32} & A_{33} - \lambda^2 & 0 \\ 0 & 0 & 0 & A_{11} - \lambda^2 \end{vmatrix} = 0$$ (A6)

$$\lambda_1 = -\sqrt{A_{11}}$$

$$\therefore \quad \lambda_2 = -\sqrt{\frac{1}{2}(A_{22} + A_{33}) + \sqrt{\frac{1}{4}(A_{22} - A_{33})^2 + A_{23}A_{32}}} \qquad , \quad \lambda_5 = -\lambda_1$$

$$, \quad \lambda_6 = -\lambda_2$$

$$, \quad \lambda_7 = -\lambda_3$$

$$\lambda_3 = -\sqrt{\frac{1}{2}(A_{22} + A_{33}) - \sqrt{\frac{1}{4}(A_{22} - A_{33})^2 + A_{23}A_{32}}} \qquad , \quad \lambda_8 = -\lambda_4$$

$$\lambda_4 = -\sqrt{A_{11}}$$

Here since the solutions with eigenvalues of $\lambda_5, \lambda_6, \lambda_7, \lambda_8$ increase exponentially as $y$ increases , they are invalid . Accordingly there are four independent solutions in the above equation .

On the other hand , the following solution $\psi_i$ is usually assumed to obtain the eigenfunction .

$$\psi_i(y) = \sum_{l=1}^{8} B_{il} \, d_l \, e^{\lambda_l y} \quad , \quad i = 1 \sim 4 \tag{A7}$$

And by inserting (A7) into Equation (A5), the expansion coefficients $\{B_{ij}\}$ are obtained as follows :

$$\{B_{ij}\} = \begin{pmatrix} 1 & B_{12} & B_{13} & 0 & 1 & B_{16} & B_{17} & 0 \\ 0 & 1 & 1 & 0 & 0 & 1 & 1 & 0 \\ 0 & B_{32} & B_{33} & 0 & 0 & B_{36} & B_{37} & 0 \\ 0 & 0 & 0 & 1 & 0 & 0 & 0 & 1 \end{pmatrix} \tag{A8}$$

where

$$B_{1l} = \frac{A_{12}A_{23} + (\lambda_l^2 - A_{22})A_{13}}{(\lambda_l^2 - A_{11})A_{23}} \quad , \quad l = 2, 3, 6, 7$$

$$B_{2l} = 1$$

$$B_{3l} = \frac{\lambda_l^2 - A_{22}}{A_{23}}$$

$$B_{4l} = 0$$

Here $d_l$ is constant numbers determined by the condition of normalization .

Finally , the four independent solutions $\overline{\varphi}_i$ are summarized in the following form .

$$\overline{\varphi}_i^{(l)}(y) = \Lambda_{il} \, e^{\lambda_i y} \quad , \quad l = 1 \sim 4 \quad , \quad i = 1 \sim 8 \tag{A9}$$

$$\left(\Lambda_{ij}\right) = \begin{pmatrix} 1 & \Lambda_{12} & \Lambda_{13} & 0 & 1 & \Lambda_{16} & \Lambda_{17} & 0 \\ \lambda_1 & \Lambda_{22} & \Lambda_{23} & 0 & -\lambda_1 & \Lambda_{26} & \Lambda_{27} & 0 \\ \Lambda_{31} & \Lambda_{32} & \Lambda_{33} & 0 & -\Lambda_{31} & \Lambda_{36} & \Lambda_{37} & 0 \\ 0 & \Lambda_{42} & \Lambda_{43} & 0 & 0 & \Lambda_{46} & \Lambda_{47} & 0 \\ 0 & \Lambda_{52} & \Lambda_{53} & 0 & 0 & \Lambda_{56} & \Lambda_{57} & 0 \\ 0 & \Lambda_{62} & \Lambda_{63} & 0 & 0 & \Lambda_{66} & \Lambda_{67} & 0 \\ 0 & 0 & 0 & 1 & 0 & 0 & 0 & 1 \\ 0 & 0 & 0 & \Lambda_{84} & 0 & 0 & 0 & -\Lambda_{84} \end{pmatrix}$$

$$\Lambda_{31} = \frac{\bar{a}_{31}}{\lambda_1}$$

$$\Lambda_{84} = \frac{\bar{a}_{87}}{\lambda_4}$$

$* B_{1l} \neq 0 \quad , \quad l = 2,3,6,7$

$$\Lambda_{1l} = 1 \quad , \quad \Lambda_{2l} = \lambda_l \quad , \quad \Lambda_{3l} = \frac{\bar{a}_{31}B_{1l} + \bar{a}_{34}B_{2l} + \bar{a}_{35}B_{3l}}{\lambda_l B_{1l}} \quad ,$$

$$\Lambda_{4l} = \frac{B_{2l}}{B_{1l}} \quad , \quad \Lambda_{5l} = \frac{B_{3l}}{B_{1l}} \quad , \quad \Lambda_{6l} = \lambda_l \Lambda_{5l}$$

$* B_{1l} = 0 \quad , \quad l = 2,3,6,7$

$$\Lambda_{1l} = \Lambda_{2l} = 0 \quad , \quad \Lambda_{3l} = \frac{\bar{a}_{34}B_{2l} + \bar{a}_{35}B_{3l}}{\lambda_l} \quad ,$$

$$\Lambda_{4l} = B_{2l} \quad , \quad \Lambda_{5l} = B_{3l} \quad , \quad \Lambda_{6l} = \lambda_l B_{3l}$$

## APPENDIX III. OUTLINE OF THE PRESENT METHOD OF SOLUTION

Usually because of four independent eigenvalues and eigenfunctions , a general solution of the present basic equation is composed with the four independent solutions as follows :

$$\varphi_i(y) = \sum_{l=1}^{4} k_l \, \varphi_i^{(l)}(y) \tag{A10}$$

Here each independent solution $\varphi_i^{(l)}(y)$ is obtained by integrating the basic equation from edge to wall . And on the initial values in this integration, we apply the following analytic solution derived in APPENDIX II .

$$\varphi_i^{(l)}(\delta) = \overline{\varphi}_i^{(l)}(\delta) \tag{A11}$$

By the way , those independent solutions generally have non-zero values at wall , namely $\varphi_i^{(l)}(0) \neq 0$ . Therefore the four expansion coefficients $k_l$ satisfied with the following equation are completely equal to 0 .

$$\varphi_i(0) = \sum_{l=1}^{4} k_l \, \varphi_i^{(l)}(0) = 0 \quad , \quad i = 1,3,5,7 \tag{A12}$$

To avoid such trivial situation , we assume the following "pseudo" boundary condition .

At first , let's consider to relax one of the boundary conditions for above four physical quantities . That is , in our method , we tentatively selected the condition for $\varphi_1$ . Then we replace it with the following condition for $\varphi_4 = \tilde{p}$ . Because we have no boundary condition for $\varphi_4$ .

$$\begin{pmatrix} \varphi_3^{(1)}(0) & \varphi_3^{(2)}(0) & \varphi_3^{(3)}(0) & \varphi_3^{(4)}(0) \\ \varphi_4^{(1)}(0) & \varphi_4^{(2)}(0) & \varphi_4^{(3)}(0) & \varphi_4^{(4)}(0) \\ \varphi_5^{(1)}(0) & \varphi_5^{(2)}(0) & \varphi_5^{(3)}(0) & \varphi_5^{(4)}(0) \\ \varphi_7^{(1)}(0) & \varphi_7^{(2)}(0) & \varphi_7^{(3)}(0) & \varphi_7^{(4)}(0) \end{pmatrix} \begin{pmatrix} k_1 \\ k_2 \\ k_3 \\ k_4 \end{pmatrix} \equiv \{\Gamma_{ij}\}\{k_j\} = \begin{pmatrix} 0 \\ 1 \\ 0 \\ 0 \end{pmatrix} \qquad \text{(A13)}$$

Here we conveniently assumed that the value of $\varphi_4$ at wall was equal 1 without lack of generality .
Accordingly the expansion coefficients $k_j$, are obtained as follows :

$$k_l = \sum_{j=1}^{4} \Gamma_{lj}^{-1} \delta_{j2} = \Gamma_{l2}^{-1} \quad , \quad l = 1 \sim 4 \qquad \text{(A14)}$$

where $\qquad \Gamma_{l2}^{-1} \equiv U_{l2} + i V_{l2}$

$$\{U_{ij}\} = \left( \{S_{ij}\}^{-1}\{T_{ij}\} + \{T_{ij}\}^{-1}\{S_{ij}\} \right)^{-1} \{T_{ij}\}^{-1}$$

$$\{V_{ij}\} = -\left( \{S_{ij}\}^{-1}\{T_{ij}\} + \{T_{ij}\}^{-1}\{S_{ij}\} \right)^{-1} \{S_{ij}\}^{-1}$$

$$\{S_{ij}\} \equiv \text{Re}\{\Gamma_{ij}\} \quad , \quad \{T_{ij}\} \equiv \text{Im}\{\Gamma_{ij}\}$$

Next we compose a general solution using these coefficients . At that time , the solution for $\varphi_1$ must be satisfied with the following true boundary condition .

$$\varphi_1(0) = \sum_{l=1}^{4} k_l \, \varphi_1^{(l)}(0) = 0 \qquad \text{(A15)}$$

Therefore to keep this condition , we must improve the values of parameters in the matrix $\{a_{ij}\}$ such as $(\alpha, \beta, \omega, R)$ and estimate the four converged independent solutions through the iterative process and the following Newton Method . After the convergence in this process , we can finally obtain the eignevalues $(\alpha, \beta)$ and eigenfunctions $\varphi_i(y)$ for stability characteristics .

To simplify our iterative process , first of all , we assumed certain values for $R, \omega, \beta (= \beta_r + i\beta_i)$ , and tried to improve the value of $\alpha (= \alpha_r + i\alpha_i)$ only . Generally the solutions at the (n+1)-th state in the iterative process can be expressed as follows :

$$\alpha_r^{n+1} = \alpha_r^{n} + \delta\alpha_r^{n}$$
$$\alpha_i^{n+1} = \alpha_i^{n} + \delta\alpha_i^{n} \qquad \text{(A16)}$$

where $(\alpha_r^{n}, \alpha_i^{n})$ stands for the solutions at the n-th state and $(\delta\alpha_r^{n}, \delta\alpha_i^{n})$ the modification quantities .

If the (n+1)-th solution satisfies the above true boundary condition , those modification quantities can be estimated under the approximation of neglecting the second order of them as follows :

$$\begin{pmatrix} \delta\alpha_r{}^n \\ \delta\alpha_i{}^n \end{pmatrix} = -\begin{pmatrix} p_{11} & p_{12} \\ p_{21} & p_{22} \end{pmatrix}^{-1} \begin{pmatrix} \mathrm{Re}\big(\varphi_1{}^n(0)\big) \\ \mathrm{Im}\big(\varphi_1{}^n(0)\big) \end{pmatrix}$$

where

$$p_{11} \equiv \left[ \frac{\partial\, \mathrm{Re}\big(\varphi_1{}^n(0)\big)}{\partial\,\alpha_r} \right]_{(\alpha_r{}^n,\alpha_i{}^n)} = p_{22} \quad,\quad p_{21} \equiv \left[ \frac{\partial\, \mathrm{Im}\big(\varphi_1{}^n(0)\big)}{\partial\,\alpha_r} \right]_{(\alpha_r{}^n,\alpha_i{}^n)} = -p_{12}$$

In calculating the derivatives $p_{ij}$ , we used the numerical approach based on the approximation of the modification $\Delta\alpha_r = \varepsilon\alpha_r$, *and* $\varepsilon \approx 10^{-3} \sim 10^{-5}$ .

## APPENDIX IV. ORTHONORMALIZATION TECHNIQUE BY GRAM-SCHMIDT

Since numerical integration generally produces an error , the orthogonarity of our independent solutions in our method is reduced . To remove this reduction , that is , to keep the orthogonality of the solutions , it is well-known that the following replacement at each integration step for $y$ is effective[3] .

$$X^{(l)} \equiv \big\{\varphi_i{}^{(l)}\big\} \quad\Rightarrow\quad Y^{(l)} \quad,\quad l = 1 \sim 4 \quad,\quad i = 1 \sim 8$$

$$Y^{(1)} = \frac{X^{(1)}}{\big|X^{(1)}\big|}$$

$$Y^{(2)} = \frac{\big(X^{(2)} - C_{12}Y^{(1)}\big)}{\big|X^{(2)} - C_{12}Y^{(1)}\big|}$$

$$Y^{(3)} = \frac{\big(X^{(3)} - C_{13}Y^{(1)} - C_{23}Y^{(2)}\big)}{\big|X^{(3)} - C_{13}Y^{(1)} - C_{23}Y^{(2)}\big|}$$

$$Y^{(4)} = \frac{\big(X^{(4)} - C_{14}Y^{(1)} - C_{24}Y^{(2)} - C_{34}Y^{(3)}\big)}{\big|X^{(4)} - C_{14}Y^{(1)} - C_{24}Y^{(2)} - C_{34}Y^{(3)}\big|}$$

$$C_{ij} \equiv Y^{(i)^*}X^{(j)}$$
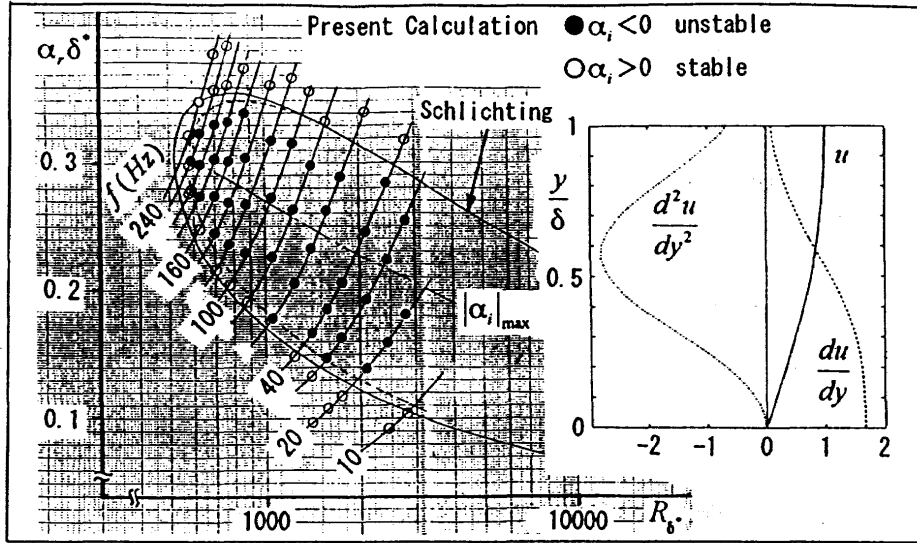
where $*$ denotes complex conjugate .

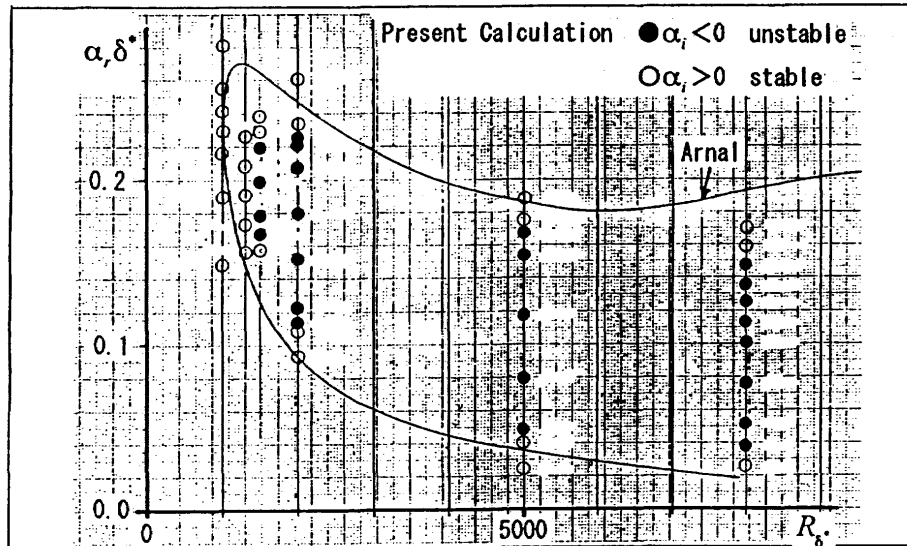Fig. 1 Stability characteristics of flat plate boundary layer : M = 0



Fig. 2 Stability characteristics of flat plate boundary layer : M = 2.2
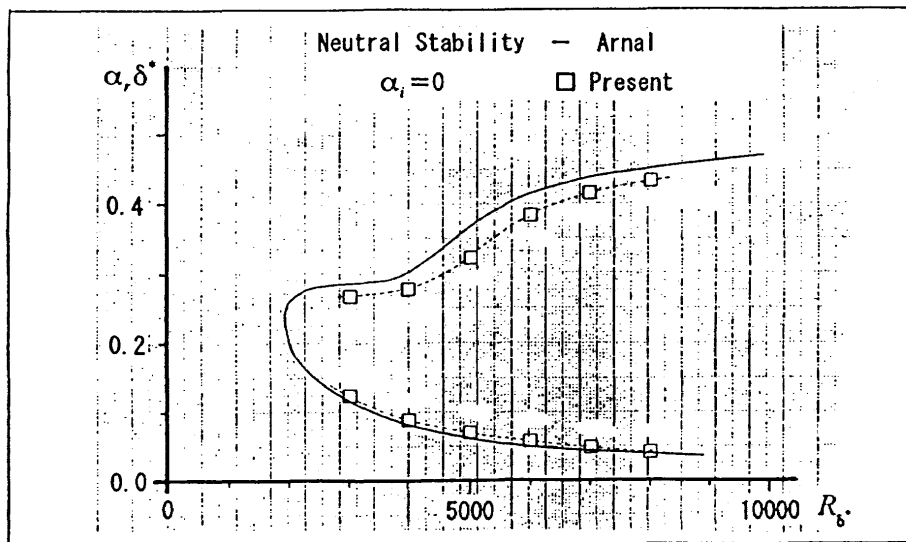


Fig. 3 Stability characteristics of flat plate boundary layer : M = 3.0

Effect of Mach number on maximum spatial amplification rate at $R = 1500$. Insulated wall.

(Ref : Mack,L.M., AIAA J. Vol.13, No.3, 1975, pp.278-289)

Fig. 4 Maximum amplification rate of compressible flat plate boundary layer
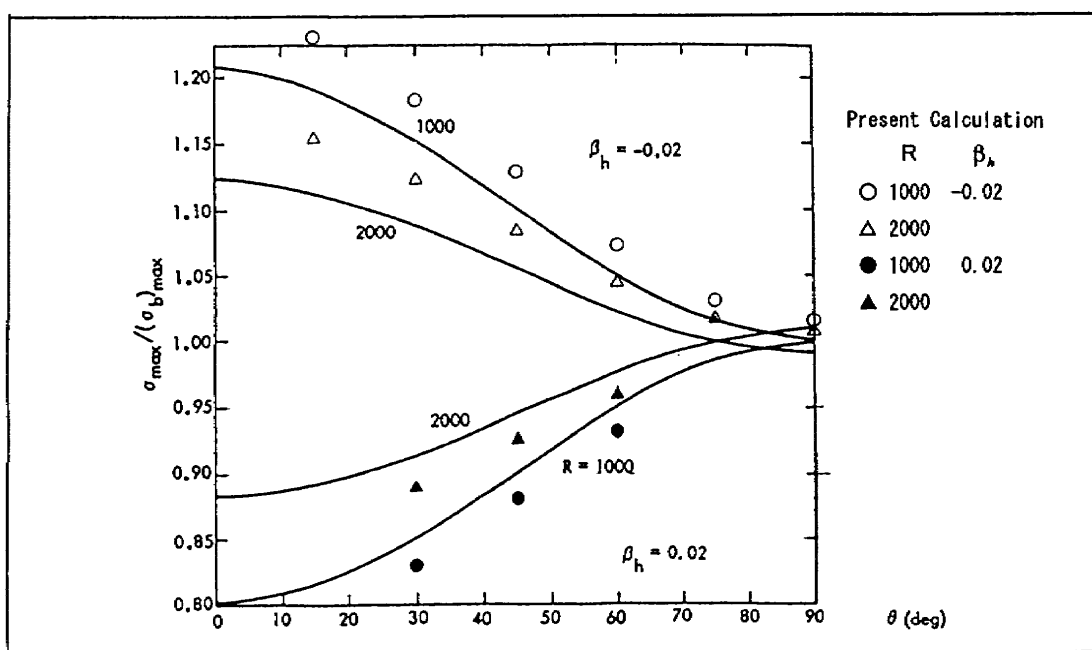


(Ref : Mack,L.M., AGARD Special Course on Stability and Transition , 1984)

Fig. 5 Maximum amplification rate of Falkner-Skan-Cooke boundary layer
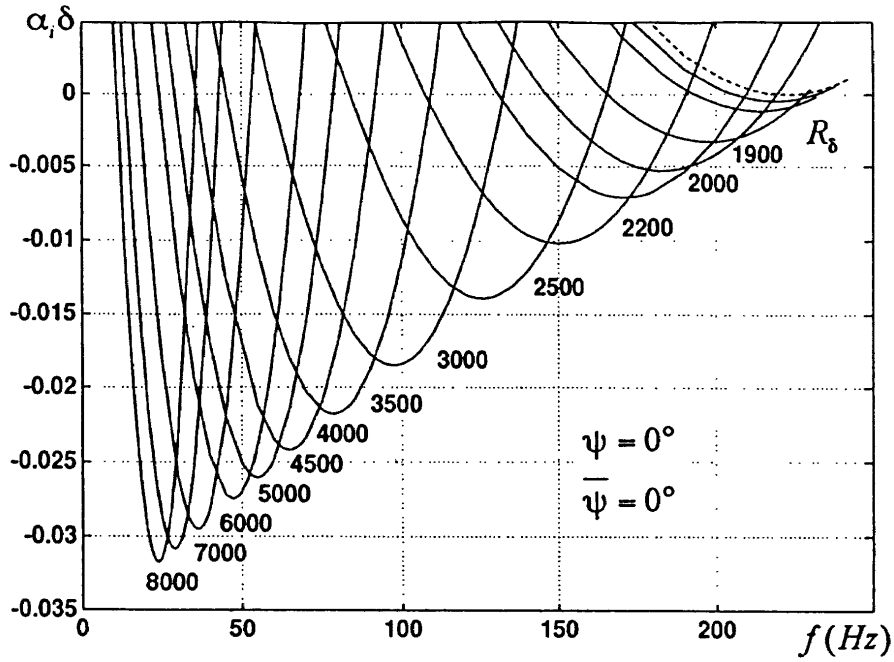
Fig. 6 Estimated amplification rate of Blasius boundary layer

## Integrated growth rates and n factor for the flat plate flow ▪◀ Kawasaki
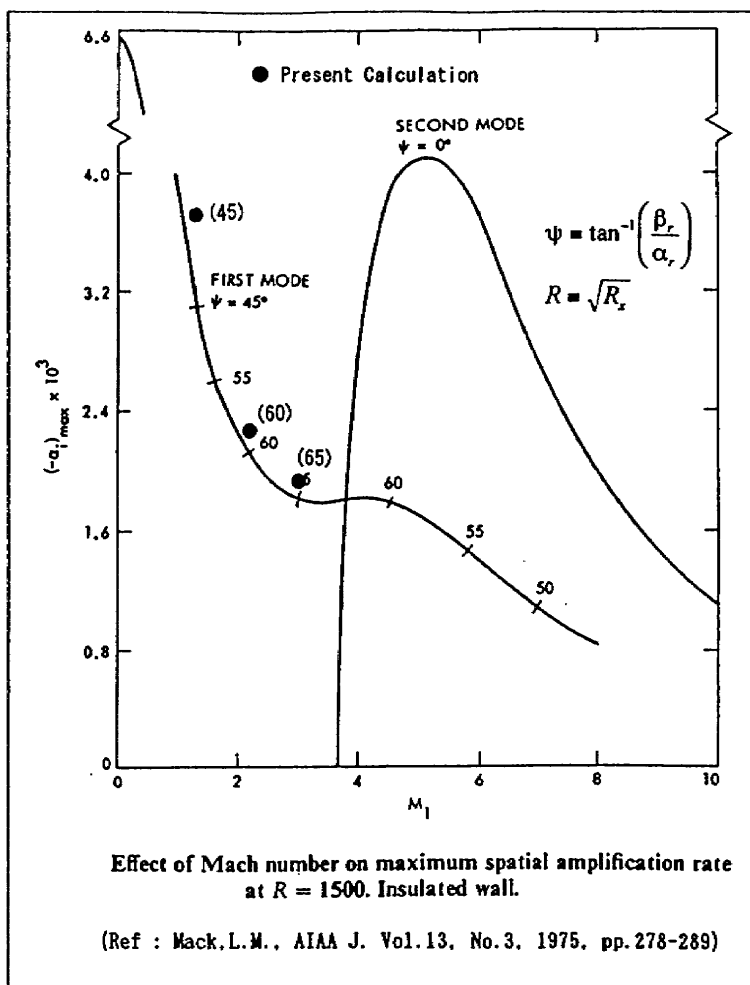
Stability of Blasius Laminar B.L. : N-Factor



*AGARD Report 793*

## DFVLR Swept Flat Plate Transition Experiment



AGARD-CP-438   16-1
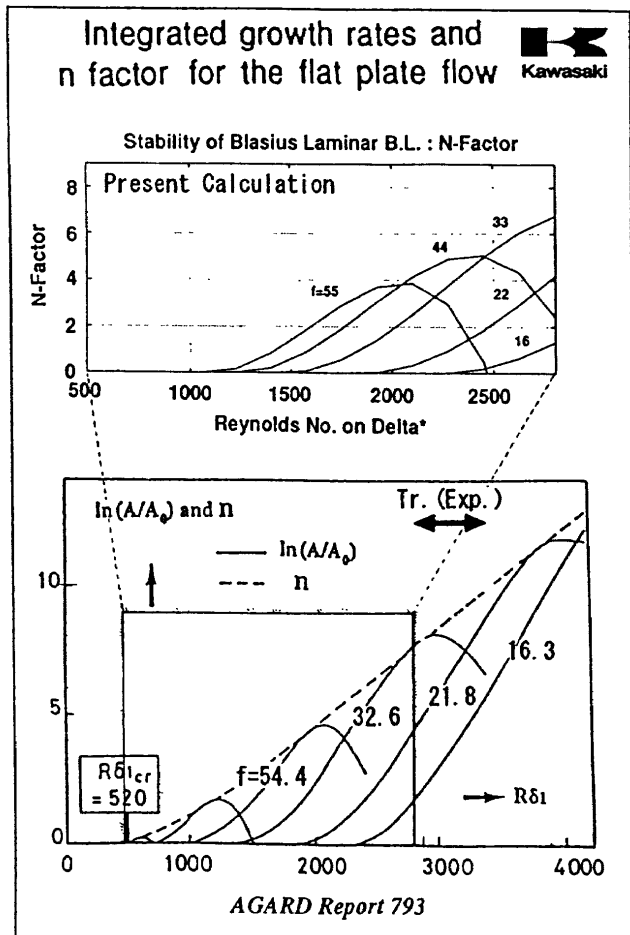
Fig. 7 Estimated N-factor of Blasius boundary layer
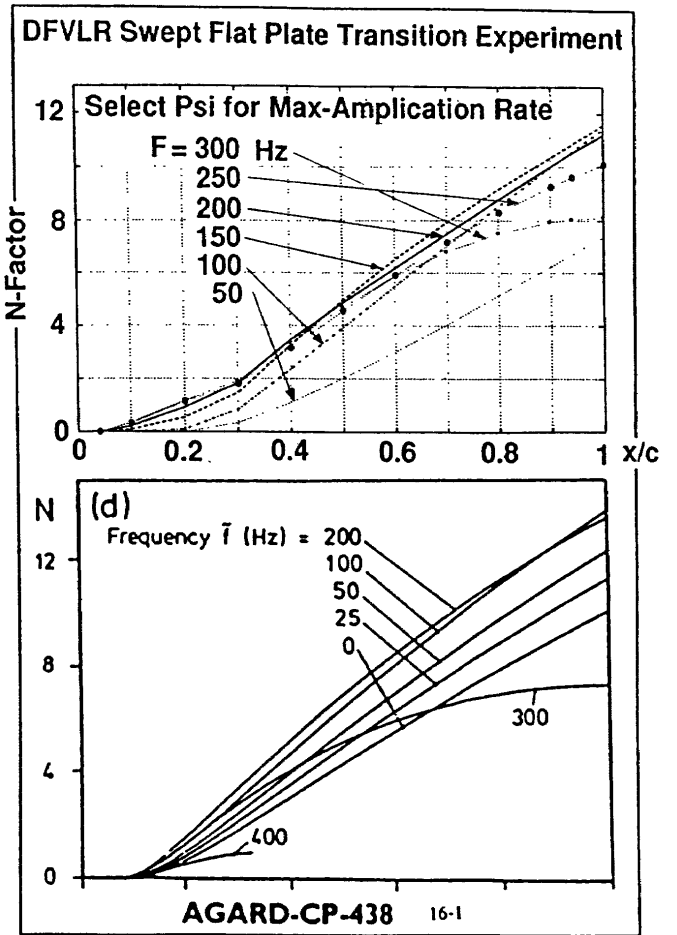
Fig. 8 Estimated N-factor of Falkner-Skan-Cooke boundary layer
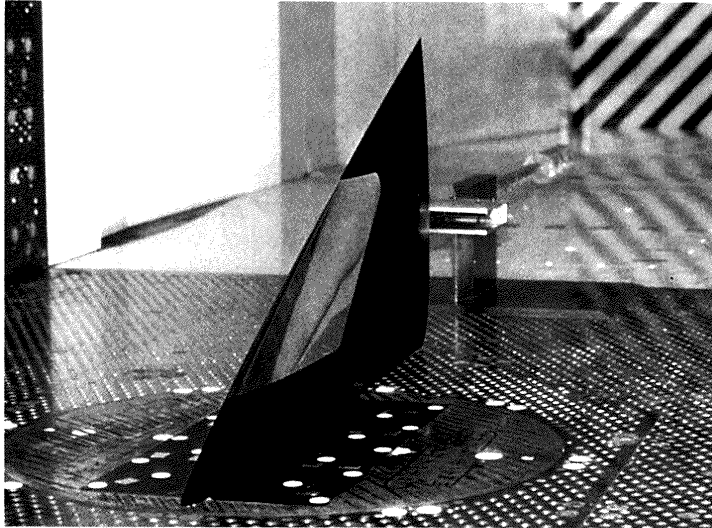
Max. Chord : $\ell$ =1072. 25 mm
Semi-span : $s$ =500 mm
L. E. Sweep : $\Lambda_{LE}$ =65°
Thick. Ratio: $t/c$ =0. 05
Suction Area: $0.03 \leqq x/c \leqq 0.3$
  $0.2 \leqq y/s \leqq 0.6$
dia. d=0. 1mm
About 60, 000 holes

Fig. 9 Wind tunnel model for supersonic laminar flow control test
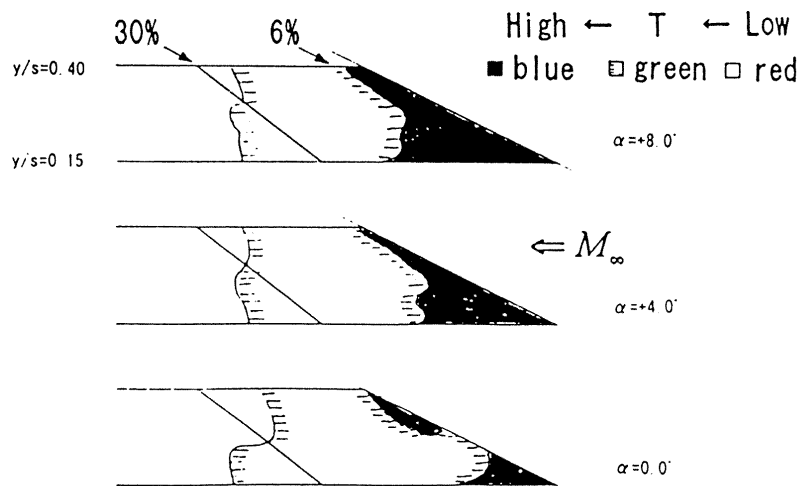


Fig. 10 Sketch on visualization of surface temperature
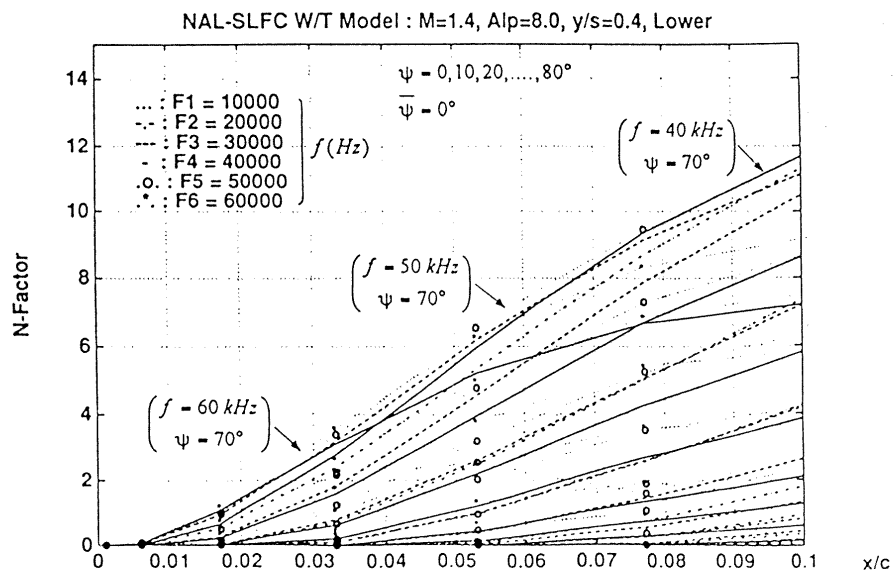


Fig. 11 Estimated N-factor on NAL-SLFC wind tunnel test

# 6

# An Experimental and Numerical Study on the Compressible Laminar Flow Control

Shigeo Yoshida, Kinya Nakano and Nobuaki Shiozawa
Fuji Heavy Industries, Ltd.

## ABSTRACT

Supersonic wind tunnel tests and numerical analyses were carried out on the boundary layer stability. Wind tunnel tests were performed on a swept wing model. Boundary layer transition locations were detected at various angles of attack and extensions of laminar flow regions by boundary layer suction were also observed. Consequently, the validity of supersonic laminar flow control was suggested.

And a boundary layer stability analyses code was developed, based on the linear stability theory, and its validity was confirmed for 2-dimensional boundary layers. Then one of the wind tunnel test cases was analyzed, and characteristics of disturbances were clarified.

## NOMENCLATURE

C:chord length

$-C_Q$:suction mass flow rate

$[(-\rho V)_{wall}/(\rho U)_0]$

M:Mach Number

Q:non-dimensional mean flow quantities

q':perturbated quantities from the mean flow

$R_C$:Reynolds number on the chord length

$R_{TR}$:transition Reynolds number

$R_x$:Reynolds number based on x

$R\delta^*$:boundary layer Reynolds number on the displacement thickness

U,V,W:velocity component in x,y,z coordinate system

x,z,y:choordinates normal and parallel to the leading edge, and upper-wise

$\alpha$:angle of attack

$\alpha,\beta$:disturbance wave numbers(real parts) and amplification rates(negative imaginal parts), in x and z direction

$\alpha\delta^*$:non-dimensional wave number

$-\sigma$:local amplification rate of wavepacket

$\delta^*$:boundary layer displacement thickness

$\Lambda$:sweep angle

$\phi$:disturbance amplification functions

$\psi$:angle between inviscid flow velocity vector and wave number direction

$\psi$:$\cos^{-1}(\psi)$

$\omega$:disturbance frequency

## 1.INTRODUCTION

Drag reduction at cruise condition is one of the most important themes in developing Supersonic Transports(SST). Among several drag reduction techniques, the laminar flow control(LFC) is the most promising one, because of its skin friction reduction benefit, as is mentioned in Ref.1. For its practical application, it is necessary to establish design tools and to validate its effectiveness.    In general, accurate transition prediction is critical in designing and analyzing laminal flow wings.    In cases of highly swept wings, like those of the SST, cross-flow(C-F) instability plays an important role in boundary layer transition phenomena, in addition to the Tollmien-Schlichting(T-S) instability.    And to realize laminar flow wings, it is necessary to suppress such 3-dimensional instabilities.    Hence, our objective is to reveal the characteristics of supresonic boundary layer transitions and the effectiveness of LFC for SST wings.

In this study, we focused on transitions caused by T-S and C-F instabilities, and aimed to accumulate 3-dimensional supersonic LFC wind tunnel test data and testing techniques, and establish numerical tools to predict effects of 3-dimensional supersonic LFC.

In this paper, we refer to the results of wind tunnel tests in section-2, numerical analyses in section-3, and conclusions in section-4.

## 2.WIND TUNNEL TEST

### WIND TUNNEL TEST OVERVIEW

We carried out wind tunnel tests in the Fuji Heavy Industries 2ft×2ft high speed wind tunnel. The test model was installed as shown in Fig.1 in the test section. The model is a non-tapered swept wing which has a 240mmC NACA64A008 airfoil section in the direction normal to the leading edge. Its upper surface between 2.5%C and 30%C is interchangeable with a perforated panel which has $0.1mm\phi$ holes distributed at 1.0mm pitch. Pressure distribution, transition locations, and suction mass flow were measured during wind tunnel run time, where transition locations were detected by the visualization technique using liquid crystals. Test conditions are shown as follows.

・Mach number(M)=2

・sweep angle($\Lambda$)=45° (supersonic leading edge)
　　　　　　　65° (subsonic leading edge)

・angle of attack($\alpha$)=-4° ~8°

・Reynolds number($R_C$)=4.4×10⁶($\Lambda$=45° )
　　　　　　　7.4×10⁶($\Lambda$=65° )

・suction mass flow rate(-$C_Q$)=0(solid)
　　　　　　　0.001(perforated)

### TEST RESULTS

The pressure distributions that were measured in the wind tunnel test are shown in Fig.2, and transition locations are also shown in Fig.3. Both results, without boundary layer suction, show that laminar regions extended as angles of attack increased, unless leading edge separation vortex caused the transition. It's known that cross-flow instability is dominant in accelerated regions on deeply swept wings. The pressure gradients, in the forward regions shown in Fig.2, got smaller as angles of attack increased. Consequently, cross-flow instability was suppressed as angles of attack increased.

Furthermore, the effect of boundary layer suction were observed in cases of $\Lambda$ =45° . Transition

Reynolds numbers were increased by about 1 million; consequently, decrease in skin frictions are suggested. In cases of $\Lambda = 65°$ , extensions of laminar boundary layer s were not observed.

## 3.NUMERICAL ANALYSIS

### PROBLEM FORMULATION

In this study, we aimed to predict boundary layer transitions by the N-factor method, which is also available for supersonic LFC wings. Hence, we have developed a 3-dimensional compressible boundary layer stability analysis code, based on linear stability theory.

The stability equations are derived from non-dimensional NS equations. Each flow variable consists of two terms. One represents the stable flow variables and the other represents the time dependent term.

$$Q(x,y,z,t) = Qs(x,y,z) + q'(x,y,z,t) \tag{1}$$

When we discuss the spatial propagating wavy disturbance, it is often expressed in the manner of a wavy function as follows:

$$q' = \phi(y) \cdot \exp[i(\alpha x + \beta z - \omega t)] \tag{2}$$

where $\alpha$ and $\beta$ are complex, and $\phi$ is amplitudes at neutral stability points. And the disturbance equations are written in the vector notation form.

$$d\phi_i / dy = \alpha_{ij} \cdot \phi_j \tag{3}$$

where $\alpha ij$ is an 8 × 8 matrix whose elements were determined corresponding to $\alpha$, $\beta$ and boundary layer profiles. The disturbance equations and boundary conditions form an eigenvalue problem.

$$F(\alpha,\beta;\omega) = 0 + 0i \tag{4}$$

In 2-dimensional analyses(i.e. $\beta$ =0+0i), to analyze the boundary layer stability corresponds to solving the eigenvalue problem. However, in 3-dimensional analyses, one more condition is required to solve the eigen value problem. In this study, a wave number direction($\alpha_r, \beta_r$) is also given as the condition, and the wavepacket assumption gives local amplifications($-\sigma$) and integrated amplification rate(N) as follows:

$$-\sigma = -\alpha_i + \beta_i(\partial\alpha_r / \partial_r\beta) \tag{5}$$

$$N = \int_{x0}^{x} (-\sigma)dx \tag{6}$$

### NUMERICAL PROCEDURE

The prediction procedure consists of 4 phases.
1)inviscid analysis[2]
2)boundary layer analysis[3]
3)stability analysis

4)transition prediction(N-factor method)

## CODE VALIDATION

To validate the analysis procedure, comparisons were made between present analyses and other analyses or experiments.

Fig.4 shows the comparison of the neutral stability profile for the Blasius' boundary layer between the one calculated in this study and Schlichting's[4]. Fig.5 shows growths of disturbances on a NACA0012 airfoil at zero incidence. Each line shows the disturbance growth of a certain frequency and the transition point was predicted as the intersection of the envelop of growth lines and transition criterion(N=9), and $\triangle$ indicates the test result[5]. Furthermore, Fig.6 shows comparison of the transition Reynolds numbers of flat plate boundary layers with experiments[6]. Each analysis(Fig.4-6) shows good agreement with other analyses and experiments.

## NUMERICAL ANALYSIS

Boundary layer stability analyses were carried out on the test case, $M=2$, $\Lambda=45°$, $\alpha=0°$, $R_C=4.4 \times 10^6$, $-C_Q=0$(solid surface). Fig.7 shows the neutral stability profile. Fig.7 shows that cross-flow instability is dominant in the region, which is consistent with the wind tunnel test results. Fig.8 shows the growth if there are disturbances. It shows that each disturbance gradually changes its direction from cross-flow instability to T-S.

## 4.CONCLUSIONS

Through supersonic wind tunnel tests, useful transition data were obtained and the extension of laminar regions were also observed; consequently, the validity of supersonic LFC was suggested. In this study on the numerical analyses, the validity of our stability analysis procedure was confirmed in 2-dimensional boundary layers. Furthermore, boundary layer stability characteristics in the leading edge region were made clear in the series of wind tunnel tests.

## REFERENCES

[1]Douglas Aircraft Company, "Study on High-Speed Civil Transports", NASA-CR-4235.

[2]Kamo. K., "Development of Three-Dimensional Compressible Navier-Stokes Analysis Code", 20th Conference on Fluid Dynamics, The Japan Society for Aeronautical and Space Science, and the Japan society for Fluid Dynamics, 1988.

[3]Kaups. T .and Cebeti. T., "Compressible Boundary Layer with Suction on Swept and Tapered Wings", Journal of Aircraft, Vol.14, No.7, Jul, 1977, pp.661-667.

[4]Schlichting. H., "Boundary-Layer Theory", 1979, p.139.

[5]Von Doenhoff. A.E., "Investigation of the Boundary-Layer about a Symmetrical Airfoil in a Wind Tunnel of Low Turbulence", Rept.L-507, 1940, NACA.

[6]Mack. L.M., "Linear Stability Theory and the Problem of Supersonic Boundary Layer Transition", AIAA Journal, Vol.13, No.3, Mar, 1975, pp.278-289.
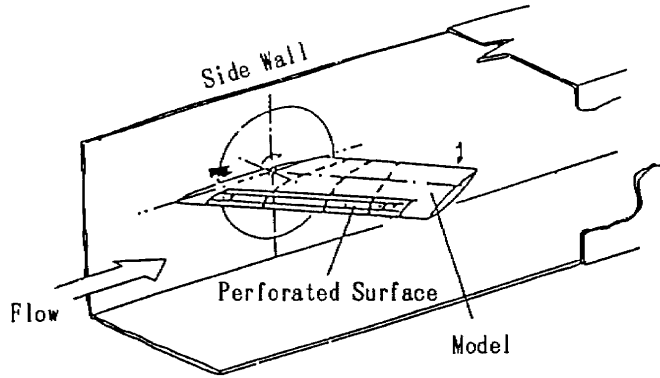
Fig. 1   Model Installation
in FHI High Speed Wind Tunnel
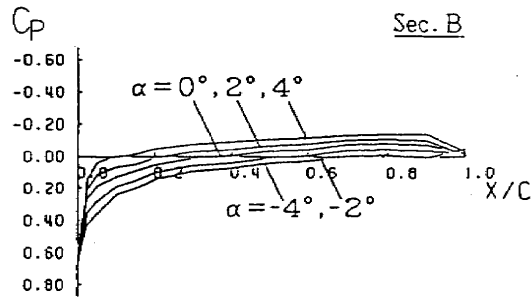


Fig.2(a)   Upper Surface Pressure Distribution
[$\Lambda = 4\,5°$ , Solid]
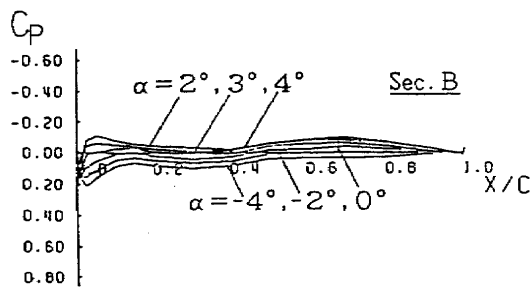


Fig.2(b)   Upper Surface Pressure Distribution
[$\Lambda = 6\,5°$ , Solid]
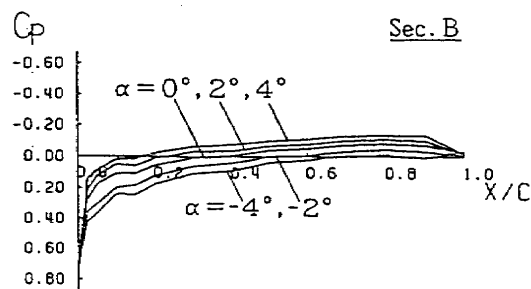


Fig.2(c)   Upper Surface Pressure Distribution
[$\Lambda = 4\,5°$ , $-C_Q = 0.001$]
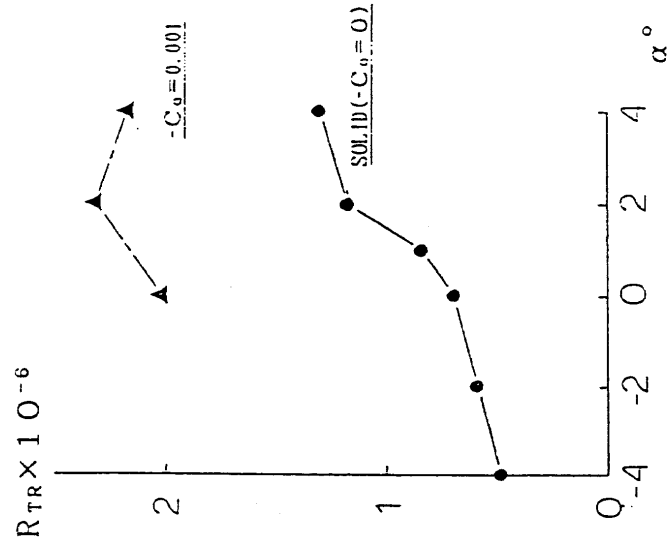
Fig. 3 (b)   Transition Reynolds Number
[$\Lambda = 45°$]
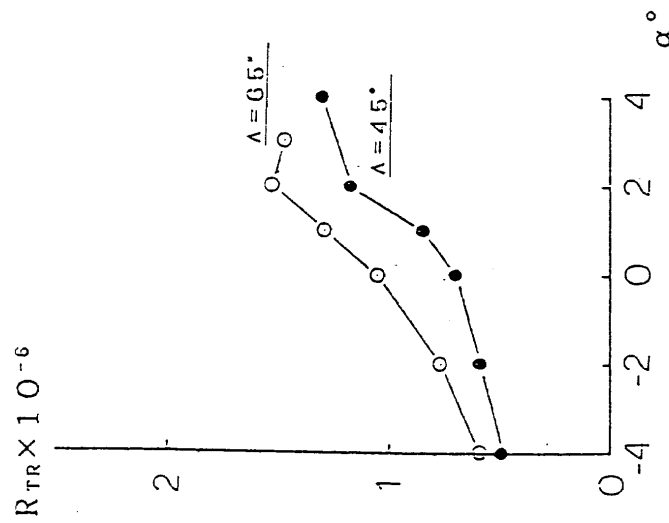


Fig. 3 (a)   Transition Reynolds Number
[Solid]
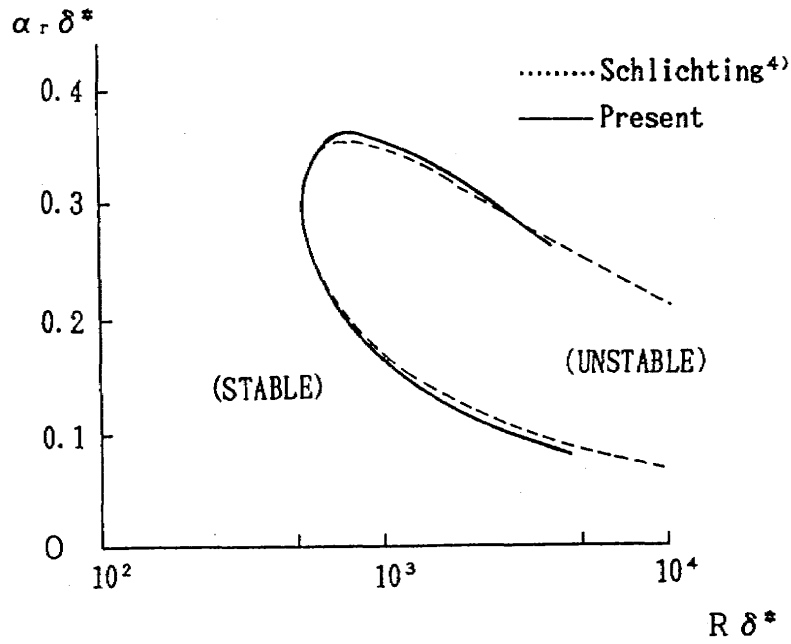
Fig. 4   Stability of Blasius Boundary Layer
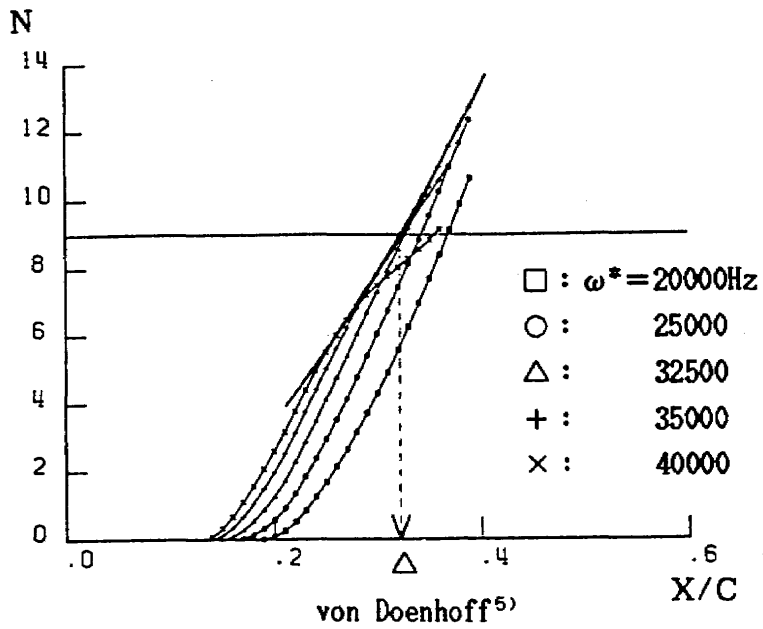


Fig. 5   Transition Location on NACA0012

Fig. 6(b)   Transition Reynolds Number
on Flat Plate
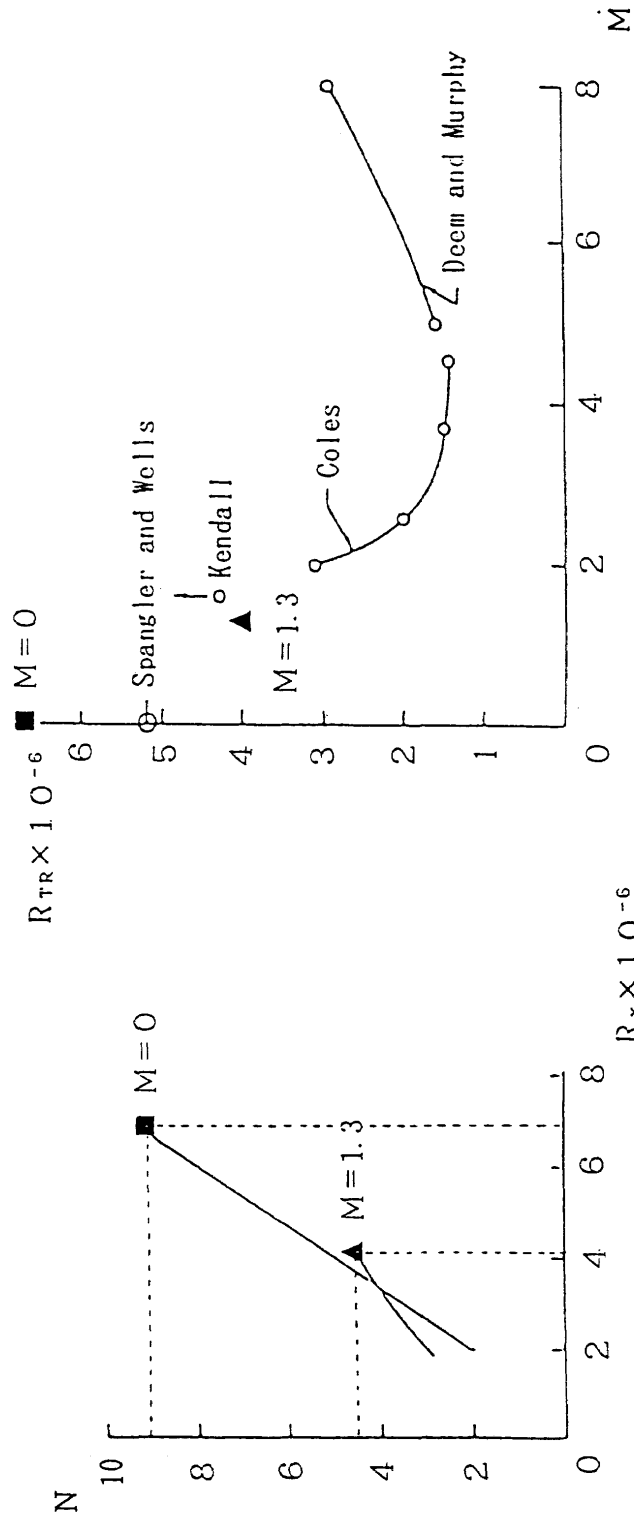
Fig. 6(a)   Integrated Amplification Ratio
and Transition Reynolds Number
on Flat Plate

Fig. 7 (b)  Neutral Stability Profile
on NACA64A008 Swept Wing
[Wave Number Direction,
$M=2$, $\Lambda=45°$, $\alpha=0°$ ]
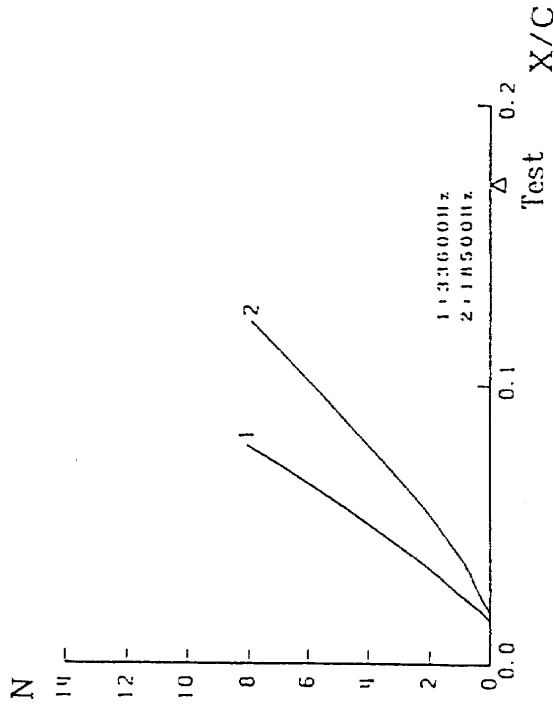


Fig. 7 (a)  Neutral Stability Profile
on NACA64A008 Swept Wing
[Amplification, $M=2$,
$\Lambda=45°$, $\alpha=0°$ ]
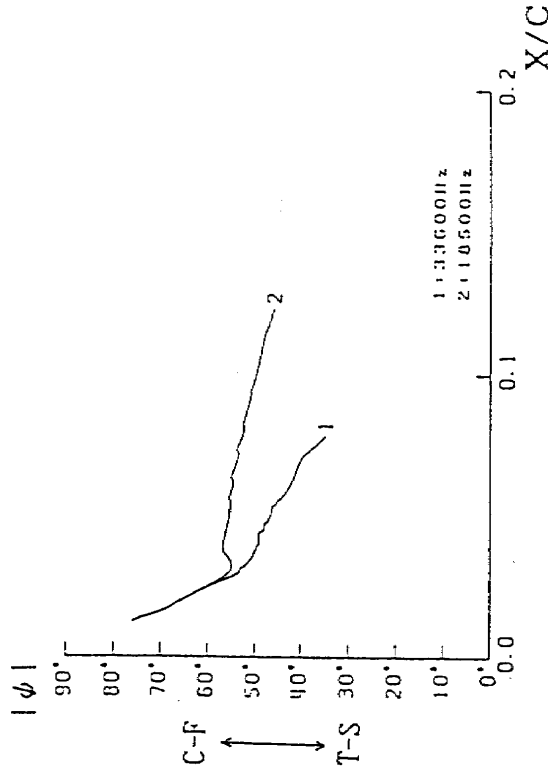
Fig. 8(b)   Growth of Disturbance
on NACA64A008 Swept Wing
[Wave Number Direction,
M=2, Λ=45°, α=0°]

Fig. 8(a)   Growth of Disturbance
on NACA64A008 Swept Wing
[Amplification, M=2,
Λ=45°, α=0°]

# 7

# Development of Heat Conduction Code THAP and its Application to the Fastener Jointed Component Analysis

## Kunihko OHTAKE
Structural Mechanics Division
National Aerospae Laboratoty
Tokyo, Japan

## Mitsuko KAMOHARA and Hiroko INOUE
Marine and River Technology
Tokyo, Japan

## Abstract

We are developing the finite element heat conduction analysis code "THAP". The main purpose of this development is the numerical simulation of the hypersonic aeroframe heat conduction. Special attention is paid to the joint structure thermal conductivity. The code can treat transient nonlinear heat conduction with temperature dependent material property, radiative and convective thermal load and contact thermal resistance. Using the code, we have examined the parametric identification of a heat conduction model for a fastener jointed structural component.

## 1. Introduction:

Recently in Japan, technology development for a hypersonic transportation system has become a very important engineering subject. There, thermal protection of aeroframes from the extremely high heat flux caused by aerodynamic heating is one of the most important design problems. It is thought that computer simulation will play an important role in the up-to-date efficient design of a heat resistant aeroframe . For the heat conduction analysis of solid configuration, Nickell[1] first developped the finite element formulation with the aid of Gurtin's variational principle[2]. Afterwards Oden[3] developped the general finite element formulation method based on the weak or Galerkin form variational principle. Thereafter it seems that, because of the development of the FEM code, heat conduction analys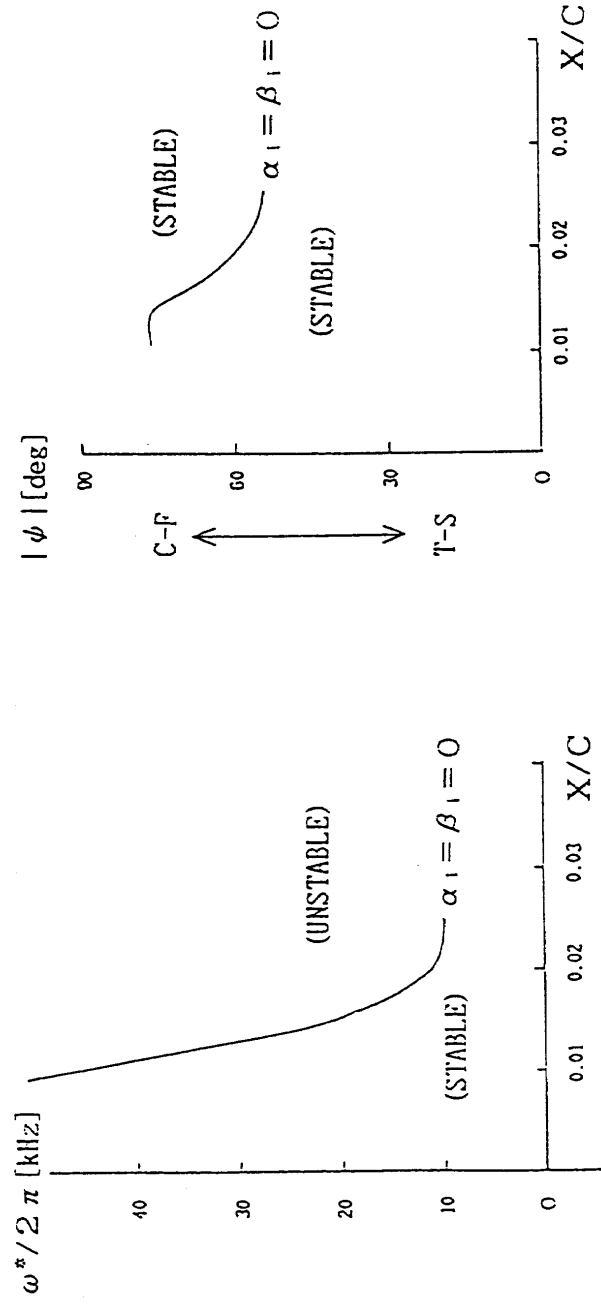is is only a problem of computer time, even for very complex configuraton. But the f acts show that the situation is not so simple for aeroframe heat conduction simulation. There are mainly three trouble sources which disturb the required precise FEM heat conduc- tion simulation. First is the uncertain material properties which is enevitable from a heat conductivity mechanism. Second is the uncertain heat input and output.The aeroframe s tructure is composed of thin plates and shells, which means that the surface dimension is much larger than the thickness dimension. Therefore heat flow through the surface has a great effect on the solid inside heat flow. In other words, the boundary condition is uncertain. Third is that the usual aeroframe contains many joints, which cause the uncer- tinty of the numerical simulation model. In order to overcome these difficulties and to supply sufficient data for design request, development of modelling or system identifica- tion technique for heat conduction simulation is important. In addition we need a compact and high performance FEM code which can treat the complex modelling requests.

## 2. The feature of our heat conduction analysis code THAP [4]

We developed a new heat conduction code, THAP (Temperature and Heat conduction Analy- sis Program), in order to cope with the above situation. The emphasis is on the treatment of boundary heat transfer including contact thermal resistance. In addition THAP can treat coupling analysis with aerodynamic heating code FIVAD and radiative heat transfer code

RHT95 .

## 2.1  Program Organization

The program is devided into five phases. The total program structure is shown in Fig. 1
1) Input control information, mesh and element data time functions.
2) The system conductivity and heat capacity matrices are assembled in the compact skyline form [5]
3) Calculation of Applied heat flow vectors

According to the time dependent load history function data, the program calculates the nodal heat flow vector. Edge(2D) or face(3D) distributed loads are converted to the nodal load data.
4) Step by step solution

Central difference time integration and the Forward Euler method is available [6].
5) Nonlinear equiliblium iteration

If the material properties are temperature dependent, incremental equiliblium iteration can be available [4].

## 2.2  Element Liblary

1) 2 node 1D element
2) 3 and 4 node 2D element
3) 3 and 4 node axisymmetic element
4) 4 node nonplaner surface element used for 3D conection or fin element
5) 6 and 8 node 3D element
6) 2 node 3D contact thermal resistance element
Every element can be available for temperature dependent material property.

## 2.3  Boundary condition

1) Applied heat flux, concentrated and distributed
2) Convection boundary, disrtibuted
3) Radiative boundary, concentrated and distributed
4) Fixed temperature boundary

## 2.4  Contact thermal resistance element [4]

Our idea of a contact element is the extension of the 1-d heat conduction element. Let's define contact thermal resistance (inverse of conductance) R by $Q = A/R*(T^+-T^-)$; where Q:total heat flux, A:contact surface area, $T^+$ and $T^-$ :contact surfacetemperature of each side, respectively [6]. Comparison of this equation to the Fourier's law of heat conduction leads us to the 2 x 2 heat conductance matrix of $K = \{k_{ij}\}$, where $k_{11}$ and $k_{22}$ = A/R, $k_{12}$ and $k_{21}$ = -A/R. This is regarded as a limit of the 1-d usual conductance element, where element length is zero. We add that the quantity R can be measured experimentaly. In Fig. 2 we demonstrate the contact element ability. Two rods, rod1 and rod2, are connected to each other. The length of rods are L1=0.1m, L2=0.05m. Thermal conductivity: k1=2000W/mK, k2=1000W/mK. Specific heat: c1=c2=500J/m³K. Contact thermal resistance:1/R= 20,000W/m²K. Contact area: A=0.01m². From one end heat flux q= 2000W/m² is given and the other end is kept to a constant initial temperature of 300K . After 100 seconds, temperature distribution reaches the steady state, as shown in the figure. The result coinsides with the theoretical value.

## 3.  Model Optimization [7]

### 3.1 Parameter Identification method

Once the FEM model or heat conductance matrix system is formed, computer simulation

is carried out and compared with some observed results. We set the measure of error as E = $\Sigma$ W*($\theta$e - $\theta$c)**2, where W is weight, $\theta$e is experimental temperature, $\theta$c is calculated temperature and summation is taken over all interested points. We want to minimize E by changing the matrix system and want to get better fitting between observation and simulation . The choice of the parameters or design variables is most important in the optimization procedure. Our general policy is to minimize the number of design variables. Usually the dimension of the FEM matrix system is large. We choose the physical thermal coefficients as the design variable base. Quite often coefficients are temperature dependent and it seems inevitable that the number of variables is of the same order as the number of elements (or even a multiple of of the element number). This is unfortunate. We don't use the coeficients directly as the design variables, but choose the multiplier of the temperature dependent coefficient function in such a case. Therefore we prepare only one variable for each material's particuler coefficient. In another case we set some special relation among the different material's coefficients and make it into one group. Then only one parameter is necessary to the related coefficients. In seeking the minimum of object functional E, we use gradient information of $\theta$ with respect to the chosen variables, and apply the information to the necessary condition of minima, which says that partial differential of E with respect to design variable should be zero. This leads us to the linear system, the solution of which tells us the minimum direction. The iteration procedure leads us to the mimina.

### 3.2 Example Demonstration of the Method

We apply the above method to a two piece fastener jointed structure. Fig. 3 shows the 2-d FEM model of this test specimen. Total height is 150mm, width is 280mm, contact surface length is 20mm, and the upper 50mm is electrically heated. Temperature measurement results, partially interpolated to coinside with the FEM node points, are compared with THAP simulation results. Then parameter identification iterations are carried out. Several different approaches are tested and convergence is obtained. Figs. 4 and 5 show a steady state example, where the thermal conductivity k, contact thermal resistance R and surface emisivity em1 and em2 is chosen as the variable base. Here em1 and em2 are related linearly. Therefore the number of design variables is three in this case. Three iterations are enough for this case. Initial and final optimised values of thermal properties, calculated from the design parameters, are tabulated in Table 1.

### References:

1) Gurtin, M. E: Variational Principles for linear initial-value Problems, Q. Appl. Math. 22, pp. 252-256 (1964)

2) Wilson, E. l> and Nickell, R. T. : Application of the finite element method to the heat conduction analysis, Nucl. Engng. Design, 4 pp. 276-286 (1966)

3) Oden, J. T. and Reddy, J. N. : Variational Methods in Theoretical Mechanics, Springer-Verlag (1976)

4) Ohtake, k. , Okumura, h. , Kamohara, M. and Inoue, H: Heat Conduction Analysis Code THAP. V3 for Joint Structure, NAL J-94004, pp. 139-178, (1994)

5) Bathe, K. J. :Finite Element Proceduresin Engineering Analysis, Prentice-Hall (1982)

6) JSME Databook: Heat Thansfer 4th ed.

7) Fox, R. L: Optimization Methods for Engineering Design, Addison-Wesley (1971)

8) ADINA ENG. : ADINAT User's Manual, Report AE81-2 (1981)

```
main - deffile
     + echinp
     + second
     + error
     + timtable
     + input  - incord
     |        + inptbc  - functn
     |        |         + inload
     |        |         + inload1 - intpltn
     |        |         + inload2 - intpltn
     |        |         + inload3 - intpltn
     |        |         + inradi
     |        |         + inconv2
     |        |         + inconv3
     |        |         - intemp  - intpltn
     |        |
     |        |                   - toned - oned - colht
     |        - inptel  -elemnt + tquad - quad - colht
     |                          |               - funct2
     |                          + thexa - hexa - colht
     |                          |               - funct3
     |                          - tcontr- contr- colht
     + addres
     + assem  - elemnt---------------------------- toned - oned - tempel
     |                                            |               + ptable  - serchpara
     |                                            |               + otdm
     |                                            |               - addban
     |                                            |
     |                                            + tquad - quad - tempel
     |                                            |               + ptable  - serchpara
     |                                            |               + qtdm    - consis
     |                                            |               - addban
     |                                            |
     +bload --- cload                             + thexa - hexa - tempel
     |       |                                    |               + ptable  - serchpara
     |       + sload -- loadedg                   |               + htdm
     |       |          + loadfce - functld       |               - addban
     |       |          |         + loadfsdm      |
     |       |          - addvec                  - tcontr- contr- tempel
     |       |                                                    + ptable  - serchpara
     |       + hload  - convedg - addban                          + ctdm
     |       |         + convfce - fnctld                         - addban
     |       |         |         + convsdm
     |       |         |         - addban
     |       |         - addvec
     |       - rload
     |
     + makels
     + fixbc
     |
     + colsol
     |
     + result
     |
     + equit  - elemnt -- *
     |         + bload  -- *
     |         + colsol
     |         + result
     |         - discrm - maxtt  - norm
     |
     - writd
```
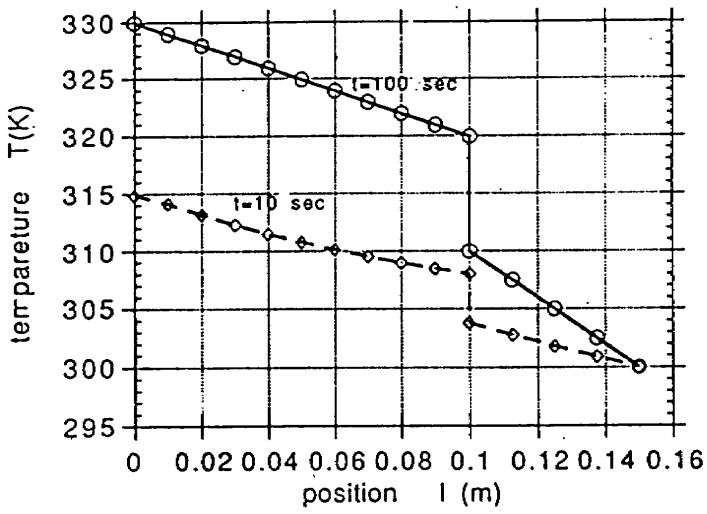
Fig.1  THAP Program Structure
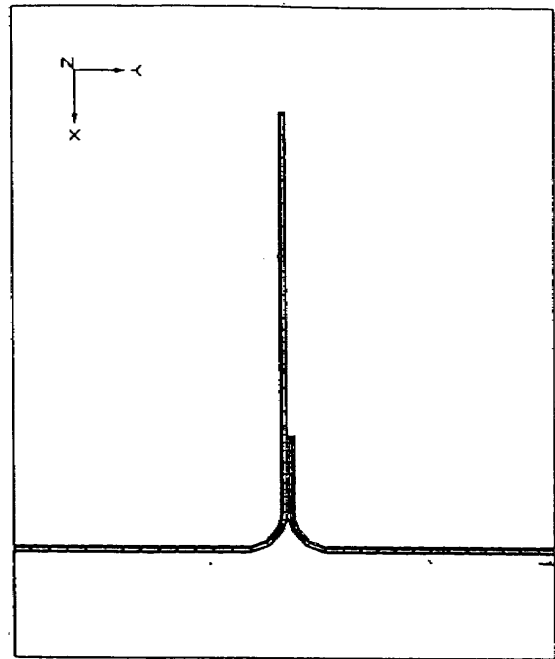
Fig.2 Contact Thermal Resistance
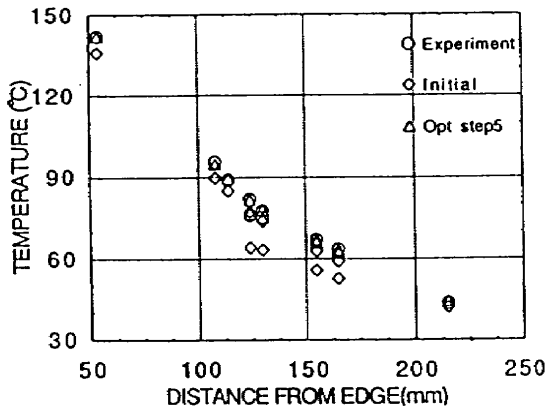Example Simulation



Fig.3 FEM Simulation Model



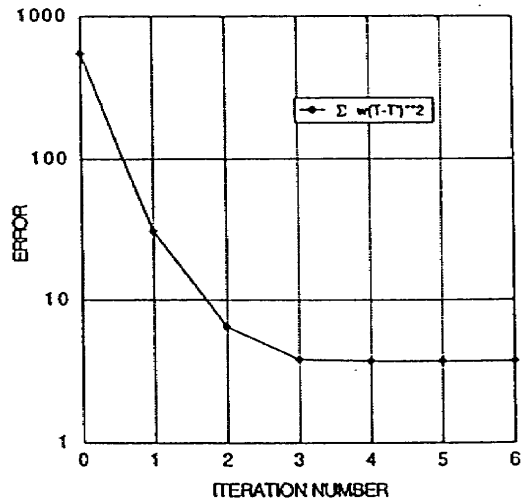Fig.4 Parametric Identification
Demonsrtation Results



Fig.5 Minimization Error
vs. Iteration Number

**8**

# Experimental Heat Conductin Study of Fastener Jointed Structural Components

## Kunihiko OHTAKE and Shuuji ENDO
Structural Mechanics Division
National Aerospace Laboratory
Tokyo, Japan

## Nobuhiro UCHIDA
Nagoya Aerospace Systems
Mitsubishi Heavy Industry Co., Ltd.
Nagoya, Japan

## Abstract

We have studied experimentally the heat conductance characteristics of an aluminium alloy, fastener jointed structure. Our study consisted of the measurement of contact thermal resistance and the temperature distribution of jointed structural components. The result shows that near the jointed edge heat conduction is disturbed because of the existence of the contact surface. This effect is remarkable when the test environment is a vacuum.

## 1. Introduction

The skin surface of a hypersonic transport aeroframe faces very high heat flux because of aerodynamic heating. Therefore the structural designer should consider the thermal stresses and heat conduction. The aeroframe structure is composed of many components, which are the assembleges of the fastener jointed thin structural members. So, for aeroframe heat conduction analysis, we suppose that the effects of contact thermal resistance between the contact surfaces should be considered.

Our experimental heat conduction study of jointed structures is devided into three phases. The first is the measurement of contact thermal resistance of two kinds of aluminium alloies, 2024-T62 and 7075-T6, which are frequently used in aeroframes. The second is the estimation of contact thermal resistance of a fastener jointed 2024 aluminuum plate component[3]. The third is the temperature responce measurement of a fastener jointed structural component with a branch. The last one is intended for example data for the numerical simulation model of jointed plate structures. In this case several heat conduction factors affect the measured temperature distribution in realistic simulation. In particular, convection effects seem very complex, and we excute our measurements both in a vacuum and in an atmospheric environment in order to treat the convection effect separately in the analysis.

## 2. Direct measurement of contact Thermal Resistance(Ph.1)

### 2.1 Test equipment and experimental method

The sketch of the test equipment is shown in Fig. 1. The test pieces are as followings;

        materials:   2024-T4 and 7075-T6, anticorrosive process on the surface
        geometries:  diameter 30mm, thickness 2.03mm, poker chip shape

Two chips of the same material are placed face to face, and are sandwiched between stainless steel rods (sus304) of the same diameter . Each  rod is equipped with  six small holes for the measurement of axial direction temperature distribution. A rubber sheet electrical heater is pasted on the upper face of one rod, and a water cooled cold plate is attached to the bottom face of the other rod. Thermocouples are inserted into the rods. The side of the whole specimen is coverd by an insulater. The universal test machine gives the axial compressive loads to the contact surface of the poker chips.

Durring the test, assumed  compressive pressure is loaded, the top is heater loaded, and the bottom is cooled for the specimen. After thermal balance is attained, temperature measurement is carried out for 12 point.  During the test, the coolant water temperature of the cold plate is hold to 20°C. The supplied heat power is 20W for the 2024-T62 test piece, 30W for the 7075-T6 testpiece. The contact surface pressure is 0.1, 1, 10 and 50MPa. Fig. 2 shows the temperature distribution model of the specimen. The heat flux density is

$$q = -\lambda_1 \frac{dT_1}{dX} = -\lambda_2 \frac{dT_2}{dX} \qquad (1)$$

where $\lambda_1$ is thermal conductivity of the test piece, $\lambda_2$ is that of the stainless rod. The thickness of the poker chip test pierce is dX , so the difference of the  upper rod contact surface temperature T21(2) and the lower rod contace surface temperature T12(2) is given by

$$T_{12(2)} - T_{21(2)} = - \{\Delta T_{21} - 2\frac{dT_1}{dX}\Delta X + \Delta T_{11} + \Delta T_{12}\} \qquad (2)$$

where suffix(2) denotes that two chips are used and:

    dT21    : temperature drop between rod and test pierce contactsurfaces
    dt11    : temperature drop between two test pierce contact surfaces.
    dt12    : temperature drop between test pierce and rod surfaces

The experimental temperature measurement gives the temperature gradient in the rod. T12(2) and T21(2) are obtained from the extrapolation of the measurement.

After that , one poker chip test pierce is removed ,and similar measuement is carried. In this case The difference of the upper contact surface temperature T21(1) and the lower contact surface temperature T12(1) is given by

$$T_{12(1)} - T_{21(1)} = - \{\Delta T_{21} - \frac{dT_1}{dX}\Delta X + \Delta T_{12}\} \qquad (3)$$

The contact surface temperatures T21(1) and T12(1) are also obtained by extrapolation. Here it is obvious that dT11 can be extruded from the easy operation using eqns. (2) and (3). Therefore we can get the value of the test pierce contact thermal resistance Rh11. as

$$R_{H11} = \frac{\Delta T_{11}}{q} \qquad (4)$$

If we assume that dT21=dT12, then we can get Rh21= Rh12. Precisely, it is observed that the contact thermal resistance from aluminium alloy to steel is less than the resistance from steel to aluminium alloy[1].

We use the following thermal conductivity values for the calculation[2].

| matelial | thermal conductivity (W / m·K) |
|----------|-------------------------------|
| 2024-T62 | 120 |
| 7075-T6 | 130 |

SUS 304                          16

## 2.2 Experimental Results

Fig. 3 shows the relation between contact pressure and contact thermal resistance. The experiment assumes one-dimensional heat conduction, but the heat leak through the side insurance is not negrigible. Therefore the temperature gradient in the rod is not linear, which disturbs the precise extrapolation of temperature at the contact surface. Under such a condition, our observations are:

(1) The contact pressure increase causes the reduction of contact thermal resistance. This is reasonable because of the fact that the pressure increase generates a larger direct contact area.

(2) The difference of contact thermal resistance between the two materials, 2024-T62 and 7075-T6, is not large in this experiment. This result is caused by the small defference of the two materials' hardness and thermal conductivity.

(3) If the contact pressure is more than 10MPa, then contact thermal resistance between aluminium surfaces, Rh11, becomes a constant value. But contact thermal resistance between stainless steel and aluminium alloy, Rh21, is still decreasing. This is considered to be due to the difference of the two materials' hardness and surface roughness.

## 3. Heat conduction test of lap jointed member.(Ph.2)

### 3.1 Test specimen and experimental method.

The specimen is a lap joint type. Two pierces of aliuminium alloy  plate is fastened by 4 bolts. The diameter of the bolt is 4.8mm. The plate is made from 2024-T62 and the thickness is 2.03mm. A rubber type electric heater is pasted at the top surfaces of the plate. A cold plate is attached at the lower angled part. The total specimen is shown in Fig. 4.

In the experiment the bolt is fastened to the defined torque. Then the specimen is set in a vacuum chamber. The heater supplies thermal loads and the cold plate takes the role of the fixed temperature boundary. After the system is thermally balanced, temperature is measured by the thermocouples which are welded on the plate surfaces. Vacuum (less than 0.5 torr) and atmosphire environments are used for the test. The electric power of the heater is 60W. The coolant water temperarute is holded to 20°C during the test.  The fastening torqu is changed to 20,40,and 60 kgf.cm.

### 3.2 Experimental Results

Fig. 5 shows the temperature plot along the heat flow direction distance. In all 6 cases, a temperature gap is observed at the lap joint part. Fig. 6 is a heat conduction model for the specimen. Fig. 6(a) is based on the assumption that the jointed part consists of one continuum body. The temperature gradient of the joined part is assumed to be one half of the gradient of the regular part, an anti-proportional assumption to the sectional area.  Fig. 6(b) shows a contact model for the lapped contact surface. Here the assumption for the temperature gradient of the lapped part is the same as for the continuum model. In addition, exsistence of a temperature drop dT due to the contact thermal resistance is assumed on the contact surface. Denoting the temperature of each contact surface as T1 and T2, and the overlapping part length as L, the temperature difference of this part is expressed as

$$T_2 - T_1 = - \{ \Delta T - \frac{1}{2} \frac{dT}{dX} L \} \tag{5}$$

T1, T2 and the temperature gradient of (5) is obtained from the experimental measurement. where :

   T21(2) : upper rod contact surface temperature

   T12(2) : lower rod contact surface temperature

THerefore dT can be calculated. In addition, heat flux q2 through the contact srface is written as

$$q_2 = \frac{t}{L}(-\lambda)\frac{dT_1}{dX}$$

(6)

where t is the single plate thickness.

Then, using this dT and q2, the contact thermal resistance extruded from this test shoud be;

$$R_H = \frac{\Delta T}{q_2}$$

(7)

Fig. 7 shows the relation between the fastening torque and contact thermal resistence Rh. In addition the upper horizontal scale stands for the contact pessure, which is calculated from the relation between fastening torque and force. From this graph, the following results are derived.

(1) The value of contact thermal resistance is larger in a vacuum than at atmospheric pressure. If the mean free path of the filler gas in the contact surface gap is less than the gap dimension, which is caused by the chamber pressure reduction, then the contribution of filler gas to the heat conduction between two surfaces should be reduced[4].

(2) The differences of resistance values among the different torques are not so distinguishable. This comes from the large fastening torque engaged in the test. Then the contact surface conditions become thermally equivalent. But precise observation detects that the increase in torque causes a small increase in resistance, which contradicts the results of the preceeding section. This is explaind by the fact that the large fastening torque causes a delicate deformation of the plate part away from the bolt, which causes insufficient contact in the area. In addition, the fastening torque of an aeroframe high rock bolt of this size is about 35 to 46 kgf. cm. Therefore the setting level of torque is reasonable for aeroframe application.

(3) The contact thermal resistance calculated in this section is about 10 times larger than that of the preceeding section. For comparison, of course, the torque is changeg to the equivalent contact pressure. The one dimensional heat conduction model assumption of Fig. 6 seems insufficient for this lap joint case. The estimated value, Rh of eqn. (7) should be called "system resistance value" , which should be regarded as a different concept from the direct measured value.

## 4. Heat conduction test for the fastener jointed component with branch member.(Ph.3)

### 4.1 Test piece, test equipment and experimental method.

Five test pierces are classified into two series which are described in Table 1. The features of the test pieces are shown in Fig. 9. In the T series, an angle member is jointed to a plate with a fastener. The material is 2024-T62 anticorrosively processed aluminium alloy. The widths of the lapped parts are 30mm and 50mm. The number of fasntener bolts are 6 x 1 and 6 x 2, where the second number stands for the column. The distance between the bolts is 25mm. The fastening torque is 46 kgf. cm. In the r series, two folded plates with a radius of 10mm are fastener jointed. The lapped part width are 12mm, 20mm and 30mm. The torque is 45 kgf. cm for r1 and r2, and 40 kgf. cm for r3. The number of fasteners is 4 x 1

for rl and r2, 4 x 2 for r3. The fastener distance is 30mm for rl and r2,50mm for r3. For all cases standard aeroframe fasteners are engaged. Rubber heaters of 50 mm x 150mm are pasted on the top face of each piece . The one heater electric capacity is 60W. We refer to the heater sides as "top" or "upper" and the opposite side as "bottom" or "lower" afterwards. At the bottom branched end, cooling tubes made of copper are connected with screws. Thermocouples are spot welded on the center line of the specimen.

The test equipment system is shown in Fig. 10. The specimen is set inside the vacuum chamber. The transformed electric power is supplied to the rubber heater through the vacuum connecter. The constant temperature water reserver supplies coolant water to the copper tube. The temperature is measured by the data logger of 60 points per second scanning speed which is operated automatically by the personal computer. The pressure condition of the chamber is the same as in the preceeding section, ie, vacuum or atmosphere.

## 4.2 Test results

Thirty minites after the power is turned on, thermal equiliblium is obtained, and temperature measurement is carried out. The results are shown in Fig. 10.

(1) In the lapped part, at least within 10mm from the upper lapped edge, the surface temperature of the heated plate, which is called the main plate, is higher than the opposite surface temperature of the branched plate.

(2) The temperature difference of (1) is remarkable in a vacuum but very small in atmospheric condition.

(3) The temperature difference is small in the off lapped, lower part.

(4) For the T series specimen, at the lapped lower edge region , the temperature of the branched plate is higher than that of the main plate.

(1) and (2) is the effect of the contact thermal resistance. This is also verified by an addditional test, where continuum and fastner joined step shaped plates are compared for the temperature measurement. The reason for (4) has not yet been well analised. There are several facts to be noted: 1) the branched plate is a little bit thin by about 0.05mm, 2) the inside of the angle corner is very thick, 3) distance definition is different between flat plate and corner.

## 5. Concluding comment

We studied, under relatively low heat flux, the heat conduction characteristics of the structural components which have lapped and fastener jointed part. The fastener jointed aeroframe is thermally very strongly connected under atmospheric conditions. We are much interested in the very weakly contacted part and /or very strong heat flux condition.

## References

1) Y. Katto: Dennetsu Gairon, Youkenndo, 1964
2) JSME: Heat transfer handbook 4th ed. 1986
3) NAL J-94004, pp. 125-132, 1994
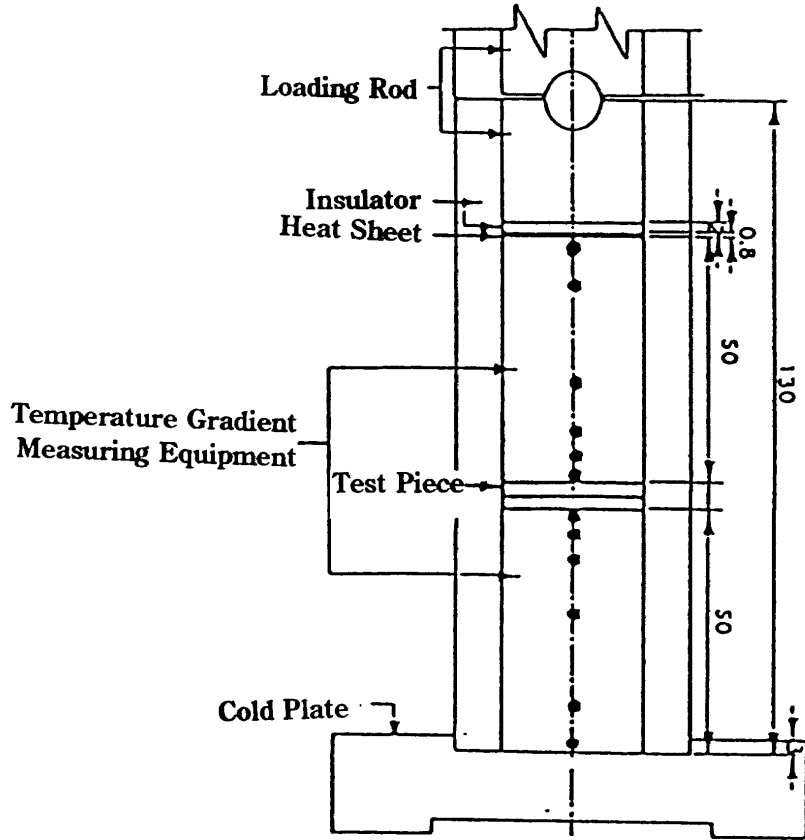4) JSAAE/JSME pp. 357-361, 1994

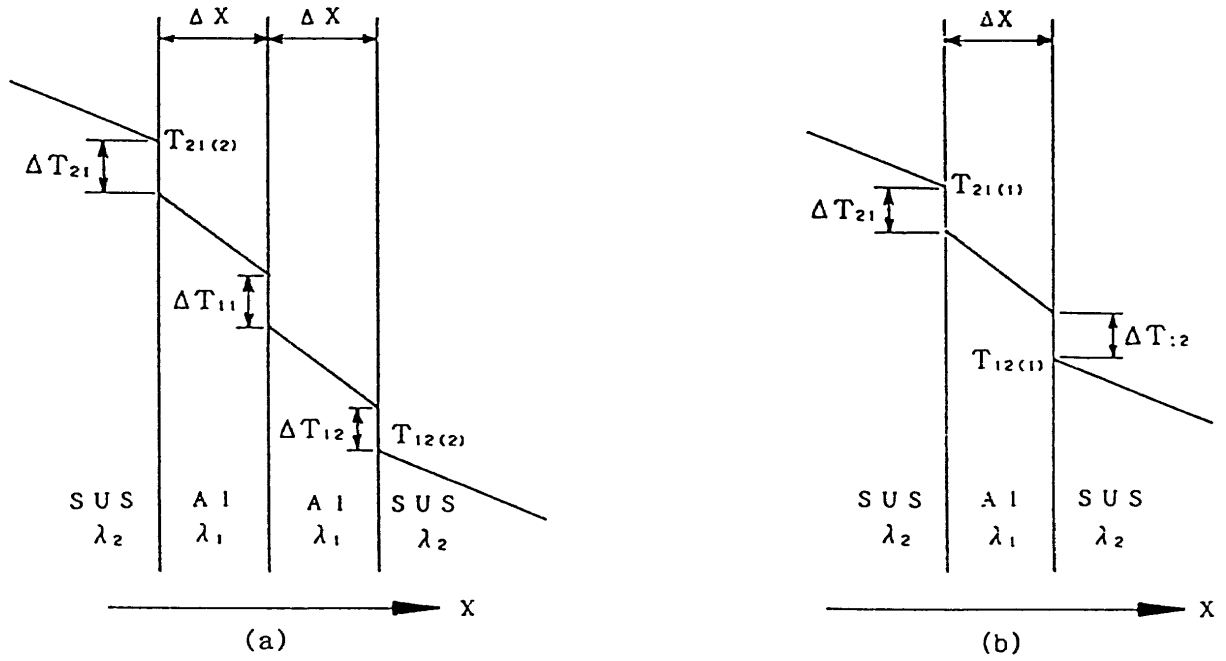**Fig.1 Test Equipment for Ph.1 Test**



(a)

(b)

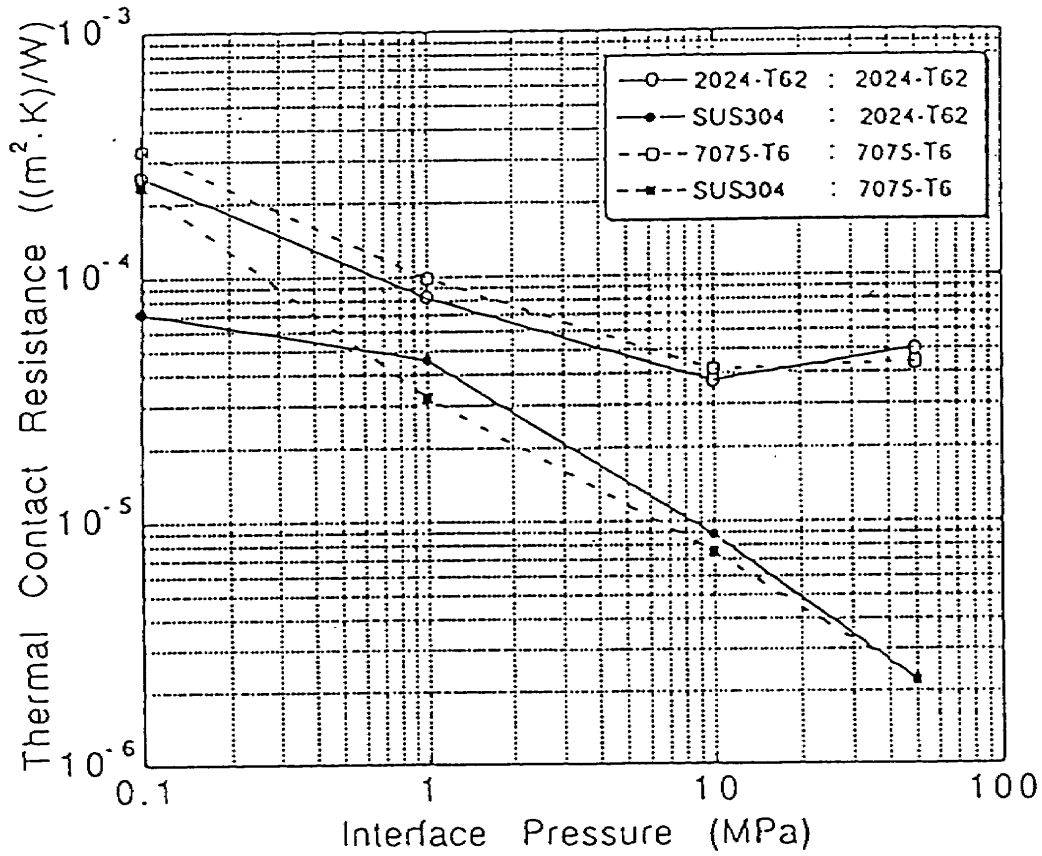**Fig.2 Temperature Distribution Model for Ph.1 Test**

**Fig.3 Relation between Contact Pressure and Contact Thermal Resistance**
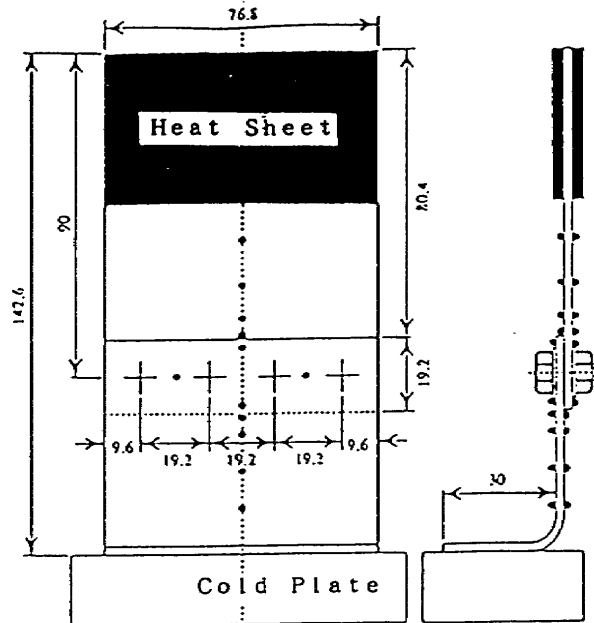


**Fig.4 Test Equipment for Ph.2 Test**
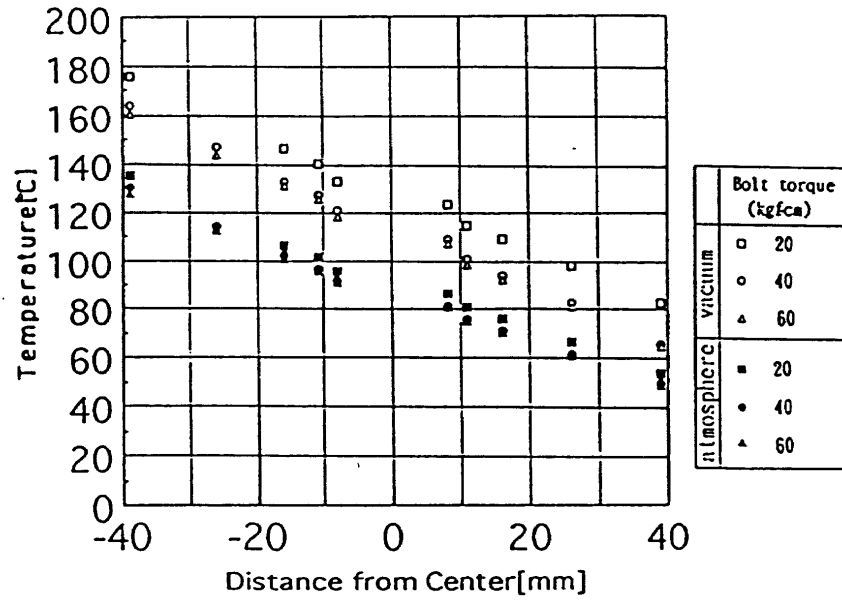
Fig.5 Temperature Distribution along the Heat Flow Direction
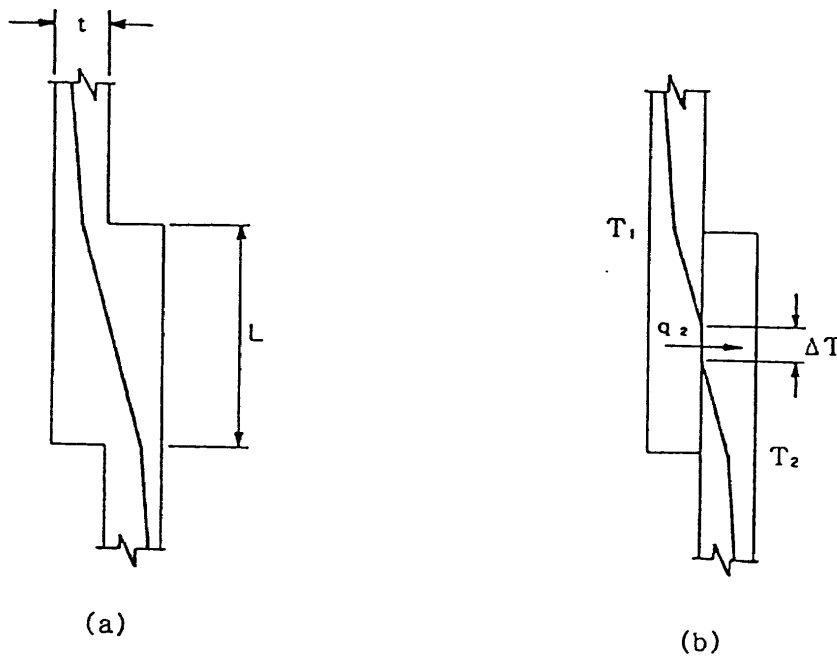
Fig.6 Temperature Distribution Model For Ph.2 Test
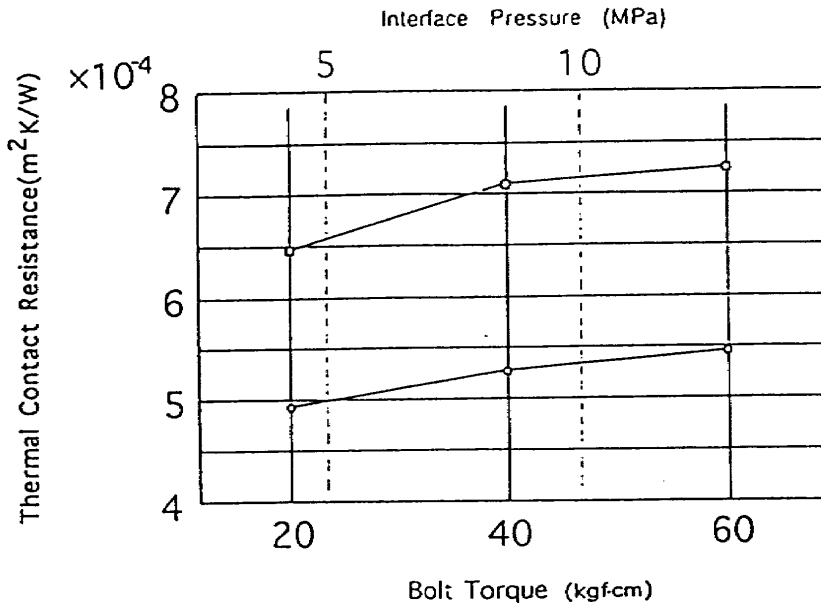
Fig.7 Relation between the Fastening Torque (or Contact Pressure)
and Contact Thermal Resistance

Table 1        Test Piece Geometrics for Ph.3 Test

| test piece type | width mm | lapped length mm | number of fastener | fastening torque | fastener pitch mm |
|---|---|---|---|---|---|
| T 1 | 150 | 30 | 6 x 1 | 40lb.inch | 25 |
| T 2 | 150 | 50 | 6 x 2 | 40lb.inch | 25 |
| r 1 | 150 | 12 | 4 x 1 | 45kgf.cm | 30 |
| r 2 | 150 | 20 | 4 x 1 | 45kgf.cm | 30 |
| r 3 | 150 | 40 | 4 x 2 | 45kgf.cm | 50 |

material:2024,  thickness:2mm,  heater:50x150mm 60Wx2,  coolant:2l/min.

|   | h | fastener |
|---|---|---|
| r 1 | 22mm | 1 row |
| r 2 | 30mm | 1 row |
| r 3 | 50mm | 2 row |

Fig.8   Test pieces for Ph.3 Test

Fig.9 Test equipment for Ph.3 Test

Fig.10- 1 Temperature Distribution along the center line at 30 min.
after the heat start for Ph.3 Test
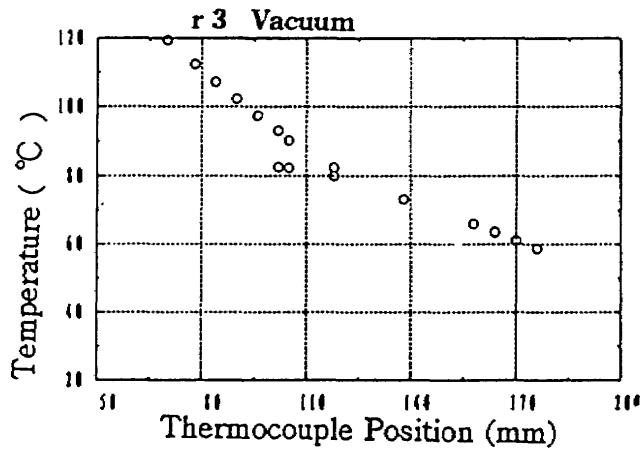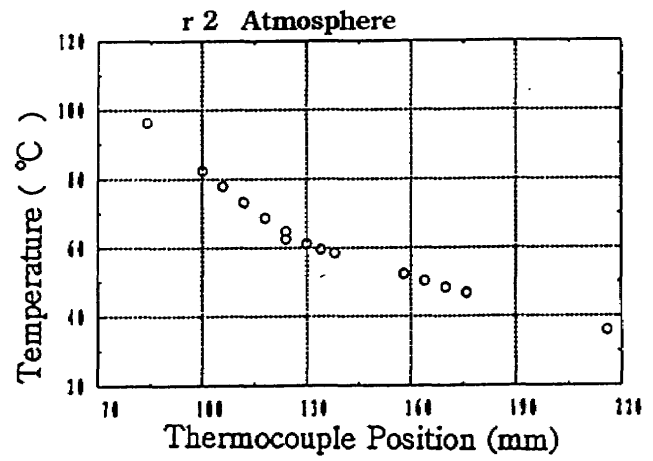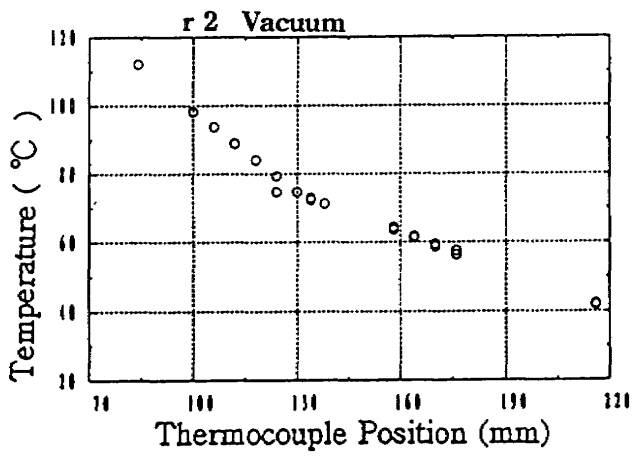
Fig.10- 2 Temperature Distribution along the center line at 30 min.
after the heat start for Ph.3 Test

# 9

# Development of an Interface Program for Coupling Analysis of Thermal Transfer between Fluid and Structure

Yasuhiro FUJIWARA

Aerospace Division

Fuji Heavy Industries,Ltd.

Utsunomiya, Japan

Kunihiko OHTAKE and Yukimitsu YAMAMOTO

National Aerospace Laboratory

Tokyo, Japan

## 1. INTRODUCTION

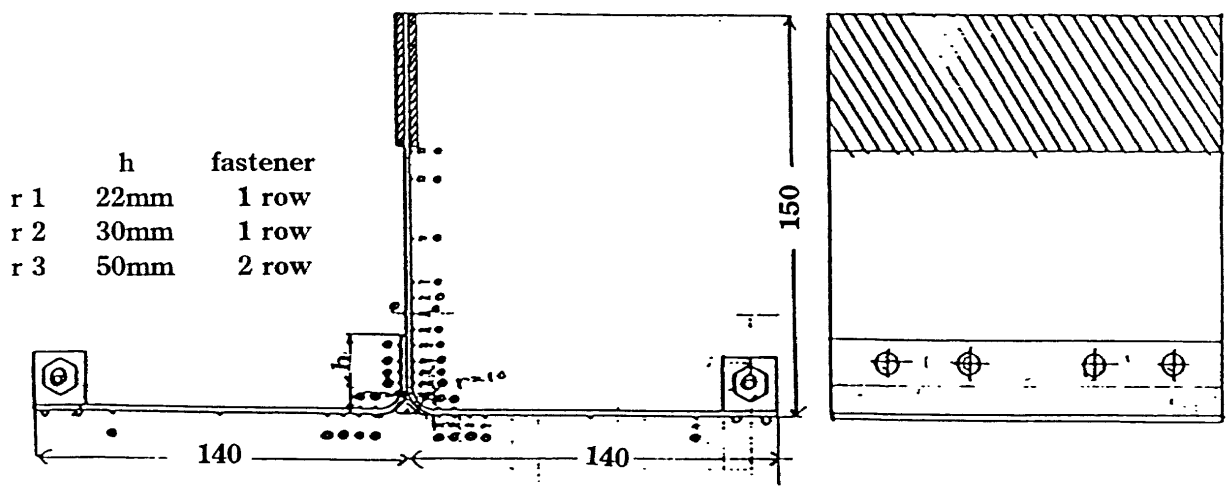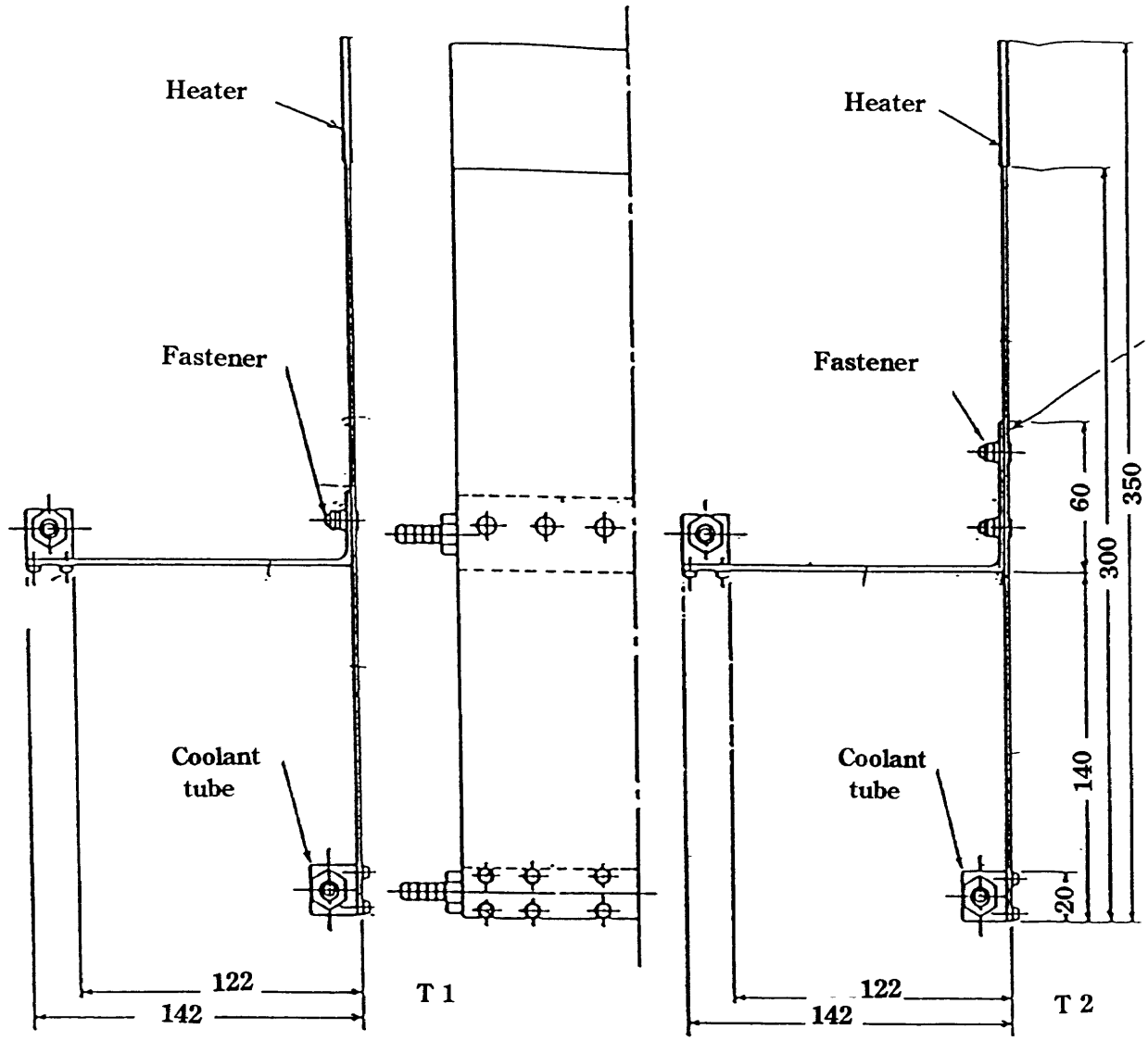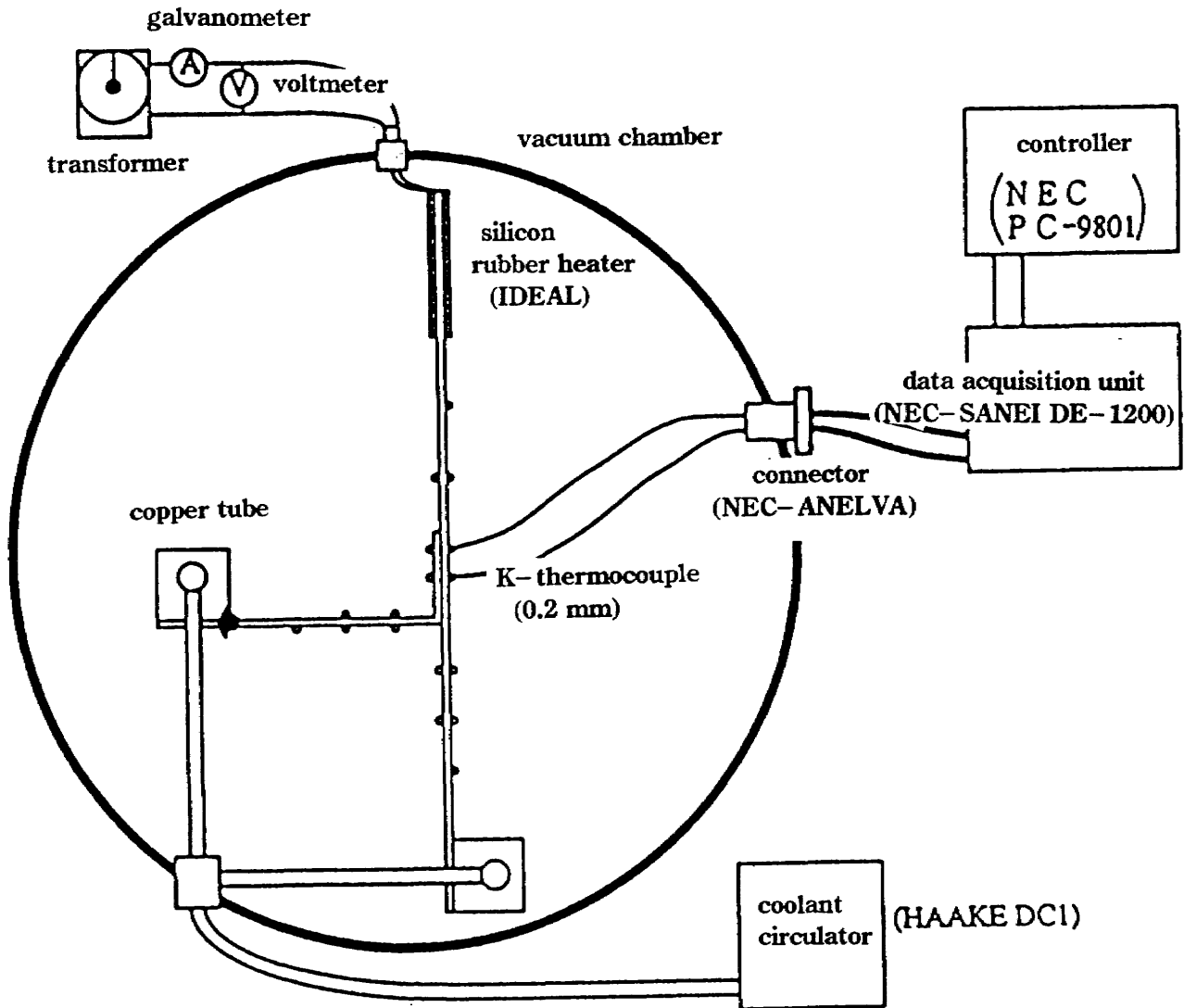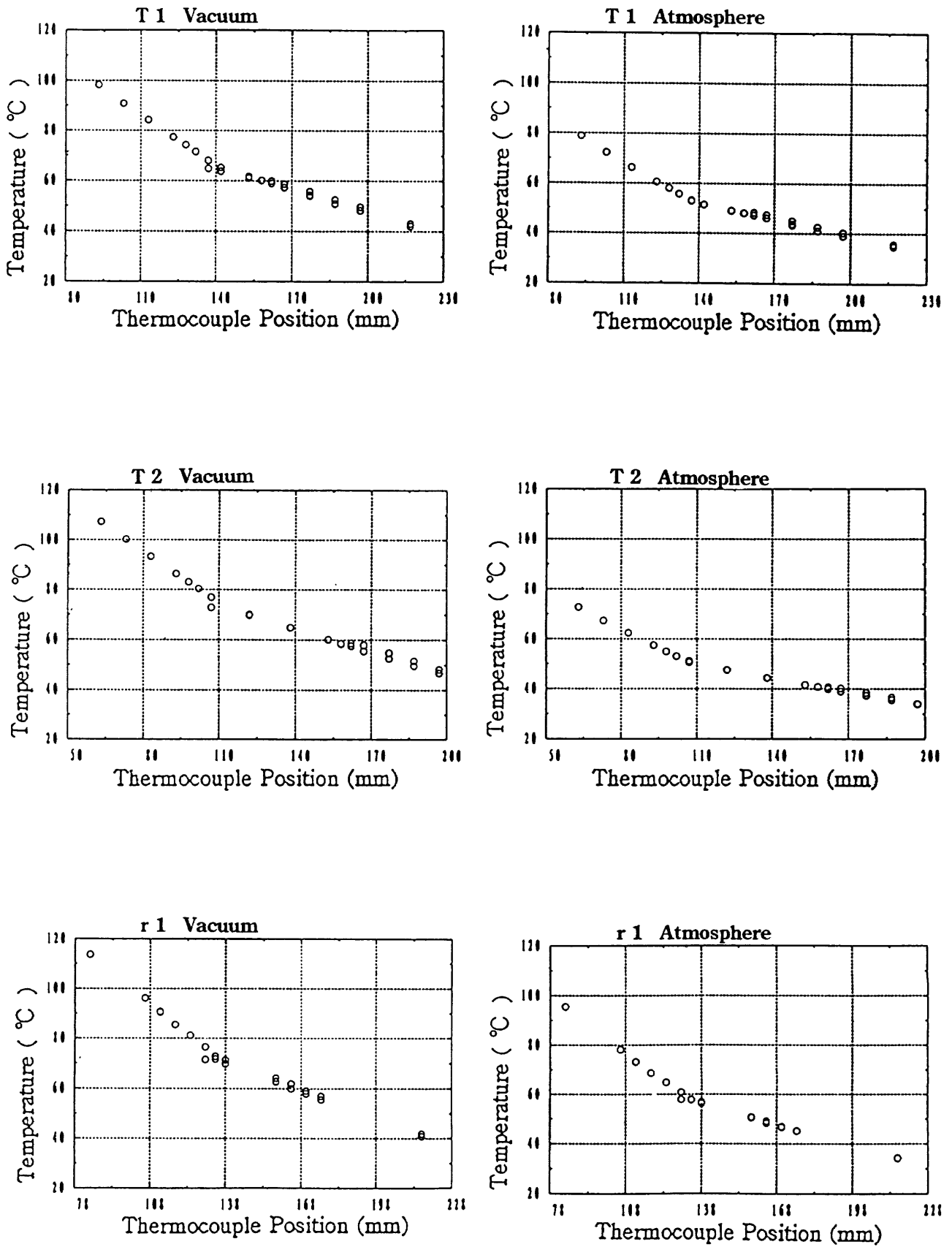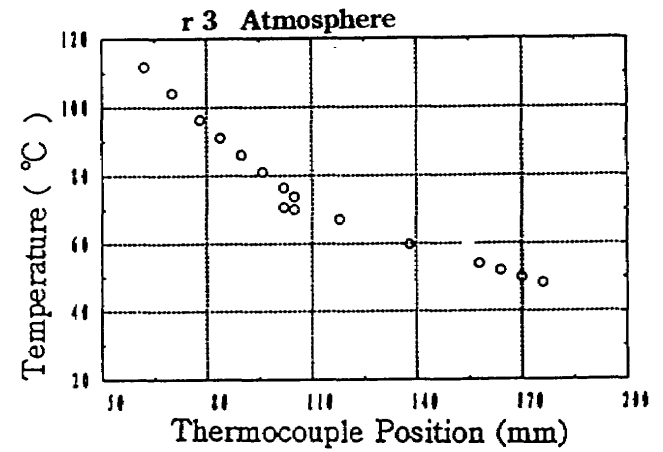In the structural design of SSTs or spacecraft, the prediction of temperature of the structural surface is important. Coupling analysis of thermal transfer between fluid and structure is useful in this prediction. But such a coupling program has not been available commercially.

In the first year of this study, a two-dimensional coupling analysis program was developed for a structural model of the leading edge of a wing.

In the second year, a two-dimensional interface program and control program were developed. These two programs run with the fluid dynamics part of the coupling program developed in the first year, and one of the commercially available structural analysis programs.

In the final year, the transfer method of the interface program was modified. The program has been available to couple analyses between fluid and structure with the different size of boundary meshes each other.

The transfer method of the interface program was designed for extension to three-dimensional coupling analysis in the future.

## 2. METHOD OF DATA TRANSFER

At the boundary between fluid and structure, two types of data are transferred by the interface program. One is heat flux through the boundary from fluid to the structure, and the other is temperature through the boundary from structure to fluid.

Figure 1 shows the method for three-dimensional data transfer. The basic mechanism of the data transfer is that the value of point D is linearly interpolated or extrapolated among the values of three points A, B, C. Then points A, B, C are selected as the nearest three points to point D.

Now, 'V' in Figure 1 is assumed as the value of heat flux, point D is the center of the mass of a boundary element of the structure, and points A, B, and C are the centers of the mass of the cells of the fluid nearest to point D. The heat flux value of these points are $V_D$, $V_A$, $V_B$, and $V_C$. If the plane including points A, B, and C is defined as X-Y plane, the positions of these points are described as $(X_D, Y_D)$, $(X_A, Y_A)$, $(X_B, Y_B)$, and $(X_C, Y_C)$. But, $(X_D, Y_D)$ is the position of point D that is projected on the X-Y plane normally.

The transfer from heat flux $V_A$, $V_B$, and $V_C$ to $V_D$ is

$$V_D = \begin{bmatrix} C_A & C_B & C_C \end{bmatrix} \begin{vmatrix} V_A \\ V_B \\ V_C \end{vmatrix} \tag{1}$$

where $C_A$, $C_B$, and $C_C$ are the coefficients of transfer and the function of position X and Y. If the heat flux around the point is described as

$$V = \begin{bmatrix} X & Y & 1 \end{bmatrix} \begin{vmatrix} C_1 \\ C_2 \\ C_3 \end{vmatrix}. \tag{2}$$

Then, these coefficients $C_1$, $C_2$, and $C_3$ are obtained from the following equation.

$$\begin{vmatrix} C_1 \\ C_2 \\ C_3 \end{vmatrix} = \begin{vmatrix} X_A & Y_A & 1 \\ X_B & Y_B & 1 \\ X_C & Y_C & 1 \end{vmatrix}^{-1} \begin{vmatrix} V_A \\ V_B \\ V_C \end{vmatrix} \tag{3}$$

According to equations (2), and (3), coefficients $C_A$, $C_B$, and $C_C$ in equation (1), which transfer the heat flux from fluid to structure, are obtained from the following equation.

$$\begin{bmatrix} C_A & C_B & C_C \end{bmatrix} = \begin{bmatrix} X_D & Y_D & 1 \end{bmatrix} \begin{vmatrix} X_A & Y_A & 1 \\ X_B & Y_B & 1 \\ X_C & Y_C & 1 \end{vmatrix}^{-1} \tag{4}$$

Similarly to the above formulation about heat flux, if 'V' in Figure 1 is assumed as the value of temperature, the coefficients $C_A$, $C_B$, and $C_C$ which transfer the temperature from structure to fluid, are obtained from equation (4).

Point D is the center of the mass of boundary cells of the fluid, and points A, B, and C are the centers of the mass of the element of the structure nearest to point D. And the temperature value of these points are $V_D$, $V_A$, $V_B$, and $V_C$.

## 3. SYSTEM OF COUPLING ANALYSIS

The system of coupling analysis consists of a fluid analysis program, a structural analysis program, interface programs, a control program, and a transfer coefficients generation program. Figure 2 shows the flow-chart of the system.

The fluid analysis program is 'HYPER-2d' which was developed in the first step of this study. The structural analysis program is 'MSC/NASTRAN-PWS' which is one of the commercially available programs.

In each step of execution of 'HYPER-2d', the temperature of the surface of the structure is assumed to be constant. And in each step of execution of 'MSC/NASTRAN-PWS', the heat flux from the fluid is assumed to be constant.

Interface programs 'HT2A3' and 'HT2B3' have been created in FORTRAN77. 'HT2A3' transfers the heat flux from fluid to structure, and 'HT2B3' transfers the temperature from structure to fluid. Figures 3 and 4 show these flow-charts.

The control program 'HEAD3' has been created in C-Shell. 'MSC/NASTRAN-PWS' exists on one engineering-work-station(EWS), and 'HYPER-2d', 'HT2A3', 'HT2B3' and 'HEAD3' exist on the other EWS. These two EWS are connected on the network. 'HEAD3' controls the loop of executions of 'HYPER-2d', 'HT2A3', 'MSC/NASTRAN-PWS', and 'HT2B3'.

The transfer coefficients generation program 'HT2C3' is created in FORTRAN77. 'HT2C3' reads the point position data on both boundary of fluid and structure, and generates the transfer coefficients by using equation (4). Figure 5 shows the flow-chart of 'HT2C3'.

## 4. EXAMPLE ANALYSIS

Two example analyses, (a) and (b), were executed to compare the data transfer. The difference between the two models is the meshes between the cells of the fluid and the elements of structure on the boundary.

Figure 6 shows two models. Figure 7 shows the result of the analysis. The difference in temperature was 0.11K at the end.

Conditions:

Mach number: 6.47, structure: a stainless steal column of 3.81 cm radius outside and 2.54 cm radius inside; initial temperature: 294.44K, time step: 0.1sec; end time: 2.0sec, meshes on fluid: 25 × 60, meshes on structure: (a);25× 6,(b);20× 6, number of convergence loops in a step of 'HYPER-2d': 300

## 5. CONCLUSIONS

The transfer method of the interface program was designed for extension to three-dimensional coupling analysis of fluid in the future. The method is also available to couple analyses between fluid and structure with the different size of boundary meshes each other.

A two-dimensional interface program was developed using the above method, and demonstrated the effectiveness of the method.

A three-dimensional coupling analysis system will be developed by using 'HYPER-3d' on the super-computer and the method designed here.

## REFERENCES

1) Y.Yamamoto, et al., "Coupling Analysis of Aerodynamically Heat and Structural Thermal Transfer", NAL J-93012, pp.145-162, Oct.1993.

2) P.Dechaumphai, E.A.Thornton, and A.R.Wieting, "Flow-Thermal-Structural Study of Aerodynamically Heated Leading Edges.", J. spacecraft Vol.26,No.4, pp201-209, 1989.

3) K.Ohtake, et al., "Management System for Coupling Analysis of Aerodynamically Heat and Structural Thermal Transfer", NAL J94004, pp.55-123, Oct.1994.
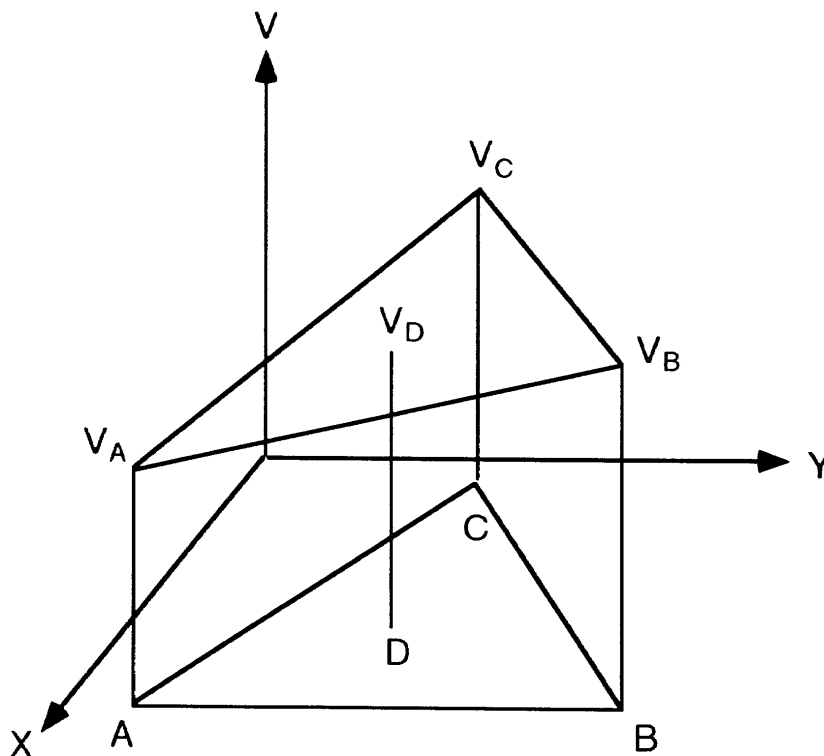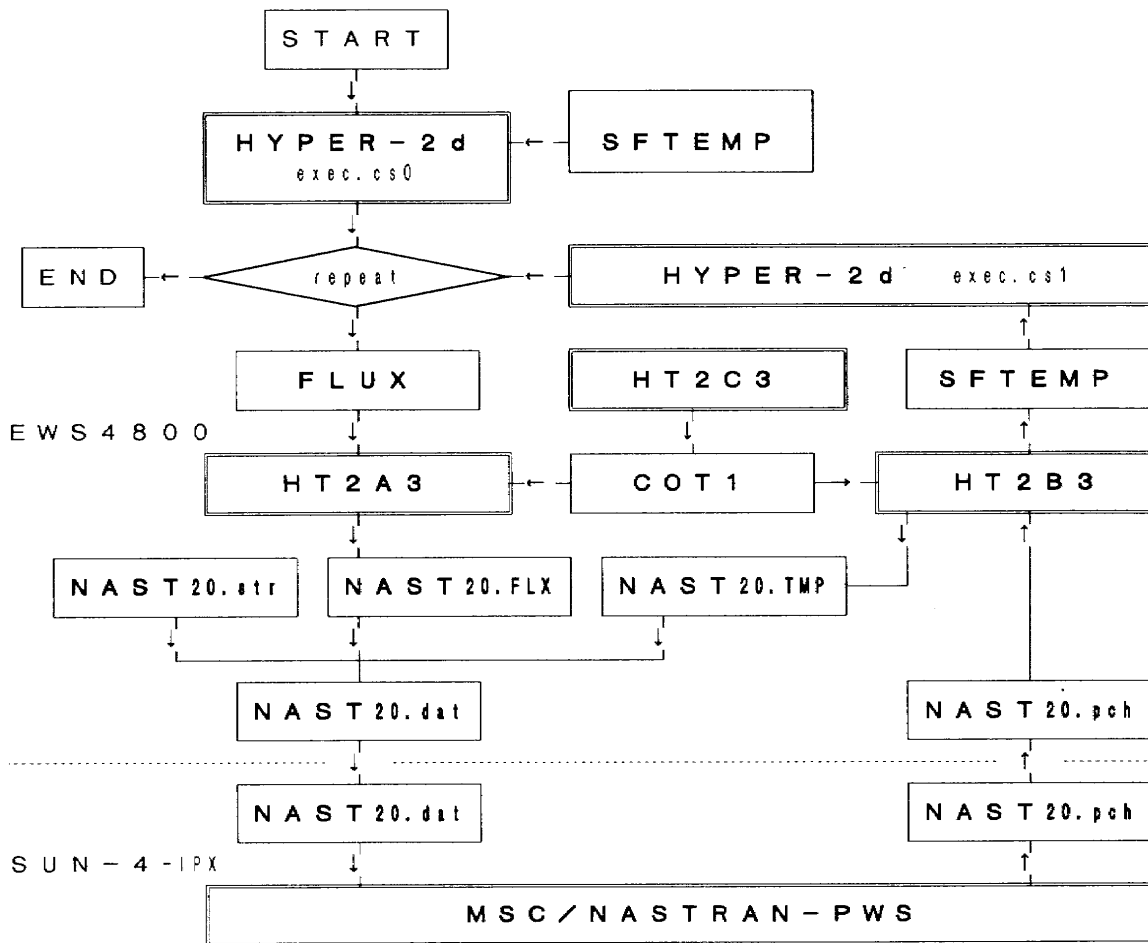


Figure 1    Method of data transfer

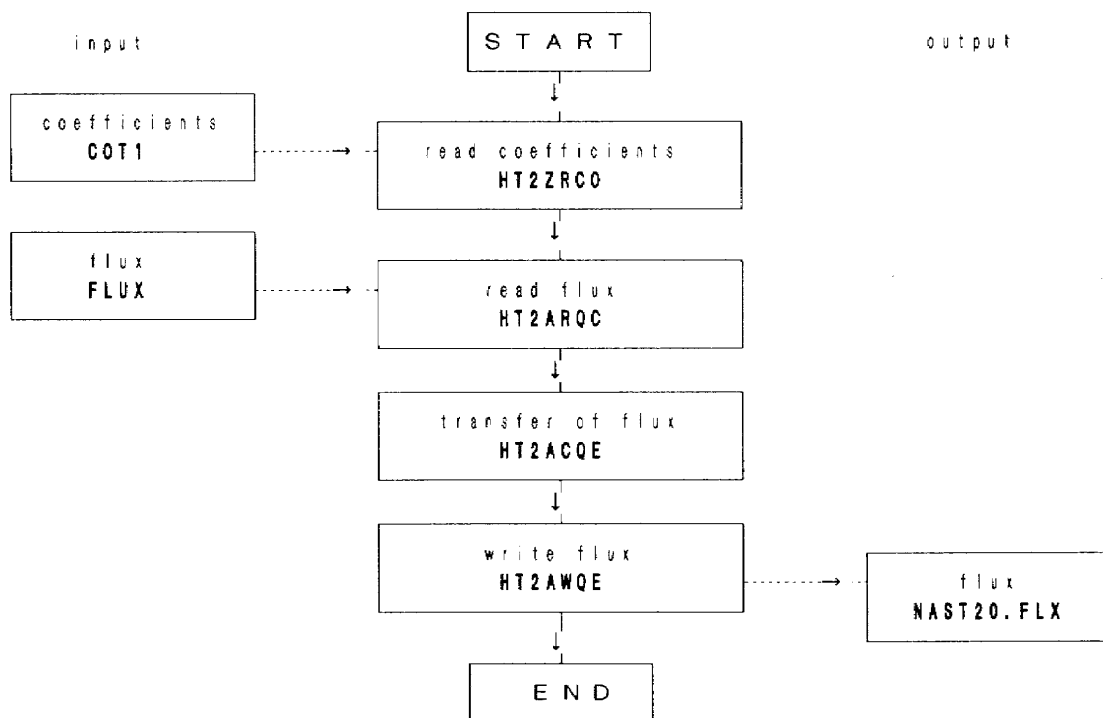Figure 2   Flow-chart of the management sysytem for the two-dimensional coupling analysis



Figure 3   Flow-chart of the program(HT2A3) which transfers the heat flux from fluid to structure
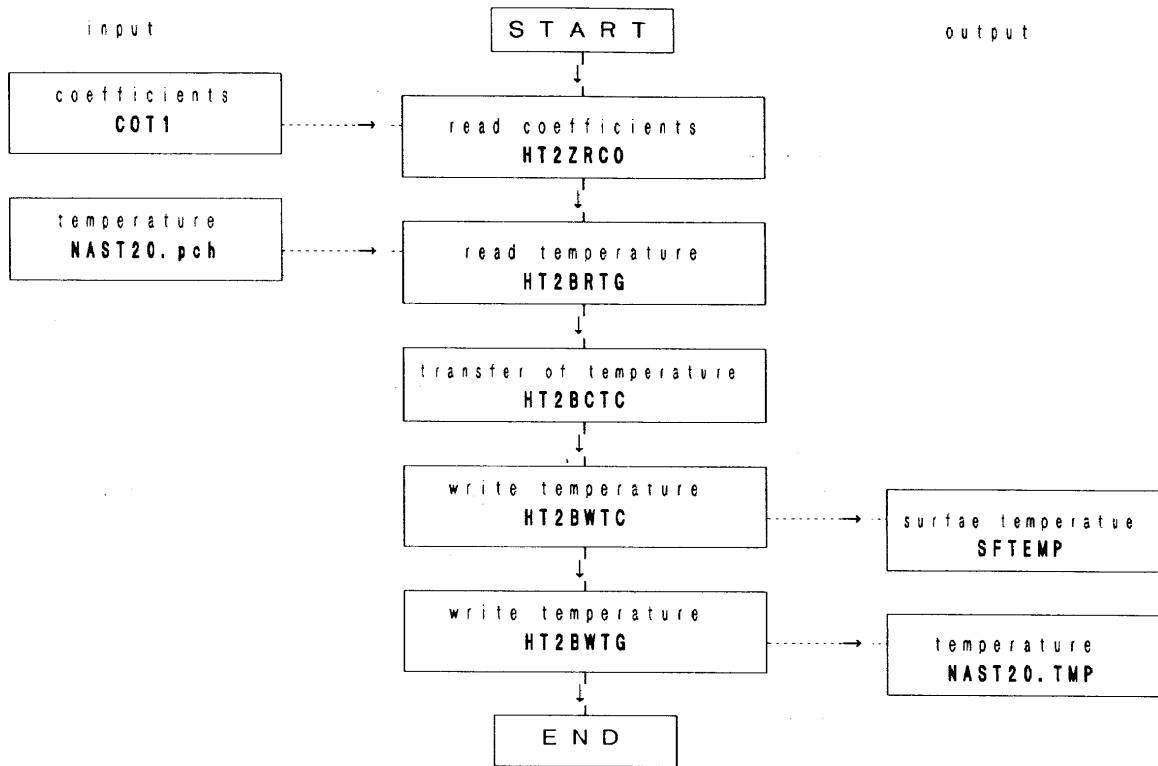
input                              S T A R T                        output

```
┌──────────────────┐            ┌──────────────────────┐
│  coefficients    │ ········→  │  read coefficients   │
│     COT1         │            │     HT2ZRCO          │
└──────────────────┘            └──────────────────────┘
                                          ↓
┌──────────────────┐            ┌──────────────────────┐
│  temperature     │ ········→  │  read temperature    │
│  NAST20.pch      │            │     HT2BRTG          │
└──────────────────┘            └──────────────────────┘
                                          ↓
                                ┌──────────────────────┐
                                │ transfer of temperature │
                                │     HT2BCTC          │
                                └──────────────────────┘
                                          ↓
                                ┌──────────────────────┐     ┌──────────────────┐
                                │  write temperature   │ ··→ │ surfae temperatue │
                                │     HT2BWTC          │     │     SFTEMP        │
                                └──────────────────────┘     └──────────────────┘
                                          ↓
                                ┌──────────────────────┐     ┌──────────────────┐
                                │  write temperature   │ ··→ │  temperature      │
                                │     HT2BWTG          │     │  NAST20.TMP       │
                                └──────────────────────┘     └──────────────────┘
                                          ↓
                                     E N D
```

**Figure 4   Flow-chart of the program which transfers the temperature from structure to fluid**

input                              S T A R T                        output

```
┌──────────────────────┐         ┌──────────────────────┐
│ point No. of surface │ ·····→  │   read point No.     │
│     NUMSUF           │         │     HT2CRNS          │
└──────────────────────┘         └──────────────────────┘
                                           ↓
┌──────────────────────┐         ┌──────────────────────┐
│ position of the point│ ·····→  │   read position      │
│ on the fluid surface │         │     HT2CRCC          │
│     KUSUGP           │         └──────────────────────┘
└──────────────────────┘                   ↓
┌──────────────────────┐         ┌──────────────────────┐
│ position of the point│ ·····→  │   read position      │
│ on the structure     │         │     HT2CRGC          │
│     NASTGR           │         └──────────────────────┘
└──────────────────────┘                   ↓
                    ┌──────────────────────────────────────────┐
                    │ calculate each center of the mass on fluid │
                    │              HT2CCCC                       │
                    └──────────────────────────────────────────┘
                                           ↓
                    ┌──────────────────────────────────────────┐
                    │ calculate each center of the mass on structure │
                    │              HT2CCGC                       │
                    └──────────────────────────────────────────┘
                                           ↓
                    ┌──────────────────────────────────────────┐
                    │ selec points which close to each center   │
                    │              HT2CCCG                       │
                    └──────────────────────────────────────────┘
                                           ↓
                                ┌──────────────────────┐
                                │ generate coefficients │
                                │     HT2CCCO          │
                                └──────────────────────┘
                                           ↓
                                ┌──────────────────────┐     ┌──────────────────┐
                                │  write coefficients  │ ··→ │  coefficients     │
                                │     HT2CWCO          │     │     COT1          │
                                └──────────────────────┘     └──────────────────┘
                                           ↓
                                     E N D
```
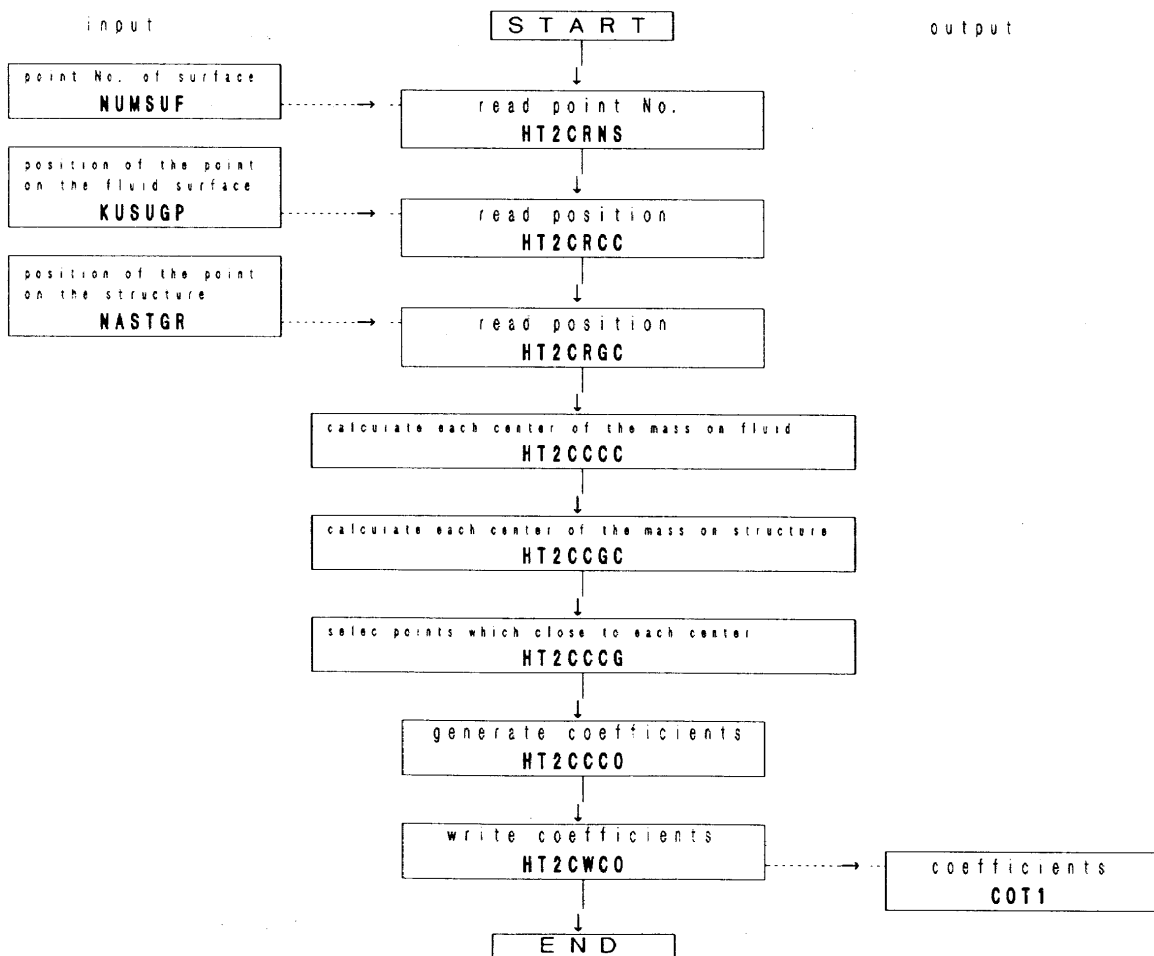
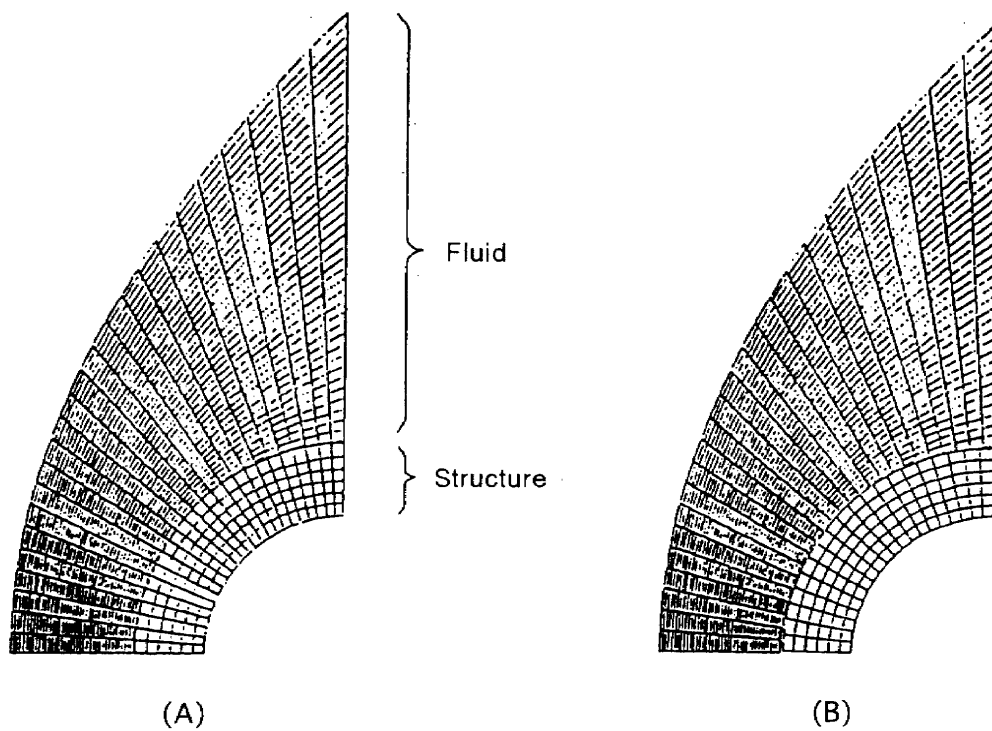**Figure 5   Flow-chart of the program which generates the transfer coefficients**
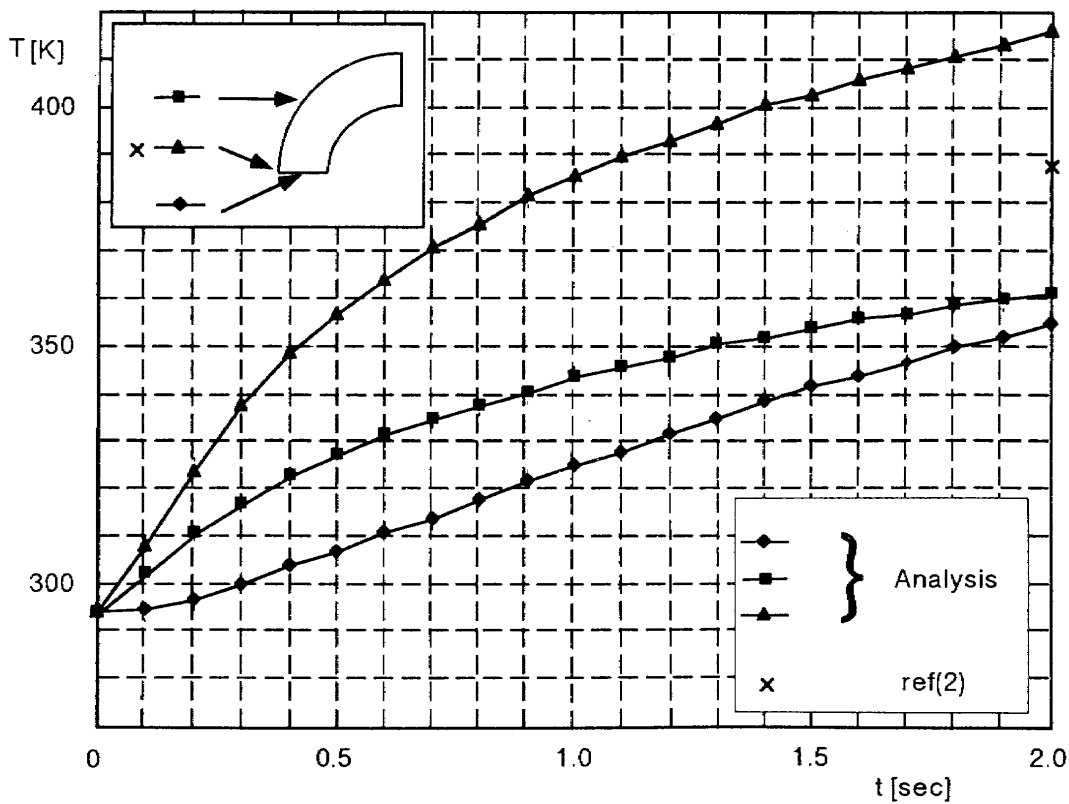
Figure 6    Analysis model



Figure 7    Time history of temperature

# 10

# Tensile Strength of Light Metallic Materials for SST Structures at Elevated Temperatures and After Thermal Aging

Toshiyuki SHIMOKAWA, Yasumasa HAMAGUCHI, Yoshiaki KAKUTA,
and Hisaya KATOH, National Aerospace Laboratory,
Tomio SANDA, Kawasaki Heavy Industries, Yasuhiro FUJIWARA, Fuji
Heavy Industries, and Hiroshi MIZUNO, Mitsubishi Heavy Industries.

**Key Words:** Light metallic materials, Supersonic transport, Tensile strength,
Elevated temperature, Thermal aging.

## 1. Introduction

The Concorde, a supersonic transport developed by the collaboration of France and the United Kingdom, commenced commercial flight in January, 1976, and has continued in service for approximately 20 years. Various kinds of sciences and technologies surrounding aircraft and aircraft industries have made great progress since the development of this aircraft. Moreover, the demand for aerial-transport has become much greater than in the days of the Concorde development. Furthermore, since the Concorde is expected to be retired from commercial flight in approximately ten years, world-wide interest in developing a Concorde successor has grown.

To participate in the future international development of the next generation supersonic transport (SST), aeronautical industries in our country, with the Society of Japanese Aerospace Companies (SJAC) and the Japan Aircraft Corporation (JADC) as leading organizations, are undertaking various kinds of surveys and investigations. In such an environment this study is performed jointly with the National Aerospace Laboratory, Kawasaki Heavy Industries, Fuji Heavy Industries, and Mitsubishi Heavy Industries.

SST's are subjected to high temperatures over a long period of time through aerodynamic heating. Accordingly, it is a fundamental problem to evaluate the effect of thermal aging on the strength of SST structural materials. On this account, candidate materials should be actually exposed to long-term high temperatures and the loss of strength should be investigated.

This study investigates the strength of six kinds of candidate metallic materials for SST structures at room and elevated temperatures before and after thermal aging. The results obtained are presented and discussed. Moreover, the possibility of accelerated environmental-simulation tests to evaluate the effect of thermal aging in a shorter time is discussed. There are no published research reports which systematically clarify the strength deterioration of the relatively new light metallic materials and thermal aging conditions tested in this paper.

## 2. Materials and Test Procedure

### 2.1 Materials
The materials tested are the following six kinds of light metallic materials.
   (1) 2618-T61 aluminum alloy: an aluminum alloy for high temperature use, identical to RR.58 or AU2GN used in the Concorde and called a Concorde material CM.001[1], is the base line material of this study.

(2) 2519-T87 aluminum alloy.

(3) 2124MMC-T4: a particulate metal matrix composite material, $Si_C$ particle reinforcement (17% wt.).

(4) 6013-T6 aluminum alloy.

(5) 7150-T77 aluminum alloy.

(6) AL-905XL: an ODS (Oxide-Dispersed Strengthening) alloy produced by a mechanical alloying method. An aluminum base material including $M_g$ and $L_j$ aimed at increasing rigidity and strength and lowering density.

## 2.2 Test Procedure

### 2.2.1 Aging Temperatures and Time, and Test Temperatures for Static Strength

120°C and 180°C were selected as the aging temperatures. This range roughly corresponds to that of Mach number 2.2-2.5. Two thermal aging times were selected, 5,000 and 10,000 hours. Room temperature (RT: 23°C), 120°C, and 180°C were selected as the temperatures used for tensile tests before and after thermal aging.

### 2.2.2 Test approach

Specimen configuration follows the JIS-13B form. Thermal aging was conducted by exposing test pieces in two air circulating ovens maintaining temperatures of 120 °C and 180 °C. Several times during aging these ovens experienced power suspensions. However, the effect of these breakdowns was ignored in this study. The number of test results are normally five in each case, though there are a few cases consisting of four test results for reasons of test pieces or tests.

## 3. Test Results and Discussion

Figure 1 indicates the relationship between tensile strength (average value) and test temperature as a parameter of thermal aging condition. This figure was transformed into the relationship between tensile strength and aging time and shown in Fig. 2.

Contents deduced from these figures and their evaluation are as follows:

(1) The tendencies of strength change indicated in 2618-T61, 2519-T87, and 6013-T6 are similar. In other words, there is practically no strength degradation with 120°C aging, though a trivial degradation for 2519-T87 is found. With 180°C aging, tensile strength deteriorated enormously in the first 5,000 hours and dropped slightly during the interval of 5,000 to 10,000 hours. The strength drop is almost saturated in the first 5,000 hours. Furthermore, the tensile strengths of 2618-T61 and 2519-T87 are close to each other. The tensile strength of 6013-T6 is comparatively lower than these values. If the three materials are arranged in favorable order, this order is 2618-T61, 2519-T87, and 6013-T6.

(2) The tendency of strength deterioration in 2124MMC-T4 is similar to that of 7150-T77. Their strength at room temperature is high and shows a relatively large drop at elevated temperature. The strength reduction through thermal aging also appeared even at 120°C. With 180°C aging the strength reduction nearly saturates in 5,000 hours.

(3) In case of AL-905XL, though the strength at room temperature is very high, it becomes lower at the higher level of test temperature. The effect of 120°C aging on the strength is very small. After

180°C aging the strength at room temperature deteriorates slightly; however, the strength reduction is very small at 180°C. Generally the aging effect on the tensile strength of this material is very small.

(4) The difference in strength after thermal aging of 5,000 and 10,000 hours is small for all six materials. The materials of which aging effect is large at 120°C or 180°C show the aging effect even after 5000 hours and this effect is confirmed by the test results at room temperature after thermal aging.

(5) If the most relevant material is selected for use at less than 120°C, 2618-T61 or the Concorde material CM.001 is still the best among the six materials tested in this study.

(6) Judging from the test results for 2124MMC-T4 and 7150-T77, it is apparently impossible to predict the residual strength after thermal aging only through tensile tests at elevated temperatures without any thermal aging.

(7) Figure 2 indicates that the difference between the strengths at room temperature and aging temperature is very close in every aging case. This is shown by the difference between a broken line and a solid line in this figure. However, with AL-905XL and 7150-T77 the difference between the strengths of non-aged materials at room temperature and 180°C is slightly larger than the value estimated by this principle.

(8) From the results described above, if it can be assumed that the aging effect at 120°C or 180°C on tensile strength almost saturates between 5,000 and 10,000 hours, the strength after any aging longer than 10,000 hours will be at least higher than that predicted by a linear extension line passing through two values of strength at 5,000 and 10,000 hours. This fact provides a possibility of developing a method for accelerated environmental-simulation tests. However, for 2124MMC-T4 and 7150-T77 at 120°C aging it is difficult to consider that the strength reaches saturation by 10,000 hours. Actual aging time of up to about 20,000 hours is thought necessary, which is as long as that for the Concorde material CM.001[1]

## 4. Concluding Remarks

(1) For application to the SST structures, no other material is found to be superior to the base line material 2618-T61, which is identical to the Concorde material CM.001.
(2) On the basis of the test results of tensile strength vs. aging time, there is a possibility of developing a method for accelerated environmental-simulation tests.

**Reference**
1) N.F. Harpur. "Structural Development of the Concorde," Aircraft Engineering, March 1968. pp. 18-30.
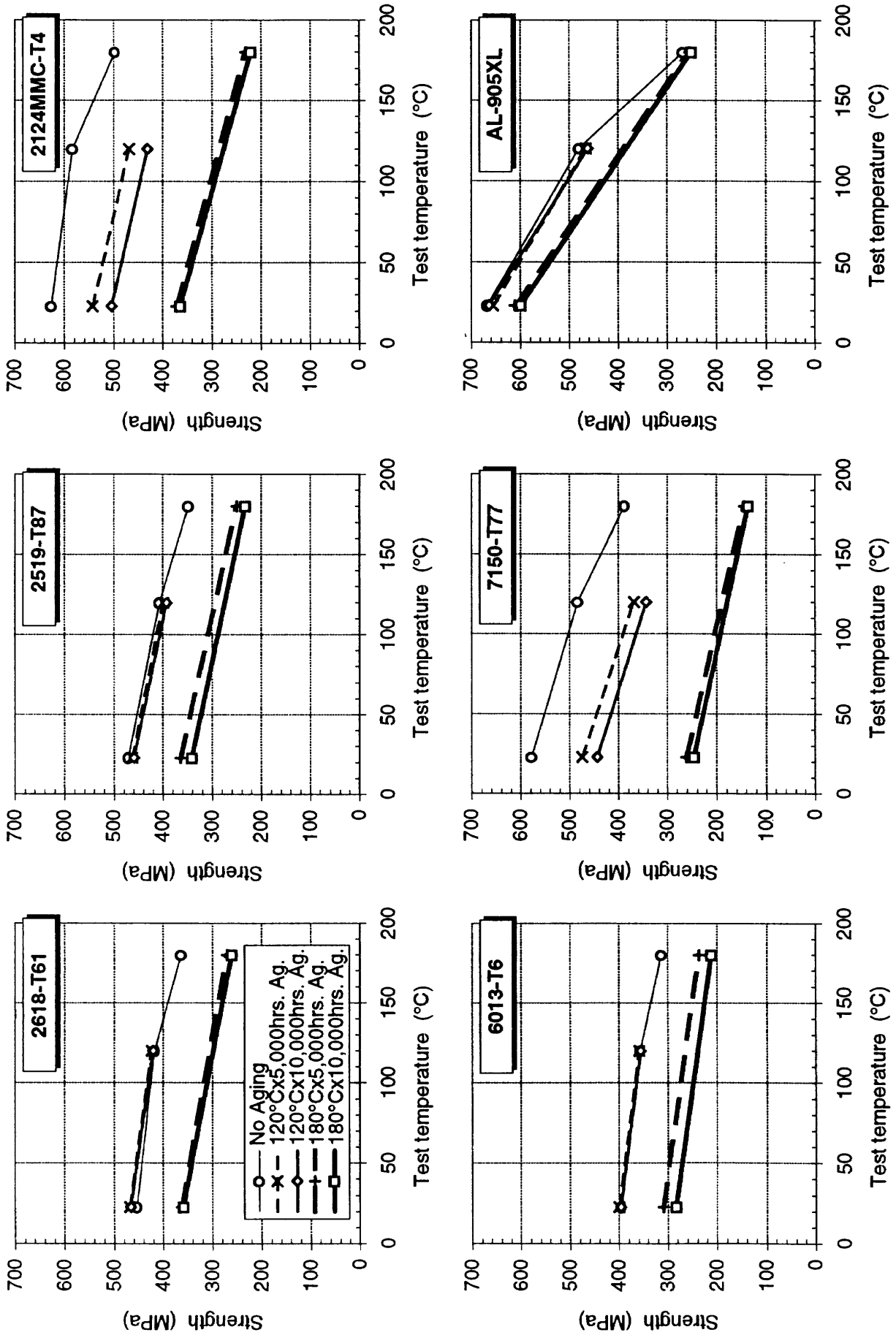
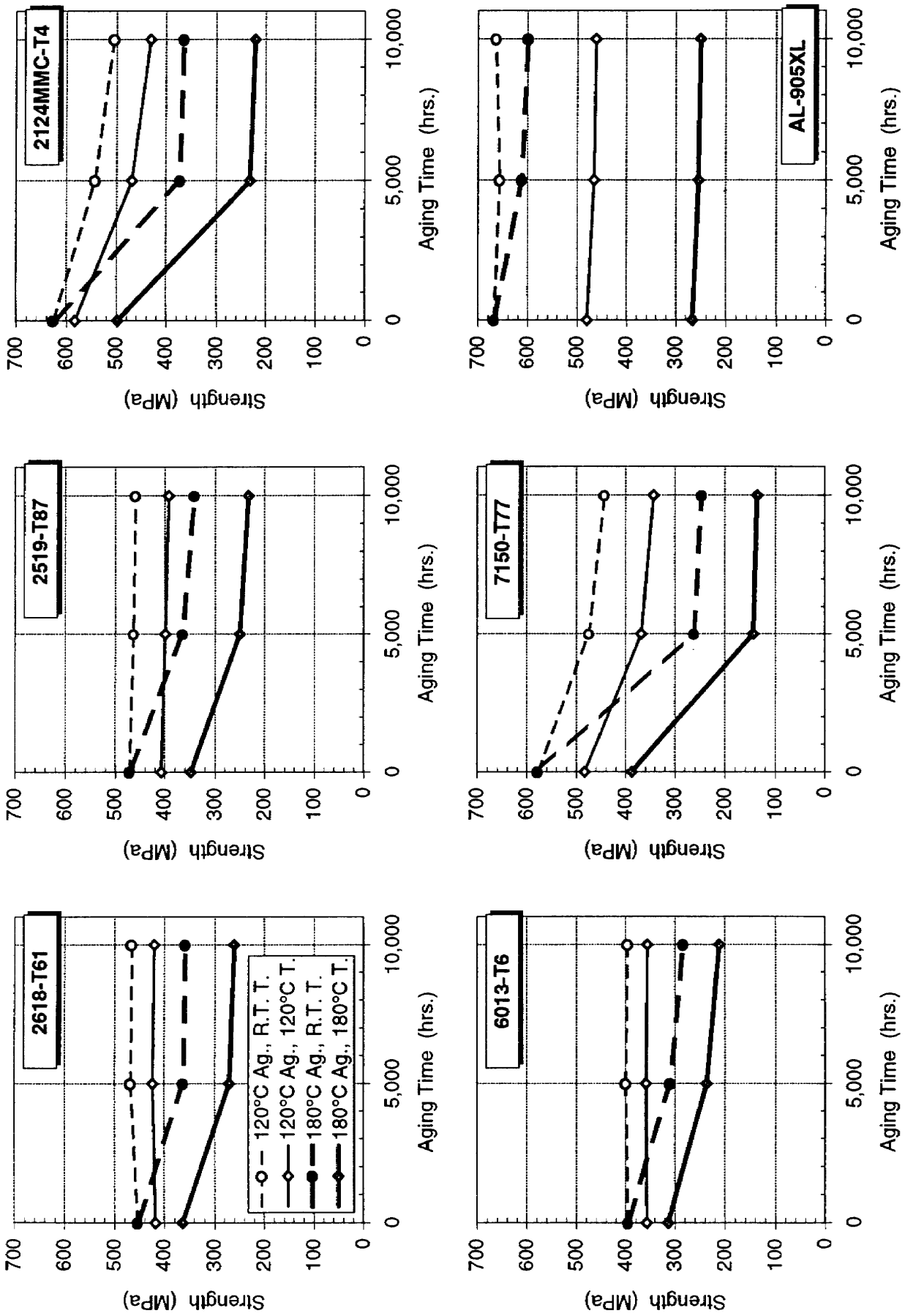Figure 1　Averaged Tensile Strength versus Test Temperature for Six Kinds of Metallic Materials

Figure 2　Averaged Tensile Strength versus Thermal-aging Time for Six Kinds of Metallic Materials

# 11

# Fatigue Characterization of Fiber/Metal Laminates

Y. TOI and Y. FUJIWARA

Aerospace Division

Fuji Heavy Industries, Ltd.

Utsunomiya, Japan

## ABSTRACT

High performance aircraft in the future need more damage tolerant materials and optimized designs. In SSTs, the prevention of lethal rapid decompression in high altitude operations is one of the issues for the structural design of the fuselage. In meeting this requirement, fiber/metal laminates are considered as one of the candidates. Fiber/metal laminates show the attractive feature of slow crack growth. So far, one problem for structural designers in the application of fiber/metal laminates has been that the estimation of crack growth is too complex and has limited generality. A new simple approach is proposed with coupon test results with Glares. Assuming a monolithic thickness and that the surface cracks go through the thickness, the modified stress intensity factor ($\Delta K_{mod}$) is introduced with the basic stress intensity factor ($\Delta K$) multiplied by the modification factor ($\beta_{fb}$). The modification factor $\beta_{fb}$ can be defined by just the crack size. The current analytical practice for aluminum alloys is effective for fiber/metal laminates with $\Delta K_{mod}$. This approach is a practical way to understand the performance limit of fiber/metal laminates and is effective in the development of new types of fiber/metal laminates.

## 1. INTRODUCTION

One of the issues in the structural design of the SST fuselages is the prevention of lethal rapid decompression in high altitude operations. The problems of multi-site cracks in the current aging transports will be more critical in SSTs. Sudden link-ups of small cracks and the isolations by flapping mechanism may be accepted in structural design, but should be avoided in view of the medical dangers of rapid decompression. In meeting this requirement, the high fatigue resistance of fiber/metal laminates is very attractive and fiber/metal laminates are considered to be one of the candidates for the next generation SST fuselage.

Fiber/metal laminates consist of alternating layers of thin metal sheets and fiber reinforced plastic sheets. Through extensive development studies by Delft University, Structural Laminates Company and other researchers, aircraft applications for the production parts of the secondary structures have been started and evaluation tests for the primary structures are being conducted now.

The crack growth rates in fiber/metal laminates are much slower than in conventional aluminum alloys. The basic mechanism of this slow crack growth is explained by 'fiber bridging' at the crack tip. Local delaminations between metal sheets and fiber layers or delaminations in fiber layers around the crack tips relieve the stress concentration of fibers. Shear deformation of the adhesive between metals and fibers also relieve the fiber stresses. The crack growth depends on the balance of strength and stiffness between fibers and adhesives. Schijve[1] explained the basic mechanism well in his report. Marissen[2] developed a break down analysis model to describe the process of crack growth in fiber/metal laminates (for ARALL Laminates).

So far, one engineering drawback in the application of fiber/metal laminates has been that the mechanism of the fiber bridging is too complex and the properties show limited generality. The purpose of this study is to develop a simpler and more practical estimation method for the crack growth of fiber/metal laminates. Crack propagation tests have been conducted with Glares, which is one of the commercially available fiber/metal laminates from Structural Laminates Company. Through the evaluation of the test results, a simple empirical crack growth model has been derived.

## 2. CRACK PROPAGATION TESTS

### 2.1 TEST SPECIMENS AND PROCEDURE

Glare is one of the commercially available types of fiber/metal laminates made by Structural Laminates Company. It consists of 2024-T3 aluminum alloy sheets and fiberglass tapes. Fiberglass layers are not post-stretched.

All test items are summarized in Table 1. In the crack propagation tests, the center cracked tension specimens made of four types of Glares were tested with four levels of constant amplitude cyclic loads at room temperature. Two types of initial starter notches are prepared at the center hole; one is the through-saw cut and the other is the corner-saw cut (one surface only). The size of the saw cuts was about 1mm to 2mm.

One multiple-site-cracks specimen which had no initial starter notches was also tested at the lowest stress level. The stress ratio was 0.05, and the cyclic loading speed was 5Hz in all tests. Residual strength tests were carried out for some specimens subsequent to the crack propagation tests.

All specimens had the same shape as shown in Fig. 1. The tests with the specimens with corner cracks and all Glare2 were carried out at Yokohama National University and the others at Fuji Heavy Industries. The crack length on both sides of the metal surfaces was measured by magnifying glasses.

See Fig.2 for the test set-up condition.

## 2.2 TEST RESULTS

An example of test results (a-N curve) is shown in Fig.3. Even when the crack length became longer, the crack growth rate did not rapidly increase. In some cases, crack growth rates looked constant and in other cases seemed to slow down.

The condition of the delamination and the broken fibers in typical specimens was examined by chemical etching (Fig.4). The results of etching show that major delaminations exist between the adhesive layers and the fiberglass layers. The cracks on the adhesive layer next to the surface aluminum layer reaches the crack tips of the surface. But most of the fibers look intact. Inside metal sheets have cracks which almost reach the surface crack tips. Delaminations in the fiberglass layers are not clearly found.

In the corner crack tests, the visible cracks at the reverse side of the starter notch side were nucleated comparatively earlier and followed the reverse side cracks. Difference in crack propagation rates da/dN between the through-saw cuts and the corner-saw cuts was sufficiently small(Fig.5).

The multiple-site crack propagation test was carried out until all of the cracks were linked up on the surface. The cracks were nucleated at both edges of all holes.

Nucleation was earlier than expected, but crack propagation was slow and not accelerated until the end of the test. After the surface cracks linked up, the specimen did not break away, and the remaining fiber layers sustained the loads. An example a-N curve of the center hole in the multiple-site-cracks specimen is shown in Fig.6.

The results of the residual strength test show clearly that not all fibers were broken along the crack of the metal layer(Fig.7).

## 3. REVIEW OF SLOW CRACK GROWTH MODEL

The schematic illustration of the fiber bridging at the crack tips is described in Fig.8. The break down analysis model developed by Marissen[2] is the basis for discussing the fiber bridging. One of the key equations is

$$K_{1a} = (S_{1a} - C_{b/a} \times S_{br}) \times ( \pi \times a)^{1/2}$$

where

$K_{1a}$; stress intensity factor in fiber/metal laminate

$S_{la}$ ;  remote stress in the total laminate

$C_{b/a}$;  correction factor on the efficiency of the crack bridging stresses , related to the axis ratio of
the delamination

$S_{br}$;  crack bridging stress calculated over the thickness of laminate.

a;   half crack length

A schematic illustration of the equation is shown in Fig.9. Actually, the term of ' $C_{b/a} \times S_{br}$ ' is not easy to determine. Complex effects of shear deformation of the adhesive (elastic /plastic), delamination growth and fiber strength are condensed into the term.

## 4. AN EMPIRICAL CRACK GROWTH MODEL

At first, the same evaluation approach to the metal sheets is tried on the Glare test results. Assuming that the laminates are monolithic in thickness and that the surface cracks go through the thickness, the apparent stress intensity factors ($\Delta K$) for laminates are calculated. Fig.10 (a), (c) and (e) show the relations between the crack growth rate da/dN and the apparent $\Delta K$ each for Glare 2-3/2, Glare 3-3/2 and Glare 4-3/2. In this approach, da/dN characteristics are not specified only by the $\Delta K$. Data seem to vary with the stress levels.

Then, the modified stress intensity factor ( $\Delta K_{mod}$) is introduced by the apparent stress intensity factor ($\Delta K$) multiplied by the modification factor ($\beta_{fb}$). The flow to determine $\beta_{fb}$ is shown in Fig.11. '$\Delta K_{mod}$' is intended to show the actual $\Delta K$ on the aluminum surface foil of the fiber/metal laminate, which is the 2024-T3 sheet. The interesting results obtained by this approach is that the $\beta_{fb}$ shows a definitive correlation to the crack length 'a'. Several test results at different stress levels tend to fall along one functional line. The summary of the obtained $\beta_{fb}$ data for Glares is shown in Fig.12, and the curves which best fit the data points of $\beta_{fb}$ are shown in Fig.13. The effectivity of the $\beta_{fb}$ can be found clearly in Fig.10(b), (d) and (f). Crack growth rates da/dN of fiber/metal laminates become available to the designer's hand by using the $\Delta K_{mod}$.

Crack growth analysis of fiber/metal laminates is easily conducted by the conventional Paris Law.

$$da/dN = C \times (\Delta K_{mod})^m$$
$$= C \times (\beta_{fb} \times \Delta \sigma_{la} \times (\pi \times a)^{1/2})$$

C, m ; material constant in Paris Law
( same as for 2024-T3 in Glares)

$\Delta \sigma_{la}$ ; average laminate stress range

An example comparison with the test data and the analysis with the above simplified equation is shown in Fig.14. Generally, good correlation is shown. A back-life from the crack length a= 60mm is compared. Back-life estimation is one of the practical engineering methods in damage tolerant analysis for current commercial airplanes . The differences after 600,000 cycles are thought to be due to the effect of the initial starter notch and the initial specific delamination growth mechanism.

## 5. CONCLUSIONS

Fiber/metal laminates have the attractive features of extremely slow crack growth, but the mechanism of fiber bridging is too complex for designers.

A simple empirical approach has been developed. With the modification factor $\beta_{fb}$ applied to the stress intensity factors, da/dN of fiber/metal laminates become available to the designer's hand. This approach is a practical way to understand the performance limit of fiber/metal laminates and is effective in the development of new types of fiber/metal laminates.

The effect of spectrum loadings is not covered here. But the approach developed herein will be a good baseline from which to discuss the phenomena.

## ACKNOWLEDGMENT

## REFERENCES

1  Schijve, J., "Development of fiber-metal laminates, ARALL and Glare, new fatigue resistant materials", Report LR-715, Faculty of Aerospace Engineering, Delft University of Technology, The Netherlands, January 1993.

2  Marissen, R., "Fatigue Crack Growth in ARALL, a Hybrid Aluminum-Aramid Composite Material", Report LR-574,Faculty of Aerospace Engineering, Delft University of Technology, The Netherlands, June 1988.

## Table 1  Summary of all test items

&lt;MATERIALS&gt;

| FIBER/METAL LAMINATES | FIBER, FIBERGLASS (S-2 0R EQUIVALENT) | METAL Al |
|---|---|---|
| GLARE 2 | 100% 0° FIBERGLASS | 2024-T3 |
| GLARE 3 | 50% 0°, 50% 90° FIBERGLASS | 2024-T3 |
| GLARE 4 | 70% 0°, 30% 90° FIBERGLASS | 2024-T3 |

&lt;CRACK PROPAGATION TESTS&gt;

| TEST SPECIMEN ID | LAMINATE TYPE | CONFIGURATION NO. OF LAYERS (METAL/FIBER) | LAMINATE NOMINAL THICKNESS | NO. OF TEST SPECIMENS |
|---|---|---|---|---|
| A | GLARE 3 | 3 / 2 | 1.12mm | 7 |
| B | GLARE 2 | 3 / 2 | 1.12mm | 6 |
| C | GLARE 4 | 3 / 2 | 1.44mm | 4 |
| D | GLARE 3 | 4 / 3 | 1.62mm | 7 |

&lt;MULTI-SITE CRACK PROPAGATION TESTS&gt;

| GLARE3-3/2     5/32IN DIA HOLES WITH 5.8D PITCH | 1 |
|---|---|

&lt;RESIDUAL STRENGTH TESTS&gt;

| GLARE3-3/2, GLARE4-3/2, GLARE2-3/2 | 1 EACH |
|---|---|
| GLARE3-4/3 | 2 |

208 mm

500mm

open hole
plus
saw cuts

doubler

**Initial Crack (Saw Cuts)**

Through                     Corner

D=4.1mm                     D=4.1mm

| Initial crack | (R=0.05) |
|---|---|
| Level 1 | 98 MPa |
| Level 2 | 147 MPa |
| Level 3 | 196 MPa |
| Level 4 | 245 MPa |
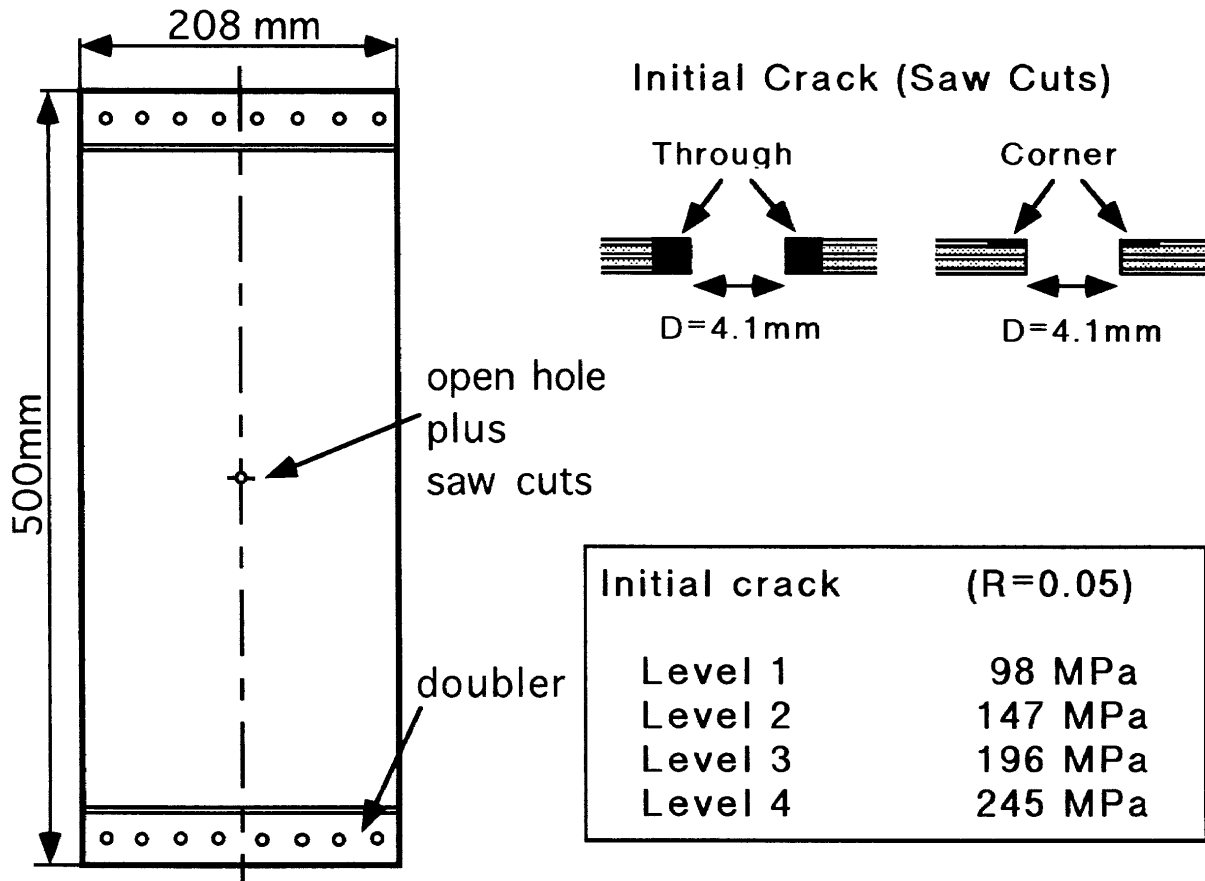
**Figure 1   Configuration of the test specimen**
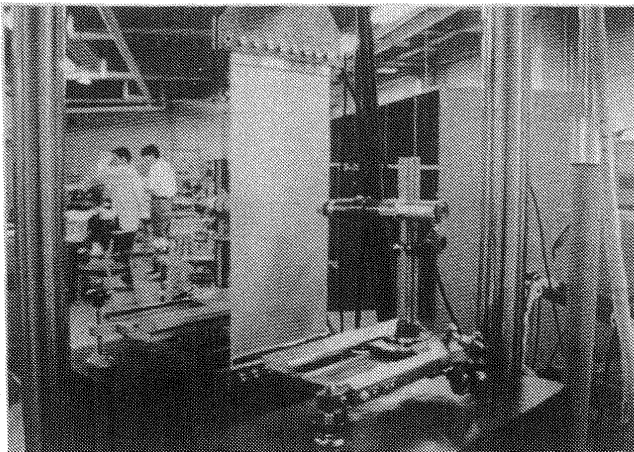
Figure 2　　Test set–up condition
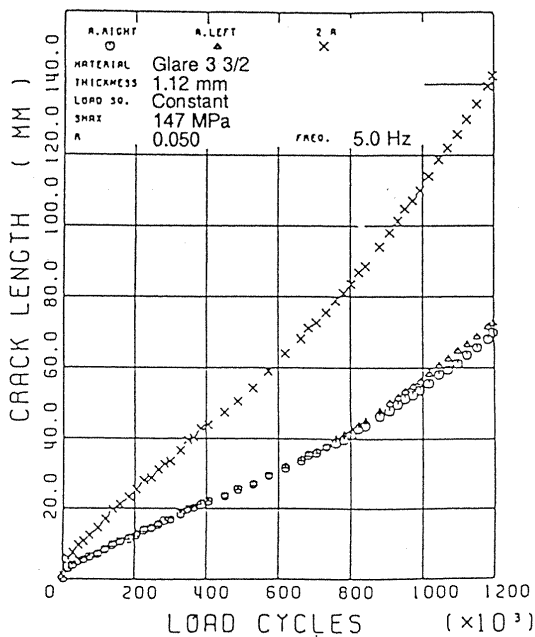


Figure 3　　'a– N' Curve in Test A



TEST A
GLARE 3-3/2, σ max=147MPa
Surface Crack Length 2a max = 146.5 mm
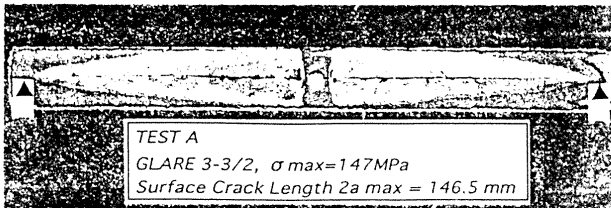
Figure 4　　Etched specimen – Test A
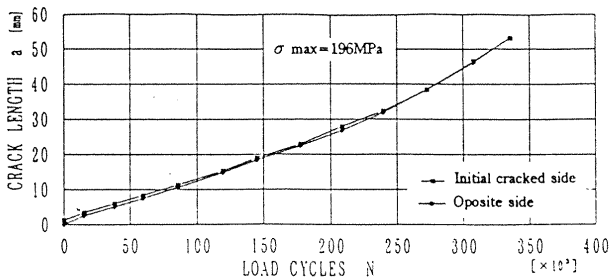


Figure 5　　'a– N' Curve of corner saw cut
in Test A (Glare3 3/2)
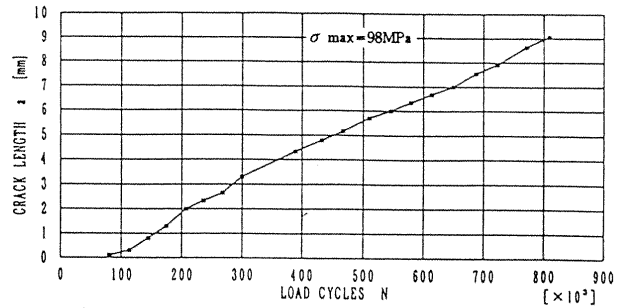


Figure 6　　'a– N' Curve of Multiple– site
crack in Test A (Glare3 3/2)



GLARE3-4/3, Center Hole Specimen
Crack Propagation Test, σmax=147MPa
Residual Strength Test, Pmax=90kN
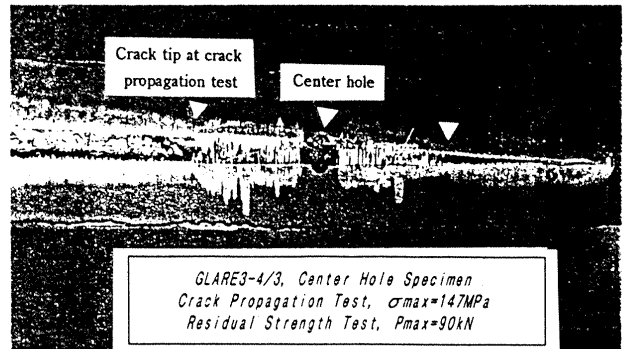
Figure 7　　Etched specimen – after the
residual strength test
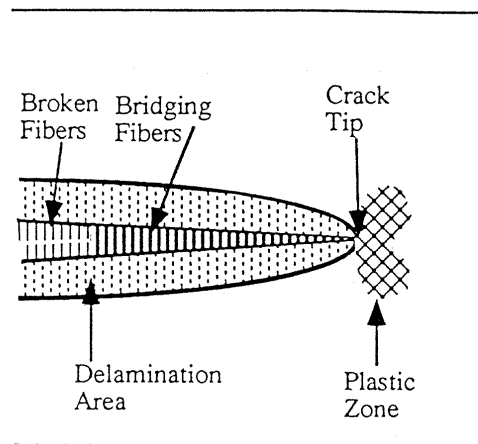


Figure 8　　Schematic illustration of fiber
bridging at the crack tip in
fiber/metal laminates
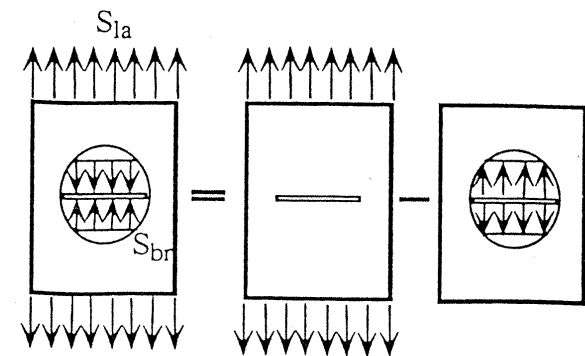


Figure 9　　Schematic illustration of the
equation
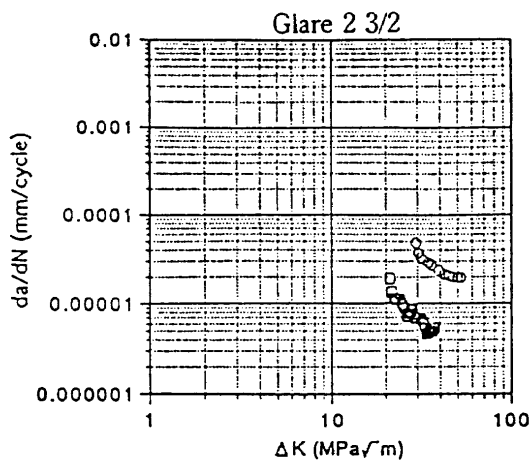
(a) original
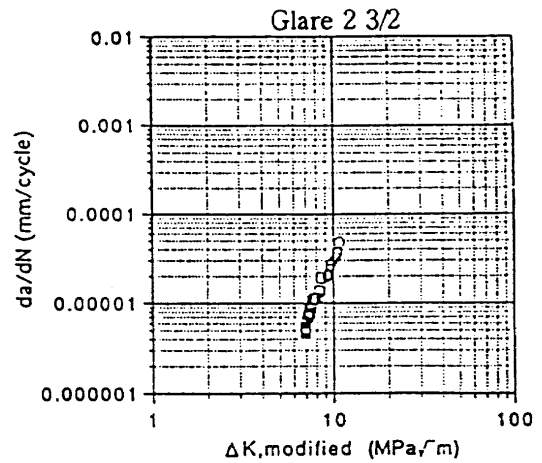
(b) 'β, fiber bridging' applied
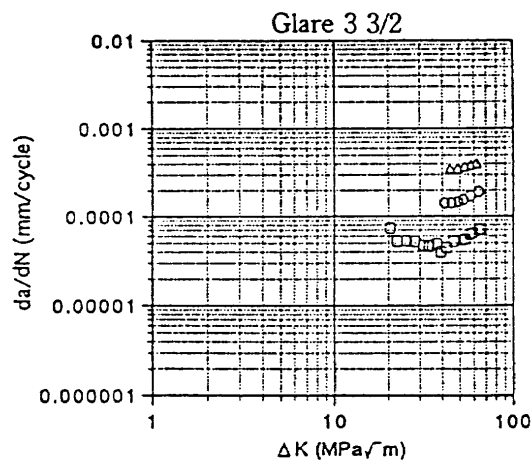
(c) original
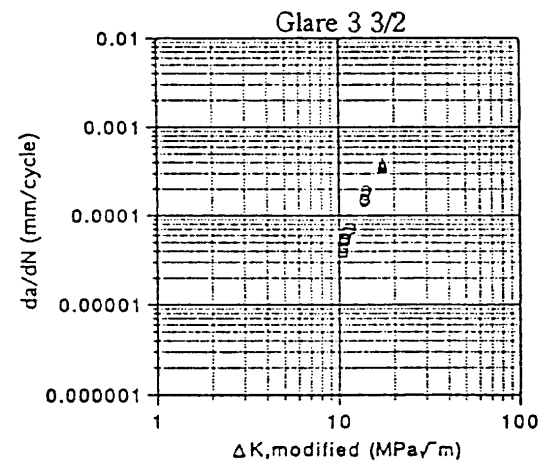
(d) 'β, fiber bridging' applied
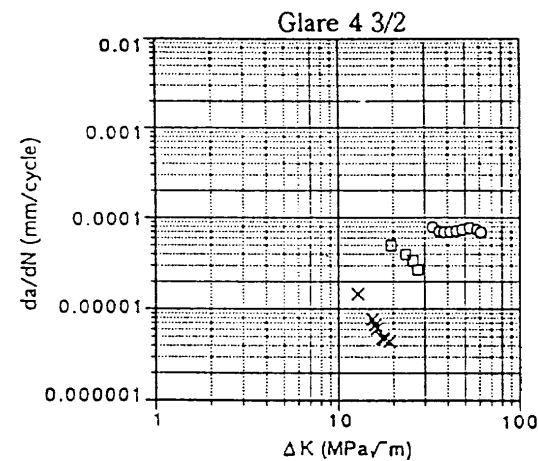
(e) original
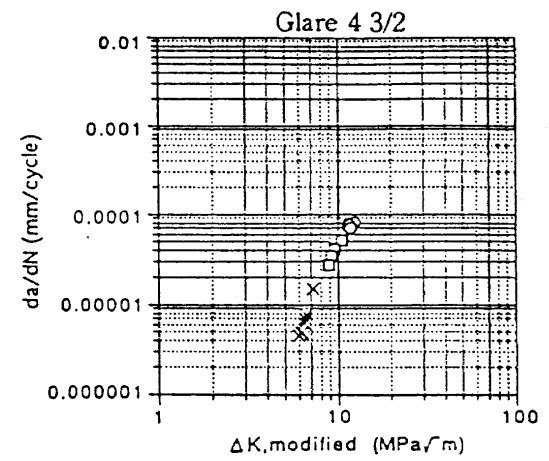
(f) 'β, fiber bridging' applied

X   σmax=  98MPa
□   σmax=147MPa
O   σmax=196MPa
△   σmax=245MPa

Figure 10    da/dN vs Δ K or Δ K,modified
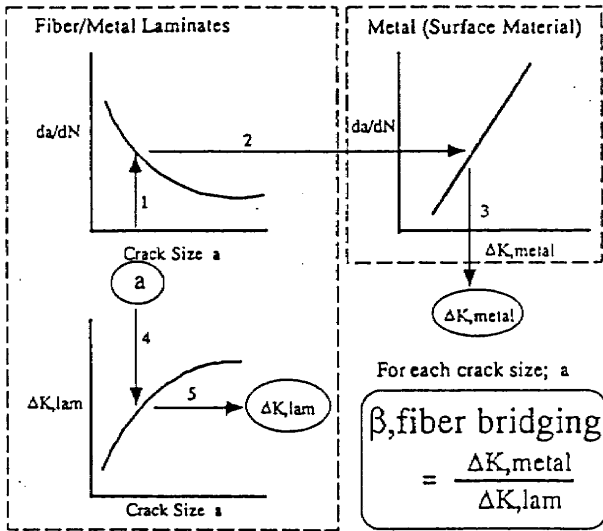
Figure 11   Flow to determine
'$\beta$ ,fiber bridging'
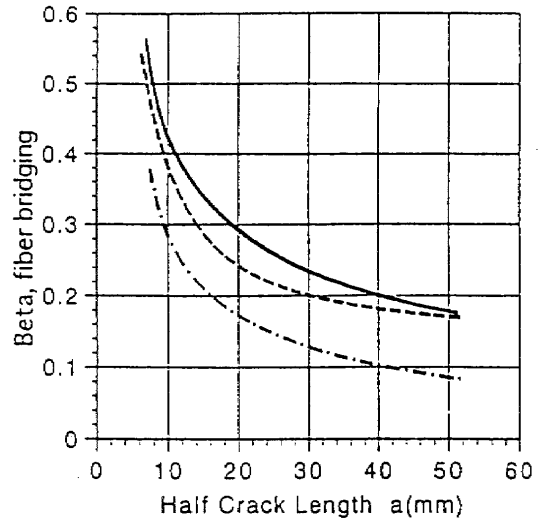


Glare 3 3/2  Glare 4 3/2  Glare 2 3/2

| | ——— | - - - - | —·—·— |
|---|---|---|---|
| A | 155. | -51.9 | 150. |
| B | -41.2 | 14.8 | -33.4 |
| C | 6.09 | 1.58 | 4.68 |
| D | .0720 | .133 | .0031 |

(Beta, fiber bridging)

$$= A/(a^3) + B/(a^2) + C/a + D$$
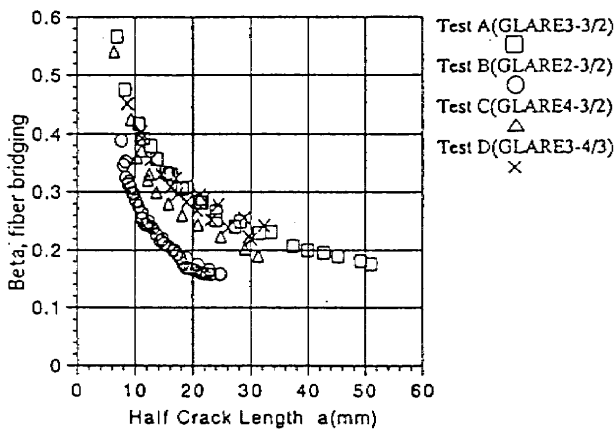
Figure 13   Best fit curves for
'$\beta$ ,fiber bridging'



Test A(GLARE3-3/2)
□
Test B(GLARE2-3/2)
○
Test C(GLARE4-3/2)
△
Test D(GLARE3-4/3)
×

Figure 12   '$\beta$ ,fiber bridging' obtained from
the tests



○  Test results

——  Analytical
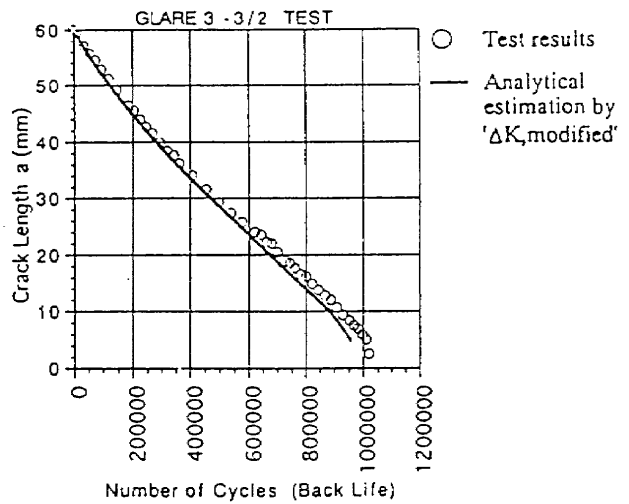estimation by
'ΔK,modified'

Figure 14   Crack growth simulation and
comparison with test results

# 12

# RELIABILITY-BASED INSPECTION SCHEDULE FOR DAMAGE-TOLERANT STRUCTURES

**Hiroo ASADA, Seiichi ITO and Hirokazu SHOUJI**
Airframe Division
National Aerospace Laboratory
Tokyo, Japan

**Yasuhiro TOI, Yasuhiro FUJIWARA, Takaharu OYAGI and Junji TAKAKI**
Aerospace Division
Fuji Heavy Industries, Ltd
Utsunomiya, Japan

## 1. INTRODUCTION

Adequate inspection schedules are considered to play increasingly an important role in maintaining the structural integrity of advanced aircraft designed by the damage-tolerant method [1-4]. A rational determination of inspection schedules, sample size, first inspection time and inspection intervals is the key to effective detection, repair and replacement of fatigue cracks, and the resulting failed elements in order to maintain the required reliability of aircraft structures. Structural reliability analysis is realized to be a useful tool [4] for developing adequate inspection schedules because several primary factors, such as initial crack length, fatigue crack initiation time, fatigue crack propagation, service loads, residual strength, and crack detection capability, are probabilistic and need to be treated in the analysis.

For the reliability analysis to be performed with a high degree of engineering soundness, the probabilistic models used for the analysis must be defined reasonably well. However, the usual paucity of pertinent data makes it difficulty for the probability density functions of those factors and of their respective parameter values to be determined. Although actual data collected during in-service inspections is limited in quantity as well as quality, it is a valuable source of highly useful information that will be utilized not only to determine reliability-based inspection schedules but also to estimate uncertain parameters in the physical model.

From this point of view, this research concentrates on the development of Bayesian reliability analysis [5-8], which can estimate subjectively appropriate values of uncertain parameters with decision-making on the basis of posterior probability and can develop optimal non-periodic inspection schedules utilizing small sample field data collected during inspections.

A fatigue-critical element model used in the present study is a two-bay fail-safe structure in the fuselage which consists of multiple components, namely, three frames and a skin panel. This element is subjected to cyclic stress due to differential pressure and is designed in accordance with the damage-tolerant method. Monte Carlo simulations are carried out to generate the failure process in the structural element and to demonstrate the validity of the proposed Bayesian reliability methodology.

## 2. FATIGUE-CRITICAL STRUCTURAL ELEMENT MODEL

### 2.1 True Element Model

For a fatigue-critical structural element in Figure 1, the materials of skin and frames are 2024-T3 and 7075-T6 aluminum alloys, respectively. The failure process consists of crack initiation, propagation and unstable crack growth. Fatigue cracks in the element propagate to the longitudinal direction of fuselage.

#### 1) Applied load

Aircraft fuselage structures are subjected to several kinds of loads. In this analysis, however, it is

considered that the structural element is only subjected to cyclic constant stress $\Delta s$ due to the cabin differential pressure for each flight. This stress depends on a location of the element, and $\Delta s$ is assumed to be a random variable normally distributed.

## 2) Fatigue crack initiation

Fatigue cracks initiate simultaneously at both sides of rivet holes in the skin and the center frame. The initial half crack length $a_0$ is assumed to be the sum of the hole radius $r_0$ and the initial through crack length $a_i$ shown in Figure 2. The time to crack initiation (TTCI) $t_0$ is a random variable governed by a two-parameter Weibull distribution:

$$f_0(t_0) = \frac{\alpha}{\beta} \left(\frac{t_0}{\beta}\right)^{\alpha-1} \exp\{-\left(\frac{t_0}{\beta}\right)^{\alpha}\} \qquad (1)$$

## 3) Fatigue crack propagation

Fatigue cracks on both sides of the rivet holes of a skin plate $a_S$ and a center frame $a_F$ subjected to cyclic loadsing propagate under the Paris law with the stress intensity factor range modified by coefficients $\beta$:

**(1) Skin** $a_S$ :

$$\frac{da_S}{dt} = C_S(\Delta K_S)^{bS} \qquad (2)$$

$$\left.\begin{array}{l} \Delta K_S = \Delta s\sqrt{\pi a_S}\ \beta_{Frame}\beta_{Bulge} \\[2mm] C_S = 10^{zS} \end{array}\right\} \qquad (3)$$

**(2) Frame** $a_F$ :

$$\frac{da_F}{dt} = C_F(\Delta K_F)^{bF} \qquad (4)$$

$$\left.\begin{array}{l} \Delta K_F = \Delta s\sqrt{\pi a_F}\ \beta_{WF}\beta_{Skin} \\[2mm] C_F = 10^{zF} \end{array}\right\} \qquad (5)$$

in which parameters $z_S$ and $z_F$ are random variables assumed to be normally distributed. The period of skin fatigue crack propagation lies between $t_0$ and $t_f$ shown in Figures 2 and 3. During that period, the crack propagates from $a_0$ to $a_f$. The variables, $t_f$ and $a_f$, denote the time and the crack length when the element fails as mentioned below.

## 4) Element failure criterion

An element can fail either before or after fatigue crack initiation. Before crack initiation, the element is considered to have failed when the stress due to differential pressure exceeds the strength of the element. After crack initiation, the following two failure modes are considered to exist. A failure due to unstable crack growth occurs when the crack length reaches a certain level $a_f$ which is derived by a failure criterion. This unstable crack is arrested at both sides of frames because the residual strength increases near the frames. The other failure mode arises when a fatigue crack reaches the 2-bay fail-safe crack length which is equivalent to $a_f$. Feddersen's criterion of residual strength is adopted for the condition of unstable crack propagating. This criterion involves yield stress $S_Y$ and fracture toughness $K_C$, both of which are random variables governed by two-parameter Weibull distributions.

## 2.2 Element Model for Bayesian Reliability Analysis

External detailed visual inspection is implemented in order to detect skin cracks in the element

shown in Figure 1. Therefore, a skin crack $a_s$ is only used in the analysis. As shown in Figures 2 and 3, $a_s$ is visually detectable when it exceeds $a_0^* = r_h + a_{min}$. The variables $r_h$ and $a_{min}$ denote the rivet head radius and the minimum detectable crack length due to visual inspection respectively. The detectable crack propagation period lies between $t_0^*$ and $t_f$. The TTCI of this model $t_0^*$ is much longer than that for the true model $t_0$.

## 1) Fatigue crack initiation

The TTCI of the model is assumed to be a random variable with the density function of a two-parameter Weibull distribution:

$$f_0^*(t_0^*|\beta^*) = \frac{\alpha}{\beta^*} (\frac{t_0^*}{\beta^*})^{\alpha-1} \exp[-(\frac{t_0^*}{\beta^*})^\alpha] \qquad (6)$$

Uncertainty is introduced in the TTCI through the scale parameter $\beta^*$ which is a random variable.

## 2) Fatigue crack propagation

The period of skin fatigue crack propagation is defined between $t_0^*$ and $t_f$ when the element fails. During that period, the crack propagates from $a_0^*$ to $a_f$. The following Paris equation is used to present a skin fatigue crack propagation:

$$\frac{da_s}{dt} = C(a_s)^{b/2} \qquad (7)$$

$$C = 10^z$$

Integrating Eq.(7) from $a_0^*$ to the current crack length $a_s$ at time $t$, the following expression is obtained:

$$a_s(t-t_0^*|z) = \{-b'10^z(t-t_0^*)-a_0^{*-b'}\}^{-1/b'} \qquad (8)$$

$$b' = (b-2)/2$$

$$a_0^* = r_h + a_{min}$$

Uncertainty in fatigue crack propagation is introduced by a random variable z.

## 3) Inspection

All structural elements are inspected by external detailed visual inspection at the time of each inspection. It is assumed that element failure can be detected always if it exists during the inspection process. Therefore, the probability of detecting the element failure is equal to unity.

## 4) Probability of crack detection for visual inspection

Information on the probabilities of crack detection (POD) is necessary in the present analysis.

### (1) Probability of detection for a crack

The probability that a crack will be detected, $D(a_s^*|d)$, by visual inspection depends on the crack size in excess of the radius $r_h$ of the rivet head shown in Figure 2 and is assumed to be given by a three-parameter Weibull function as shown below:

$$D(a_s^*|d) = 1 - \exp\{-(\frac{a_s-a_{min}}{d-a_{min}})^\epsilon\} \qquad (9)$$

Then, the probability that the crack will not be detected is given by:

$$\overline{D}(a_s^*|d) = 1 - D(a_s^*|d) \qquad (10)$$

where $a_s^* = a_s - r_h$ and $a_{min}$ denote the inspectable and the minimum detectable crack length.

### (2) Probability of detection for cracks at a rivet

Both sides of the rivet head are inspected for cracks. As it is assumed that the skin crack is always symmetric about the central axis, the probability $D_t(a_s^*|d)$ that at least the crack on the one side is detected is given by:

$$D_t(a_s^*|d) = 1 - \overline{D}_t(a_s^*|d) \qquad (11)$$

where $\overline{D}_t(a_s^*|d)$ is:

$$\overline{D}_t(a_s^*|d) = [\overline{D}(a_s^*|d)]^2 \qquad (12)$$

### 5) Repair or replacement

If a crack is detected in the skin of the element, the skin and frame are repaired or replaced and the element regains its initial strength.

### 6) Failure rate and element reliability

Based on the element failure criterion, following two failure rates are defined.

### (1) Before crack initiation

The failure rate at time instant t before crack initiation is a very small constant and given by:

Failure rate: $\qquad h(t) = \exp(r) = h_0 \qquad (13)$

Reliability:

$$U(t\text{-}T_l) = \exp\{-\int_0^{t\text{-}T_l} h(\tau)d\tau\} = \exp\{-(t\text{-}T_l)\bullet\exp(r)\} \qquad (14)$$

### (2) After crack initiation

A two-parameter Weibull function is adopted for the failure rate after crack initiation at time instant t:

Failure rate: $\qquad h(t) = \dfrac{\alpha_f}{\beta_f} (\dfrac{t}{\beta_f})^{\alpha_f - 1} + \exp(r) \qquad (15)$

Reliability:

$$V(t\text{-}t_0^*) = \exp\{-\int_0^{t\text{-}t_0^*} h(\tau)d\tau\} = \exp\{-\dfrac{1}{\beta_f^{\alpha_f}} (t\text{-}t_0^*)^{\alpha_f} - (t\text{-}t_0^*)\exp(r)\} \qquad (16)$$

### 7) Uncertain parameters

Two parameters $\beta^*$ and z are estimated from inspection data such as the number of cracks, crack sizes and whether or not failures were observed. Other parameters are assumed to be known.

## 3. FORMULATION OF BAYESIAN RELIABILITY ANALYSIS

### 3.1 Possible Events at Time of Inspection

At the time of the j-th inspection performed at time $T_j$ on a certain element, one of the following

five events may occur (knowing that this element was repaired or replaced during the $l$-th inspection performed at time $T_l$ with $l < j$ ):

1) { A: j, $l$} :  event that the element is found to have failed at the time of the j-th inspection $T_j$. This event consists of the following two mutually exclusive events:

   [1] $E_{1,j}$ :  event that the element failed before crack initiation, sometime during the time interval $[T_{j-1}, T_j]$.

   [2] $E_{2,j}$ :  event that the element failed after crack initiation, sometime during the time interval $[T_{j-1}, T_j]$.

2) { $B_1(a_j)$: j, $l$} :  event that a crack of length between $a_j$ and $a_j + da_j$ is detected in the element :  $E_{3,j}$.

3) { $B_2$: j, $l$} :  event that no crack is detected in the element.  This event consists of the following two mutually exclusive events:

   [1] $E_{4,j}$ :  event that the element did not fail in the time interval $[T_{j-1}, T_j]$ and no crack exists in the element at the time of inspection $T_j$.

   [2] $E_{5,j}$ :  event that the element did not fail in the time interval $[T_{j-1}, T_j]$ but a crack exists in the element which is not detect at the time of inspection $T_j$.

The probabilities of these five events will be evaluated for a particular element in terms of the probability density and distribution functions $f_0^*(t|\beta^*)$ and $F_0^*(t|\beta^*)$ of the TTCI, a skin crack $a_s$, reliability functions $U(t)$ and $V(t)$ and probability of crack detection $D_t(a|d)$.

## 3.2 Reliability of an Element After the Latest Inspection $T_j$

The reliability of two types of elements at time instant $t^*$ after the j-th inspection is calculated in the following:

1) Elements repaired or replaced at the j-th inspection

Elements are repaired or replaced at the j-th inspection in the case of events {A: j, $l$} or {$B_1(a_j)$: j, $l$}, respectively:

Reliability:

$$R(t^*; \text{Repair}) = \{1 - F_0^*(t^*-T_j|\beta^*)\} \cdot U(t^*-T_j) + \int_{T_j}^{t^*} f_0^*(t-T_j|\beta^*) \cdot U(t-T_j) \cdot V(t^*-t) dt \quad (17)$$

2) Elements not Repaired at the j-th Inspection

An element is neither repaired nor replaced at the j-th inspection in the case of event {$B_2$: j, $l$}:

Reliability:

$$R(t^*; \text{No Repair}) = \frac{Q}{P\{B_2: j, l\}} \quad (18)$$

$$Q = \{1 - F_0^*(t^*-T_j|\beta^*)\} \cdot U(t^*-T_j) + \int_{T_j}^{t^*} f_0^*(t-T_j|\beta^*) \cdot U(t-T_j) \cdot V(t^*-t) dt$$

$$+ \sum_{i=1}^{j-1} \int_{t_i}^{t_{i+1}} f_0^*(t-T_i|\beta^*) \cdot U(t-T_i) \cdot V(t^*-t) \cdot [\prod_{k=i+1}^{j} \{1 - D_t(as(T_k-t|z))\}] dt \quad (19)$$

## 3.3 Uncertain Parameters by Bayesian Analysis

1) Prior joint density function of uncertain parameters

Initially, it is assumed that $b^*$ and $z$ are jointly and uniformly distributed according to the following

prior joint density function:

$$f^0(\beta^*, z) = \frac{1}{(\beta^*_{max}-\beta^*_{min})(z_{max}-z_{min})} \qquad (20)$$

where:

$$\beta^*_{min} \leq \beta^* \leq \beta^*_{max} \; ; \quad z_{min} \leq z \leq z_{max} \qquad (21)$$

## 2) Likelihood function resulting from j-th inspection

The likelihood function $LF_j$ for the entire structure as a result of the j-th inspection is calculated as:

$$LF_j = \prod_{m=1}^{M} LF_j^{(m)} \qquad (22)$$

where $LF_j^{(m)}$ is the likelihood function for element m resulting from the j-th inspection and M is the total number of elements in the structure.

## 3) Posterior joint density function of uncertain parameters

The posterior joint density function of the two uncertain parameters b* and z immediately after the j-th inspection, is given by:

$$f^j(\beta^*, z) = \frac{LF_j \cdot f^0}{\int_{\beta^*_{min}}^{\beta^*_{max}} \int_{z_{min}}^{z_{max}} (Numerator) \, d\beta^* dz} \qquad (23)$$

## 3.4 Reliability of Entire Structure at Time Instant t* After the Latest Inspection T_j

The reliability of the entire structure consisting of M elements at time instant t* after the latest inspection $T_j$ is denoted by $\overline{R}_M(t^*)$ and calculated as:

$$\overline{R}_M(t^*) = \int_{\beta^*_{min}}^{\beta^*_{max}} \int_{z_{min}}^{z_{man}} R_M(t^*|\beta^*, z) \cdot f^j(\beta^*, z) d\beta^* dz \qquad (24)$$

where:

$$R_M(t^*|\beta^*, z) = [\prod_{m=1}^{M_1} R_m(t^*; Repair)] \cdot [\prod_{m=1}^{M_2} R_m(t^*; No\ Repair)] \qquad (25)$$

where $M_1$ is a number of elements either repaired or replaced at the j-th inspection, $M_2$ is a number of elements found intact at the j-th inspection and $M_1 + M_2 = M$. In Eq.(25), $R_m(t^*; Repair)$ and $R_m(t^*; No\ Repair)$ are identical with the reliabilities $R(t^*; Repair)$ and $R(t^*; No\ Repair)$ defined in Eqs.(17) and (18), respectively. Note that $R_m(t^*; Repair)$ and $R_m(t^*; No\ Repair)$ are conditional to given values of $\beta^*$ and z.

## 3.5 Calculation of Time T_{j+1} for Next Inspection

Assuming that the entire structure must maintain its reliability above a prespecified design level throughout its service life, the time $T_{j+1}$ for the next inspection after the latest one performed at $T_j$ is calculated using:

$$\overline{R}_M(t^*) \geq R_{design} \qquad (26)$$

where $R_{design}$ denotes the prespecified design level of reliability for the entire structure. The time $T_{j+1}$ of

the (j+1)-th inspection is then estimated as the maximum value of t* that satisfies Eq.(26) as follows:

$$T_{j+1} = t^* = \overline{R}_M^{-1}(R_{design}) \qquad (27)$$

It is obvious that the reliability of the entire structure remains above the prespecified design level $R_{design}$, through-out the service life of the structure.

## 4. NUMERICAL EXAMPLE

All the values of a true structural element model and a Bayesian analysis model listed in Table 1 are approximately corresponding to these applicable to an actual fuselage structural design. Monte Carlo simulations are performed to generate the failure process in the true structural element.

Two essential uncertain parameters $\beta^*$ and z are set to be jointly and uniformly distributed according to the following initial prior joint density function shown by Eq.(20). The minimum and maximum values of these parameters, and their ranges and increments are given by the engineering judgment as follows:

$\beta^*_{min} = 17{,}000$ flights ; $\beta^*_{max} = 66{,}000$ flights ; $\overline{\beta^*} = \beta^*_{max} - \beta^*_{min} = 49{,}000$ flights;
$\Delta\beta^* = 3{,}500$ flights

$z_{min} = -4.1$ ; $z_{max} = -2.7$ ; $\overline{z} = z_{max} - z_{min} = 1.4;$ $\Delta z = 0.1$

The aircraft is assumed to have 100 or 200 fatigue-critical elements. The service life is 50,000 flights and the minimum reliability level for the entire structure throughout its service life is set equal to $R_{design} = 0.8$. This indicates that the reliabilities of one element for both 100 and 200 fatigue-critical elements are 0.998 and 0.999, respectively under the assumption of independence. The standard deviation $\sigma_z$ of z for the parameters of fatigue crack propagations of skin and frame in Eqs.(2) to (5) is set at 0.154. This indicates that the speeds of fatigue crack propagation between twice and half the mean crack propagation speeds of skin and frame account for 95% of all fatigue cracks. The values of the parameters $\varepsilon$ and $a_{min}$, in the POD of Eq.(9) are given as $\varepsilon = 1.4$ and $a_{min} = 0.04$ inches based on the field data [9] of fatigue cracks visually detected. A parametric study on the parameter d in the POD is performed for d = (1.2, 1.4, 1.6, 1.8) inches, in order to investigate its effect on crack detection capability.

The reliability curves of the entire structure as a function of time for each combination of M = (100, 200) and d = (1.2, 1.4, 1.6, 1.8) inches are depicted in Figures 4 and 5 with numbers of failed elements and of detected cracks. It is shown that the inspections are implemented non-periodically. The reliability returns to the unity after inspections and decreases along operation. The following inspection is implemented at the reliability equal to $R_{design} = 0.8$ and shorter inspection intervals are given with the progress of operation. The first inspection times $T_1$ for M = (100, 200) and d = (1.2, 1.4, 1.6, 1.8) inches are performed after approximately 30,000 flights due to the ranges of the parameter values, $\beta^*$ and z, introduced by the engineering judgment in this analysis. In the case that the number of critical elements increases, the number of inspections during service life for each parameter d in the POD increases in order to maintain the same target reliability $R_{design}$, and the numbers of failed elements and detected cracks also increase. When the value of the parameter d in the POD gets larger, namely the crack detection becomes less efficient, the number of inspections increases, and the inspection intervals become shorter to keep the minimum level of reliability $R_{design}$, for the entire structure. When the number of critical elements and the value of the parameter d become large, several elements would have failed before they were detected by external detailed visual inspection.

The posterior joint density functions of the uncertain parameters, $\beta^*$ and z, after the third inspection are plotted in Figures 6 and 7 for M = (100, 200) and d = (1.2, 1.4, 1.6, 1.8) inches,

respectively. The concentration of posterior joint density at the modal values for M = 100 is sharper than that for M = 200, because the number of cracks found at the third inspection for M = 200 is smaller than that for M = 100. It is anticipated that the concentration is around the reasonable modal value.

## 5. CONCLUSIONS

The damage tolerant fuselage structure of an aircraft is analyzed and the usefulness of the Bayesian reliability analysis has been demonstrated. The results of the numerical examples verify that this analysis can indeed generate appropriate non-periodic inspection schedules with the estimation of uncertain parameters even if a large number of crack data could not be collected during inspections. If a fleet of aircraft can be inspected as in the actual case, a large number of cracks and possibly failures will be found and it makes the Bayesian analysis even more practical. It is also pointed out that the present study has evaluated the generation of the failure process consisting of fatigue crack initiation and propagation and final failure in the structure element.

## ACKNOWLEDGMENTS

## REFERENCES

1) Swift, T. ; Damage Tolerance Capability, *International Journal of Fatigue*, Vol.16, No.1 (1/1994), pp.75-93.

2) Swift, T. ; Widespread Fatigue Damage Monitoring -Issues and Concerns, Proceedings of FAA/NASA International Symposium on Advanced Structural Integrity Methods for Airframe Durability and Damage Tolerance, NASA Conference Publication 3274 Part 1 (5/1994), pp.829-870.

3) Federal Aviation Administration, FAR 25.571(Draft)(7/1993) ; Damage-Tolerance and Fatigue Evaluation of Structure, and Advisory Circular AC No.25.571-1B(Draft) (7/1993).

4) Goranson, U.G. ; Damage Tolerance - Facts and Fiction, Proceedings of the 17th Symposium of the International Committee on Aeronautical Fatigue, ICAF, Vol.1 (6/1993) pp.3-105.

5) Asada, H., Itagaki, H. and Ito, S. ; Effect of Sampling Inspections on Aircraft Structural Reliability, Proceedings of ICOSSAR '85, the 4th International Conference on Structural Safety and Reliability, IASSAR Publication, Vol.1 (5/1985) pp.I.87-I.96.

6) Deodatis, G., Fujimoto, Y., Ito, S., Spencer, J. and Itagaki, H. ; Non-Periodic Inspection by Bayesian Method I, *Probabilistic Engineering Mechanics J.*, Vol.7, No.4 (1992) pp.191-204.

7) Ito, S., Deodatis, G., Fujimoto, Y., Asada, H. and Shinozuka, M. ; Non-Periodic Inspection by Bayesian Method II: Structures with Elements Subjected to Different Stress Levels, *Probabilistic Engineering Mechanics J.*, Vol.7, No.4 (1992) pp.205-215.

8) Shinozuka, M., Deodatis, G., Sampath, S. and Asada, H. ; Statistical Property of Widespread Fatigue Damage, AGARD, the 80th Meeting of the Structures and Materials Panel, Specialists' Meeting on Widespread Fatigue Damage in Aircraft (5/1995).

9) Endoh, S., Tomita, H., Asada, H. and Sotozaki, T. ; Practical Evaluation of Crack Detection Capability for Visual Inspection in Japan, Proceedings of the 17th Symposium of the International Committee on Aeronautical Fatigue, ICAF, Vol.1 (6/1993) pp.259-280.

## Table 1　Values of Parameters in Numerical Example

| Item | Values for true model | Bayesian analysis Model value | Range for estimation |
|---|---|---|---|
| ·Service life (flights) | | 50,000 | |
| ·Minimum level of reliability　$R_{design}$ | | 0.8 | |
| ·Total number of critical elements　M | | 100, 200 | |
| ·Parameters of TTCI in Eq.(1) | | | |
| 2-parameter Weibull　$\alpha$ | 4 | 4 | |
| $\beta$(flights) | 40,000 | | |
| $\beta^*$(flights) | | Unknown | 17,000 to 66,000 |
| ·Rivet head radius　$r_h$(in) | 0.18 | 0.18 | |
| ·Initial half crack length | | | |
| for true model　$a_0$(in) | 0.1 | | |
| ·Initial half crack length | | | |
| for Bayesian analysis　$a_0^*$(in) | | 0.22 | |
| ·Minimum detectable crack length　$a_{min}$(in) | | 0.04 | |
| ·Effective width (in)　Skin　$W_S$ | 40 | | |
| Frame　$W_{F1}$ | 14 | | |
| $W_{F2}$ | 2 | | |
| ·Maximum allowable crack length | | | |
| $a_{max}=W/2$ (in)　Skin　$a_{S,max}$ | 20 | 20 | |
| Frame　$a_{F1,max}$ | 7 | | |
| $a_{F2,max}$ | 1 | | |

| | 2024-T3 (Skin:S) | 7075-T6 (Frame:F) | |
|---|---|---|---|
| ·Yield stress　$S_y$(ksi) | | | |
| 2-parameter Weibull　$\alpha_{Sy}$ | 19 | 19 | |
| $\beta_{Sy}$(ksi) | 49 | 70 | |
| ·Fracture toughness　$K_c$(ksi√in) | | | |
| 2-parameter Weibull　$\alpha_{Kc}$ | 12 | 12 | |
| $\beta_{Kc}$(ksi√in) | 140 | 65 | |
| ·Fatigue crack propagation | | | |
| in Eqs.(2) & (3)　b | 3.8 | 3.4 | |
| Normal　$\mu_z$ | -9.5 | -9.0 | |
| $\sigma_z$ | 0.154 | 0.154 | |

| Item | Values for true model | Model value | Range for estimation |
|---|---|---|---|
| in Eq.(5)　b | | 4.0 | |
| z | | Unknown | -4.1 to -2.7 |
| ·Cyclic stress range | | | |
| in Eqs.(2) & (3)　$\Delta s$(ksi) | | | |
| Normal　$\mu_{\Delta s}$ (ksi) | 18 | | |
| $\sigma_{\Delta s}$ (ksi) | 0.9 | | |
| ·Parameters of POD in Eq.(7)　$\varepsilon$ | | 1.4 | |
| d (in) | | 1.2, 1.4, 1.6, 1.8 | |
| ·Parameters of failure rate in Eq.(11)　r | | -18 | |
| in Eq.(13)　$\alpha_f$ | | 5.5 | |
| $\beta_f$ (flights) | | 37,000 | |

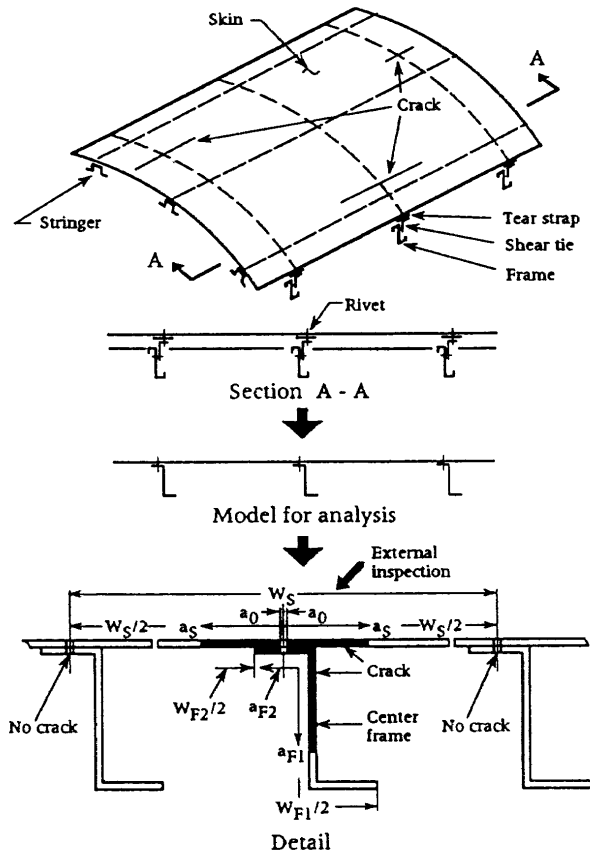Note:　1 ksi=6.895 MPa,　1 in=2.54 cm,　1 ksi√in=1.099 MPa√m

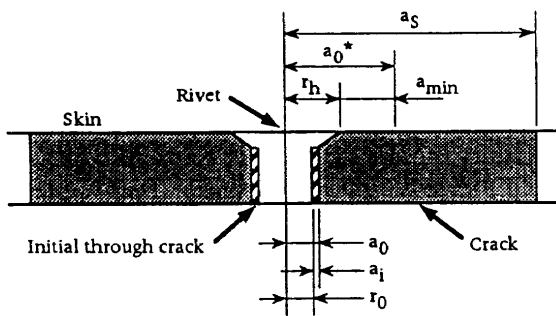Figure 1   Fuselage Structural Model

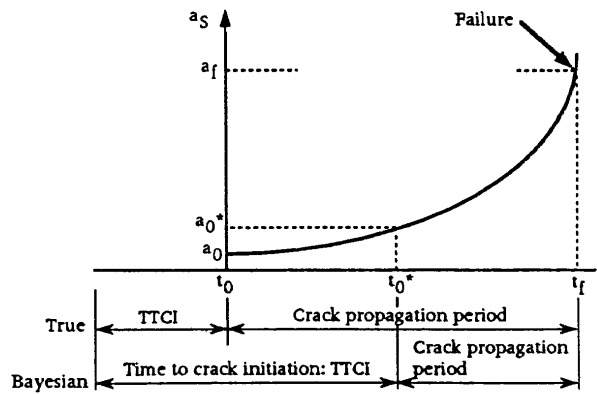Figure 2   Definition of Rivet and Crack

Figure 3   Fatigue Crack Initiation and Propagation for
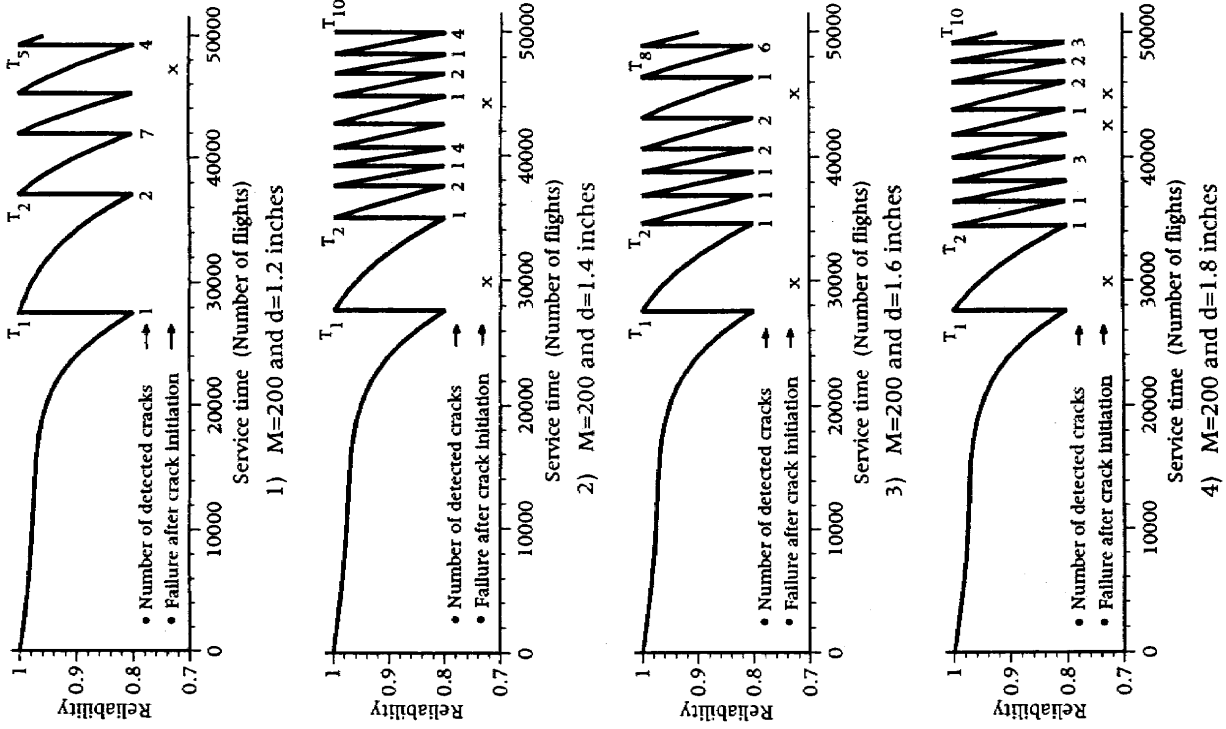True Model and Bayesian Analysis Model

Figure 5   Inspection Schedule and Structural Reliability
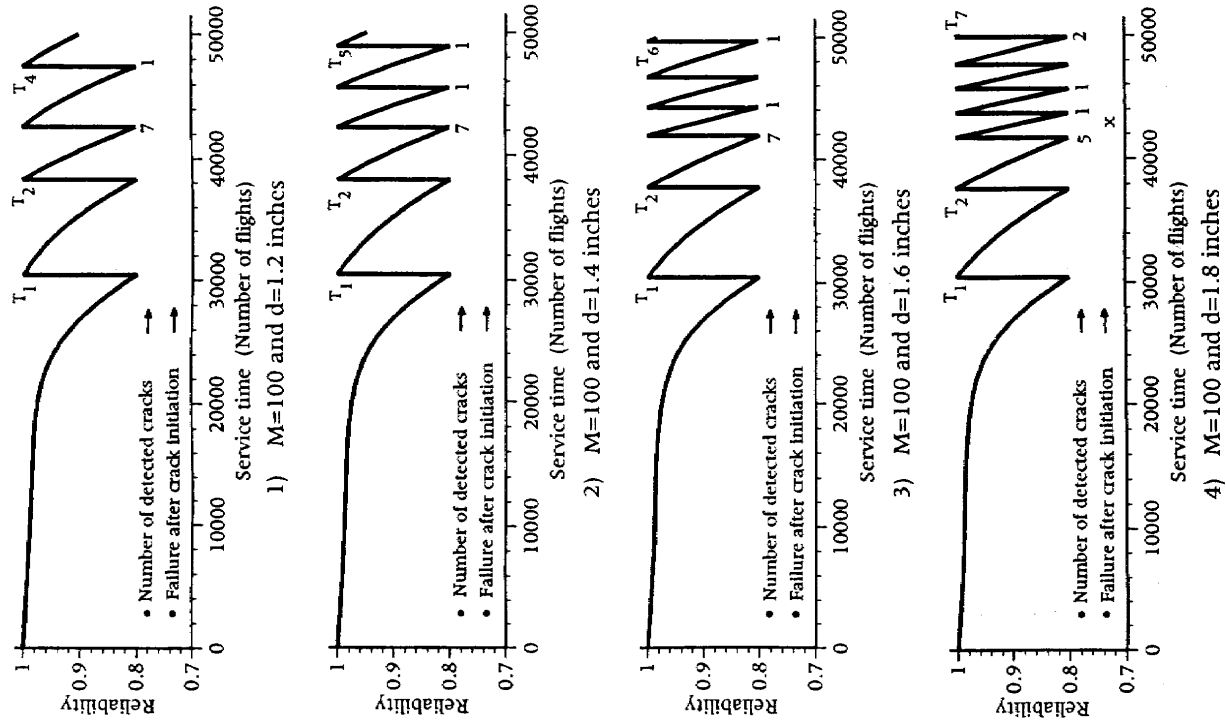(M=200 and Uncertain Parameters : β* and z)

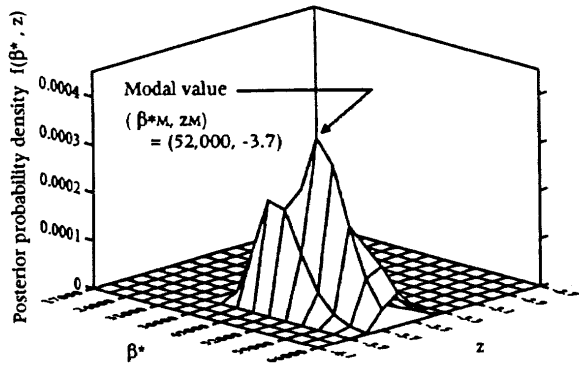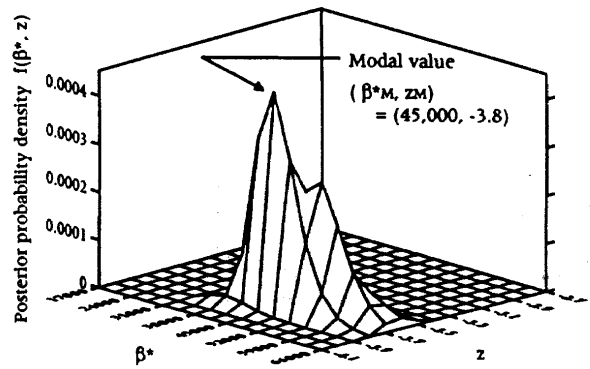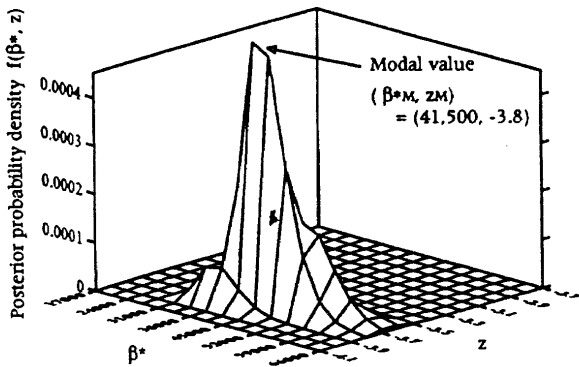Figure 4   Inspection Schedule and Structural Reliability
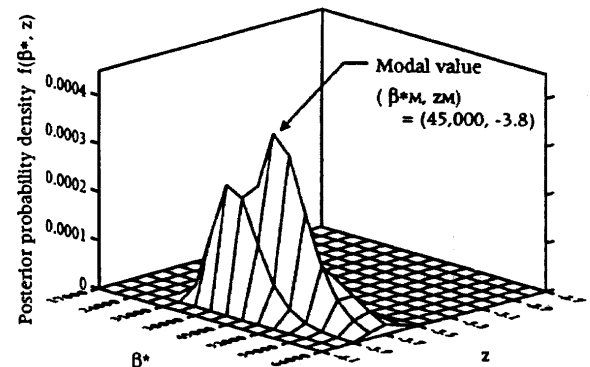(M=100 and Uncertain Parameters : β* and z)

1)   M=100 and d=1.2 inches

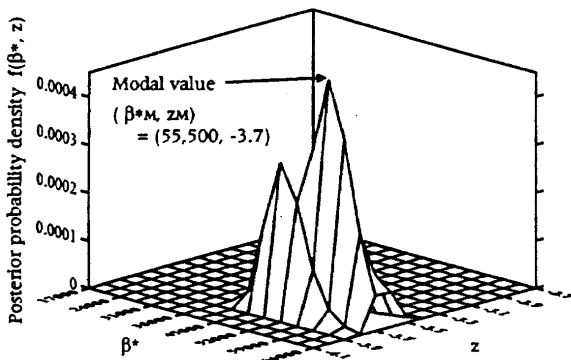2)   M=100 and d=1.4 inches

3)   M=100 and d=1.6 inches
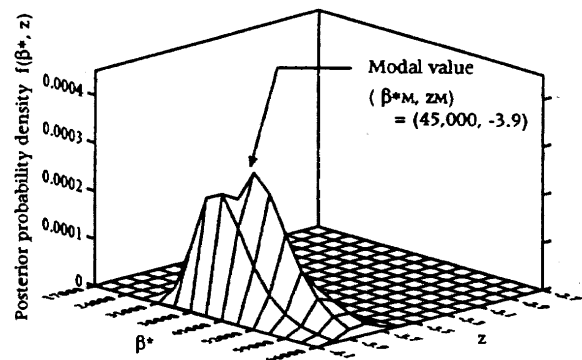
4)   M=100 and d=1.8 inches
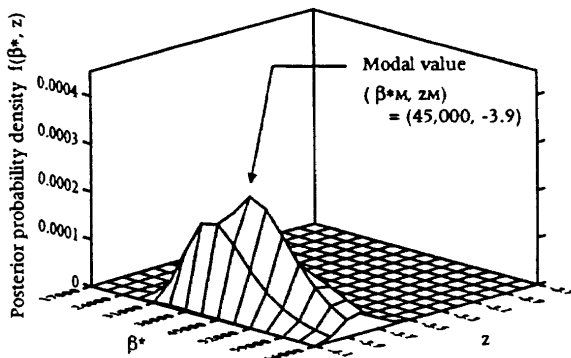
Figure 6     Posterior Joint Probability Density Functions at 3rd Inspection
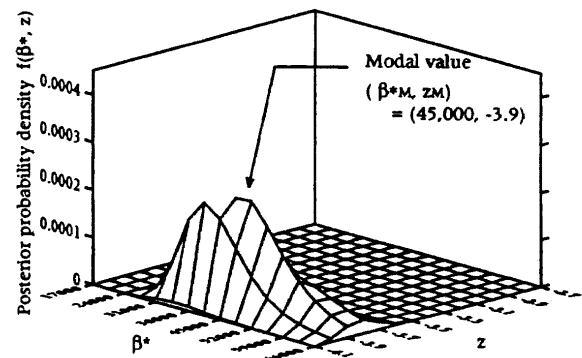(M=100 and Uncertain Parameters : β* and z)

1)   M=200 and d=1.2 inches

2)   M=200 and d=1.4 inches

3)   M=200 and d=1.6 inches

4)   M=200 and d=1.8 inches

Figure 7     Posterior Joint Probability Density Functions at 3rd Inspection
(M=200 and Uncertain Parameters : β* and z)

# 13

# Application of Infrared Stress Graphic System to Non-Destructive Evaluation of Composites

Sunao SUGIMOTO and Takashi ISHIKAWA

Composite Structure Section
Airframe Division
National Aerospace Laboratory

## ABSTRACT

An Infrared Stress Graphic System is applied to some CFRP composites for the purpose of non-destructive evaluation. Delaminations or matrix cracks exist in these example components. It is demonstrated that this system is appropriate for in-situ non-destructive evaluation of composites. The obtained stress distribution outputs basically agree with damage patterns by other non-destructive evaluation techniques and compare favorably with the numerical results of some available cases.

## 1. INTRODUCTION

It is difficult to apply some non destructive evaluation (NDE) techniques to objective test pieces under in-situ conditions. However, the infrared stress measurement technique shows an advantage as an in-situ NDE method due to its optical and non-contact nature. Based on such considerations, its potential and limitations must be examined in detail. Stress distribution on the surface of a specimen under applied cyclic loading is measured using an infrared stress graphic system (ISGS) for delaminated regions and transverse cracks in CFRP laminates, as a first step. The ISGS used here is JTG-8000 made by JEOL Co. LTD. in Japan. The measured temperature fluctuation amplitude at the surface is converted into applied stress amplitude with measured thermo-elastic stress coefficient. In the case of CFRP laminates, the temperature amplitude is almost proportional to transverse stress amplitude to fiber. The measured stress distributions are compared with ultrasonic C-scan outputs and soft X-ray radiograph, and in some cases, finite element calculations. Four typical examples of stress patterns as an NDE device are demonstrated in this paper. Prior to demonstration of the experimental results the theory of the measurement is briefly reviewed.

## 2. BRIEF REVIEW OF INFRARED STRESS MEASUREMENT THEORY

It is common for a temperature change to be caused by pressure variation in gaseous media under adiabatic conditions. In parallel to gas, it is also caused by stress in solid continua. A linear relation between a temperature change and an applied stress must hold. However, since the temperature change is often very small in the case of solids, it cannot be observed easily. The ISGS used in this paper aims at graphic presentation of a stress distribution by means of precise measurement of the small temperature change.

The basic physical principle of this system and thermo-mechanical characteristics of CFRP laminates are described in this chapter. The first key point is that temperature variation is measured in correlation with the applied cyclic loadings. Thus, a temperature change in this measurement is identified with a temperature amplitude in one period. In the case of an isotropic solid, measured temperature amplitude corresponds to the summation of applied principle stresses. In the case of in orthotropic media, such as a CFRP ply, it can be described [1] in a plane stress state as follows :

$$dT = -\frac{T}{\rho \cdot C_\sigma}(\alpha_L \cdot d\sigma_L + \alpha_T \cdot d\sigma_T) \qquad (1)$$

where

$dT$ : Temperature variation amplitude by cyclic stresses,

$T$ : Background temperature (in Kelvin)

$\rho$ : Density,

$C_\sigma$ : Specific heat at constant stress

$\alpha_L$, $\alpha_T$ : Coefficient of thermal expansion (CTE) in the longitudinal (L) and transverse (T) directions

$d\sigma_L$, $d\sigma_T$ : Cyclic stress amplitude in the L and T directions.

In this formulation, an irreversible temperature change caused by internal friction is neglected. By introducing two material constants, $K_{mL} = \alpha_L / (\rho \cdot C_\sigma)$, $K_{mT} = \alpha_T / (\rho \cdot C_\sigma)$, Equation (1) is rewritten as:

$$dT = -T(K_{mL} \cdot d\sigma_L + K_{mT} \cdot d\sigma_T) \qquad (2)$$

where $K_m$ is hereafter denoted as a thermo-elastic constant. The CTE property of CFRP, $\alpha_L \ll \alpha_T$, is well known [2]. Therefore, the thermo-elastic constant in the fiber direction is much smaller than the other, $K_{mL} \ll K_{mT}$. This means that the $dT$ by a stress in the fiber direction is relatively small. Consequently, the measured temperature variation amplitude at a specimen surface is dominated by $dT$ caused by a transverse stress. Thus, equation (2) can be approximated by the next equation [1].

$$dT = -K_{mT} \cdot T \cdot d\sigma_T \qquad (3)$$

It is also clear that dT for the same stress amplitude are ranked as $dT_T > dT_{(45)} \gg dT_L$ in cases of unidirectional (UD) CFRP.

## 3. BASIC MEASUREMENTS

The first step in the present method is a determination of a thermo-elastic constant, $K_{mT}$. Some 90 UD coupon specimens without any damage are loaded by a hydraulic testing machine, Instron 8501, in constant amplitude. Components of the ISGS system used, JTG-8000, are shown in Figure 1. This system provides us $dT$ as a result of frame by frame computation on temperature images. Stress amplitude $d\sigma_T$ is obtained through a load cell output and room temperature data $T$ is also required.

Before the following discussion, it should be pointed out that Equation (3) holds exactly for 90 UD. Averages of $dT$ in defined regions on coupon surface images of 90 UD are plotted as to some levels of stress amplitude $d\sigma_X$ in Figure 2 where a suffix X denotes the loading direction. An example of $dT$ distribution for this 90 UD is shown in Figure 2. These plotted data are best approximated by the next equation using the least square method.

$$dT = -6.58 \times 10^{-9} d\sigma_T \qquad (4)$$

This equation is indicated by a solid line in Figure 2. This result and the measured room temperature $T = 298 \, [\text{K}]$ are substituted in Equation (3). Then, we have

$$K_T = 2.21 \times 10^{-11} \, [1 / \text{Pa}] \qquad (5)$$

For checking the level of approximation in Equation (3), 0 and 45 UD coupons are measured in the same way. The results are also plotted as to stress amplitudes $d\sigma_X$ in Figure 2. The results of 45 UD are converted into transverse stress amplitude and plotted by a dashed line in Figure 2. The solid and dashed lines are very close to each other. In 0 UD measurements, it is clear that $\sigma_T = 0$. Hence, the following value is obtained from the measured data and Equation (2).

$$K_L = -1.16 \times 10^{-13} \, [1 / \text{Pa}] \qquad (6)$$

In the following, some practical procedures related to an actual measurement is described. Temperature amplitude images by this ISGS must be accumulated and averaged to increase the signal to noise (S/N) ratio. Therefore, applied loading must be cyclic with constant amplitude and period. A schematic explanation of a relation between a temperature history at a certain surface point and applied stress variation is indicated in Figure 3. A gradual temperature change off the

applied stress frequency is eliminated as shown. According to the simplest theory described in the previous chapter, the maximum tensile stress generates the minimal temperature. In other words, the peak and bottom in a stress waveform correspond respectively to the bottom and peak in a temperature waveform. However, a time lag between the stress peak and the temperature bottom is often observed in actual measurements. This time lag leads to a phase shift between two signals. In a real measurement procedure, it is necessary to find the optimum phase shift by which an absolute value of temperature difference is maximized.

## 4. APPLICATION TO DELAMINATION IN CF/EPOXY LAMINATE

This ISGS system is first applied to the measurement of quasi-isotropic [(45/-45/0/90)sym.] coupon specimens of CF/Epoxy (T400/#3631) laminate under tension - tension cyclic fatigue loading. Free edge delamination starts and propagates during loading for this type of laminates due to Poisson's ratio mismatch. The loading conditions used in the tests described in this chapter are as follows: Tension-tension with stress ratio R=0.1, load control mode and constant amplitude sine wave of 5 Hz. The total area of the specimen is inspected by the ISGS and by a ultrasonic C-scanner at an appropriate interval of loadings. Applied loading level during stress measurements is maintained at a lower level than delamination propagation criticals in this area scan. When a ultrasonic C-scan inspection for monitoring delamination propagation is done, specimens are detached from the hydraulic machine used. For a trace purpose of rapidly changing delamination propagation by the ISGS, line scan inspection is used to reduce the measurement time. It should be noted that measured stress here is $d\sigma_T$, the normal stress to the fiber direction, at the surface.

Delamination onset and propagation between 0/90 and alternately 90/0 are observed in this fatigue test. These delaminations develop with increasing loading cycles and stop with a remaining strip of delamination area of 1 ~ 2 mm in width. Measured results of stress distribution transverse to loading direction by the line scan are shown in Figure 4. In order to clearly indicate C-scan edges and delamination tips symbols of ↕ and ▲, respectively, are used in Figure 4. The measured stress pattern obtained by the area scan agrees well with an ultrasonic C-scan delamination image as indicated in Figure 5. The fact that free edge delaminations liberate surface stresses well plays a key role in such a good correlation.

Variation in stress distribution along with delamination propagation is calculated by using 20 node iso-parametric elements of a FEM software package, COMPOSIC. The true delamination experiments is located alternately appearance between in 0/90 and 90/0 interfaces as mentioned earlier. In the analysis, however, delamination location is hypothetically specified at the central plane of 90 layers for simplicity. Computations are done only for the region of $Z \geq 0$ by virtue of the assumed symmetry. Dimensions of this model are 25 mm in width, 0.6 mm in thickness and 25 mm in length. Element numbers in the X-, Y-, Z-directions are 8, 20, 4, respectively. Mesh size is uniform in the X- and Z-directions and variable in the Y-direction. Fine pitch is employed around the delamination tips and the edges. Boundary conditions concerning delamination are assumed so that nodes on the Z=0 plane are fixed in the Z-direction except for the delaminated area. Loading is modelled by sets of conditions so that nodes on the X=0 plane are fixed in the X-direction and nodes on the X=25 plane are given specified uniform displacement in the X-direction. Stress states are computed for three delamination width ratios, 0, 40 and 92%. After reaction nodal forces in the non-delaminated model are computed for given displacements corresponding to 0.8% strain, 40% and 92% delamination models are recalculated so as to have the same total reaction forces. This procedure implies the load control mode in the real experiment. The elastic constants used are assumed based on measured elastic constants in the test coupons and listed in Table 1.

The delaminated area shows an out-of-plane deformation because the delamination violates the symmetry condition. Transverse nodal stresses to fiber, $\sigma_T$, on the top 45 layer surface (at Z=0.6) are computed along the center line. These results for the above mentioned three delamination ratios are shown in Figure 6. It can be recognized that the initial stress plateau is decayed, corresponding to delamination propagation, and that stresses drop at delamination edges. The stress

drop moves inside as the delamination propagates. Numerical results indicate the stress drop and sharp stress rise across the delamination edge. Calculated results also indicate that stress level at the center decreases when the delamination is seriously propagated. In a broad sense, experimental and numerical results qualitatively coincide well with each other. In a rigorous sense, however, the measured stress level converted by $K_{mT}$ of the unidirectional material deviates from the predicted results to some extent. Possible causes of such deviation are now being pursued for approaching a final quantitative agreement. In summary, this ISGS can be used at least as an in-situ means of non-destructive evaluation for composite laminate if damage clearly affects the surface stress state.

## 5. MATRIX CRACK OBSERVATION IN
## CF/PI-SP LAMINATE

The second example is specimens made of CF/thermoplastic (T800/PI-SP) laminates where the main concern is how matrix cracks can be seen through the ISGS. PI-SP is a new thermoplastic resin developed by Mitui-Touatu Co. LTD. The quasi-isotropic stacking sequence is the same as in the previous chapter, (45/-45/0/90)sym. The specimen is a coupon with GFRP tabs. Loading conditions including frequency, waveform, control mode and R are also the same as the previous example. Applied loading level ($\sigma_{Xmax}$ =100MPa) during the stress measurement is again maintained at a lower level. Soft X-ray radiography is used mainly for checking matrix cracks. Frame by frame summation and average is repeated for improved S/N ratio. Thus, it takes almost twenty-five minutes to measure these specimens.

Figure 7 depicts a measured stress pattern for a cracked specimen on a surface 45 layer. Matrix crack locations are indicated by the soft X-ray picture of Figure 8. Lower stress regions are observed along the matrix crack line on the surface 45 layer in Figure 7. Thus, stress liberation in the vicinity of the matrix cracks can be visualized to some extent.

Stress distribution with the matrix crack is calculated again by using 20 node iso-parametric elements of COMPOSIC. The model size is assumed to be the same as reality and only one matrix crack is supposed to exist at the center of the surface 45 layer along the fiber direction. As in the previous chapter, symmetry is also assumed. Therefore, the FEM model implies two matrix cracks symmetrically arranged with respect to the central plane. The numerical result of this model is shown in Figure 9. This graphic data indicate a narrow strip region of reduced stress and they agree basically with experimental data.

## 6. DELAMINATION PATTERN IDENTIFICATION IN CF/EPOXY LAMINATE FOR CAI SPECIMENS

CF/Epoxy (AS/410) CAI specimens with impact delamination are inspected by the ISGS next. The laminate stacking sequence is quasi-isotropic, [(45/0/-45/90)6]sym.. Loading conditions are as follows: compression - compression cyclic loading, load control mode and sine waveform of one Hz with a constant amplitude. Applied nominal stress amplitude is specified between -2 and -23 MPa during stress measurement. The level of this compression peak stress is almost half that of local initial buckling stress of the delaminated region [3] and is considered to be much lower than the delamination propagation trigger.

Figure 10 shows a typical ISGS stress distribution image in an impact side. Stress deviation from a uniform level can be found in regions surrounding the impact point. Higher stress regions opposite each other around the impact correspond to regions of small thickness above the first delamination. This fact implies that compressive stresses can be carried across matrix cracks in the impact side. Figure 11 shows a typical ISGS image in a back side of the impact. Wide open matrix cracks exist in the delaminated region in the back side surface ply and they create completely separated, rather floating strips from substrate laminates. Therefore, load transferring capacity in such floating strips is almost lost even for compression. Large low stress regions in Figure 11 correspond to accumulated floating strip delaminations. These ISGS stress observations contribute to examination and evaluation of the mechanical model [3] for CAI behavior prediction.

## 7. INSPECTION OF CF/PEEK WING BOX WITH IMPACT DAMAGE

A CF/PEEK wing box structure with an impact delamination under fatigue loading is inspected by the ISGS system as the final example here. Dimensions of this box are 900 by 452 by 150 mm. The impact side is located in a bottom surface where compression stress dominates. Although simulated quasi-random load spectrum is used in the main fatigue tests, cyclic loadings of constant amplitude and frequency are required for the ISGS measurement. Therefore, simple constant sine loadings appearing about 10 times in the last phase in each modelled flight [4] are extracted from the loading sequence and used here. The extracted parts are cancelled in the later loading patterns.

Figure 12 depicts stress distribution on the bottom panel where a schematic illustration of the loading situation and a target area is also given. A clear impact delamination identification cannot be obtained because the delamination size is very small in this case judging from C-scan image. If delamination type damage is isolated from any free edges, its effect upon surface stress is considered to be limited. The present example looks like a typical case. Note that the ISGS data indicate stress fluctuation caused by back stiffeners. An advantage of the ISGS technique as an in-situ measurement devise of stress in structure is suggested.

## 8. CONCLUSIONS

An ISGS system is applied to some CFRP composite components for an NDE purpose. In CF/Epoxy coupon fatigue tests, the measured stress pattern obtained by an area scan mode agrees well with an ultrasonic C-scan delamination image. The fact that free edge delaminations liberate surface stresses well plays a key role in such good correlation. However, a slight difference can be found between calculated and measured stress levels. Possible causes of such difference are now being pursued for approaching a final quantitative agreement. In CF/PI-SP specimens, matrix crack locations are identified by lower stress regions along them and agree well with a soft X-ray picture. Higher stress regions opposite each other around the impact are found in CF/Epoxy CAI specimens and they correspond to regions of small thickness above the first delamination. Such ISGS stress data contribute to an evaluation of the mechanical model for CAI behavior. In a CF/PEEK wing box application, a clear impact delamination identification can not be obtained due to small delamination size. Relations between a delamination and free edges affect the sensitivity of the ISGS measurement. In summary, it is demonstrated that the ISGS system can be used as an in-situ NDE device for composite if damage affects the surface stress state. Some limitations and problems to be solved are also clarified. The rest of the work remains to be challenged in the future.

## REFERENCES

[1] K. Kageyama: Materials Science, Vol. 26 No. 1, 1989, pp.16-21 (in Japanese).

[2] T. Ishikawa: J. Composite Materials, Vol. 12, 1978.4, pp.153-168.

[3] T.Ishikawa, S. Sugimoto, M. Matsushima and Y. Hayashi: Composite Science and Technology, VOL. 55, 1996, pp. 349-363.

[4] T.Ishikawa, Y. Hayashi, S. Sugimoto and M. Matsushima: Proceedings of 7th Japan-US Conference on Composite Materials, Kyoto Japan 1995.6, pp.433-440.

Table 1 Used Elastic Constants

| $E_X$ | 120.0GPa | $G_{XY}$ | 4.62GPa |
|-------|----------|----------|---------|
| $E_Y$ | 10.4GPa | $G_{YZ}$ | 3.47GPa |
| $E_Z$ | 10.4GPa | $G_{ZX}$ | 4.62GPa |
| $\nu_{XY}$ | 0.36 | $\nu_{ZX}$ | 0.36 |
| $\nu_{YZ}$ | 0.50 | | |
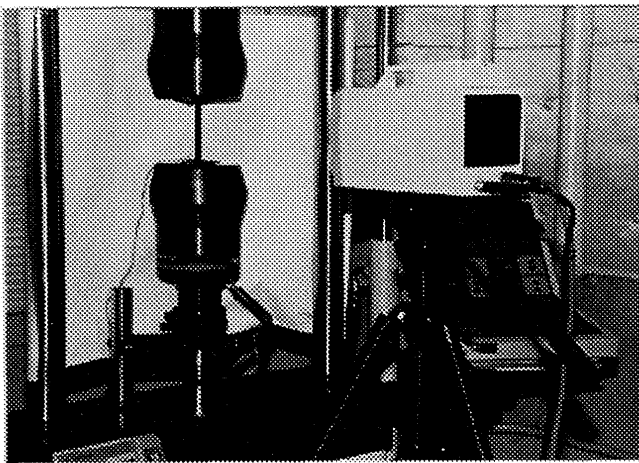


a) Sensor
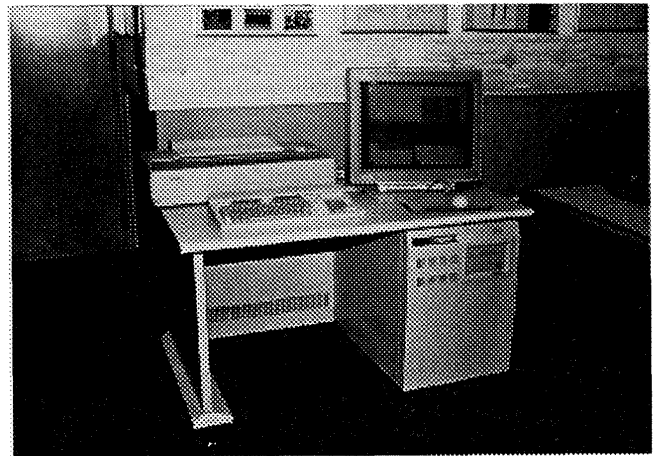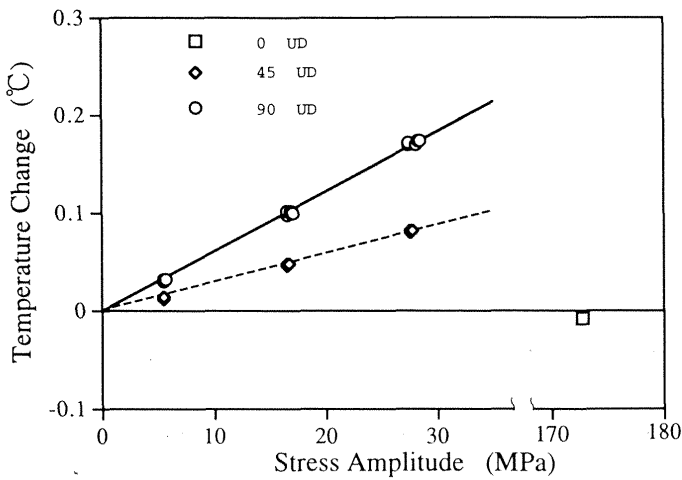


b) Data Processor

Figure 1 Infrared Stress Graphic System JTG-8000



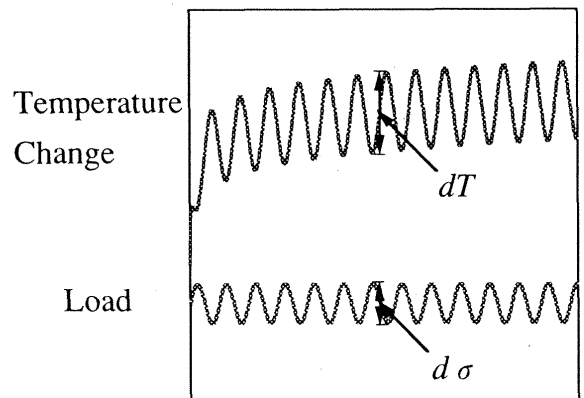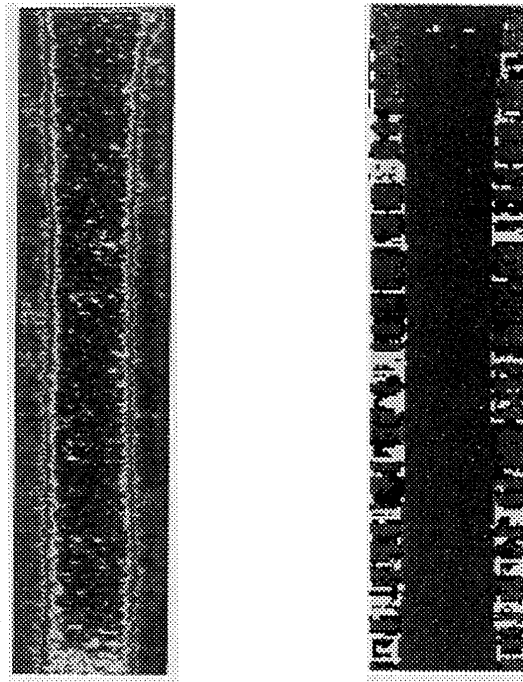Figure 2 Relationshipsbetween $dT$ and $d\sigma_x$



Figure 3 Schematic Situation in Temperature and Load History

Stress Measurement          C-scan Picture

Figure 4  A Comparison Measured Stress Pattern with a C-scan Result for
CF/Epoxy Coupon Specimen with Edge Delamination.



N=0                 N=1000                 N=9000
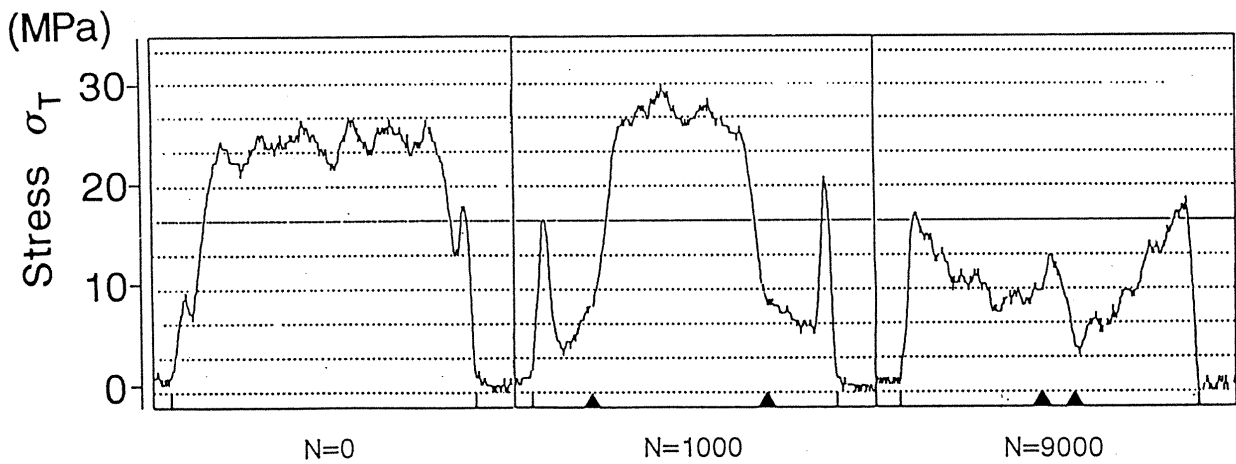
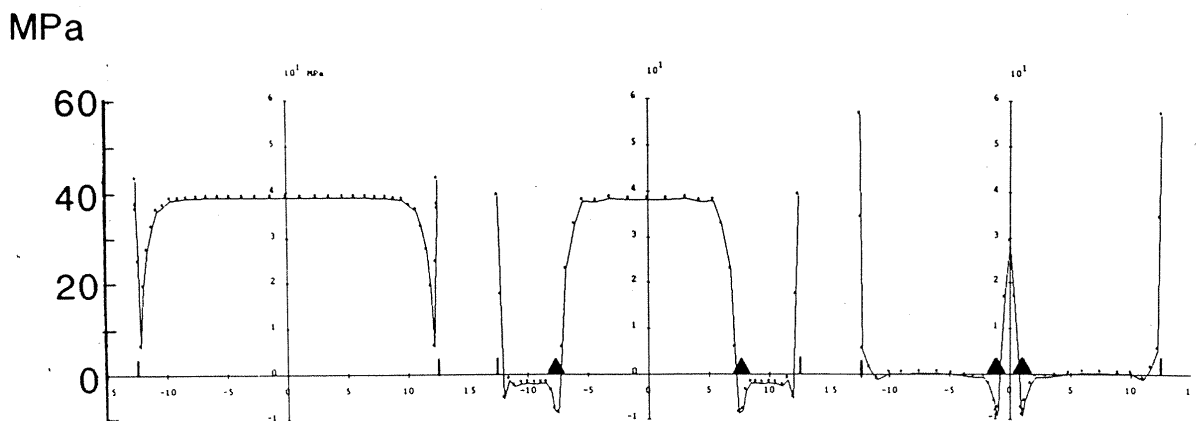Figure 5  Measured Results of Transverse Stress on Top 45 Layer Surface



Figure 6 Numerical Results of Transverse Stresses $\sigma_T$ in Top 45 Layer Surface of Delaminated Coupon
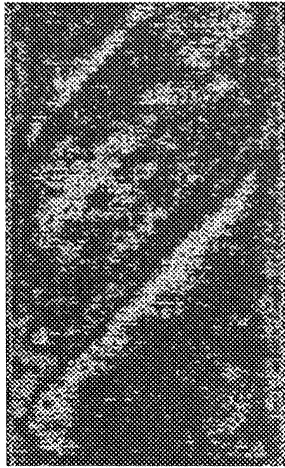
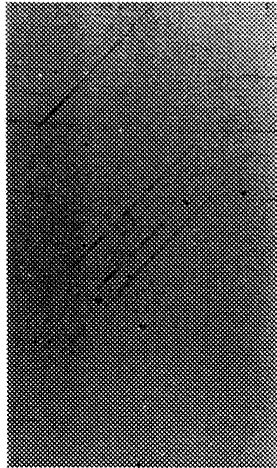Figure 7 Measured Stress in
CF/PI-SP with Matrix Cracks
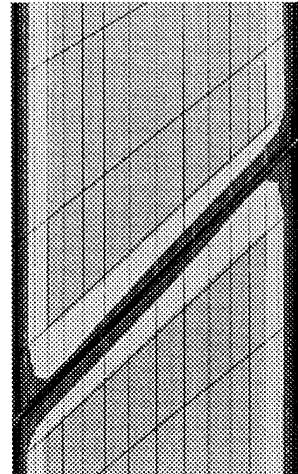


Figure 8 Soft X-ray Picture of
CF/PI-SP



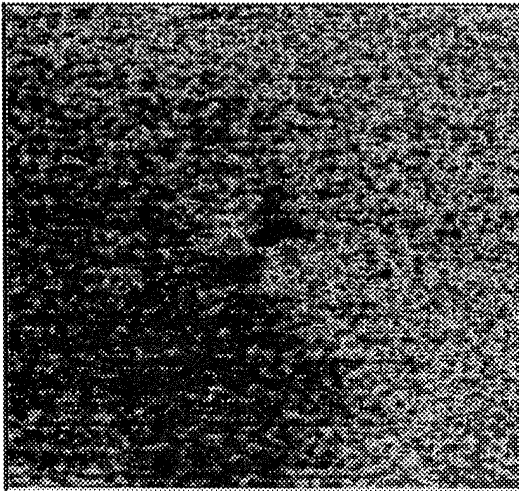Figure 9 Numrical Sulution for
CF/PI-SP with Matrix Crack



Figure 10 A Typical ISGS Result for a
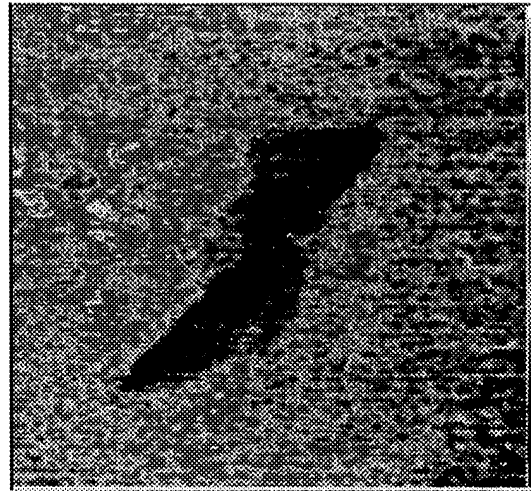CF/Epoxy CAI Specimen in an Impact Side



Figure 11 A Typical ISGS Result for a
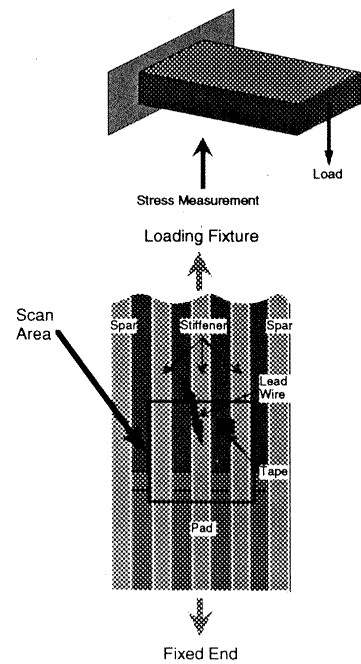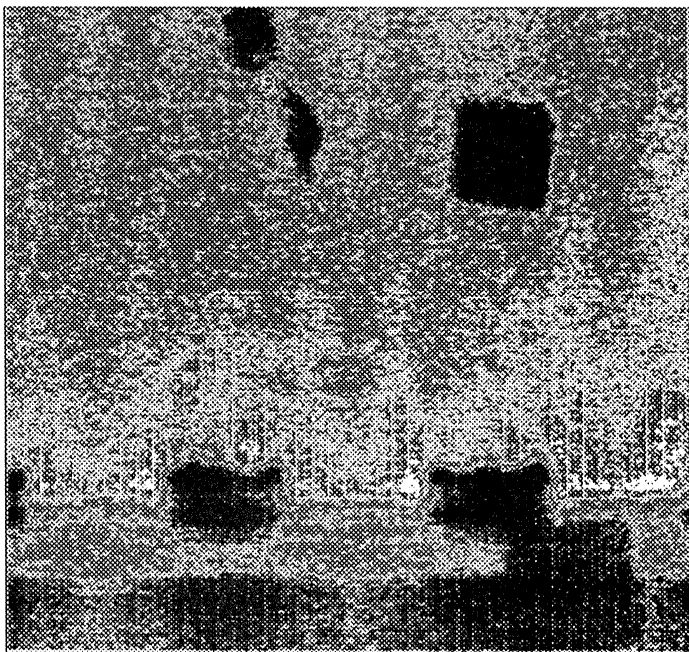CF/Epoxy CAI Specimen in an Back Side



Figure 13 A Measured Stress Pattern by ISGS for a CF/PEEK Box Model
with a Schematic Illustration about Scan Area.

# 14

# ANALYSIS AND EXPERIMENTS OF POSTBUCKLING BEHAVIOR OF T-SHAPED CFRP STIFFENERS

**Takashi Ishikawa, Yoichi Hayashi and Masamichi Matsushima**
Airframe Division
National Aerospace Laboratory
Tokyo, JAPAN

## 1. INTRODUCTION

In the strength design of composite primary aircraft structures, initial buckling prediction and postbuckling behavior description are the major critical factors. The present paper describes a comparison between numerical and experimental results for linear buckling stress and postbuckling behavior of T-shaped carbon fiber/polymer composite (CFRP) stiffeners used commonly in actual aircraft structures. The final goal is to estimate numerically the ultimate strength after buckled state based on rather simple assumptions. The software used here is the commercial level code, NISA-II. Some auxiliary numerical method such as Rayleigh-Ritz method is also used. The tested stiffeners are made of CF/epoxy and CF/PEEK(Poly-Ether-Ether-Ketone). The latter material is a potential candidate for a drastic weight reduction of aircraft structure.

## 2. BRIEF DESCRIPTION OF COMPRESSION TESTS OF T-STIFFENERS

T-stiffeners made of CFRP were fabricated by Fuji Heavy Industries (FHI) LTD[1]. An overview of the shape and dimension of the specimens is shown in Fig.1. Some comments are given here for better description of the model. The materials used are CF/PEEK (APC-2) and CF/epoxy (P3060). Flange width, $b_f$, of most specimens is 42mm, referred as N-type. Specimens with some wider flange width referred as W-type are also prepared for CF/epoxy. Web width, $b_w$, is determined as the following equation so that it exceeds half of $b_f$ slightly. Model length is mostly 140mm and the rest is 280mm.

$$(b_w - t) / \{(b_f - t) /2 \} = 1.09 \qquad\qquad 1)$$

Model thickness is well controlled into 2.6 - 2.7mm range in the case of CF/epoxy. For CF/PEEK models, the thickness control was not perfect and it tended to thinner with considerable scatter than the designed thickness because the fabrication was done a few years ago under unmatured know-how. In the present situation, accuracy of the thickness in CF/PEEK components is reaching the level of CF/epoxy. A global warping or distortion of the model was measured for some specimens in order to determine initial imperfection extent.

Stacking sequence used mainly, designated A, is shown in Fig.1 where the total ply number is 20. A few specimens have the other sequence of B with 20 plies, $(45/0_2/-45/0_2/45/0/-45/90)_{sym.}$, in order to examine the effect of $D_{16}$ and $D_{26}$ on initial buckling behavior.

Compression tests were done by a stroke controlled testing machine (Instron 1128). A flat steel compression plate was used without any potting end. For doing that, a precise fitting between the plate and specimen was required through pressure-sensor paper. Crosshead speed used was 0.5mm/min. An examination of the boundary conditions to describe the real situation is one

focussing point of the present paper. A picture of the test for a specimen of 140mm in length is shown in Fig.2. At actual testings, sampled data of a load, two lateral deflections of web and flange centers in terms of the loading direction, and 13 strain gage indications were continuously recorded by a computer data logger at a 200msec. sampling interval.

## 3. OUTLINE OF NUMERICAL METHODS AND INPUT MATERIAL DATA

The main tool for the numerical calculation was a commercial level finite element code, NISA-II. The used element type was an isoparametric laminate shell element of 4 nodes. This element is capable of consideration of transverse shear deformation. The number of elements was mostly 168, which will be shown indirectly later. The lowest eigenvalue means the buckling load and then buckling stress is obtained. Convergence check told that this subdivision was practically good enough within 1% error of buckling load.

The other tool of calculation is a sort of Rayleigh-Ritz method which was used for a prediction of linear buckling stress at the initial phase of research. The purpose of this method is to examine the effect of $D_{16}$ and $D_{26}$ on initial buckling behavior. However, the detail of description is skipped here.

Regardless of the numerical tools, the assumed elastic moduli of a unidirectional CFRP lamina is crucial for the numerical prediction. For the CF/PEEK material system, verified values in the authors' work[2] are also adopted. For the CF/epoxy material, the estimated moduli based on the author's method[3] are modified corresponding to $V_f = 67\%$. They are summarized in Table 1 where the values of transverse Poisson's ratio which do not provide serious effects might be greater than reality.

## 4. COMPARISON OF PREDICTION AND EXPERIMENTS FOR LINEAR BUCKLING BEHAVIOR

The first point of discussion is the effect of $D_{16}$ and $D_{26}$ on the linear buckling stress. However, the detail is skipped here except for a brief comment that larger $D_{16}$ reduces the buckling stress.

The second but the most practical point is a dependency of the buckling stress upon the ratio of the flange or web width to its thickness. If fabrication technology of stiffener is not matured enough, flange or web thickness may show some fluctuation. So, such a dependency is considered to be important. Comparison between numerical initial buckling stresses by NISA-II and experimental results are shown in Fig.3. Numerical results are based on the combination of stacking sequence A, fixed loading and supporting edge conditions, and realistic corner radii (R=3mm for CF/epoxy and R=2mm for CF/PEEK). It should be also noted that initial imperfection of the order of 1/100 thickness is included in modelling to keep compatibility with nonlinear analysis stated later, and that Eq.(1) is applied for changing $b'_w$ ($=b_w - t/2$).

Numerical predictions are generally in excellent agreement with experimental results. One crucial point for such good correlation is fixed boundary conditions at the edges. Figure 3 shows that the initial buckling stress rapidly decreases as $b'_w/t$ increases. This finding leads to unintentional loss of buckling stress margin due to slightly less thickness than designes. The experimental results for CF/PEEK indicated by filled legends correspond to some scattered values of $b'_w/t$ which resulted unintentionally because of the unestablished fabrication technique of those days. This point is very important for practical application of CF/PEEK aircraft structures.

The third point of discussion about the initial buckling behavior is an effect of unidirectional filler string inserted at the intersection line of the T-stiffener upon the buckling stress. The amount of this filler can be geometrically related to a corner radius along the line. So, it can be translated as the effect of the corner radius. This problem has been treated in some literature[4],[5]. A target on this research is to find the simplest approach for consideration of this effect. Although the detail is omitted here, it is revealed that the FEM model using the laminate element with UD core material can provide reasonable results and that neglect of this corner radius effect gives considerably poor agreement with experiments.

## 5. COMPARISON OF NUMERICAL AND EXPERIMENTAL POSTBUCKLING DEFORMATION

The next point of discussion is postbuckling behavior, particularly out-of-plane deformation. Capability of geometrical nonlinear analysis is indispensable for FEM software to obtain this type of solution. Another indispensable factor is to introduce the initial imperfection. An imperfection shape sinusoidal in the x direction and linear in the y direction is assumed where the maximum amplitude is specified as $1/100$ of the thickness after the average of measured imperfection amplitudes. The element used and mesh pattern are the same as in the linear solution.

Numerical postbuckling analysis was conducted for the case of W-type CF/epoxy T-stiffener, $L=140$, $b_f=51.0$, $b''_w=26.5$, $t=2.54$, and $R=3$ (unit:mm). Two types of loading edge boundary conditions were tried: simply supported and fixed. Two loading modes of displacement controlled (flat compression) and load controlled are also tried in the calculation. Flat compression is modelled so that every node has a common value of displacement in the compression direction. At the first stage, numerical deformation results were compared with experimental deformation shapes. It was found that the agreement was excellent. Next, stress -out-of-plane deflection relations at the center are plotted and compared in Fig.4. The plot of numerical results was done for a 2mm inside point from the edge of the web corresponding to the deflection sensor pickup location. An experimental curve was chosen from the results of four specimens where only a small scatter in data was observed.

Figure 4 indicates first that the results based on the simply supported boundary conditions provide the poorest result plotted by a line with triangles. It can be understood that the fixed condition was almost realized by the flat compression for the present T-stiffener. The load controlled mode (Load Cnt.:dashed line in the Fig.4) apparently provides the best solution. However, load re-distribution after buckling can not be included and axial deformation is different from the flat compression condition in this loading mode. Therefore, this coincidence is regarded merely as "apparently". The most realistic loading mode must be the displacement controlled (Disp. Cnt.:lines with filled and open circles) mode. Thus, some other reason should exist to explain why the numerical prediction curve deviates from the experimental one, particularly at higher stress regions. A convergence check for such a nonlinear portion of behavior was done for cases of a baseline 168 and a fine 672 element and the result was plotted by lines with filled and open circles respectively in Fig.4. Although a slight drop in the stress can be observed by the finer mesh, the tendency of the behavior is considered to be identical. By eliminating some other possibilities, we can reach the following estimation. A most probable reason for the present discrepancy between numerical and experimental postbuckling behavior can presumably be ascribed to material nonlinearity of CF/polymer composites in the fiber direction[2],[6]. Due to this effect, longitudinal elastic modulus of unidirectional CFRP decreases seriously at higher stress. Unfortunately, this effect is not considered in the current analysis. The proof is left for future work.

A similar comparison was done for the case of N-type CF/epoxy T-stiffener, $L=140$, $b''_w=21.6$, $t=2.66$, and $R=3$ (unit:mm). The indication of the chart is skipped here and it is merely mentioned that prediction coincides well with the experiments.

## 6. COMPARISON OF NUMERICAL AND EXPERI-MENTAL POSTBUCKLING LOCAL STRAIN AND FINAL FAILURE STRENGTH

After the confirmation of an agreement between the prediction and experiments for lateral deformation, the next interest is the comparison of local strain behavior in the postbuckling range. Experimental back-to-back strain outputs for W-type CF/epoxy at the flange center and 5mm inside from the edge are shown in Fig.5 by solid and solid with bar lines. Numerical predictions are also indicated by circles and triangles. It can be understood that they agree very well. This fact implies the possibility of prediction of the final failure behavior of the present T-stiffeners.

As the final goal of the present research, the final strength prediction was conducted next under three major assumptions. The first is that material strength can be determined as unique values and predicted by a certain failure law in one lamina. The second is that the final failure of the T-stiffener occurs instantaneously when the highest stress at a certain point in a lamina reaches the designated failure law. This assumption implies that no progressive failure is considered here. By AE signal monitoring in the actual tests, this assumption is shown to be rather realistic, particularly for the CF/epoxy pieces. The third assumption is the neglect of a interlaminar stress state near free edges.

Geometrical nonlinear FEM calculations were done for CF/epoxy stiffeners. The assumed failure law is the simplest maximum stress (equivalent to strain) law. Employed baseline strength values are as follows; $F_L=1726MPa$, $F_L'=1079MPa$, $F_T=69MPa$, $F_T'=196MPa$, and $F_{LT}=108MPa$. Unfortunately, these values were not necessarily obtained through experiments. The active limit for the failure was eventually $F_L'$ for all the calculations. The maximum compressive stress in the fiber direction always reaches this limit at the closest $0°$ lamina from the back surface of the flange (16th lamina of 20 from the web-intersection surface), or the 16th lamina which is $0°$ in the web (5th from the back).

In the actual determination of the failure load, linear interpolation of the load steps is required before and after reaching the maximum stress criterion. By repeating such nonlinear calculations and interpolation for various shape parameters, $b_f$, $b''_w$, $t$, and $\ell$, we can obtain compressive strength prediction curves for T-stiffeners. Those parameters were varied under the condition of Eq.1). The results are shown in Fig.6 for cases of CF/epoxy $L=140$ and 280mm. The experimental data around 7 and 9 of $(b_f-t)/2/t$ values correspond to N and W types, respectively. It can be observed that experimental values for the N type are slightly lower than the prediction and that those for the W type are higher, although the general agreement is rather good. This figure can be regarded as the verification of predictability of the final strength through the present calculation if the failure happens rather instantaneously.

## 7. CONCLUDING REMARKS

Linear and nonlinear buckling behavior of CFRP T-stiffeners were successfully analyzed by a FEM code. The width to thickness ratio is a very important parameter for good prediction. Corner radius is also important. Longitudinal material nonlinearity of UD-CFRP will provide better agreement in the nonlinear part of the prediction. Final compressive strengths are also predictable.

## ACKNOWLEDGMENTS

## REFERENCES

1. Ishikawa, T., et al., Proceedings of 14th Symposium of Composite Materials, Japan Soc. for Comp. Mater., Kanazawa, Japan, (1989), p.53 (in Japanese).
2. Ishikawa, T., et al., Composite Structures, Vol.23, (1993), p.25.
3. Ishikawa, T., et al., J. Composite Materials, Vol.11, (1977), p.332.
4. Bonanni, D.L., et al., Proceedings of AIAA 29th SDM Conf., Baltimore, MD USA, (1988), p.313.
5. Sambongi, S., Proceedings of 33th JSASS/JSME Structures, Japan Soc. for Aero. Astro. Sci., Yonezawa, Japan, (1989), p.58 (in Japanese).
6. Ishikawa, T., et al., J. Materials Science, Vol.20 (1985), p.4075.

Table 1   Assumed Elastic Moduli of UD-Lamina (unit:GPa)

|  | $E_L$ | $E_T$ | $G_{LT}$ | $\nu_L$ | $\nu_{TT}$ |
|---|---|---|---|---|---|
| CF/PEEK | 117.3 | 10.30 | 4.62 | 0.38 | 0.5 |
| CF/epoxy | 137.0 | 12.00 | 5.50 | 0.34 | 0.5 |

**Nxcr**
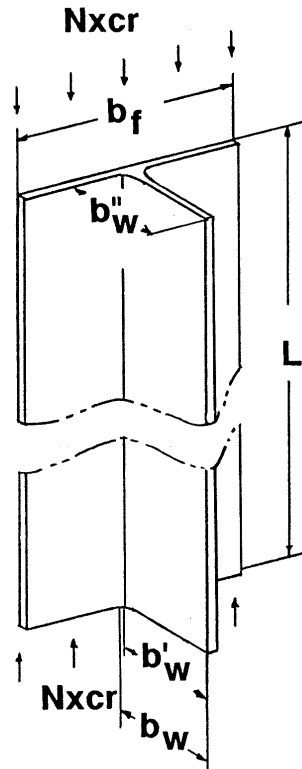
**N-Type bf=42**

**bw=24**

**L=140**
**(L=280)**

**W-Type bf=51**

**bw=29**

**L=140**

**Typical Ply Thickness:**

**0.118; C/PEEK**

**0.127;**
**0.133;** **C/Epoxy**
**(unit: mm)**

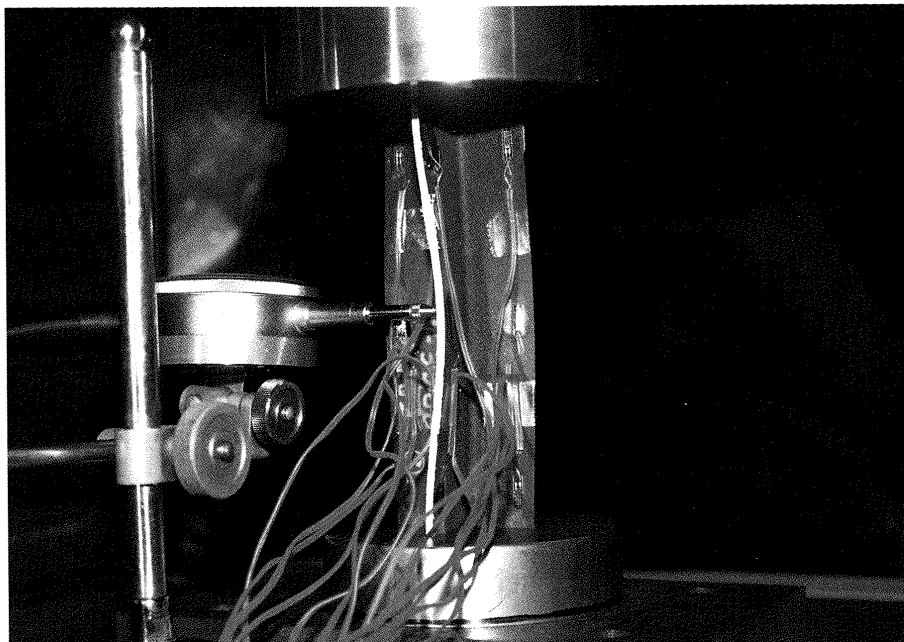**Stacking Sequence:**

**A: (45/-45/-45/45/0³/90/0²)sym.**

$b'_W = b_W - t/2$     $b''_W = b_W - t$

**Figure 1   Shape and Dimensions of T-Shaped Stiffeners**



**Figure 2   Picture of Compression Test of T-Stiffener**
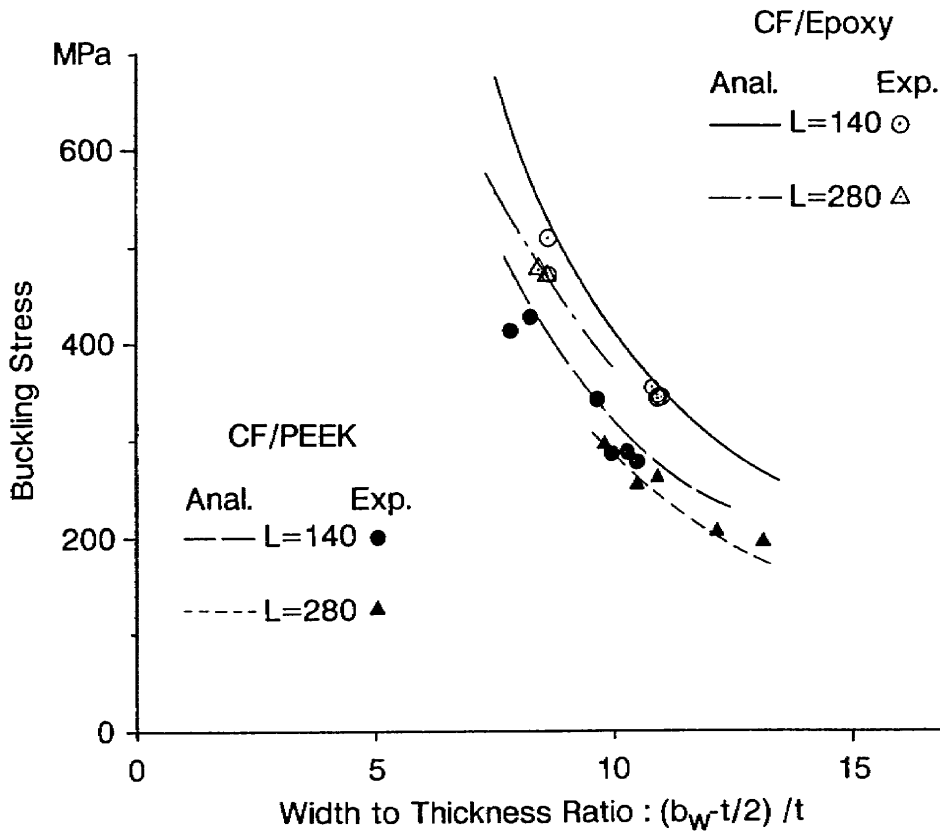
**Figure 3  Dependency of Initial Buckling Stress on Width to Thickness Ratio (b'$_w$ / t)**
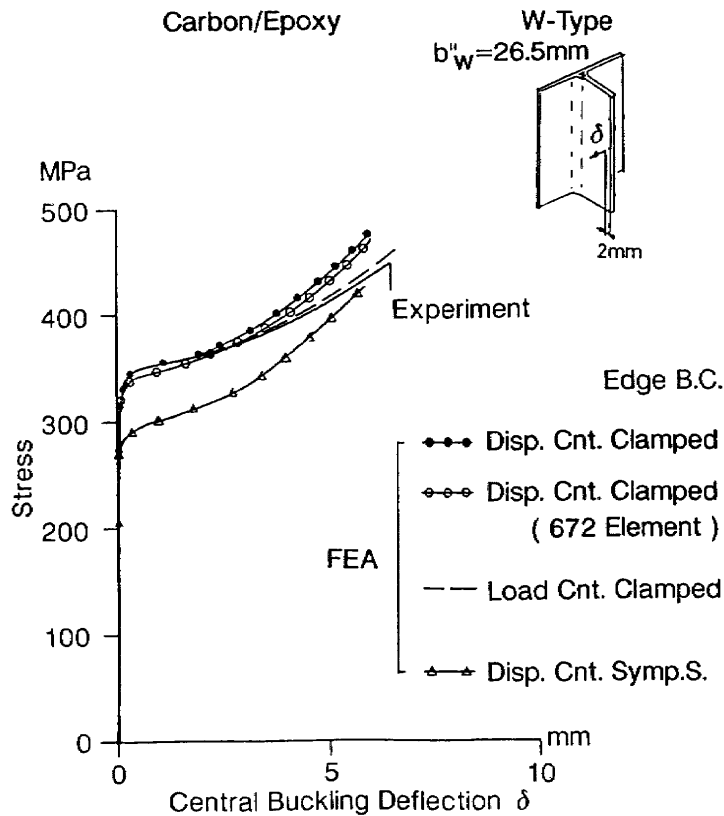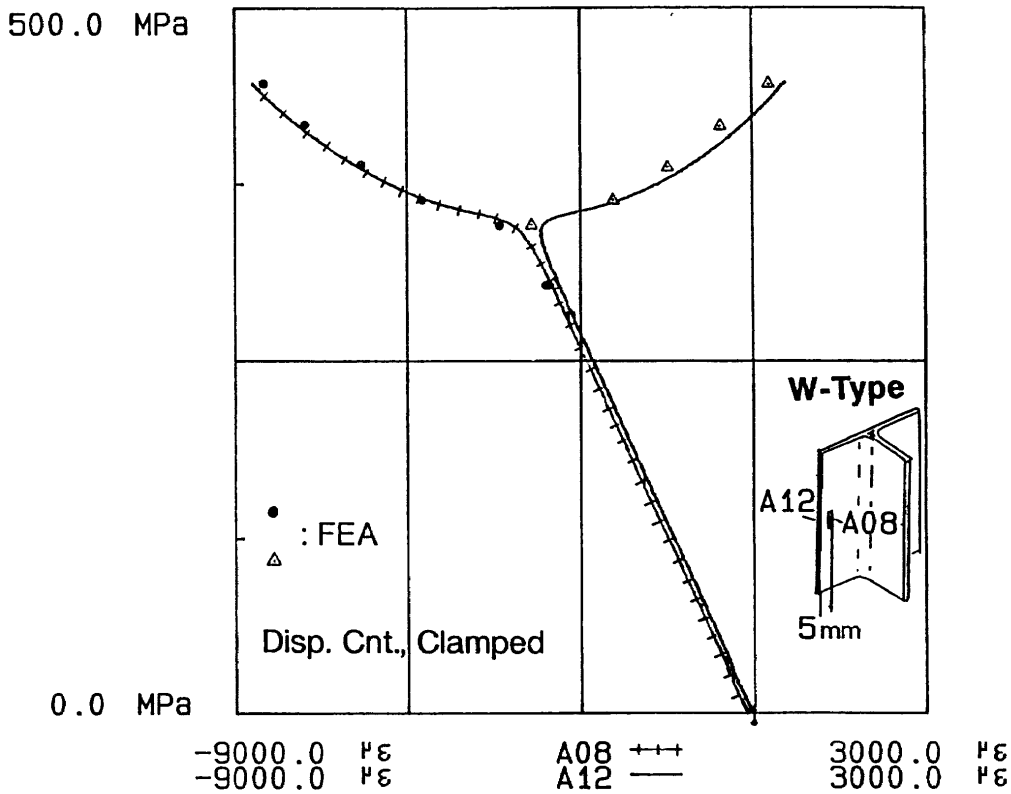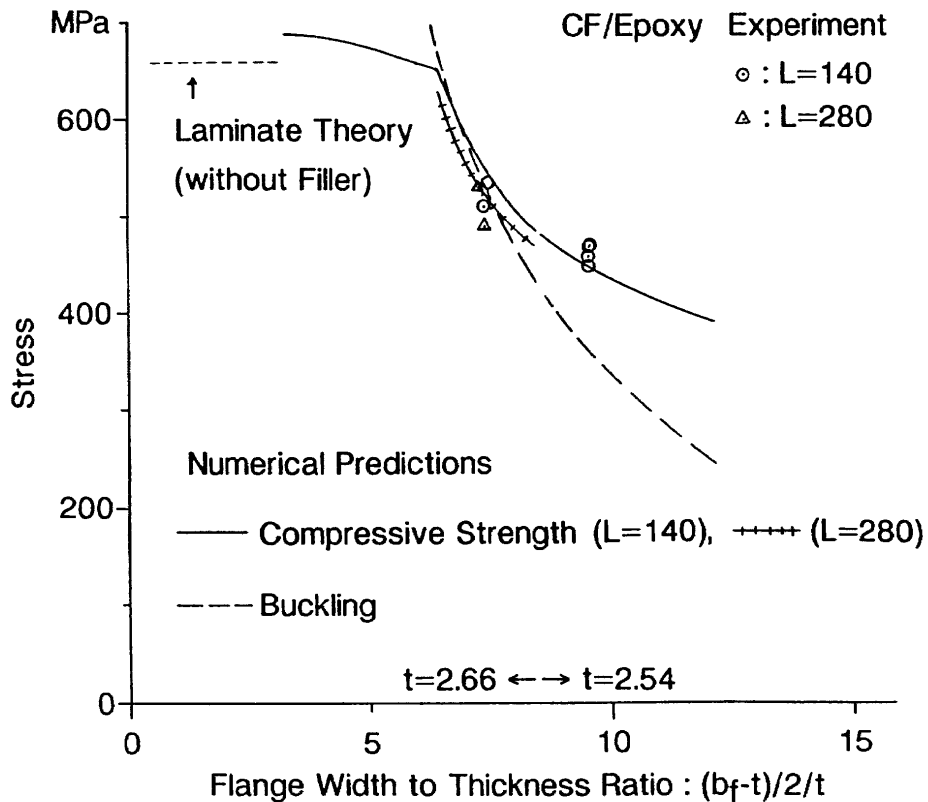


**Figure 4   Comparison of Predicted Postbuckling Central Out-of-plane Deflection with Experimental Results for W-Type CF/epoxy Specimen (L = 140mm)**

500.0 MPa

0.0 MPa

-9000.0 με
-9000.0 με

A08 ┼┼┼
A12 ──

3000.0 με
3000.0 με

- : FEA
△

Disp. Cnt., | Clamped

W-Type

A12  A08

5mm

**Figure 5 Comparison of Predicted Back-to-back Strain Behavior on Mid-Flange with Experimental Results**

MPa

CF/Epoxy Experiment

⊙ : L=140
△ : L=280

Laminate Theory
(without Filler)

600

Stress

400

Numerical Predictions

200

── Compressive Strength (L=140), ┼┼┼┼ (L=280)

── ── Buckling

t=2.66 ←──→ t=2.54

0

0        5        10        15

Flange Width to Thickness Ratio : (b$_f$-t)/2/t

**Figure 6 Comparison of Predicted Final Compressive Failure Stress with Experimental Results**

# 15

## Fracture Mechanics Approach to Stiffener/Skin Disbond

Toshimi Taki and Tomohiro Kitagawa

Kawasaki Heavy industries, Ltd.

Kenji Inaba

Mitsubishi Heavy Industries, Ltd.

## 1. INTRODUCTION

Stiffened panel is one of the basic structural elements of fibrous composites and it has been extensively applied to aircraft structures.

It is well known that composite stiffened panels fail with stiffener/skin disbond triggered by out-of-plane deflection of skin local buckling. Though the stiffener/skin disbond is the critical failure mode of composite stiffened panels, the methodology of the failure load prediction has not been established.

The authors propose to apply fracture mechanics to the stiffener/skin disbond. Coupon tests for stiffener/skin disbond are conducted to prove the applicability of the theory.

## 2. METHODOLOGY FOR PREDICTION OF STIFFENER/SKIN DISBOND STRENGTH

### (1) Strength Approach and Fracture Mechanics Approach

There are two approaches to treat the failure of stiffener/skin interface. They are the "strength approach" and the "fracture mechanics approach". The "strength approach" has been much more common than the "fracture mechanics approach" so far. Recent progress of fracture mechanics of fibrous composites enables us to apply the theory to the stiffener/skin disbond phenomenon. Fracture mechanics has some advantages over the "strength approach". They are :

* Closed form equations

* Applicability to fatigue strength

* Applicability to interface with initial delamination.

The authors intend to apply fracture mechanics to the prediction of stiffener/skin disbond strength.

### (2) Previous Work

Intensive research based on fracture mechanics was conducted for adhesively bonded metal structure in 1970s. The result of the research program, "Primary Adhesively Bonded Structure Technology (PABST)[1]" shows that fracture mechanics is applicable to the strength prediction of disbond of adhesively bonded joints.

Recently, there have been many investigations on delamination of fibrous composites and most of them are based on fracture mechanics[2],[3]. Fracture tests (DCB and ENF) for material evaluation have become very popular among fibrous composite suppliers and airframe manufactures. Inspite of the progress in such investigation, there have been few applications of fracture mechanics to the design of composite structures.

(3) Fracture Mechanics Model for Stiffener/Skin Disbond

The strain energy release rate is a measure of stiffener/skin disbond. Strain energy release rates for bending and tension are expressed as follows.

For bending moment ;

$$G_{total} = \frac{1}{2}\left(\frac{1}{EI_s} - \frac{1}{EI_0}\right)M^2$$

For tension load ;

$$G_{total} = \frac{1}{2}\left(\frac{1}{Et_s} - \frac{1}{Et_0}\right)T^2$$

where,

| | | |
|---|---|---|
| $G_{total}$ | : | strain energy release rate |
| $M$ | : | bending moment per unit width |
| $T$ | : | tensile load per unit width of skin |
| $EI_S$ | : | bending stiffness per unit width of skin |
| $EI_0$ | : | bending stiffness of stiffener/skin bonded region |
| $Et_S$ | : | axial stiffness per unit width of skin |
| $Et_0$ | : | axial stiffness of stiffener/skin bonded region |

Several criteria are proposed to determine the onset of disbond. The criterion by Wu[6] is used in this study.

$$\left(\frac{G_I}{G_{Ic}}\right)^m + \left(\frac{G_{II}}{G_{IIc}}\right)^n = 1$$

where,

| | | |
|---|---|---|
| $G_I$ | : | strain energy release rate for mode I |
| $G_{II}$ | : | strain energy release rate for mode II |
| $G_{Ic}$ | : | critical strain energy release rate for mode I |
| $G_{IIc}$ | : | critical strain energy release rate for mode II |
| $m, n$ | : | constants |

## 3. COUPON TESTS FOR STIFFENER/SKIN DISBOND

(1) Materials

The materials used for this study are two kinds of graphite/bismaleimides, which are the candidate materials for supersonic transport.

* NARMCO G40-800/5260

    - Nominal thickness : 0.134mm/ply

    - Tested by Kawasaki Heavy Industries

* Mitsubishi Rayon XMR/2002A

    - Nominal thickness : 0.143mm/ply

    - Tested by Mitsubishi Heavy Industries

(2) Tests

Coupon tests consist of material tests and disbond tests. Fracture toughness data, $G_{Ic}$ and $G_{IIc}$ of the materials are obtained by the material tests. The strengths for stiffener/skin disbond are also obtained by the disbond tests. Table 1 shows the number of test coupons for the material tests and disbond tests.

* Material tests

    - DCB test

    - ENF test

* Disbond Tests : see figure 1 and table 2.

    - 4-point bending test

    - 3-point bending test (Modified ENF test [5])

Tables 3 and 4 show the summary of the test results.

## 4. DISCUSSION

### (1) Strain Energy Release Rate for Disbond

The strain energy release rates, $G_{total}$ for the disbond onset are calculated from the disbond onset bending moments of the stiffener/skin disbond tests using the theory described above. The compliance matrices calculated from the lamina stiffness and the stacking sequences of the test coupons are used to calculate the strain energy release rates. The contribution of the mode I and mode II energy release rates to the total strain energy release rate are obtained by the method in ref.[2] and the local field solution is applied.

Figure 2 shows the relation between the mode I contribution and the critical strain energy release rate for the disbond onset. The figure contains additional data of tension disbond tests conducted by Kawasaki.

### (2) Disbond Onset Criterion for NARMCO Material

The interaction curve of disbond onset for the NARMCO material is also shown in figure 2 (curve A). The curve fits the test data well. It should be noted that the interaction curve B which uses $G_{Ic}$ and $G_{IIc}$ obtained from the material tests shows smaller disbond onset strength than curve A. This fact shows that multi-directional laminates have greater fracture toughness than unidirectional laminates.

### (3) Notes on Mitsubishi Rayon Material

From the data obtained in this study, it is not clear whether fracture mechanics is applicable to Mitsubishi Rayon material or not. The mode II fracture toughness obtained by ENF test is considerably larger than that of NARMCO material while $G_{Ic}$ of DCB tests are the same. There is a large difference between 3-point bending and 4-point bending. More data will be required to make some conclusions.
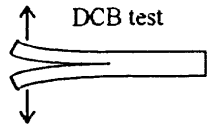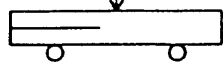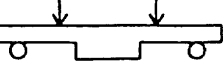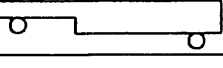
## 5. CONCLUSION

The preliminary data obtained in this study shows that fracture mechanics is applicable to the stiffener/skin disbond for stiffened panels made of fibrous composites. Further study is required to confirm the applicability of fracture mechanics to the disbond phenomenon.

6. REFERENCES

[1] Brussat, T. R., Chiu, S. T. and Mostovoy, S., "Fracture Mechanics for Structural Adhesive Bonds — Final Report," AFML-TR-77-163, AD-A054023, 1977.

[2] Williams, J. G., "On the Calculation of Energy Release Rates for Cracked Laminates," International Journal of Fracture, No.36, 1988, pp.101-119.

[3] Hashemi, S., Kinloch, A. J. and Williams, G., "Mixed-Mode Fracture in Fiber-polymer Composite Laminates, Composite Materials: Fatigue and Fracture (Third Volume), ASTM STP 1110, 1991, pp.143-168.

[4] Johnson, W. S. and Mall, S., "A Fracture Mechanics Approach for Designing Adhesively Bonded Joints, Delamination and Debonding of Materials, ASTM STP 876, ASTM STP 876, W. S. Johnson, Ed., American Society for Testing and Materials, 1985, pp.189-199.

[5] Hong, C. S., Yoon, S. H. and Kim, H. J., "Mixed Mode Interlaminar Fracture of Laminated Composite Using Modified End-Notched Flexure Specimen," Proceedings of the 9th International Conference on Experimental Mechanics, Vol.2, pp.472-483.

[6] Wu, E. W., "Application of Fracture Mechanics to Anisotropic Plates," Journal of Applied Mechanics, 34, pp.967-974.

### Table 1. Coupon Tests

| test | | materials | number of coupons |
|---|---|---|---|
| material tests | DCB test | NARMCO G40-800/5260 | 5 |
| | | Mitsubishi Rayon XMR/2002A | 5 |
| | ENF test | NARMCO G40-800/5260 | 5 |
| | | Mitsubishi Rayon XMR/2002A | 5 |
| disbond tests | 4-point bending test | NARMCO G40-800/5260 | 3type x 5each |
| | | Mitsubishi Rayon XMR/2002A | 1type x 5each |
| | 3-point bending test | NARMCO G40-800/5260 | 3type x 5each |
| | | Mitsubishi Rayon XMR/2002A | 1type x 5each |

## Table 2. Stacking Sequence of Disbond Test Coupons

|  | type 1 | type 2 | type 3 |
|---|---|---|---|
| stiffener | [+-45/90/0/90/+-45/90/0/90/-+45] 12plies | [+-45/90/0/90/+-45/90]s 16plies | [+-45/90/0/90/+-45/90]s 16plies |
| skin | [+-45/0/90/+-45/0/90/+-45/0/90]s 24plies | [+-45/0/90/+-45/0/90/+-45/0/90]s 24plies | [+-45/0/90/+-45/0/90]s 16plies |

## Table 3. Result of Material Tests

| material | critical strain energy release rate (kgf/mm) | |
|---|---|---|
|  | $G_{Ic}$ (DCB test) | $G_{IIc}$ (ENF test) |
| NARMCO G40-800/5260 | 0.0269 | 0.0876 |
| Mitsubishi Rayon XMR/2002A | 0.0238 | 0.235 |

## Table 4. Results of Disbond Tests

|  | material | coupon type | critical energy release rate $G_{c,total}$ (kgf/mm) | mode I contribution $G_I/G_{total}$ (%) |
|---|---|---|---|---|
| 4-point bending | NARMCO G40-800/5260 | type 1 | 0.111 | 52.9 |
|  |  | type 2 | 0.107 | 54.8 |
|  |  | type 3 | 0.074 | 57.3 |
|  | Mitsubishi Rayon XMR/2002A | type 1 | 0.124 | 51.9 |
| 3-point bending | NARMCO G40-800/5260 | type 1 | 0.076 | 52.0 |
|  |  | type 2 | 0.070 | 54.2 |
|  |  | type 3 | 0.073 | 56.6 |
|  | Mitsubishi Rayon XMR/2002A | type 1 | 0.058 | 52.2 |

4-Point Bending Test

3-Point Bending Test

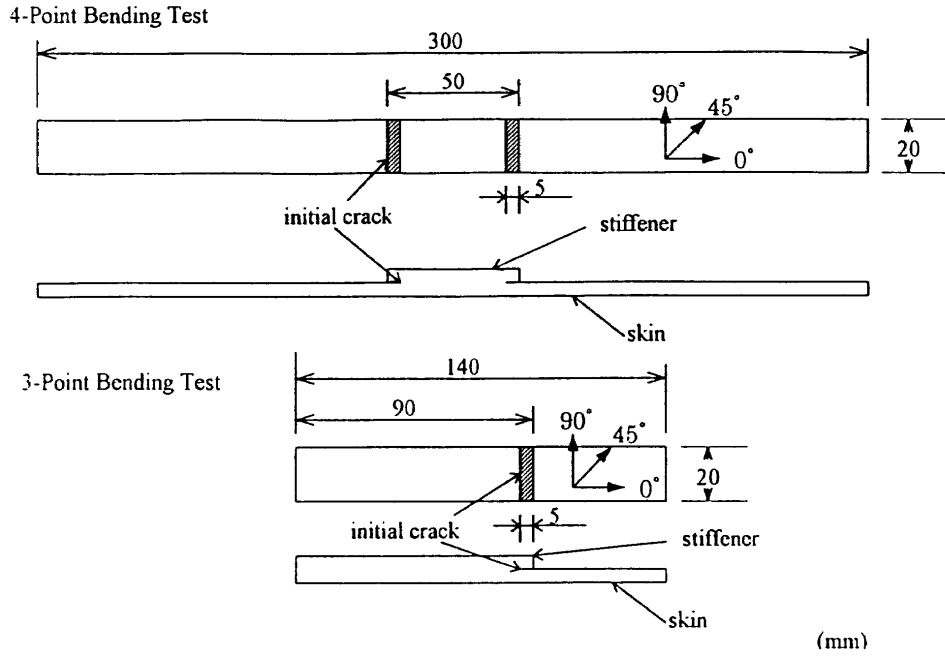Figure 1. Dimension of Disbond Test Coupons

curve A :  $G_{Ic} = 0.050$ kgf/mm, $G_{IIc} = 0.22$ kgf/mm

$m = n = 1.5$

curve B :  $G_{Ic} = 0.027$ kgf/mm, $G_{IIc} = 0.088$ kgf/mm

$m = n = 1.5$

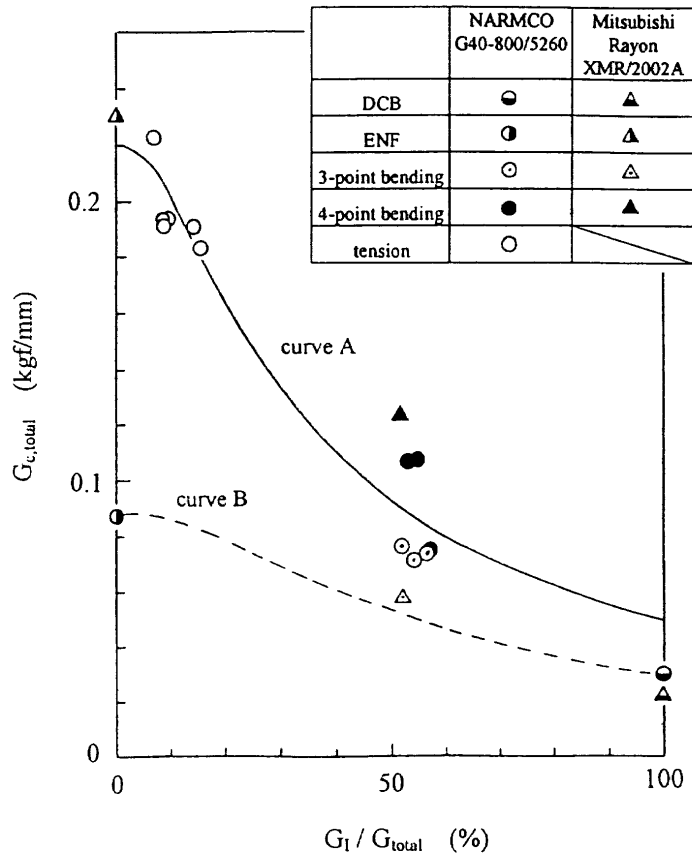| | NARMCO G40-800/5260 | Mitsubishi Rayon XMR/2002A |
|---|---|---|
| DCB | ◓ | ▲ |
| ENF | ◑ | ▲ |
| 3-point bending | ⊙ | △ |
| 4-point bending | ● | ▲ |
| tension | ○ | |

curve A

curve B

Figure 2.  Critical Strain Energy Release Rate
for Stiffener/Skin Disbond Onset

Printed in Japan